Development of a Novel Data Acquisition and Processing Methodology Applied to the Boresight Alignment of Marine Mobile LiDAR Systems

Thèse

Mohsen Hassanzadeh Shahraji

Doctorat en sciences géomatiques
Philosophiæ doctor (Ph. D.)

Québec, Canada

Development of a Novel Data Acquisition and Processing Methodology Applied to the Boresight Alignment of Marine Mobile LiDAR Systems

Thèse

Mohsen Hassanzadeh Shahraji

Sous la direction de :

Christian Larouche, directeur de recherche
Marc Cocard, codirecteur de recherche

Résumé

Le système LiDAR mobile (SLM) est une technologie d'acquisition de données de pointe qui permet de cartographier les scènes du monde réel en nuages de points 3D. Les applications du SLM sont très vastes, de la foresterie à la modélisation 3D des villes, en passant par l'évaluation de l'inventaire routier et la cartographie des infrastructures portuaires. Le SLM peut également être monté sur diverses plateformes, telles que des plateformes aériennes, terrestres, marines, etc.

Indépendamment de l'application et de la plateforme, pour s'assurer que le SLM atteigne sa performance optimale et sa meilleure précision, il est essentiel de traiter correctement les erreurs systématiques du système, spécialement l'erreur des angles de visée à laquelle on s'intéresse particulièrement dans cette thèse. L'erreur des angles de visée est définie comme le désalignement rotationnel des deux parties principales du SLM, le système de positionnement et d'orientation et le scanneur LiDAR, introduit par trois angles de visée. En fait, de petites variations angulaires dans ces paramètres peuvent causer des problèmes importants d'incertitude géométrique dans le nuage de points final et il est vital d'employer une méthode d'alignement pour faire face à la problématique de l'erreur des angles de visée de ces systèmes.

La plupart des méthodes existantes d'alignement des angles de visée qui ont été principalement développées pour les SLM aériens et terrestres, tirent profit d'éléments *in-situ* spécifiques et présents sur les sites de levés et adéquats pour ces méthodes. Par exemple, les éléments linéaires et planaires extraits des toits et des façades des maisons. Cependant, dans les environnements sans présence de ces éléments saillants comme la forêt, les zones rurales, les ports, où l'accès aux éléments appropriées pour l'alignement des angles de visée est presque impossible, les méthodes existantes fonctionnent mal, voire même pas du tout.

Par conséquent, cette recherche porte sur l'alignement des angles de visée d'un SLM dans un environnement complexe. Nous souhaitons donc introduire une procédure d'acquisition et traitement pour une préparation adéquate des données,

qui servira à la méthode d'alignement des angles de visée du SLM. Tout d'abord, nous explorons les différentes possibilités des éléments utilisés dans les méthodes existantes qui peuvent aider à l'identification de l'élément offrant le meilleur potentiel pour l'estimation des angles de visée d'un SLM. Ensuite, nous analysons, parmi un grand nombre de possibles configurations d'éléments (cibles) et patrons de lignes de balayage, celle qui nous apparaît la meilleure. Cette analyse est réalisée dans un environnement de simulation dans le but de générer différentes configurations de cibles et de lignes de balayage pour l'estimation des erreurs des angles de visée afin d'isoler la meilleure configuration possible. Enfin, nous validons la configuration proposée dans un scénario réel, soit l'étude de cas du port de Montréal. Le résultat de la validation révèle que la configuration proposée pour l'acquisition et le traitement des données mène à une méthode rigoureuse d'alignement des angles de visée qui est en même temps précise, robuste et répétable. Pour évaluer les résultats obtenus, nous avons également mis en œuvre une méthode d'évaluation de la précision relative, qui démontre l'amélioration de la précision du nuage de points après l'application de la procédure d'alignement des angles de visée.

Abstract

A Mobile LiDAR system (MLS) is a state-of-the-art data acquisition technology that maps real-world scenes in the form of 3D point clouds. The MLS's list of applications is vast, from forestry to 3D city modeling and road inventory assessment to port infrastructure mapping. The MLS can also be mounted on various platforms, such as aerial, terrestrial, marine, and so on.

Regardless of the application and the platform, to ensure that the MLS achieves its optimal performance and best accuracy, it is essential to adequately address the systematic errors of the system, especially the boresight error. The boresight error is the rotational misalignment offset of the two main parts of the MLS, the positioning and orientation system (POS) and the LiDAR scanner. Minor angular parameter variations can cause important geometric accuracy issues in the final point cloud. Therefore, it is vital to employ an alignment method to cope with the boresight error problem of such systems.

Most of the existing boresight alignment methods, which have been mainly developed for aerial and terrestrial MLS, take advantage of the *in-situ* tie-features in the environment that are adequate for these methods. For example, tie-line and tie-plane are extracted from building roofs and facades. However, in low-feature environments like forests, rural areas, ports, and harbors, where access to suitable tie-features for boresight alignment is nearly impossible, the existing methods malfunction or do not function.

Therefore, this research addresses the boresight alignment of a marine MLS in a low-feature maritime environment. Thus, we aim to introduce an acquisition procedure for suitable data preparation, which will serve as input for the boresight alignment method of a marine MLS. First, we explore various tie-features introduced in the existing ways that eventually assist in the identification of the suitable tie-feature for the boresight alignment of a marine MLS. Second, we study the best configuration for the data acquisition procedure, i.e., tie-feature(s) characteristics and the necessary scanning line pattern. This study is done in a simulation

environment to achieve the best visibility of the boresight errors on the selected suitable tie-feature. Finally, we validate the proposed configuration in a real-world scenario, which is the port of Montreal case study. The validation result reveals that the proposed data acquisition and processing configuration results in an accurate, robust, and repeatable rigorous boresight alignment method. We have also implemented a relative accuracy assessment to evaluate the obtained results, demonstrating an accuracy improvement of the point cloud after the boresight alignment procedure.

Table of Contents

List of Figures

List of Tables

List of Abbreviations

APPS	Advanced Post Processing Software
ARW	Angle Random Walk
CW	Continuous Wave
DCM	Direction Cosine Matrix
DEM	Digital Elevation Model
DTM	Digital Terrain Model
FOG	Fiber Optic Gyroscope
GNSS	Global Navigation Satellite System
GPS	Global Positioning System
GUI	Graphical User Interface
ICP	Iterative Closest Point
IMU	Inertial Measurement Unit
INS	Inertial Navigation System
KF	Kalman Filter
LGF	Local Geodetic Frame
LiDAR	Light Detection and Ranging
MLS	Mobile LiDAR System
POS	Positioning and Orientation System
PPS	Pulse Per Second
RANSAC	RANdom SAmple Consensus
RMSE	Root Mean Square Error
SBET	Smoothed Best Estimation Trajectory
SDK	Software Development Kit
SONAR	Sound Navigation and Ranging
TIN	Triangulated Irregular Network
TOF	Time of Flight
UTM	Universal Transverse Mercator
ZF	Zoller Fröhlich

To my dear and lovely parents,
Baba Ali and Maman Azam.

Acknowledgment

This thesis is the result of the collaboration of several partners. First, I would like to thank the organizations that primarily funded my Ph.D. project, the Interdisciplinary Development Centre for Ocean Mapping (CIDCO) and Mitacs through the **Mitacs Accelerate** Partnership Program. I sincerely thank Mitacs for all their efforts to advance research and fuel the knowledge economy in Canada. To avoid forgetting anyone, I will divide my thanks into three sections: Laval University, CIDCO, and Jakarto.

LAVAL UNIVERSITY - My first thanks go to my supervisor, Professor Christian Larouche, who offered me the precious opportunity to continue my studies at the Ph.D. level at Laval University. I had the chance to continue my research in a new and exciting field of mobile mapping. With his years of industry experience, Christian always did his best to help me confront the demanding technical and scientific problems I faced during my research and solve them with patience and insightful advice. Also, I am grateful for his constructive reviews while writing the papers and this thesis. His comments have improved the quality of my writing in both French and English. Thank you, Christian. I appreciate all the advice and help you have given me over the years.

I am also very grateful to my co-supervisor, Professor Marc Cocard. I took the advanced least squares adjustment course with him, which helped me a lot in the continuation of my Ph.D. research. I also thank him for his constructive reviews and comments on my papers and thesis.

I also sincerely thank Professor Sylvie Daniel for her efficient and rigorous pre-reading of my thesis and for taking the time to write a complete pre-reading report and an annotated version. She made several constructive comments that immensely helped improve the thesis's quality.

My sincere acknowledgments also go to all the people involved in my academic studies, especially Professor Mir Mostafavi, for his valuable comments and

encouragement. I also thank the jury members who kindly agreed to take several hours of their precious time to read, evaluate and provide any recommendations that would improve this thesis.

I also thank Stéphanie Bourgon, a teaching and research professional at the Department of geomatics sciences, for explaining some aspects of the iterative least squares method and reviewing my MATLAB codes.

I thank Guy-Jr Montreuil, the expert technician at the Metrology Laboratory, for fabricating the planar target prototypes and assembling the in-house mobile LiDAR systems.

CIDCO – I would like to thank Jean Laflamme, Executive Director of CIDCO. His active collaborations with Laval University led to projects such as my research project. Also, his generous sharing of CIDCO's human resources and equipment allowed my research project to progress efficiently.

I thank Nicolas Seube, former scientific director of CIDCO and my co-supervisor between 2017 and 2018. Even though we could not collaborate for long, I appreciated his scientific and technical vision, and I am very grateful for the help he gave me during these first two years.

I sincerely thank CIDCO's IT team, Guillaume Morissette, CIDCO's Director of Research and Development, and Jordan McManus, programmer-analyst, who worked hard to transform my prototype versions into professional software.

A big thank you to the hydrographic team of CIDCO, especially Papa Médoune Ndir, for the realization of the surveys at the Port of Montreal. The data acquired played an essential role in designing and evaluating the method proposed in this thesis.

Jakarto – I would like to thank the entire Jakarto team, especially Félix Laroche and Cédric Pelletier, for helping us set up our mobile LiDAR system and sharing their technical knowledge. They also generously lent us their LiDAR scanner (Z+F Profiler) for surveys at the Port of Montreal.

A big thank you to everyone who warmly welcomed me when I arrived at Laval University. It was an absolute pleasure to join this great and friendly team.

Finally, I sincerely thank my dear parents, Baba Ali and Maman Azam, my dear brother, Hossein, whom I missed a lot, and my beautiful and kind fiancée, Cynthia, for their continuous support over these years. Their warm encouragement gave me the greatest motivation to pursue this doctoral journey.

Preface

This thesis is with the insertion of two peer-reviewed scientific articles. The first author of these two articles is also the author of this thesis. All the material extracted from the articles has been rearranged according to the thesis template of the Faculty of Graduate and Postdoctoral Studies (FESP) of Laval University, which contains the chapters: introduction, bibliographic review, methodology, data acquisition system setup, results, discussion, and conclusion. The following is the publication status information of the inserted articles:

Paper # 1 – Integrated as Chapter 3

The title of this paper[1] is **"Analysis of Systematic Errors of Mobile LiDAR Systems: A Simulation Approach,"** and it has been published in ISPRS Annals of the Photogrammetry, Remote Sensing and Spatial Information Sciences, Volume V-1-2020, 2020 XXIV ISPRS Congress (2020 edition) (https://www.isprs-ann-photogramm-remote-sens-spatial-inf-sci.net/V-1-2020/253/2020/isprs-annals-V-1-2020-253-2020.html). I am the first author of this article, and I was involved in the following tasks: Conceptualization, Methodology, Software development, Investigation, Data collection, Validation, Visualization, Original draft writing, Reviewing, and editing the final version. The co-authors' roles in preparing this article are conceptualization, methodology, reviewing and editing the last version (**Christian Larouche**), and reviewing and editing the final version (**Marc Cocard**).

Furthermore, there are some modifications between the integrated version of the article and the original published version:

- Section 3.9, **"Complementary for Chapter 3,"** has been added at the end of Chapter 3. It provides additional analysis to adapt the topic to the maritime context and better link Chapter 3 to Chapter 4.

[1] Shahraji, M. H., C. Larouche, and M. Cocard. 2020. "ANALYSIS OF SYSTEMATIC ERRORS OF MOBILE LiDAR SYSTEMS: A SIMULATION APPROACH." *ISPRS Annals of Photogrammetry, Remote Sensing and Spatial Information Sciences* V-1–2020 (August): 253–260. https://doi.org/10.5194/isprs-annals-V-1-2020-253-2020.

- Figure 3.7 has been changed to meet a pre-reading recommendation of the thesis.

Paper # 2 – Integrated as Chapter 4

The title of this paper[2] is **"Case Study: Rigorous Boresight Alignment of a Marine Mobile LiDAR System Addressing the Specific Demands of Port Infrastructure Monitoring**,**"** published in Marine Geodesy journal and accessible online on 11 January 2022. (https://doi.org/10.1080/01490419.2022.2025503)

I am the first author of this article. I was involved in the following tasks: conceptualization, methodology, software development, investigation, data collection, validation, visualization, original draft writing, reviewing, and editing the final version. The role of the co-author, **Christian Larouche**, in preparing this article is as follows: conceptualization, methodology, reviewing, and editing of the final version.

[2] Shahraji, Mohsen H., and Christian Larouche. 2022. "Case Study: Rigorous Boresight Alignment of a Marine Mobile LiDAR System Addressing the Specific Demands of Port Infrastructure Monitoring." *Marine Geodesy*. Taylor & Francis, 1–33. doi:10.1080/01490419.2022.2025503.

Introduction

Context

For more than two decades, mobile LiDAR systems (MLS) have played a pivotal role in mapping our world to 3D point cloud datasets with unprecedented accuracy and density (Kalenjuk and Lienhart 2022; Heinz et al. 2020). An MLS comprises two main components, the positioning and orientation system (POS) and the LiDAR scanner. With the novel advances in sensor hardware technology, on the one hand, these components have reduced drastically in terms of size and price, and on the other hand, they have increased significantly in terms of accuracy and efficiency. Therefore, nowadays, these systems can be mounted on a variety of kinematic platforms (Kukko et al. 2012), e.g., aerial (Skaloud and Lichti 2006), drone (Keyetieu and Seube 2019), terrestrial (Leslar, Wang, and Hu 2016; Glennie 2008), marine (Shi et al. 2017; Thies 2011; Dix et al. 2012), backpack (Rönnholm et al. 2016; Hyyppä et al. 2020), and motorcycles (Shi et al. 2021; Yan et al. 2019). As a result, they can be applied in various environments and multiple applications, such as digital terrain model generation (Kraus and Pfeifer 2001; Costantino and Angelini 2013; Wang et al. 2019; Ziyue Chen, Gao, and Devereux 2017), forest inventory mapping (Mokroš et al. 2021; Bauwens et al. 2016; Ryding et al. 2015), 3D city modeling for digital twin creation (Wang et al. 2019; Huang et al. 2013), transportation corridor mapping (Vosselman and Maas 2011), road assets inventory (Guan et al. 2016; Heinz et al. 2019), and marine infrastructure monitoring (Thies 2011; Shi et al. 2017). In this thesis, the center of interest is a mobile LiDAR system mounted on a marine platform, also known as a marine mobile LiDAR system (marine MLS), used for marine infrastructure monitoring applications.

A marine MLS's main advantage is its ability to navigate through maritime environments such as ports, harbors, and coastal areas. It can regularly acquire 3d point clouds and is mainly used in maritime infrastructure inspection and coastal area management applications. To ensure that these infrastructures remain operational, they must be monitored regularly, have a clear assessment of the various infrastructure conditions, and finally, make a list of priorities of the required

maintenance and repair works based on the severity of the infrastructure damages. In general, for the infrastructure inspection, we need a 3D point accuracy at a 95 % confidence interval of less than 5 cm with a density of more than 200 pts/m^2 (Olsen et al. 2013; Guan et al. 2016), which is approximately the accuracy and density delivered by an MLS. However, to attain the accuracy needed for the infrastructure monitoring task, various factors that can influence the 3D point accuracy of an MLS must be addressed.

As mentioned earlier, an MLS comprises a POS and a LiDAR scanner. The POS comprises an inertial measurement unit (IMU) that measures the orientation and a GNSS antenna that receives the necessary data for measuring the platform's position. The LiDAR scanner measures the coordinates of each point of a point cloud in its local frame. We utilize these observations to generate a 3D point cloud of the area of interest. Thus, the sources that impact the 3d point cloud accuracy are observations from the LiDAR scanner and the POS. The other source of error is the POS and LiDAR scanner mounting error which can cause systematic errors and, as a result, degrade the accuracy of 3D points (Skaloud and Lichti 2006; Hebel and Stilla 2012). The mounting errors are divided into two main parts, the lever arm error and the boresight error (Schenk 2001). The lever arm error, which is the translation vector between the optical center of the LiDAR and the gravity center of the position and orientation system (POS), is typically measured with conventional surveying methods, and it is considered constant in calculations (Skaloud and Lichti 2006; Kalenjuk and Lienhart 2022), which is also the case in this thesis. The second mounting error, the boresight error, is the rotational misalignment between the POS and the LiDAR frames.

Contrary to the lever arm error, the boresight error cannot be measured directly with an external measurement tool, and as a matter of fact, it is preferable to estimate this error in a dynamic (in-flight) mode midst of the scanning operation (D. Li et al. 2016; Ravi and Habib 2020; Lindenthal et al. 2011). Therefore, by doing this, we ensure that the POS initialization has been done correctly and that the POS observation uncertainties are as small as possible. The reason for that is to reduce

the impact of the POS attitude observations on the estimation of the boresight error as much as possible, which means that if the POS attitude observations have high uncertainty, this will indeed affect the boresight error estimation.

Suppose we do not adequately address the errors of an MLS when scanning objects of interest with multiple passages. We can witness accumulated positional deviation and displacement in the final datasets, as shown in Figure a.

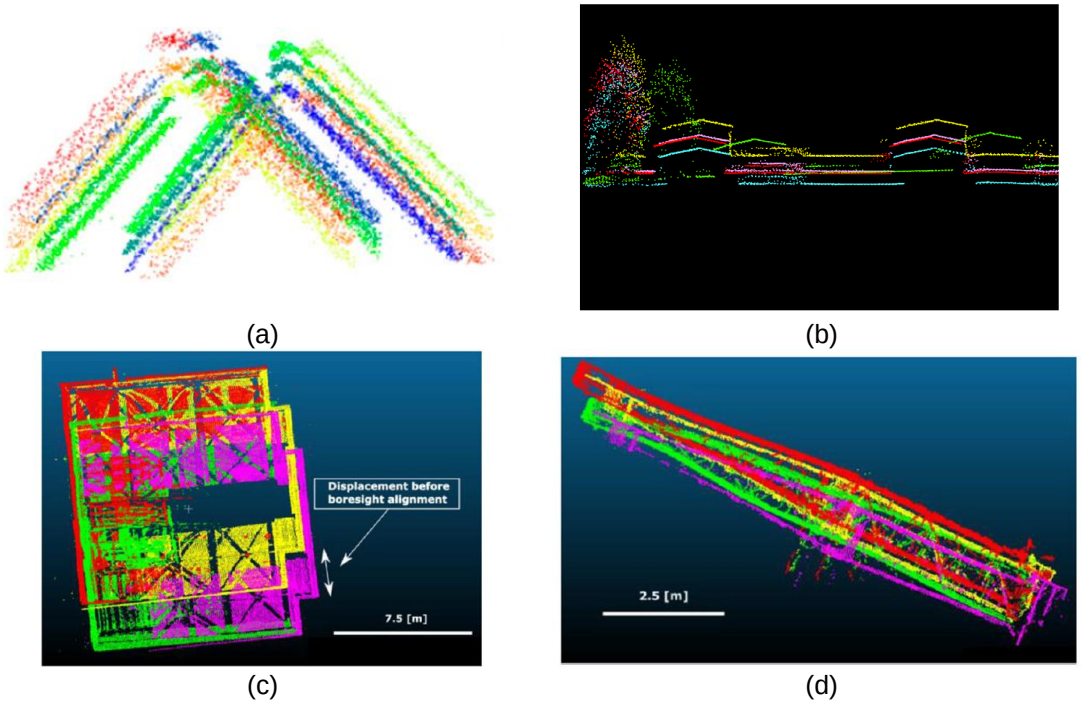

Figure a - Systematic errors effect on MLS point cloud that scanned an object of interest with multiple passages illustrated with a different color for each passage. (a) Drone MLS (Ravi et al. 2018). (b) Drone MLS (Keyetieu and Seube 2019). (c-d) Marine MLS (Shahraji and Larouche 2022).

In general, approaches that address MLS error reduction consist of two main categories: rigorous methods and non-rigorous methods.

The rigorous methods, also known as system-driven methods, determine the source of errors and estimate their standard deviations. Meanwhile, they require access to raw data of each component of the system, such as the trajectory observations in

the POS frame and the LiDAR point coordinates in the scanner frame, which are not always available to the end-user.

On the other hand, the non-rigorous methods, also known as data-driven methods, reduce the MLS error and utilize the final georeferenced point cloud as input. They do not need further information on the trajectory or LiDAR scanner raw data.

Generally, the methodology for handling MLS errors, such as boresight systematic error, can be described in three main steps. The first step is scanning a scene with overlapped strips of different directions and a specific line pattern that magnifies the discrepancies between generated point clouds. The second step is to connect the overlapped strips with tie-features. This step includes the detection of the tie-features and the matching of the accurate correspondences between various strips. The third step is to reduce the discrepancies between the tie-features on overlapped strips by adjustment methods such as the least squares technique.

The prevailing tie-features that are used in the MLS errors reduction methods are tie-point (Morin and El-Sheimy 2002; J. Zhang, Jiang, and Jiang 2012; Glira et al. 2015; Z. Li, Tan, and Liu 2019), tie-line (Vosselman 2002; Le Scouarnec et al. 2014; Ndir 2019), and tie-plane (Skaloud and Lichti 2006; Ravi and Habib 2020; Heinz et al. 2020). As mentioned before, these tie-features reveal the discrepancies between overlapped strips. These discrepancies are formed primarily because of the errors of the MLS, especially the boresight error. The performance of the MLS error reduction methods largely depends on the availability of these geometric tie-features and their respective configurations (D. Li et al. 2016; Ravi and Habib 2020; Heinz et al. 2020). The existing methods usually perform better in dense urban areas, where we have access to many geometric tie-features like planes with various configurations and orientations (Hebel and Stilla 2012). Therefore, these methods may encounter severe issues in low-feature environments like forest areas, rural zones, or port and harbor sections, which suffer from the lack of suitable geometric tie-features.

It is also essential to address the maritime context of this research. Figure b shows examples of marine infrastructure like quay wall surfaces. We can notice that these infrastructures suffer from corrosion due to the humidity of the port area. Also, due to the permanent exposure to salty water, the infrastructures built from iron or steel usually are corroded and oxidized and, thus, deformed. Therefore, we cannot count these surfaces as adequate tie-features for the MLS reduction methods.

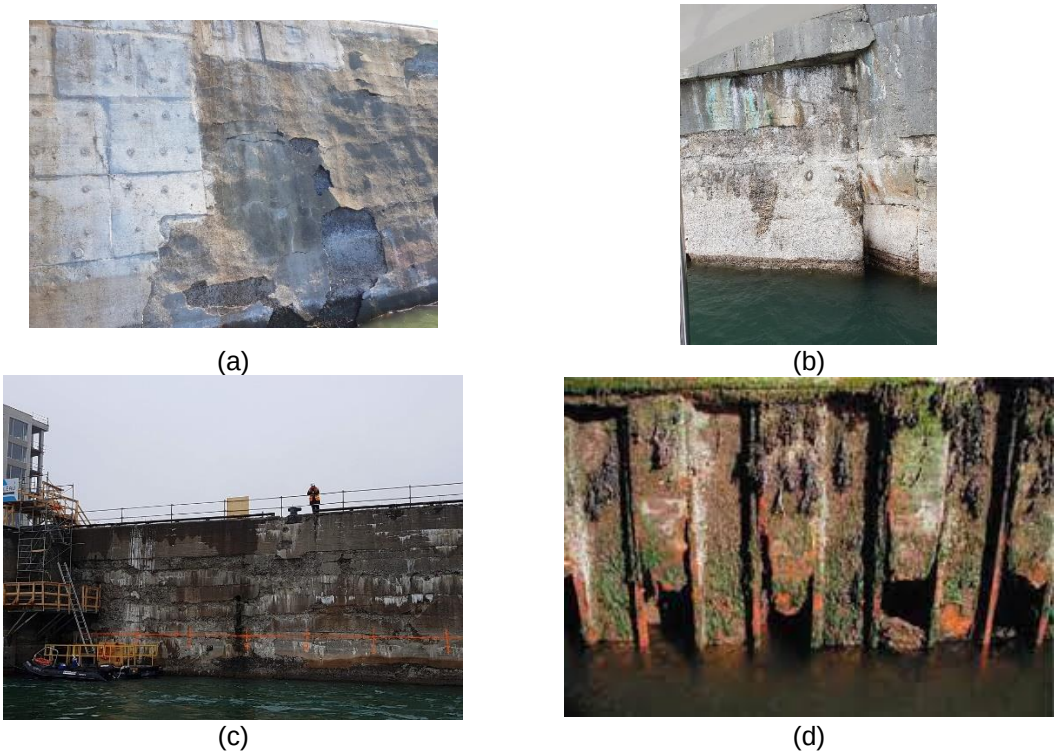

(a) (b) (c) (d)

Figure b - (a) (b) (c) Damaged quay walls as the central port infrastructure (Courtesy of CIDCO) (d) Corroded steel quay wall with submerged steel surface (Allianz Global Corporate & Specialty 2016).

Research Aim and Objectives

In summary, the problem we want to address in this thesis is the reduction of errors, especially the boresight error of a marine mobile LiDAR system that operates in a low-feature maritime environment. This problem motivated the CIDCO, an R&D center for hydrographic mapping, and Université Laval to collaborate on a research project financed by Mitacs Acceleration Funding, which led to this thesis.

This study aims to define, design, and evaluate the optimal configuration of a suitable data acquisition procedure to accomplish the boresight alignment of a marine MLS for infrastructure inspection. Based on the aim of the study, we define the research objectives in the context of port infrastructure monitoring as follows,

Objective # 1: Identify a suitable geometric tie-feature for the boresight alignment of a marine mobile LiDAR system.

Objective # 2: Design an optimal site configuration and an efficient data acquisition procedure for extracting suitable geometric tie-features for the boresight alignment of a marine mobile LiDAR system.

Objective # 3: Evaluate the proposed configurations of the data acquisition procedure for the boresight alignment of a marine mobile LiDAR system in terms of robustness, accuracy, and repeatability.

Thesis Outline

The thesis is divided into three main sections, each responding to one of the threefold objectives.

Mobile LiDAR system, its errors, and existing method for reduction of MLS errors. Chapter 1 introduces an MLS and its components while describing the errors that may affect the system. This chapter also represents survey-grade monitoring applications that require high-precision, high-accuracy, and high-density point clouds. **Chapter 2** presents a comprehensive review of the existing methods for reducing MLS errors and, as a result, improving the generated point cloud accuracy. This section responds to the first objective of the thesis.

Optimal configuration of boresight alignment site design with a simulated approach. Chapter 3 addresses the development of an MLS point cloud generator we named ‘MLS simulator’ in this thesis. The MLS simulator puts together a virtual environment for the analysis of each of the systematic errors of the system individually and collectively with different combinations, which leads to an optimal

design of the best configuration for the boresight alignment site design in the context of port infrastructure monitoring. A peer-reviewed scientific paper entitled "*Analysis of systematic errors of mobile LiDAR systems: a simulation approach*" represents the main content of this chapter. This section addresses the second objective of the thesis.

Implementation in the real world and accuracy assessment of the proposed method. Chapter 4 presents the proposed boresight alignment site design and configuration of a mobile LiDAR system in the real-world context of port infrastructure monitoring. In this chapter, we also use the MLS simulator to select the best configuration of the suggested geometric tie-features. It also presents the implementation procedure of the developed boresight alignment method to a real dataset acquired at the Port of Montreal. The detail of the implementation procedure and each part's results are described in this chapter. This chapter also describes the evaluation of the proposed method and the obtained results. A peer-reviewed scientific paper entitled "Case Study: *Rigorous Boresight Alignment of a Marine Mobile LiDAR System Addressing the Specific Demands of Port Infrastructure Monitoring*" represents the main content of this chapter. This section addresses the third objective of the thesis.

The **Conclusion and Future Works Section** presents a summary of the thesis, emphasizing its main contributions and perspectives for future works. The bibliography and the appendices follow it. **Appendix A** describes the assembly phase of the in-house customized MLS. **Appendix B** presents algorithms and a portion of the source codes developed for this research. Finally, **Appendix C** is a complementary analysis of all the systematic errors using our simulation approach.

Chapter 1 - Mobile LiDAR Systems

1.1 Introduction

This chapter aims to give a broad description of mobile LiDAR systems (MLS), and at the same time, a more specific view of the in-house customized MLS mounted on a hydrographic vessel (marine MLS) in the context of the research presented in this thesis.

Besides the overall presentation of an MLS, we discuss its main components, i.e., the LiDAR scanner and the positioning and orientation system (POS), with a particular emphasis on the errors that reduce the quality of the point cloud generated by an MLS. The last section of this chapter discusses two survey-grade applications of an MLS, e.g., road inventory assessment and port infrastructure monitoring.

1.2 Main Components

In this section, we introduce all components of an MLS and explain in detail the procedure that generates the 3D georeferenced point cloud of the scanned scene of interest from raw observations produced by every sensor individually.

1.2.1 LiDAR Scanner

The LiDAR (Light Detection and Ranging) scanner measures the distance between its optical center and a point on the object of interest by emitting a light pulse and subsequently calculating the time delay that the emitted light pulse creates by traveling this distance (Vosselman and Maas 2011; Shan and Toth 2008). If we directly measure the time delay by an internal clock, the method is called time-of-flight or TOF (Vosselman and Maas 2011). However, if we measure the phase difference measurement of the transmitted and received laser beam, it is called the continuous wave (CW) method (Shan and Toth 2008). The TOF-based systems cover a much longer distance (up to 1000 m) than the CW-based systems that have a much shorter operating range (less than 120 m). On the other hand, the data acquisition rate of the CW-based systems (for example, for Z+F Profiler 9012® is

1.016 million points per second) is higher than the TOF-based systems (for example for RIEGL® VZ-400i is 500,000 points per second) (Vosselman and Maas 2011).

In this research, we utilize a 2D profiler as a LiDAR scanner, the Z+F Profiler® 9012 manufactured by Zoller + Fröhlich GmbH company, which is considered a CW-based system and is a high-speed phase-based laser scanner with a data acquisition rate of more than 1 million points per second (1 MHz) and maximum scan speed frequency of 200 scans (profiles) per second (Zoller & Frohlich GmbH 2012; Heinz et al. 2018). Table 1.1 provides the main characteristics of the Z+F Profiler® 9012. The Z+F Profiler® 9012 records single 2D profiles; therefore, to deliver 3D point clouds of the environment, this 2D scanner must be mounted on a mobile platform, such as a terrestrial vehicle or a hydrographic vessel, and traverse a 3D trajectory (Zoller & Frohlich GmbH 2012; Heinz et al. 2018) as shown in Figure 1.1.

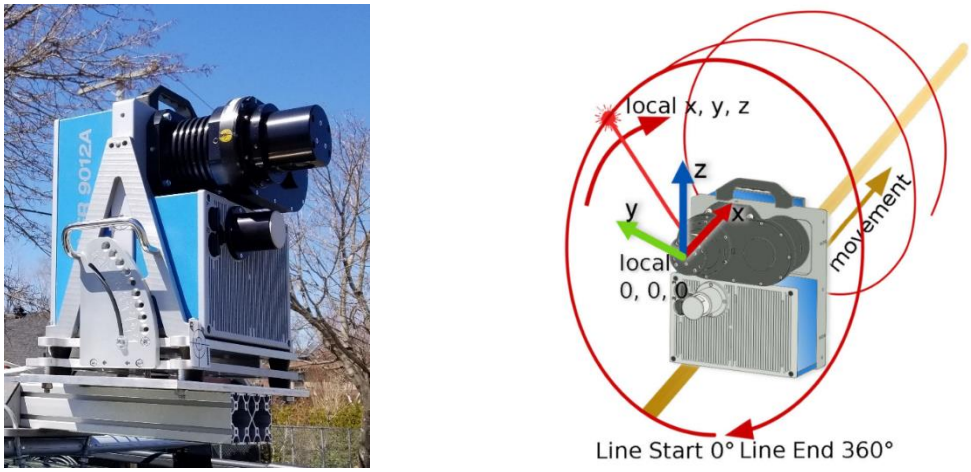

(a) (b)

Figure 1.1 – Z+F Profiler ® 9012. (a) mounted on a terrestrial platform (b) scanner local frame with the center of phase and the scanner rotation convention

The Z+F Profiler® 9012 has a 360º field of view, and the coordinates of the point of interest are first calculated in the local coordinate system (LiDAR scanner frame) with the origin (0, 0, 0) at the optical center of the laser scanner. Based on the specifications of this scanner in terms of accuracy and density, the Z+F Profiler® 9012 has the potential to produce a 3D point cloud for survey-grade applications such as port infrastructure monitoring.

Table 1.1 – Specifications of ZF Profiler 9012 (Zoller & Frohlich GmbH 2022)

Sensor Type	Technology	Range Error	Angular Resolution	Beam Divergence	Angular Uncertainty
ZF LiDAR 2D Profiler® 9012	Continuous Wave	0.0087 m	0.0088 °	< 0.5 mrad	0.02 °

1.2.2 Positioning and Orientation System (POS)

As mentioned in the previous section, to generate a 3D point cloud presentation of the real-world environment, we need to integrate the LiDAR scanner data with a POS that estimates the trajectory of the moving platform at a rate between 50 to 200 Hz. The POS comprises two main parts: an inertial navigation system (INS) and a global navigation satellite system (GNSS) receiver. In the following, we explain in detail these two components.

An INS consists of an inertial measurement unit (IMU) and a processing unit, which its IMU comprises three gyroscopes for the angular rates measurement and three accelerometers for the linear accelerations measurement of the system in three sensitive axes. The output of such a system is an estimation of the position and the platform's velocity (Lefevre et al. 2020).

The GNSS receiver consists of an antenna and an embedded processor. The position of each satellite in the Earth’s orbit and its precise atomic time are transmitted to the GNSS receiver by electromagnetic signals. With the information of a minimum of four visible satellites, we can estimate the system's position, velocity, and time (Schaer 2010).

INS and GNSS can both estimate the position and velocity of the system. However, there are some differences between these two technologies. The INS estimates the six degrees of freedom or parameters at a higher frequency (up to 200 Hz) with reasonable accuracy for a short period. However, it usually drifts drastically after that short time. Some studies show that a trajectory adjustment using INS observations

only is feasible for distances below 100 m (Hussnain, Elberink, and Vosselman 2018). On the other hand, although the GNSS receiver collects data at a lower frequency (below 10 Hz) and contains more noise, the capability to re-adjust its position frequently makes this technology a more stable source of position data for a more extended period. Thus, the natural approach is to integrate these two technologies for the estimation of the position and velocity of the trajectory in a long scanning operation on mobile platforms.

One approach to integrating GNSS and INS technologies is the GNSS-aided INS technique. The GNSS-aided INS estimates unknown variables, i.e., position, orientation, and velocity, based on a series of uncertain measurements. The GNSS-aided INS is done with the help of a Kalman Filter estimation/prediction algorithm (Petovello 2003; Skog 2007; Kalman 1960). Thus, using a Kalman Filter, the GNSS-aided INS technique provides more accurate position, velocity, and attitude (orientation) parameters than each GNSS or INS in a standalone mode. Also, the GNSS-aided INS can fill the gap between the GNSS and INS measurements. As mentioned earlier, the GNSS measurements typically have 1 Hz (one measurement per second), and the INS measurements typically have 200 Hz (200 measurements per second). Therefore, GNSS measurements can adjust the drift issue of INS measurements (Farrell 2008; Jekeli 2012; Groves 2013).

In the following, we describe the characteristics of the GNSS-aided INS used in the customized in-house MLS that was conceived in this research, the Hydrins GNSS-aided INS manufactured by iXBlue company. This navigation-grade INS designed explicitly for hydrographic surveys is composed of an IMU with three fiber-optic gyroscopes (FOG), three high-precision pendulum-type accelerometers, and a Septentrio GNSS receiver (Lefevre et al. 2020; IXblue 2019), as shown in Figure 1.2.

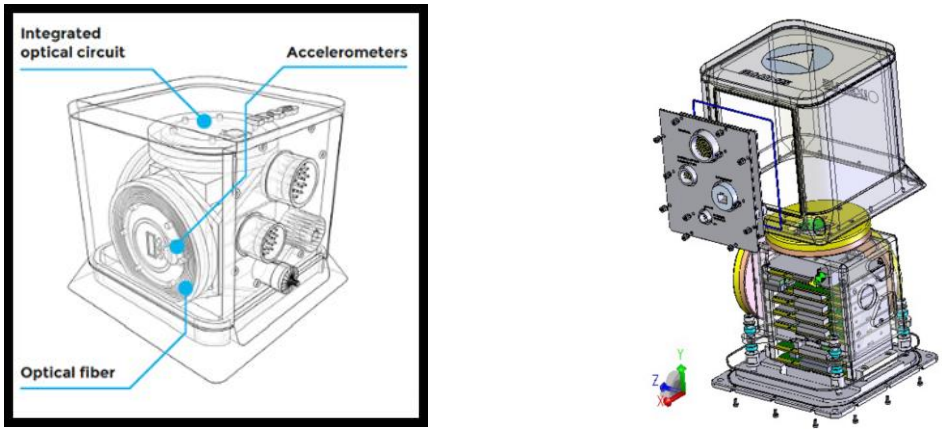

Figure 1.2 – Hydrins/iXBlue gyroscope conceptual model (courtesy of iXBlue.inc)

Here, we present two essential characteristics of the IMU component of the Hydrins/iXblue GNSS-aided INS.

Bias Stability: This parameter presents the deviation of the gyroscope from its mean value. Since the FOG is a solid-state sensor, it does not produce any acoustic vibration over a high dynamic range. For Hydrins/iXblue, this value is 0.0065 (deg/hr), which means that it will take approximately six days for a drift of 1 deg with this gyroscope, which shows its stability.

Angle Random Walk (ARW): This parameter is a noise specification of the sensor in units of deg/(hr)$^{1/2}$. It describes the average deviation or error the gyroscopes will have when the integrated signal (Stockwell 2003). In Hydrins/iXblue, the FOG has an ARW of 0.003 deg/(hr) ^{½}, which means after 10,000 sec (2.7 h), the standard deviation will be 0.3 deg, which is considered a shallow level of noise.

These two characteristics of Hydrins/iXblue justify their utilization in integrating with the LiDAR scanner. Figure 1.3 illustrates a GNSS-aided INS, which integrates the IMU with the GNSS receiver and an embedded processor that implements the Kalman filter algorithm.

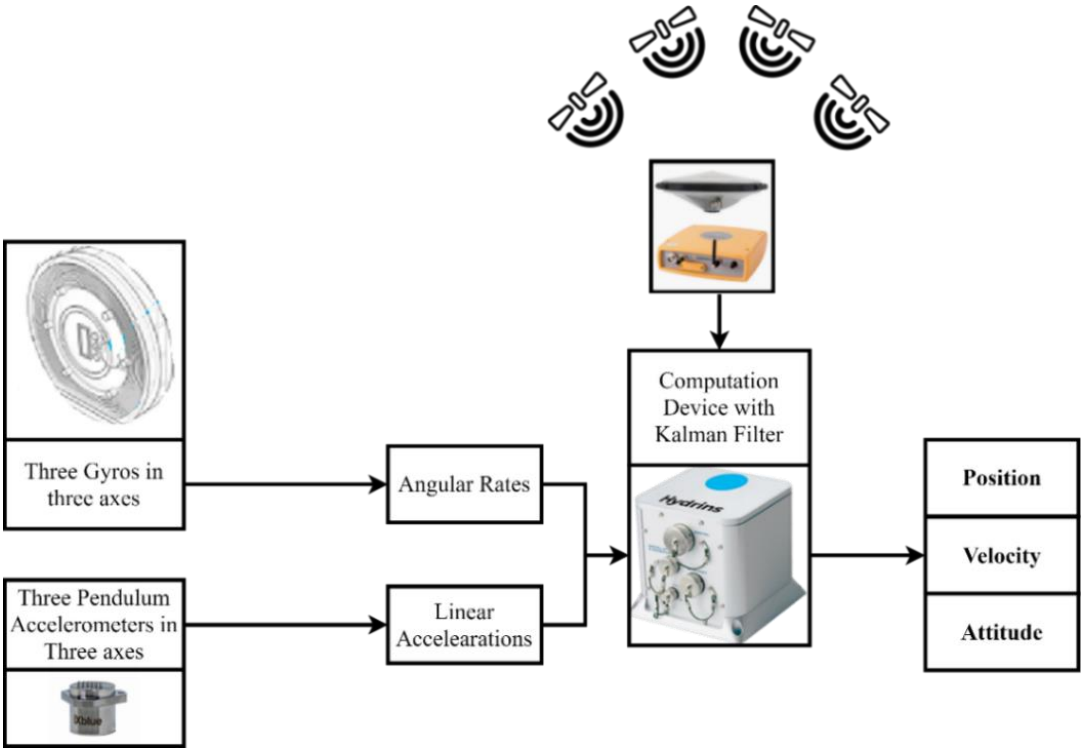

Figure 1.3 – Hydrins/AsteRx GNSS-aided inertial navigation system

The embedded computer in the INS uses these measurements and, through its algorithms, calculates the 3D angular positions, also known as orientations (roll, pitch, and heading), 3D velocity, and 3D position of the moving platform. The algorithm in the embedded computer also uses data from the GNSS receiver to provide initial values for the integrations and to refine the estimated parameters.

One of the main advantages of Hydrins INS is the possibility to calculate the true heading only with a single GNSS receiver. A Kalman filter also does this calculation in the embedded computer inside the INS (Petovello 2003; Angrisano 2010). With some specific maneuver on the trajectory, we initiate a necessary variation on the velocity vector, which eventually leads the Kalman filter to converge the initial approximative heading towards a true heading estimation.

The marine MLS is exposed to a vertical displacement due to the rise and fall movements of the vessel, which is caused by the sea wave motion and often occurs

in marine survey environments. This vertical displacement can cause an error relative to the mean sea level, called the heave (see Figure 1.4). Hydrins INS measures this vertical displacement and implements a post-processing adjustment to reduce its impact on the final trajectory data. (IXblue 2019; Novatel 2021; Applanix 2021).

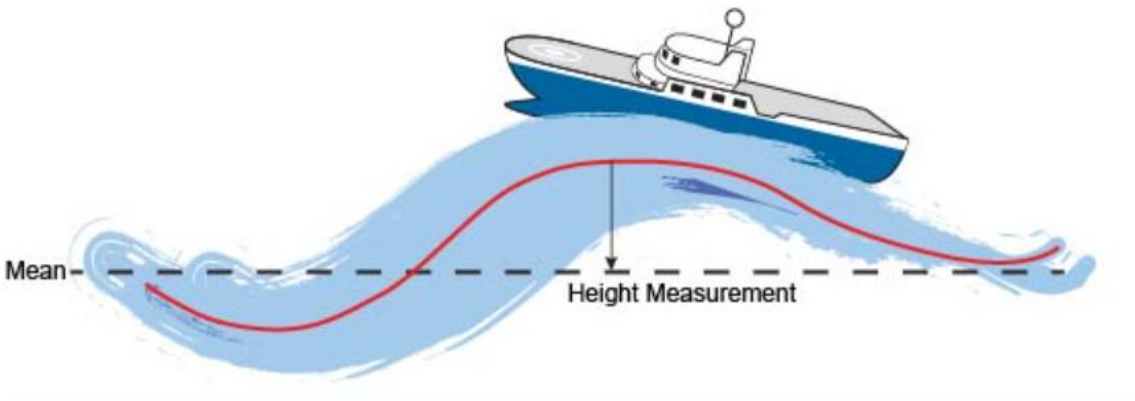

Figure 1.4 – Heave measurement relative to the mean sea level (Novatel 2021)

Heave measurements mainly aid the acquisition system sensors like SONAR and LiDAR to mitigate the impact of this vertical error that can cause a significant error in the range measurement. Table 1.2 represents the specifications of the iXblue Hydrins.

Table 1.2 – Hydrins specifications (IXblue 2019)

Sensor Type	Type	Heading accuracy	Roll and Pitch accuracy	Horizontal accuracy	Vertical accuracy
Hydrins iXblue	Navigation grade INS	0.01 °	0.01 °	0.006 + 0.5 ppm	0.01 + 1 ppm

Finally, we employ a post-processing procedure on the logged trajectory data to reduce the uncertainty of the orientation and positioning data. Offline post-processing procedure makes it easy to access the data for each epoch of the trajectory and before and after that epoch. Thus, we can use all this information to

optimize the orientation and positioning data and produce a so-called “smoothed best estimation trajectory” or SBET solution (Vosselman and Maas 2011).

1.3 Direct Georeferencing Mathematical Model

In this section, we define the direct georeferencing procedure that takes the raw point cloud data observed by the LiDAR scanner and the trajectory data observed by the POS and delivers a georeferenced 3D point cloud of the scanned scene. As shown in Figure 1.5, we transfer the raw data into three coordinate systems (or frames); from the LiDAR local frame to the POS frame and finally to the Local Geodetic Frame (LGF). When applying the boresight alignment, only a tiny portion of the earth is used, which can be considered tangential to the earth's surface. This assumption allows us to simplify the calculation of the georeferenced coordinates of the points onto a local geodetic frame.

Equation (1.1) represents the mathematical model of the direct georeferencing module of an MLS, similar to the formulation presented in different articles (Ackermann 1999; Wehr and Lohr 1999).

The output of the Equation (1.1) model is the georeferenced point in a coordinate system such as the Local Geodetic Frame (LGF), which is a relative frame with respect to the tangential plane on the area of interest on the earth.

$$\begin{bmatrix} X^{LGF} \\ Y^{LGF} \\ Z^{LGF} \end{bmatrix} = \begin{bmatrix} P_X^{LGF} \\ P_Y^{LGF} \\ P_Z^{LGF} \end{bmatrix} + R_{POS}^{LGF}(r,p,h) \left(R_{LiDAR}^{POS}(\alpha,\beta,\gamma) \begin{bmatrix} x_{LiDAR} \\ y_{LiDAR} \\ z_{LiDAR} \end{bmatrix} + \begin{bmatrix} a_X^{POS} \\ a_Y^{POS} \\ a_Z^{POS} \end{bmatrix} \right) \tag{1.1}$$

In Equation (1.1), we recognize three frames, the *LiDAR* sensor local frame, the *POS* navigation frame, and the LGF mapping frame.

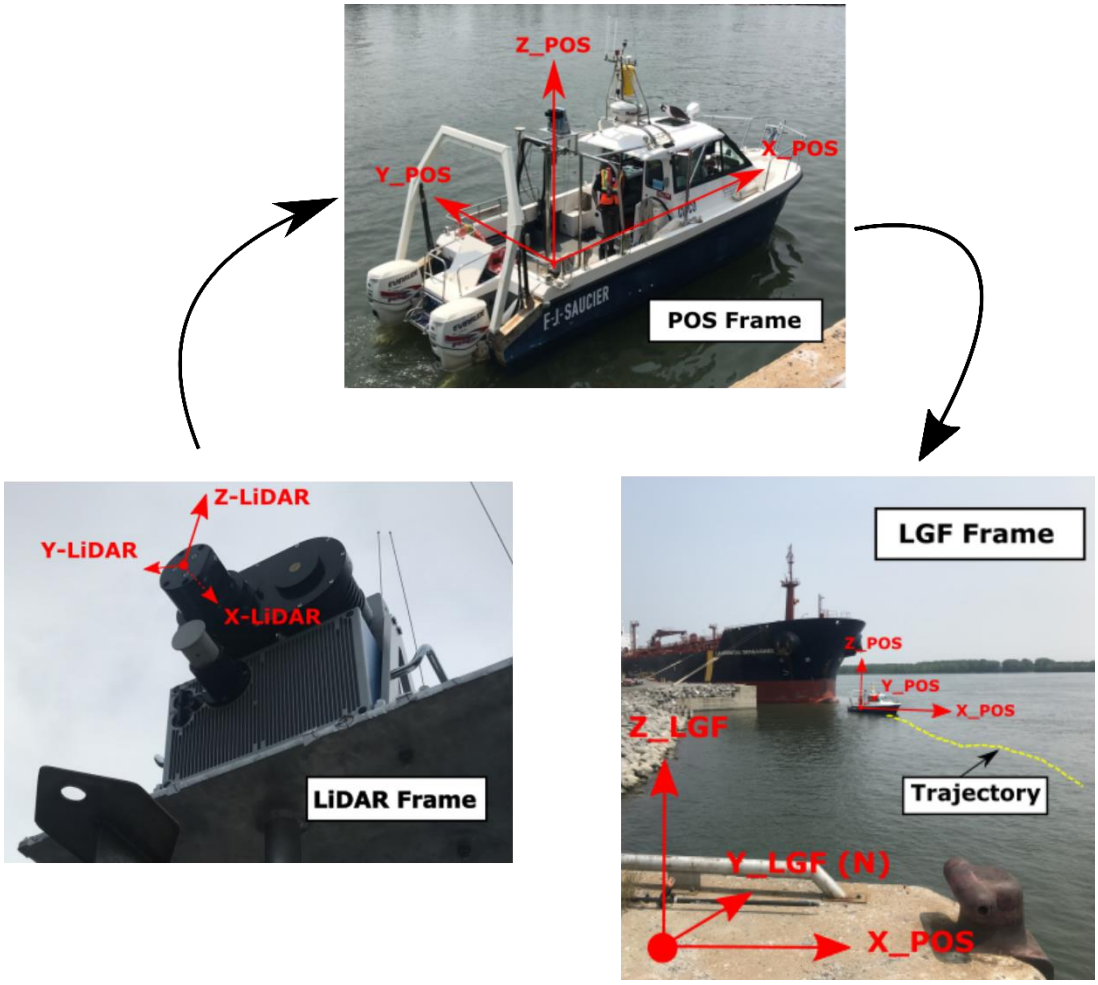

Figure 1.5 – Transformation between three main reference frames (LiDAR, POS, and LGF)

Here, we describe each part of the direct georeferencing mathematical model,

- $[X^{LGF} \quad Y^{LGF} \quad Z^{LGF}]^T$ is the computed 3D position vector of the georeferenced point in the *LGF* frame.
- $[P_X^{LGF} \quad P_Y^{LGF} \quad P_Z^{LGF}]^T$ is the observed 3D position vector for each trajectory point in the *LGF* frame by the GNSS receiver.
- $R_{POS}^{LGF}(r,p,h)$ is the rotation matrix, made of three attitude angles: roll (r), pitch (p), and heading (h) observed by the IMU, between the gravity center of the *POS* frame and the reference point of the *LGF* frame.
- $R_{LiDAR}^{POS}(\alpha,\beta,\gamma)$ is the rotation matrix, which consists of three boresight angles (α,β,γ) estimated by calibration between the *LiDAR* frame and the *POS* frame.

- $[x_{LiDAR} \quad y_{LiDAR} \quad z_{LiDAR}]^T$ is the observed 3D position vector of each target point by the LiDAR scanner with respect to the optical center of the scanner in the *LiDAR* frame.
- $[a_X^{POS} \quad b_Y^{POS} \quad a_Z^{POS}]^T$ is the 3D lever arm vector between the LiDAR scanner and the *POS* origin estimated by calibration.

Figure 1.6 illustrates the three principal coordinate systems that enable us to generate a 3D georeferenced point cloud.

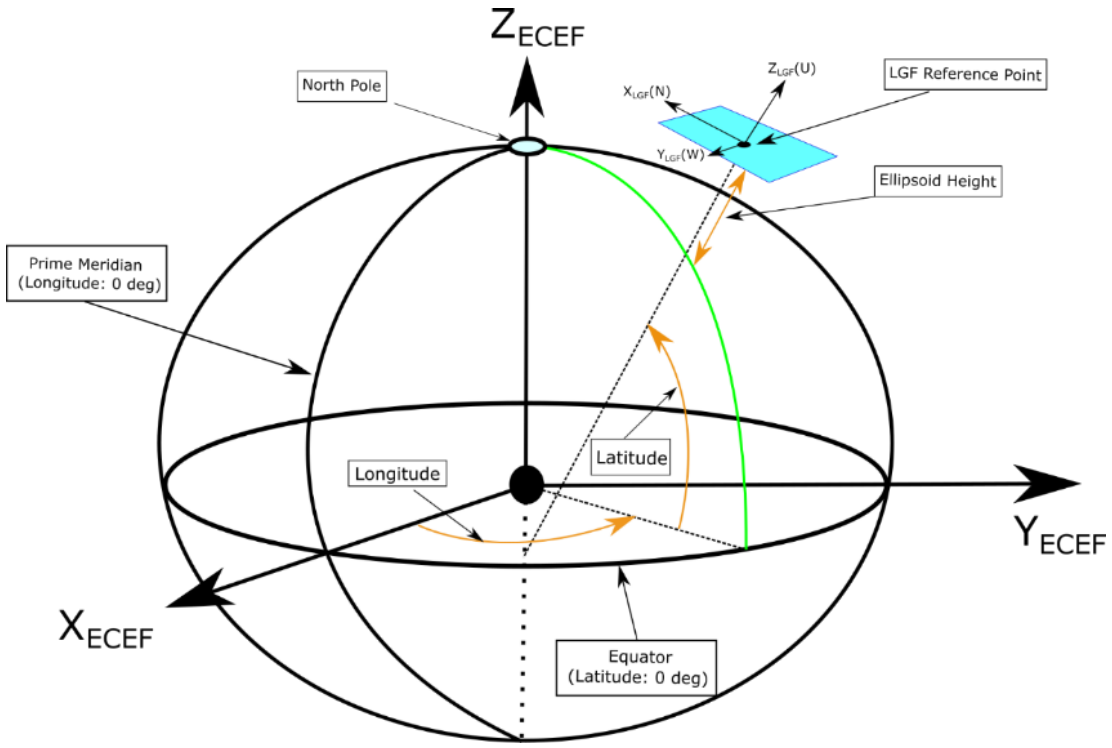

Figure 1.6 – Three main coordinate systems in a georeferencing mathematical model, Geographic coordinate system (latitude, longitude, and ellipsoidal height), Earth-Centric-Earth-Fix (ECEF), and North-West-Up (NWU). (Groves 2013)

The GNSS receiver delivers the position of the platform in a geographic coordinate system, which consists of latitude (φ), longitude (λ), and ellipsoid height (h).

The positioning coordinates from the geographic coordinate system are passed through the Earth-Centric-Earth-Fix (ECEF) coordinate system to achieve the coordinates in the local geodetic frame. The transformation between various coordinate systems is illustrated in Figure 1.7. Also, the positions of the points are

at the GNSS receiver in a geographical coordinate system with latitude (φ), longitude (λ), and ellipsoid height (h). The points from the geographic coordinate system with (φ, λ, h) are transformed to coordinates of the terrestrial reference frame (TRF) of the ECEF coordinate system (Cai, Chen, and Lee 2011).

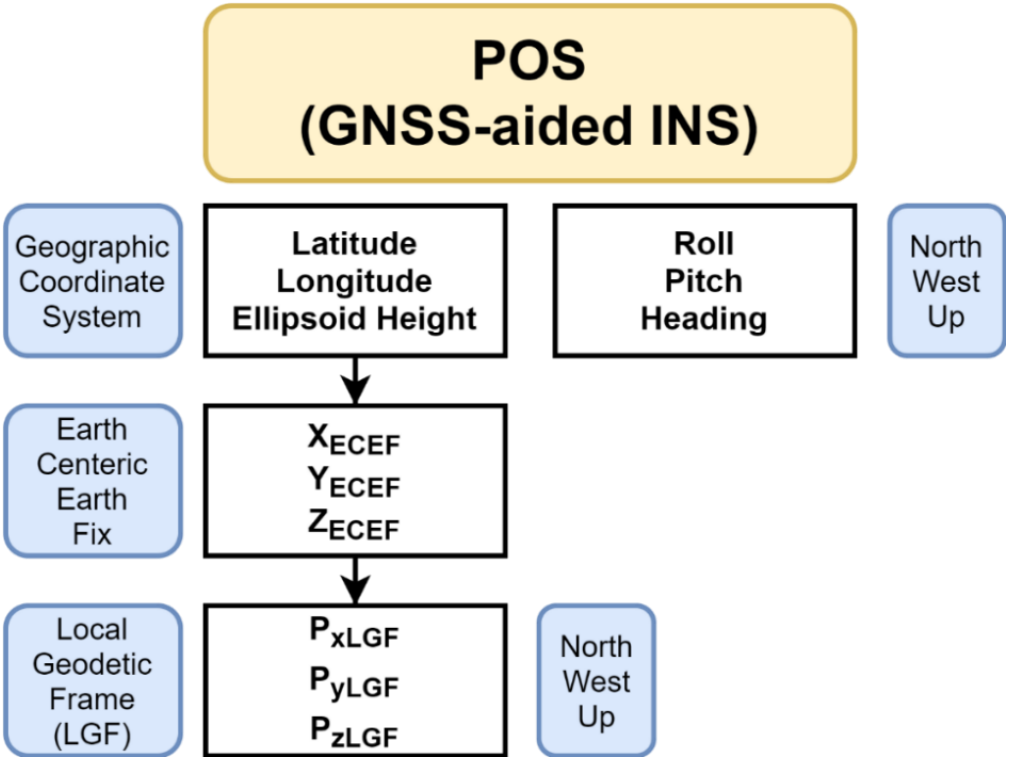

Figure 1.7 – Transformations between coordinate systems

Finally, the coordinates from TRF are then transformed to a local geodetic frame (LGF) with NWU (North-West-Up) convention in our case (IXblue 2019). All these transformations are available in Equation (1.2).

$$P_{LGF} = R_{ECEF}^{LGF}\left(\lambda_{Ref}, \varphi_{Ref}\right)\left[P_{ECEF}(\lambda, \varphi) - P_{ECEF}(\lambda_{Ref}, \varphi_{Ref})\right] \quad (1.2)$$

Equation (1.2) consists of the coordinates of the points in the ECEF coordinate system (P_{ECEF}), which are calculated with Equation (1.3) from the geographical coordinates of each point (φ, λ, h),

$$P_{ECEF} = \begin{pmatrix} x \\ y \\ z \end{pmatrix}_{ECEF} = \begin{bmatrix} (N_E + h)cos\varphi cos\lambda \\ (N_E + h)cos\varphi sin\lambda \\ (N_E(1 - e^2) + h)sin\varphi \end{bmatrix} \quad (1.3)$$

Radius of curvature in the vertical prime	*WGS84 datum*	
	Semi-major axis	*First eccentricity*
$N_E = \frac{a}{\sqrt{1 - e^2 \sin^2 \varphi}}$	$a = 6378137.0\ m$	$e = 0.08181919$

Another part of Equation (1.2) is the rotation matrix between the ECEF and LGF (R_{ECEF}^{LGF}). Figure 1.8 illustrates this rotation matrix, composed of two inner rotation matrices.

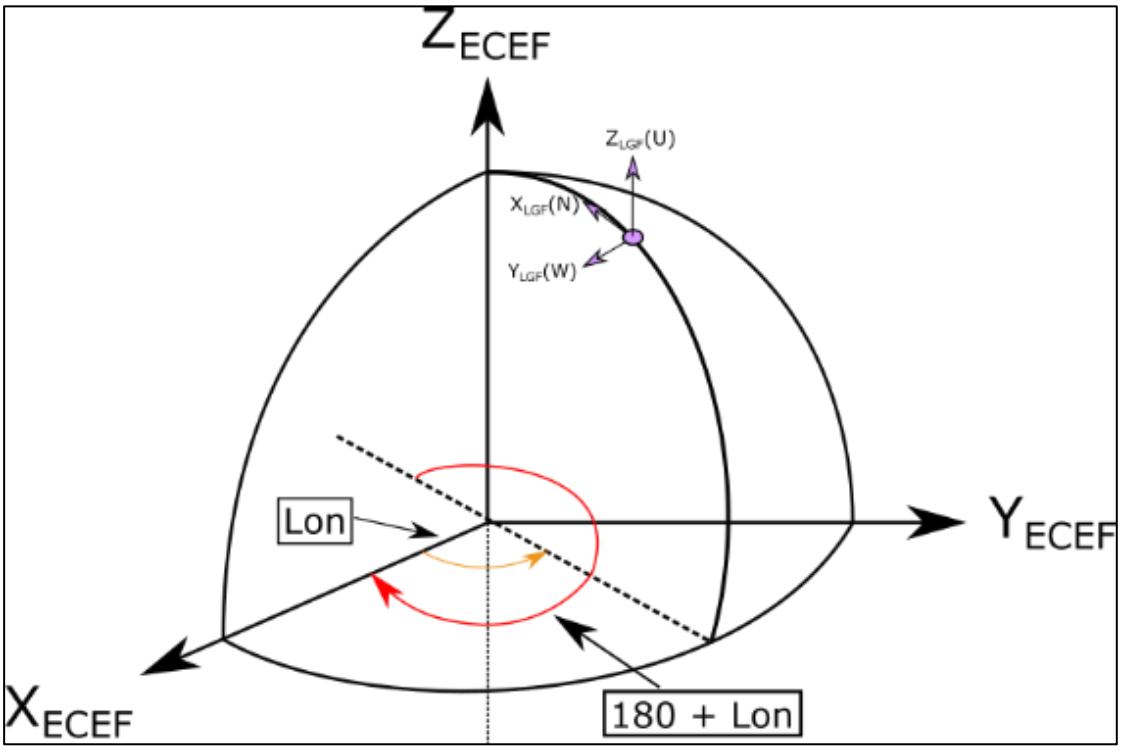

(a)

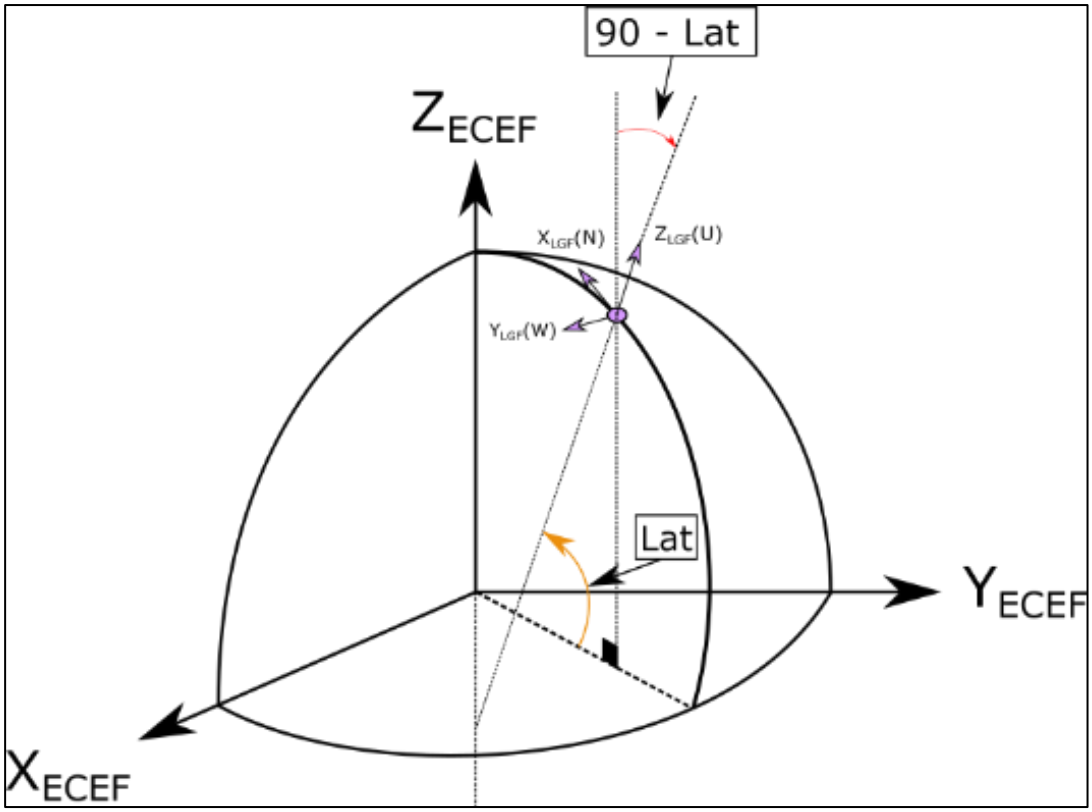

(b)

Figure 1.8 – Two rotations from LGF to ECEF coordinate system with their respective rotation matrix. (a) Rotation around the Z axis. (b) Rotation around the Y axis

Equation (1.4) represents the formulation to calculate R_{ECEF}^{LGF} based on the schematic illustration of the rotations in Figure 1.8.

$$R_{ECEF}^{LGF}(\lambda,\varphi) = [R_{LGF}^{ECEF}(\lambda,\varphi)]^T = \left[R_Z(\pi+\lambda)R_Y(\frac{\pi}{2}-\varphi)\right]^T \tag{1.4}$$

$$R_Z(\pi+\lambda) = \begin{bmatrix} \cos(\pi+\lambda) & -\sin(\pi+\lambda) & 0 \\ \sin(\pi+\lambda) & \cos(\pi+\lambda) & 0 \\ 0 & 0 & 1 \end{bmatrix} \qquad R_Y\left(\frac{\pi}{2}-\varphi\right) = \begin{bmatrix} \cos(\frac{\pi}{2}-\varphi) & 0 & -\sin(\frac{\pi}{2}-\varphi) \\ 0 & 1 & 0 \\ \sin(\frac{\pi}{2}-\varphi) & 0 & \cos(\frac{\pi}{2}-\varphi) \end{bmatrix}$$

Finally, to calculate the latitude and longitude of the reference point $(\lambda_{Ref}, \varphi_{Ref})$, we use the average of the latitudes and longitudes of all the *'n'* points on the trajectory, described in Equation (1.5),

$$\lambda_{Ref} = \frac{\sum \lambda}{n} \qquad \varphi_{Ref} = \frac{\sum \varphi}{n} \tag{1.5}$$

This section briefly introduced the direct georeferencing procedure that generates 3D point clouds used as input for the boresight alignment. A complete explanation of this process is presented in Appendix B.

1.4 Sources of Errors

The direct georeferencing model is based on abstraction, which means the acquisition system and the environment are both errorless and ideal (Schenk, 2001), which is necessary for the error analysis of the system. However, we know that the real world in which the measuring procedure occurs consists of imperfect instruments and uncertainties due to the environment (Keyetieu et al. 2018). Eventually, atmospheric conditions interfere with the scanning operation and impose errors on the direct georeferencing abstract model, which generates the georeferenced point cloud (Schenk, 2001). Thus, the georeferenced point coordinates based on the direct georeferencing model are not the same as the real ground truth point coordinates. In this section, we will address the main factors that result in errors in a mobile LiDAR system.

Four main factors cause errors in a mobile LiDAR system measuring procedure; POS-related, LiDAR-related, POS/LiDAR mounting, and errors related to object properties and scanning geometry (Schenk 2001; Schaer 2010; Soudarissanane et al. 2009). These errors have a three-fold nature, i.e., random, systematic, and blunders (Heinz et al. 2020; Glennie 2008). In this research, we are mainly concerned about the systematic errors, e.g., POS/LiDAR assembly errors, of an MLS and the methods that reduce them and result in more accurate data.

1.4.1 LiDAR-Related Errors

The LiDAR system is a sensor for measuring the range and scan angle of the emitted beam in the local coordinate system of the LiDAR (Schenk 2001). In this regard, the LiDAR system consists of two main parts, i.e., range finder and scan angle encoder, which carry out the measurement procedure, but at the same time, they may be

sources of errors. Considering the LiDAR-related error model, which depends on physical parameters and the design of the range finder and the scan angle encoder, it is not easy to distinguish between random and systematic errors (Schenk 2001; Vosselman and Maas 2011). However, LiDAR-related errors are constants (Schenk 2001; Skaloud and Lichti 2006). As mentioned in Section 1.2.1, the LiDAR scanner used in this research is exact, and in the worse scenario, the range error is 3.1 mm, which plays a minor role in the error budget of the MLS. Therefore, errors related to the scanner range finder and scan angle encoder can be neglected in this research.

1.4.2 POS-Related Errors

The POS consists of two main components, a positioning sensor, i.e., GNSS, and an orientation sensor, i.e., INS. In the following, we will address each of the two components, their uncertainties, and solutions to overcome these errors.

Two main factors affect the positioning accuracy of the GNSS positioning sensor. The first one is the satellite configuration and signal observability and the second one is the accuracy of the observations that can be affected by the differential troposphere and ionosphere and multipath effects (Schenk 2001). The second can be improved with corrections from regional or national reference networks (Vosselman and Maas 2011). Uncertainties influence the positioning data due to the environment (Keyetieu and Seube 2019). In urban canyons, with various obstacles, the GNSS signals can be blocked or deviated, which can considerably affect the precision in relative positioning (Vosselman and Maas 2011). Also, it is worth mentioning that while using a navigation-grade instrument, e.g., Hydrins iXblue system, the relative positioning will remain precise for 1 to 2 minutes after the loss of GNSS signals (Vosselman and Maas 2011). In recent years, a novel trajectory adjustment method was introduced in GNSS-deprived environments, which augments the spatial consistency and reduces the errors related to the estimated trajectory (Hussnain, Oude Elberink, and Vosselman 2021; Hussnain, Elberink, and Vosselman 2019; Gao et al. 2015).

The errors related to the INS are caused mainly by initialization errors, misalignment, and gyro drifts (Schenk 2001). These errors might be time-dependent, even dependent on the line pattern, and affect the platform's position (Skaloud and Schaer 2007; Schenk 2001). Therefore, a Kalman filter is used to remove a part of the non-overlapping errors and, as a result, refine the trajectory, but it cannot eliminate all the residual errors (Vosselman and Maas 2011). Once again, with an adaptation of a navigation-grade INS like Hydrins, we can assume that the effects of INS error are negligible.

1.4.3 POS/LiDAR Mounting Errors

As mentioned earlier, the MLS comprises two distinguished components, i.e., POS and LiDAR, with different locations on the platform and measuring frequency. Therefore, we must know the 3D rigid body transformation between the POS and LiDAR frames to georeference the point cloud with the observations from these two components. Also, they must be synchronized properly. These procedures lead to three significant POS/LiDAR mounting errors, i.e., boresight, lever arm, and latency, that must be addressed carefully to generate data with high accuracy.

The latency error, also known as the synchronization error (Schenk 2001), is defined as the time difference between the LiDAR system and the POS. The reason for that is the different measuring rates of the two components. The LiDAR scanner points and the POS trajectory points have been acquired in separate procedures with different systems. To synchronize these two components, each time the GNSS receiver acquires the platform's position, it sends a signal to the LiDAR sensor, called a pulse per second (PPS) signal. The latency error can mitigate significantly if the PPS signal is transferred adequately between the GNSS receiver and the LiDAR sensor. However, this is not always the case; sometimes, the latency error remains in MLS and causes errors of synchronization, which is addressed in existing research (Seube, Picard, and Rondeau 2012; W. Liu 2017; Keyetieu et al. 2018). Seube (2012) proposed an estimation method for total latency based on rotating the LiDAR/IMU with various rotation rates while scanning a spherical target. The method observes position shifts of the target center and requires a precise rotating table. Liu

(2017) proposed a fusion method that combines the iterative closest point (ICP) and the iterated sigma point Kalman filter (ISPKF) where the ICP estimates the transformation between the LiDAR/IMU and the ISPKF estimates the time delay error (W. Liu 2017). Keyetieu (2018) introduced a latency estimation method for a multibeam echosounder and IMU, which requires a scan with a survey strip over a flat, smooth, and regular seafloor with a surveying platform with a relatively high attitude rate (Keyetieu et al. 2018). These methods estimate whether there is a latency error in the final point cloud and how to reduce them. This thesis considers that the PPS signal between the two components transfers correctly and without interruption, and the latency error is negligible.

The lever arm error is caused by the translation vector measurement between the POS and LiDAR system origins (Vosselman and Maas 2011). The lever arm is usually measured by the conventional surveying method, i.e., tacheometric means (Skaloud and Schaer 2007), after installing the sensors on the platform with sub-centimetric accuracy (Schenk 2001; Vosselman and Maas 2011; Skaloud and Schaer 2007). We must also measure the translation vector between the GNSS phase center and the IMU gravity center within the POS, which can also be accurately measured by the surveying method. Some methods estimate the lever arm in a calibration procedure (Heinz et al. 2020).

The boresight error, also known as mounting errors (Schenk 2001), is defined as the uncertainty of the relative orientation measurement between the LiDAR system local frame and the POS body frame, which has a significant role in the MLS error budget and the overall accuracy of the point cloud (Vosselman and Maas 2011). The angular nature of the boresight error magnifies its effect. Thus, the impact of boresight error on the target accuracy increases with the range value (Schaer 2010). As discussed earlier, it is preferable to estimate the boresight error in dynamic (in-flight) mode, where we decorrelate the boresight angles with the attitudes observed by the POS (Schaer 2010).and as a result, the boresight angles accuracies will be below the average attitude noise level of POS which is approximately 0.01° in the case of this thesis (Schaer 2010).

Chapter 2 will address the state-of-the-art methods for reducing MLS errors, emphasizing the boresight errors.

To have a clear idea about the impact of the error sources of an MLS, we take the example of the customized in-house system used in this thesis. This system comprises the Z+F 2D Profiler® LiDAR scanner and the Hydrins/iXBlue INS POS device. Table 1.3 represents the impact of the error sources on the positioning error of a point scanned at a 50 m distance.

Table 1.3 – Example of the impact of individual sources of error on a point position at a 50 m distance.

Sources of Error		Point Positioning Error at 50 m distance
POS	GNSS-related errors (PPK)	1.3 cm
	IMU-related errors	1.5 cm
LiDAR Scanner	Ranging accuracy	0.9 cm
	Footprint size	2.5 cm
Leverarm error		2 cm
Boresight error of 1.2°		105 cm

The impact of the various sources of error on a point positioning accuracy located at a 50 m distance from the platform is 1 to 3 cm, except for the boresight error. The value estimated for the boresight error is based on a real-world experiment of the port of Montreal survey. In this survey, we estimated an a priori boresight error of 1.2 degrees (before calibration), resulting in a positioning error of over 100 cm due to the angular errors, which increase with distance. Thus, it is crucial to accurately estimate the minor variations in the angular deviations between the POS and the LiDAR frames, which is the main interest of our research.

1.4.4 Object Properties and Scanning Geometry-Related Errors

The surface property, such as the material and the shape, and the scanning geometry, such as the incidence angle, the local range, and the local point density of the scan points (Schaer 2010; Soudarissanane et al. 2009), have a significant

impact on the final data error in-situ and have a significant effect on the target accuracy and the measured range parameter (Schaer 2010; Vosselman and Maas 2011). Thus, it is necessary to consider these factors in the MLS data quality assessment procedure.

If the surface properties, e.g., the roughness of the surface, and scanning geometry, e.g., incidence angle, do not change dramatically, the accuracy evolution pattern remains homogeneous (Vosselman and Maas 2011).

In the context of this thesis, we deal with harsh maritime environments where in-situ surfaces that construct this environment can be deformed and corroded and affect the accuracy of the generated point clouds. The limited number of reliable in-situ features for the alignment of the LiDAR scanner in this type of low-feature environment makes the systematic error reduction method challenging to apply and may result in erroneous solutions.

1.5 Survey Grade Applications

Mobile LiDAR systems can be mounted on various platforms, and the generated 3D point cloud can be applied to several applications. MLS has proved its capabilities to acquire high accuracy and high-density 3D point clouds. For engineering surveys such as road pavement and infrastructure inspection, a 3D accuracy of less than 5 cm at a 95 % confidence interval with a density of more than 200 pts/m^2 is required and achievable (Olsen et al. 2013; Guan et al. 2016).

In this research, we are particularly interested in survey-grade applications, e.g., infrastructure monitoring that demands high accuracy and high-density point cloud (Vosselman and Maas 2011). The utilization of a mobile LiDAR system in infrastructure monitoring was first employed in the roads and highways corridor mapping context (Guan et al. 2016), and then, it was adapted to the port infrastructure monitoring application (Wyllie et al. 2012; Thies 2011). Thus, in this section, we will first discuss the monitoring and inventory assessment task in the road and highways context, and then, we will present the more recent MLS application for port infrastructure monitoring.

1.5.1 Road Asset Inventory Context

To rapidly and accurately generate a 3D geospatial representation of long corridors like roads and highways, one solution is to mount a mobile LiDAR system on a vehicle platform (Guan et al. 2016). The MLS provides two main advantages that distinguish it from other corridor mapping measuring systems. The first one is the safety and feasibility aspect of MLS that allows a safe drive along the road corridor without interrupting the actual traffic flow (Guan et al. 2016; Soilán et al. 2019; Williams et al. 2013; De Blasiis, Di Benedetto, and Fiani 2020). The second one is associated with the sufficiently accurate, precise, and dense 3D point clouds generated by MLS (Puente et al. 2013), which can be used for planarity verification, subsidence analysis in the order of a few centimeters of road surfaces (Heinz et al. 2019) and pavement surface distress analysis (De Blasiis, Di Benedetto, and Fiani 2020). Figure 1.9 illustrates (a-b) commercialized terrestrial MLS and (c) customized in-house MLS.

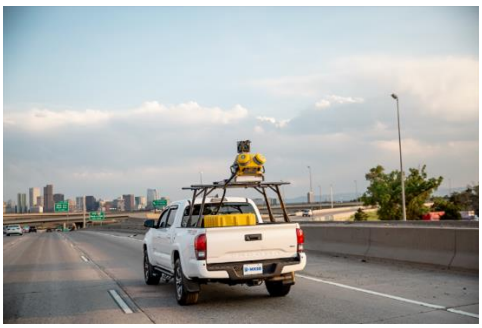

(a)

(b)

(c)

Figure 1.9 – Terrestrial MLS. (a) Trimble MX50 (TrimbleGeospatial 2022) (b) Riegl Mobile Laser Scanning System VMX-250 (Riegl 2022). (c) Jakarto Mobile Mapping Unit (Courtesy of Jakarto)

1.5.2 Port Infrastructure Monitoring Context

As a prominent part of the maritime transport system, port infrastructure plays a significant role in national and international economic growth (Munim and Schramm 2018). More than 80% of the merchandise transport is through seawater transport systems (United Nations Publications 2020).

Due to specific conditions of the maritime context, i.e., the permanent exposure to a highly aggressive and humid environment (Ruggeri, Fruzzetti, and Scarpelli 2021; Valdez et al. 2016), an accurate and regular infrastructure inspection is highly recommended. The inspection results lead to rapid identification of damaged and ruined sections and allow the port authority to apply essential maintenance and repairment procedures (Alho et al. 2009; Kishi et al. 2015; Moisan et al. 2015; Rondeau and Pelletier 2013; Ruggeri, Fruzzetti, and Scarpelli 2021; Böder et al. 2011).

Routine and accurate surveillance operation of port infrastructure, e.g., quay walls, which support all the existing infrastructures and play a crucial role in the loading and unloading procedure of the cargos, is of crucial importance. The quay walls must be monitored periodically, and their maintenance must be prioritized based on the 3D as-built models of such structures. We must be able to estimate the verticality of quay walls and compare them to previous scans. Therefore, routine monitoring is essential to prevent early damage and catastrophes, as illustrated in Figure 1.10.

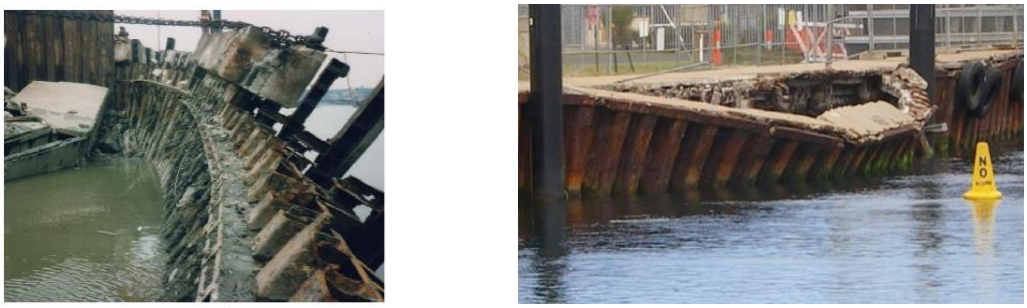

(a) (b)

Figure 1.10 – Example of failure of a quay wall. (a) (Sentry et al. 2007). (b) (Stewart and Bastidas-Arteaga 2019)

Thus, we must consider an acquisition system with geometric stability and flexibility that can perform routine monitoring tasks. Additionally, based on the highly active circulation in a maritime environment, especially ports and harbors, we must adopt a data acquisition system that produces data with a high level of detail using a dynamic acquisition method without interfering with the port traffic. An MLS mounted on a hydrographic vessel can offer this capability.

Based on the reasonable time and cost of terrestrial MLS for roads and highways monitoring applications, we suppose that a mobile LiDAR system mounted on a hydrographic vessel (Marine MLS), also known as a vessel-based mobile LiDAR System (Thies 2011), boat-based laser scanning (Alho et al. 2011), ship-borne mobile surveying system (Lu et al. 2019), and vessel-mounted LiDAR system (Wyllie et al. 2012), would have the same capability and efficiency for the acquisition of high-quality LiDAR data applied to port infrastructure monitoring. Hydrographic vessels are already equipped with SONAR sensors integrated with POS for bathymetric surveying. The addition of a LiDAR sensor to the SONAR and POS integrated acquisition system enables full 3D scans of the above (emergent) and under the water (submergent) surface infrastructure simultaneously (Dix et al. 2012; Lu et al. 2019; Shi et al. 2017; Thies 2011; Böder et al. 2011; Kishi et al. 2015). This integration leads to a possible all-inclusive solution for simultaneous monitoring of under and above the water surface, which is beneficial for most of the port infrastructure that is partly under and partly above the water surface. Figure 1.11 presents the mobile LiDAR system mounted on the hydrographic vessel used in this Ph.D. project.

Figure 1.11 – Mobile LiDAR system mounted on a hydrographic vessel (Courtesy of CIDCO)

The mobile LiDAR system employed in this thesis consists of a high-resolution and precise LiDAR scanner and a navigation-grade GNSS/INS, introduced in Section 1.2. This system can achieve survey-grade accuracy while generating high-density point clouds of port infrastructure for monitoring applications. This state-of-the-art 3D geospatial data acquisition technology with high density and high accuracy data acquisition capacity perfectly satisfies all the infrastructure requirements of ports monitoring data (Wyllie et al. 2012; Thies 2011).

1.6 Discussions and Conclusions

This chapter introduced an in-house mobile LiDAR system mounted on a hydrographic vessel platform. We presented its main components and the principal

errors that impact the point cloud. We also introduced the direct georeferencing procedure that produces the 3D point cloud from data collected with this in-house MLS. We also addressed the errors this MLS can encounter to using this system for survey-grade applications, such as port infrastructure monitoring.

Among the different errors, we considered that the POS/LiDAR assembly error has more influence on the data quality. We also discussed the importance of minimizing the effect of the object properties and scanning geometry-related errors on the calibration data. In low-feature environments like maritime areas, to minimize the error related to the object properties and scanning geometry, one solution can be the utilization of well-designed targets that can be installed in proper places that can be scanned with the specific scanning geometry. This solution involves designing appropriate calibration targets, developing an efficient calibration data acquisition procedure, and configuring an appropriate acquisition site, which is the central subject of this thesis and will be covered in detail in Chapters 3 and 4.

Before that, in the next chapter, we will address the state-of-the-art methods that aim to reduce MLS errors with a comprehensive review of the existing literature on this subject.

Chapter 2 – Overview of Error Reduction Methods in Mobile LiDAR Systems

2.1 Introduction

The objective of this chapter is to review the existing error reduction methods that can be applied to mobile LiDAR systems. As mentioned earlier, errors cause discrepancies on overlapping strips of the same scene scanned by the MLS. We can take advantage of the discrepancies on overlapping strips to mitigate their effects on the generated point cloud. The existing methods aim to reduce discrepancies and enhance the point cloud's accuracy (Shan and Toth 2008). In the introduction, we mentioned that these methods are categorized into two main categories, rigorous and non-rigorous. Moreover, they use tie-features such as tie-points, tie-lines, and tie-planes as input.

2.2 Rigorous Methods

The rigorous methods, also known as system-driven methods, address the causes of the errors in the overlapping point clouds. These methods can derive statistical analysis such as the estimated error standard deviation due to their access to the raw measurements (Skaloud and Lichti 2006). This group of methods was inspired by the bundle block adjustment procedure applied in photogrammetric operations (Morin and El-Sheimy 2002; Skaloud and Schaer 2003). In rigorous methods, the raw observations mentioned earlier are the position and orientation of the platform, i.e., POS trajectory data from INS/GNSS and LiDAR sensor measurements (Y. Zhang et al. 2015). These methods use the direct georeferencing equation as the adjustment model to estimate the parameters that cause the errors of the MLS (Le Scouarnec et al. 2014; Y. Zhang et al. 2015).

In summary, in rigorous methods, while addressing the reduction of the discrepancies between the tie-features of overlapping strips, we model and estimate the unknown systematic errors that cause these discrepancies in the first place. Therefore, rigorous methods have three main characteristics. The first characteristic

is their consideration of all the raw measurements of each sensor of the MLS. The second characteristic is the utilization of the direct georeferencing model as the functional model for further adjustment procedures. The third characteristic is the provision of statistical quality assurance measures for the estimated parameters. In the following, we categorize the rigorous methods based on the option of tie-feature used in their procedures.

2.2.1 Tie-Point

This category's first series of methods do not require external reference control points. They were first applied for estimating boresight angles of an aerial MLS while inserting interpolated tie-points within an iterative least-squares adjustment model (Morin and El-Sheimy 2002). A method based on the virtual corresponding point model, which consists of a corresponding point and three real laser footprints, was proposed to overcome the correspondence interpretation problem within discrete points of aerial MLS (J. Zhang, Jiang, and Jiang 2012). To compensate for the systematic measurement errors in aerial MLS, Glira et al. (2015) suggested a fully automatic strip adjustment using point correspondences from overlapping strips. This approach is considered rigorous due to the utilization of the original scanner measurements and the trajectory observations. While estimating the ALS scanner calibration parameters, the method minimizes the point-to-plane distances of all correspondences based on Iterative Closest Point (ICP) algorithms. Z. Li et al. (2019) suggest a direct point-to-point correspondence for estimating the boresight errors of an MLS mounted on terrestrial and drone platforms. The reason for this choice is the high density of point clouds we can obtain due to the recent advances in hardware technology. An ICP algorithm also sets the correspondences between points in overlapping strips (Z. Li, Tan, and Liu 2019).

The second series of rigorous methods, based on tie-point features, require external ground truth, such as reflective signalized surveyed control points, which are used as observations in the adjustment procedure (Talaya et al. 2004). These control points generate higher intensity points and facilitate the extraction procedure, which is used as observations in the adjustment procedure. Also, for estimating the

mounting parameters of pair of LiDAR scanners on a terrestrial platform, five to seven control points distributed on horizontal and vertical surfaces can satisfy the required accuracy (Leslar, Wang, and Hu 2016).

Additionally, inspired by the sonar multibeam patch test (Brahim, Daniel, and Guériot 2008), a rigorous tie-point laser patch test method is applied to marine MLS that calculates three rotational angles: roll, pitch, and yaw between the POS and LiDAR scanner. This method requires scanning specific objects like poles and bridge pillars with a specific line pattern as input data. Based on the discrepancies of the point cloud generated with different passages, the LiDAR patch test tries to approach them while estimating the boresight angles. The disadvantage of this method is the requirement of clean data without noise, the procedure is relatively long and time-consuming, and in the end, it does not deliver any standard deviation for the estimated parameters.

2.2.2 Tie-Line

This category of methods utilizes linear features (tie-line), e.g., long edges, gable roofs intersections, and ditches for height and planimetric offsets estimation, in case finding suitable tie-points between strips becomes a non-trivial task (Vosselman 2002).

Le Scouarnec et al. (2014) proposed a position-free method that does not depend on the GNSS observations to estimate the boresight angles while constraining a set of lines on a planar surface. Based on this method, the same boresight alignment method was adapted to a terrestrial MLS (Ndir 2019), which scans a vertical planar surface with different orientations, and each orientation forms a linear feature (tie-line) on the surface. Due to the boresight misalignment, the linear features do not lie perfectly on the planar surface. Thus, the adjustment model estimates the boresight error while fitting the linear features on the planar surface. This method necessitates that the MLS operates in a static mode and with multiple exaggerated line patterns near a vertical planar surface with a noticeable height, like a very high wall, which is not always accessible. Also, near a vertical surface like a wall, the GNSS signal can

be blocked, or multipath effects can arise, which will seriously affect the coordinates of the georeferenced point. This approach has two main disadvantages. First, the MLS does not arrive at the optimal performance (minimum uncertainties) like in a dynamic (in-flight) mode. Second, the data is affected by POS-related errors due to the close distance of the system from the vertical planar surface like a wall.

2.2.3 Tie-Plane

This section introduces the planar surface as the tie-feature, also known as tie-plane. The methods that use tie-planes are divided into two main categories. First, the methods that do not have access to prior information of the tie-plane (without external reference information). This category of methods is considered independent, and its advantage is that it does not require any ground truth of the tie-plane. Second, methods that have access to the tie-plane information are usually measured by an external instrument (with external reference information). In the following, these two categories based on tie-plane are discussed with specific attention to methods that address the boresight error of an MLS.

2.2.3.1 Tie-Planes without External Reference Information

At first, discrepancies between overlapping strips generated by the MLS mounted on aerial platforms were mainly on the elevation data (Burman 2000). Therefore, elevation and intensity data of distinct tie-planes were used for the estimation of the boresight errors of the system (Burman 2000). Multiple overlapping strips with different directions were employed to increase the accuracy of the estimated boresight angles (Toth, Csanyi, and Grejner-Brzezinska 2002). However, the fact that the surface points were converted to a regular grid reduces the accuracy of the estimated parameters due to the interpolation process (Toth, Csanyi, and Grejner-Brzezinska 2002). Filin (2003) suggests the utilization of natural and man-made surfaces with moderate slopes oriented in different directions to overcome the surface-to-grid point interpolation issue (Filin 2003). The solution is based on conditioning a set of points to lie on a planar surface while introducing an error recovery model for the system (Filin 2003; Skaloud and Lichti 2006). This solution proposed a method that simultaneously estimates the three boresight angles and

the rangefinder offset (Skaloud and Lichti 2006). In this category of methods, the only a priori information considered is the surface's planar form. A similar method based on planar surfaces was tested on simulated aerial MLS data (Friess 2006).

Further studies illustrate the impact of planar features characteristics, such as shape, size, smoothness, low curvature, variation in slope, and orientation that can be found in roof planes in urban areas, on the performance of the boresight alignment method (Lindenthal et al. 2011; Pothou et al. 2008). The same method was adopted for an oblique forward-looking LiDAR installed on a helicopter, emphasizing precise POS accuracy and accessibility to various roof shapes and varying building orientations to achieve an optimal result (Hebel and Stilla 2012). Moreover, the boresight alignment of drone MLS was addressed using tie-planes extracted from parallel and crossing overlapping survey strips over an area containing roofs or regular natural slopes (Keyetieu and Seube 2019). This method concentrates mainly on the best local horizontal planar patch selection based on boresight errors observability criteria defined by a sensitivity function (Keyetieu and Seube 2019). The latter method, designed for aerial platforms, will face some difficulties for terrestrial platforms with a lateral point of view on the scene of interest. As we can notice, most of the mentioned methods rely on tie-planes that are abundant in urban areas and man-made structures (Skaloud and Lichti 2006).

The rigorous boresight alignment of aerial MLS based on in-situ tie-planes was adapted to terrestrial MLS (Glennie and Lichti 2010), which emphasizes the utilization of points with low incident angles that confirm once again the importance of considering the object properties and scanning geometry in the boresight alignment procedure (Glennie and Lichti 2010; Glennie 2012).

All the above methods rely on in-situ tie-planes abundant in urban scenes, such as building facades, ground surfaces, bridge bottoms, and inclined large traffic signs (Chan, Lichti, and Glennie 2013). These in-situ features and their accessibility are crucial to the efficiency of the MLS error reduction methods.

2.2.3.2 Tie-Planes with External Reference Information or Ground Truth

This category of methods takes advantage of reference ground truth in the error reduction procedure.

We know that systematic errors such as boresight errors have a symmetric characteristic, which means the effect of boresight errors on tie-planes on overlapping areas with opposite directions is equal. Li (2016) presented a method for estimating the boresight errors of an aerial MLS that takes advantage of planar reference surfaces from four gable-roof buildings with various orientations and distributions (D. Li et al. 2016). The disadvantage of this method is the complexity of having access to the reference planar surfaces of buildings' roofs.

Contrary to the aerial MLS, the MLS error reduction method with known reference tie-planes has gained more popularity with the terrestrial platform due to the simplicity of acquiring reference ground truth in the terrestrial context. The precise and accurate in-situ reference planar surface can be generated by a static terrestrial laser scanner that will eventually be utilized in the adjustment procedure for estimating mounting parameters of the MLS, i.e., boresight angles and lever arms (Hong et al. 2017).

Using prefabricated tie-planes is a solution in low-feature environments with low accessibility to in-situ reference data (Hong et al. 2017). The first step is that the prefabricated tie-planes are installed in a calibration field and scanned by a static terrestrial laser scanner to generate the ground truth. The second step is scanning the same prefabricated tie-planes setup with a terrestrial MLS (Heinz et al. 2020). Due to the errors of the MLS, the two datasets acquired from the mobile and static systems reveal discrepancies when compared to each other. The error reduction method minimizes these discrepancies while adjusting the terrestrial MLS mounting parameters, i.e., boresight angles and lever arms, until the two datasets fit together (Heinz et al. 2020).

A similar MLS alignment method was applied to a marine MLS, which uses ten planar reference targets with various orientations and sizes inside a pool used as a

calibration site (Lu et al. 2019). This calibration site might present an ideal environment, but it can hardly be reproduced.

2.3 Non-Rigorous Methods

The other main MLS error reduction method category is non-rigorous, also known as data-driven methods. In this category of methods, the problem is viewed from the end user's perspective (Kalenjuk and Lienhart 2022), and the reduction of errors occurs by solely manipulating the final georeferenced point clouds and estimating a rigid body transformation (Filin and Vosselman 2004). In this method, end-users do not need access to raw measurements such as the POS or LiDAR scanner raw data. The non-rigorous methods' sources of error are not the focal point.

Additionally, there are different possible transformations from one dataset to another one. Only three positional translations are considered if the method addresses the positional biases (Filin and Vosselman 2004). For complex transformation, a seven parameters similarity transformation is pertinent (You and Lee 2020). If the rotations between strips are also considered, an affine transformation is used (van der Sande, Soudarissanane, and Khoshelham 2010). In a complete case, a total 3D rigid body transformation is used (K. Liu et al. 2019). Although these rigid body transformation parameters reduce the discrepancies between strips, they are not representative of physical parameters in the real world, which is considered one of the disadvantages of non-rigorous methods.

Non-rigorous methods also take advantage of tie-features as input data. Thus, in the following, we present three types of non-rigorous methods based on their entry tie-features.

2.3.1 Tie-Point

As mentioned earlier, this category of methods uses only the final point cloud (Csanyi et al. 2005; Ressl, Mandlburger, and Pfeifer 2009; Ressl, Pfeifer, and Mandlburger 2012; Bang et al. 2009) or a byproduct of the point cloud, e.g., Triangulated Irregular

Network (TIN) structure (Maas 2002) or digital terrain model (DEM) form (M. Crombaghs et al. 2002).

In the earlier methods, point data such as height were used as correspondences for matching strips within a triangulated irregular network (TIN) to reduce the discrepancies (Maas 2002; Filin and Vosselman 2004; Zequan Chen, Li, and Yang 2021). The accuracy of methods based on the TIN can be affected by the uncertainties related to the presentation of the earth's surface by this kind of structure.

To facilitate the detection and matching of the tie-point on a point cloud, Csanyi (2005) suggests the utilization of circular LiDAR-specific ground targets as input. These tie-points enter as correspondences on a 3D similarity transformation module, resulting in centimeter-level engineering scale mapping accuracy for the final point clouds (Csanyi et al. 2005). The 3D similarity transformation replaced a 3D affine transformation with more output parameters to increase the method's accuracy, inspired by the photogrammetry bundle block adjustment (Ressl, Pfeifer, and Mandlburger 2012; Munjy 2015).

Recently, a novel profile-based method has emerged, similar to the tie-point non-rigorous method (Ravi and Habib 2020; Kalenjuk and Lienhart 2022). The main objective of the profile-based methods is to minimize the discrepancies between the corresponding profiles of two datasets while estimating the transformation parameters, such as shifting and rotating parameters. The advantage of this method is that high-frequency errors can be detected and corrected within a small portion of the point cloud (profiles) (Kalenjuk and Lienhart 2022).

2.3.2 Tie-Line

This category of methods aims to reduce the systematic residual errors based on tie-lines, which are found abundantly on man-made structures in urban areas, e.g., roof ridgelines and roof planes intersection (Lee et al. 2007; Rentsch and Krzystek

2012). The advantage of tie-line features is that the extraction procedure is generally much more straightforward than tie-point features (Lee et al. 2007).

2.3.3 Tie-Plane

In this approach, the input is the tie-planes extracted from the georeferenced point cloud on overlapping areas, and the aim is to minimize the discrepancies between these tie-planes. To considerably mitigate the correlation between the 3D rigid body transformation parameters, natural in-situ planar surfaces with different orientations, various slopes, and evenly distributed are chosen as tie-planes, resulting in better accuracy and efficiency (K. Liu et al. 2019). Here, we present some examples of these in-situ planar surfaces; sloped terrains (Filin and Vosselman 2004) and man-made in-situ surfaces, i.e., gable building roofs (van der Sande, Soudarissanane, and Khoshelham 2010; K. Liu et al. 2019; You and Lee 2020). These methods are more applied to aerial platforms in urban areas with many planar surfaces. However, its success is more limited in areas without man-made tie-planes, e.g., rural and forest areas (Song, Guoqing, and Wang 2021).

2.4 Other Tie-Features

In this section, a few other tie-features that are used in MLS reduction methods are discussed. In urban areas, power cables on highway sides and transmission lines across the highways are considered common geometric objects that can be used for the estimation of mounting parameters of an MLS (Chan, Lichti, and Glennie 2013). The disadvantage of using cables is the instability of these features, especially in extreme meteorological conditions like windy weather constantly displacing the cables.

Other tie-features are prefabricated spherical targets used for the MLS boresight alignment (Landry 2017; Guo et al. 2021). Landry (2017) presents the rigorous boresight alignment consisting of spherical targets with known positions as ground truth scanned with an MLS in a laboratory. The actual location of the spheres and their position extracted from the point cloud generated by the MLS will have discrepancies due to the misalignment parameters of the MLS. The mounting

parameters are then simultaneously estimated. Because of the high cost of laboratory installation and the time-consuming procedure of establishing a high-precision network, this method is considered a less practical solution for boresight alignment problems. A similar method was presented for outdoor scenes with spherical reference targets measured a priori with a total station (Guo et al. 2021). The terrestrial MLS scans the spheres, and then, discrepancies between the two datasets have been reduced with an adjustment procedure. The output of the adjustment procedure is an estimation of the mounting parameters, boresight, and lever arms errors (Guo et al. 2021). Both methods are dependent on to ground truth of the prefabricated spherical targets.

Another surface used for estimating the mounting parameters of an MLS is a foldable corner-cube trilateral pyramid made from white corrugated plastic, which can be determined precisely within a point cloud acquired by a drone MLS (Wilkinson et al. 2019). These pyramids are placed along strips, while their positions are established using post-processed kinematic (PPK) GNSS. A modified ICP relates to these dispersed pyramids from various strips (Wilkinson et al. 2019). Next, discrepancies between the strips are minimized by an adjustment solution that simultaneously estimates the mounting parameters, i.e., boresight and lever arm errors (Wilkinson et al. 2019).

2.5 Discussions and Conclusions

This chapter comprehensively reviews the existing MLS error reduction methods, especially the boresight systematic errors. We categorized these methods primarily by two main characteristics: the rigorousness of the method and the type of tie-features that connect dispersed overlapped strips, as illustrated in Figure 2.1.

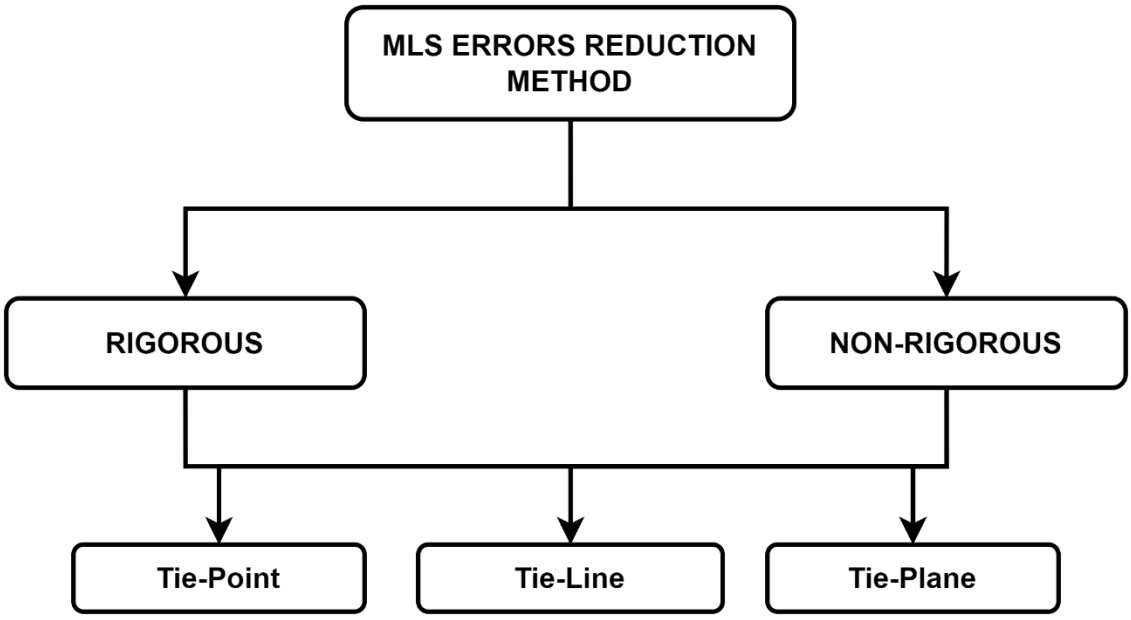

Figure 2.1 – Categorization of the MLS error reduction methods.

Table 2.1 and Figure 2.2 summarize MLS error reduction methods with related references in the existing literature.

In summary, the main advantage of rigorous methods is the determination of sources of error with their standard deviation, and their main disadvantage is the requirement for the raw data from the POS and LiDAR scanner. On the other side, the main advantage of non-rigorous methods is that they do not require access to raw data of the system that facilitates their utilization for the end user, while their main disadvantage is not addressing the cause of the errors.

Table 2.1 – MLS Systematic Errors Reduction Methods

	Tie Feature	Advantages	Drawbacks	Papers
Rigorous Methods	Tie-Point	Simplicity in detection	Difficulty in correspondence	(Morin and El-Sheimy 2002) (Talaya et al. 2004) (J. Zhang, Jiang, and Jiang 2012) (Glira et al. 2015) (Z. Li, Tan, and Liu 2019) (Leslar, Wang, and Hu 2016)
	Tie-Line	Simplicity in correspondence	Difficulty in detection	(Vosselman 2002) (Le Scouarnec et al. 2014) (Ndir 2019)
	Tie-Plane	Simplicity in correspondence Simplicity in detection	-	(Burman 2000) (Toth, Csanyi, and Grejner-Brzezinska 2002) (Filin 2003) (Skaloud and Lichti 2006) (Friess 2006) (Glennie and Lichti 2010) (Hebel and Stilla 2012) (Chan, Lichti, and Glennie 2013) (Keyetieu and Seube 2019) (D. Li et al. 2016) (Hong et al. 2017) (Heinz et al. 2020) (Lu et al. 2019)
Non-Rigorous Methods	Tie-Point	Simplicity in detection	Difficulty in correspondence	(Maas 2002) (Csanyi et al. 2005; Ressl) (Mandlburger, and Pfeifer 2009) (Ressl, Pfeifer, and Mandlburger 2012) (Bang et al. 2009) (Ravi and Habib 2020) (Kalenjuk and Lienhart 2022)
	Tie-Line	Simplicity in correspondence	Difficulty in detection	(Lee et al. 2007) (Rentsch and Krzystek 2012)
	Tie-Plane	Simplicity in detection Simplicity in correspondence	-	(Filin and Vosselman 2004) (van der Sande, Soudarissanane, and Khoshelham 2010) (K. Liu et al. 2019) (You and Lee 2020) (Song, Guoqing, and Wang 2021)

The overall MLS reduction methods take advantage of tie-features such as tie-point, tie-line, and tie-plane. In the following, we discuss each of the tie-features in detail.

The point as a feature to tie the strips together is not a good choice. The reason for that goes back to the unorganized, discrete, and random nature of the point cloud generated by an MLS, which demands an interpretation process for finding the corresponding points between two overlapping strips (van der Sande, Soudarissanane, and Khoshelham 2010; Nagarajan and Moafipoor 2018). In other words, the LiDAR footprints have a sparse and unorganized nature, and we cannot localize a well-defined object with the same LiDAR point in various strips (Friess 2006; Gonsalves 2010). Thus, interpreting the corresponding tie points between strips is not always a straightforward task (Ressl, Mandlburger, and Pfeifer 2009). The methods based on tie-points are prevalent in areas with insufficient in-situ geometric objects, i.e., mountainous areas (Zequan Chen, Li, and Yang 2021) or forest areas (Fekry et al. 2021). Therefore, the detection of tie-points is a trivial task. However, the correspondence between two tie-points belonging to two datasets is a challenging task due to the irregular nature of the MLS point cloud.

Tie-lines are not easy to detect in an individual point cloud, but if we can define a tie-line in an overlapped area of two individual point clouds, the corresponding task is simple due to the known mathematical model of a line.

Finally, tie-planes detection and corresponding tasks in an overlapped area are considered trivial. Most existing methods required in-situ dispersed planar surfaces, e.g., roofs, walls, and slope terrain, with different orientations and configurations (Kager 2004; Friess 2006; Skaloud and Lichti 2006). However, this is not always the case in certain areas like rural, natural environments, vegetated and forest areas, and seaport areas (Ressl, Pfeifer, and Mandlburger 2012). Therefore, using prefabricated planar targets seems to be a reasonable solution for featureless environments (Heinz et al. 2020; Ravi et al. 2018).

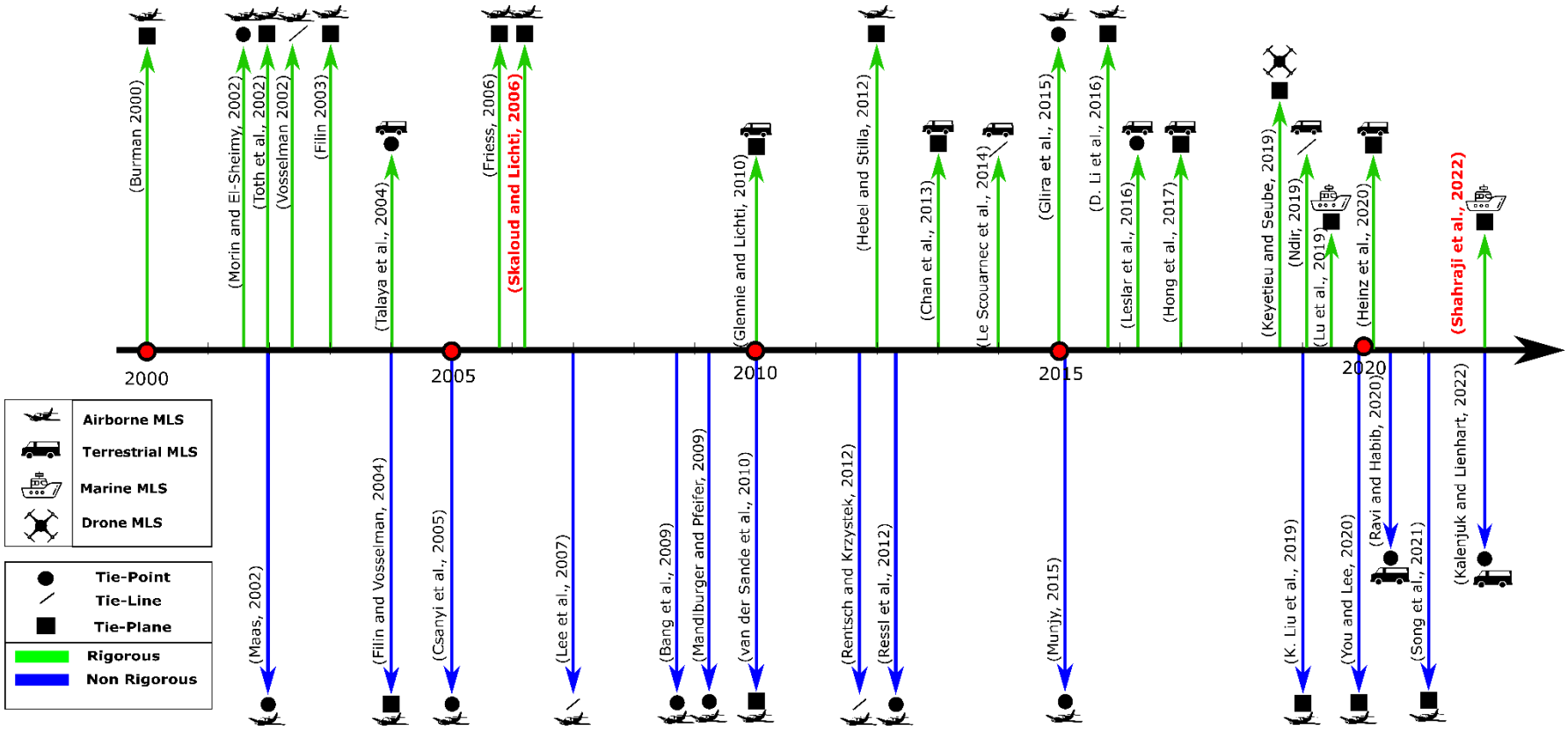

Figure 2.2 – Chronological overview of MLS error reduction methods

Based on the review of existing methods, we choose to reduce the errors of the MLS by a rigorous method. The main reason is that we have access to the raw measurements of the POS and LiDAR data; therefore, we can estimate the causes of errors and their uncertainties. We do not choose the non-rigorous method because it applies a rigid transformation between two dispersed datasets in a blindly and unjustifiable way (Vosselman and Maas 2011), and as a result, the exact georeferenced position of the points will be blurred (Hebel and Stilla 2012).

Also, based on the above comprehensive review of the existing methods that address the reduction of errors in an MLS, we decided to go forward with a rigorous method that uses prefabricated tie-plane features. This thesis will also concentrate on one sort of MLS error: boresight errors.

We must also consider that having reference ground truth in certain circumstances is nearly impossible, e.g., quay wall of port environment, which leads to methods independent of external reference ground truth. Therefore, apart from the planar form of the targets used, the proposed method must not require any a priori information.

In summary, based on the comprehensive review of the existing methods that address the reduction of errors in an MLS, we decided to go forward with a rigorous method based on prefabricated tie-plane features without any a priori information except the planar form of the target. Therefore, apart from the planar form of the targets used, the proposed method must not require any a priori information.

In the next chapter, based on the selected tie-feature, we address the optimal configuration of these targets to achieve the best result for the reduction of error of an MLS in the low-feature and challenging context of this thesis, the maritime environment.

Chapter 3 – Analysis of Systematic Errors of Mobile LiDAR Systems: A Simulation Approach

To achieve the required accuracy for marine infrastructure monitoring applications, we must address the various sources of error of a marine MLS. The literature review presented in Chapter 2 led to the conclusion that for the context of this research, it is recommended to insert and install prefabricated planar targets as tie-features which could eventually be served as input for marine MLS error reduction methods.

This chapter aims to analyze the impact of MLS errors on prefabricated tie-planes with various configurations. In this thesis, the term configuration is referred to the setup of prefabricated tie-planes and the line pattern used for the data acquisition procedure. This analysis will ultimately demonstrate which configurations of prefabricated planar targets result in better visibility of the MLS errors.

For this analysis, it is essential to understand the impact of each error, individually and collectively, on prefabricated tie-planes, known as error analysis (Schenk 2001) or biased impact analysis (Ravi and Habib 2020) in the existing literature.

There are two approaches for MLS error analysis, first, an analysis based on a normalized scan line, in which the MLS platform is fixed in a stationary mode (Schenk 2001; Cassol 2018), and second, the utilization of a simple point cloud generator or simulator to emulate systematic errors of an MLS on geometric features like planes on a dynamic mode (Heinz et al. 2020; Ravi et al. 2018).

This chapter adopts the second approach for the MLS error analysis. We elaborate in detail on the design of an MLS simulator. This simulator generates a point cloud on a hypothetical tie-plane using the mathematical georeferencing model that allows the insertion of different errors individually and collectively. The advantage of using a simulator is that the error analysis is performed without all other sources of error, like random noise and blunders due to positioning errors. We can also define various configurations, such as characteristics for tie-planes, like the dimension and

orientation of targets, the number of required tie-planes, and the specification of the scanning line patterns.

To study the systematic error visibility analysis, we introduce two types of criteria, ***Type I*** and ***Type II***, which we discussed in detail in this chapter. Based on these criteria, we can study the best configuration for the MLS, resulting in higher visibility of systematic errors.

In this thesis, these analyses are performed on eight systematic errors: three boresight errors, three lever arm errors, the range offset, and the scan angle offset. Considering eight systematic errors gives a better understanding of the impact of each error on a tie-plane and the correlation between errors.

Furthermore, we applied the suggested configuration to a real-world dataset generated by a terrestrial MLS, which approved the analysis result based on the simulated dataset.

Although the configuration validation is done on a terrestrial MLS, we can adapt the same configuration for another platform, like a marine MLS.

While the simulator introduced in this chapter is tailored for planar surfaces, we can readily adapt the simulator to other types of surfaces, such as spheres and pyramids, by solely adapting the mathematical model to the one proper to the surface.

This chapter presents the integral of a peer-reviewed conference paper published in the International Society for Photogrammetry and Remote Sensing (ISPRS) Congress 2020 annals[3].

Moreover, due to the limited page capacity of the peer-reviewed conference paper, we could not publish all the results of the analysis of the systematic errors. Appendix

[3] Shahraji, M. H., C. Larouche, and M. Cocard. 2020. “ANALYSIS OF SYSTEMATIC ERRORS OF MOBILE LiDAR SYSTEMS: A SIMULATION APPROACH.” *ISPRS Annals of Photogrammetry, Remote Sensing and Spatial Information Sciences* V-1–2020 (August): 253–260. https://doi.org/10.5194/isprs-annals-V-1-2020-253-2020.

C provides the detailed results of the impact of all eight systematic errors of a terrestrial MLS using the simulation approach based on ***Type I*** and ***Type II*** criteria.

Finally, Section 3.9, "***Complementary of Chapter 3,***" has been added. It provides a similar analysis for a marine MLS that is the focus of this thesis.

3.1 Résumé

L'analyse des erreurs systématiques du système LiDAR mobile (SLM) est toujours une tâche difficile dans des situations réelles. Ce défi est principalement dû au mélange d'erreurs systématiques et d'erreurs non systématiques. Pour résoudre ce problème, nous présentons un modèle conceptuel d'un simulateur SLM. Dans l'approche de simulation proposée, nous ne prenons en compte que les erreurs systématiques qui affectent le nuage de points géoréférencés simulé. Pour simplifier notre analyse, nous nous concentrons uniquement sur la modélisation des effets des erreurs systématiques sur les cibles planaires et nous nous concentrons uniquement sur la plateforme terrestre. Nous suggérons l'utilisation de deux cibles planaires de dimensions 1m x 1m, une avec une inclinaison verticale et l'autre inclinées et un patron de cinq lignes d'acquisition. Pour valider notre méthodologie, nous avons effectué un levé réel avec notre SLM maison sur un site comprenant un ensemble de 3 cibles planaires avec différentes inclinaisons.

3.2 Abstract

The systematic error analysis of the mobile LiDAR system (MLS) is always a challenging task in real-world situations. This challenge is mainly due to the mixture of systematic and non-systematic errors. To tackle this issue, we introduce a conceptual model of an MLS simulator in this paper. The main advantage of the simulation-based approach is complete control over the incorrect systematic and non-systematic parameters that affect an MLS's output. We only consider systematic errors that affect the simulated georeferenced point cloud in the proposed simulation approach. These systematic errors are as follows, POS-LiDAR boresight angles, POS-LiDAR lever arms, range offset, and scan angle offset. To simplify our analysis, we concentrate only on modeling the effects of systematic errors on planar targets,

and we focus solely on the terrestrial platform. Based on an independent analysis performed on each of the eight systematic errors of an MLS, to obtain strong visibility over systematic errors of an MLS, we suggest two planar targets of 1m x 1m dimensions with vertical and inclined inclinations and a five-line pattern for MLS, two parallel and three side-looking passages. The proposed configuration generates an ideal input point cloud for detecting systematic errors (except for the Z lever arm error), and ultimately it will lead to the correct input data for the calibration of a terrestrial MLS. To validate our methodology, with an in-house assembled terrestrial MLS, we scanned a set of planar targets with three different inclinations (vertical, inclined, and horizontal). This real-data validation test illustrated that with only two out of three planar targets (vertical and inclined) and with five out of six passages (two parallel to the planar targets and three side-looking passages), we would obtain expected visibility over the systematic errors of a terrestrial MLS, which approves the results with the simulation data.

KEYWORDS: Mobile LiDAR System, Systematic Errors, Simulation, Planar Target, Systematic-error visibility criteria.

3.3 Introduction

In the last four decades, mobile LiDAR systems (MLS) have evolved from a cutting-edge, expensive, and unreachable geomatics technology into a more user-friendly and accessible surveying technique for acquiring georeferenced point clouds. We categorize them based on their platforms as terrestrial, marine, and aerial MLS. MLS has enabled geomatics professionals to rapidly generate millions of georeferenced points at a lower cost than other surveying techniques. The product of these systems can be used in various fields and applications, such as 3D city modeling, autonomous vehicle, and virtual reality (Vosselman and Maas 2011; Shan and Toth 2008).

An MLS consists of two main components: a position and orientation system (POS) and a LiDAR scanner (Ackermann 1999; Wehr and Lohr 1999; Shan and Toth 2008; Vosselman and Maas 2011). The POS combines a GNSS antenna with an inertial

measurement unit (IMU). However, the interconnection between these components can be affected by systematic and non-systematic errors degrading the quality of the final georeferenced points.

The main systematic errors are POS-LiDAR boresight angles, POS-LiDAR lever arms, range offset, and scan angle offset. These errors have a systematic, repetitive, and constant effect on the data. The non-systematic errors consist of two categories; blunders or gross errors, such as GNSS multipath error, which affects the platform trajectory, and random errors, such as noise originating from the sensors (LiDAR or POS), which affects the quality of the point cloud. It is relatively difficult to separate these two kinds of errors to study them independently without the influence of one on the other. For example, we must acquire trajectory data to georeference the points to generate an accurate and precise point cloud. Thus, the georeferenced points will inevitably influence the trajectory errors, and as a result, the impact of other systematic errors will not be clear on the georeferenced points; therefore, the analysis of such errors will be complex.

In recent years, there have been two significant tendencies in MLS simulation-based approach in the geomatics world. The first type is a radiometric simulation approach based on the radiometric and spectral interaction of LiDAR photons with environmental complex scenes like forest canopy (Brown, Blevins, and Schott 2005; Cifuentes et al. 2018; Kukko et al. 2007). The second type is a geometric simulation approach in which a direct georeferencing mathematical model constitutes the base of the simulator (Friess 2006; Lohani, Reddy, and Mishra 2006; Kim et al. 2009; Heinz et al. 2015). Lohani (2006) introduced a simulation of aerial altimetry MLS to generate specific terrain surfaces with objects on top of that surface. In Friess (2006), simulated data are used as input data to test the proposed boresight error estimation algorithms without discussing the data production details (Skaloud and Lichti 2006). Kim (2009) proposed a geometric model of the LiDAR sensor to simulate aerial mobile LiDAR data of a ray-tracing algorithm and to facilitate the assessment of data quality and the development of the data processing algorithms. Heinz (2015) generates simulated planar targets with a robotic simulation toolbox

called (V-REP). Most geometric-based simulation approaches produce simulated data from airborne MLS with a nadir look at scenes (Friess 2006; Kim et al. 2009).

Moreover, as we can see, the most famous geometric feature in the geometric-based simulation approach is a planar target. Indeed, a planar target shows a simple mathematical model and can be used to demonstrate the effect of MLS systematic errors very well (Filin 2003). In various MLS systematic error estimation approaches, for geometric features of their algorithms, they consider in-situ planar targets like building roofs and facades (Glennie, Kusari, and Facchin 2016; Skaloud and Lichti 2006; Zeng et al. 2018; Heinz et al. 2015).

In this paper, the objective is to analyze the effects of the systematic errors of an MLS on simulated planar targets. For this purpose, we introduce the concept of an MLS simulator that generates simulated point clouds on a pre-defined hypothetical planar target. This design makes it easy to choose each of the systematic errors of an MLS individually and study its impact on the simulated point cloud. This ability allows one to study systematic errors separately and independently without influencing other systematic and non-systematic errors. After generating various simulated point clouds, we present the systematic-error visibility criteria to find the best configuration for planar target inclinations and MLS passages for each systematic error separately.

The subsequent sections of the paper are organized as follows. Section 3.4 presents the conceptual model of the proposed simulator and the visibility criteria index. Section 3.5 discusses the results of analyzing the systematic errors for the simulated data. The validation procedure with the real-data point clouds is presented in Section 3.6. Finally, conclusions and future works are recommended in Section 3.7.

3.4 Methodology

This section introduces the conceptual model of the simulator that enables us to study the effect of systematic errors of an MLS in a simulated environment. Figure 3.1 illustrates this conceptual model and different parts of the methodology that

generates an MLS simulated point cloud. As shown in Figure 3.1, two kinds of input data enter the direct georeferencing module function: the positioning and orientation system (POS) as observations and the LiDAR range with systematic error effects as the result of the LiDAR range estimation function. The following section describes the mathematical model of direct georeferencing and its components.

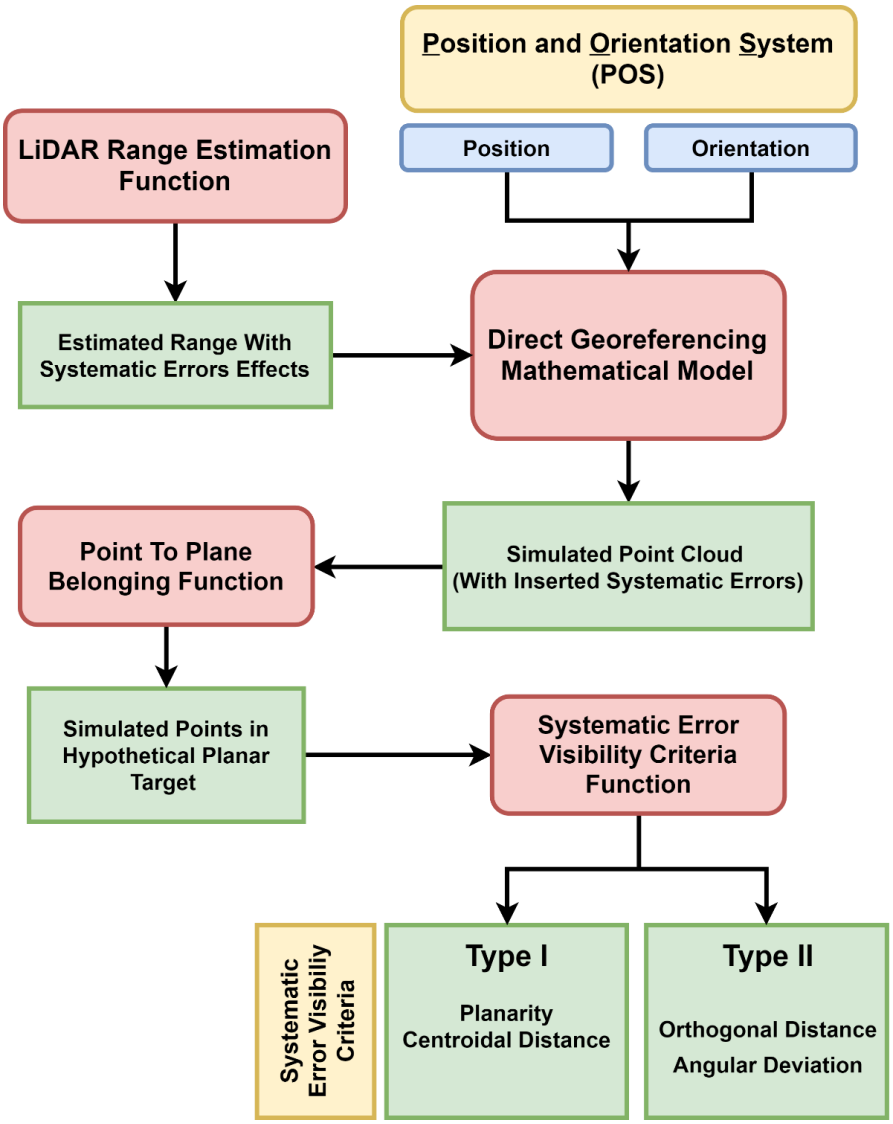

Figure 3.1– Flowchart of the methodology to produce a simulated point cloud with inserted systematic errors. Red boxes represent the functions and green boxes the functions' results. Blue boxes are for simulated observations and the yellow boxes are for common observations or functions.

3.4.1 Direct georeferencing mathematical model

Equation (3.1) presents the mathematical model of the direct georeferencing of an MLS (Ackermann 1999; Wehr and Lohr 1999; Shan and Toth 2008; Vosselman and Maas 2011). The output of the Equation (3.1) model, $(X \quad Y \quad Z)'_{LGF}$, is the 3D position vector of the georeferenced point in a relative coordinate system such as the Local Geodetic Frame (LGF).

In Equation (3.1), we have two transformations between three frames, from the LiDAR frame to the POS frame and from the POS frame to the LGF frame. Here also, to simplify our simulation design, we consider that the GNSS antenna phase center and the IMU gravity center are located at the POS reference center.

$$\begin{bmatrix} X^{LGF} \\ Y^{LGF} \\ Z^{LGF} \end{bmatrix} = \begin{bmatrix} P_X^{LGF} \\ P_Y^{LGF} \\ P_Z^{LGF} \end{bmatrix} + R_{POS}^{LGF}(r,p,h) \left(R_{LiDAR}^{POS}(\alpha,\beta,\gamma) \begin{bmatrix} x_{LiDAR} \\ y_{LiDAR} \\ z_{LiDAR} \end{bmatrix} + \begin{bmatrix} a_X^{POS} \\ a_Y^{POS} \\ a_Z^{POS} \end{bmatrix} \right) \qquad (3.1)$$

We choose to georeference the data in a relative coordinate system such as LGF instead of a projection system like UTM because the survey and the area we consider for analyzing systematic errors, such as boresight error, typically covers a small area. Thus, we avoid using a projection coordinate system to simplify calculations and remain in a relative local coordinate frame.

The following section explains each part of the direct georeferencing mathematical model by considering their respective contribution to the proposed simulation design and concept.

3.4.1.1 *Trajectory Position Vector*

In the simulator design, the positions of the trajectory, $(P_x \quad P_y \quad P_z)'_{LGF}$, a 3D position vector for each trajectory point in the Local Geodetic Frame (LGF) system is represented by a sequence of points. Figure 3.2 shows a sample of trajectory points (in black) and simulated LiDAR points (in red) on a hypothetical planar target. We consider that the trajectory follows a straight line at a fixed height from the ground.

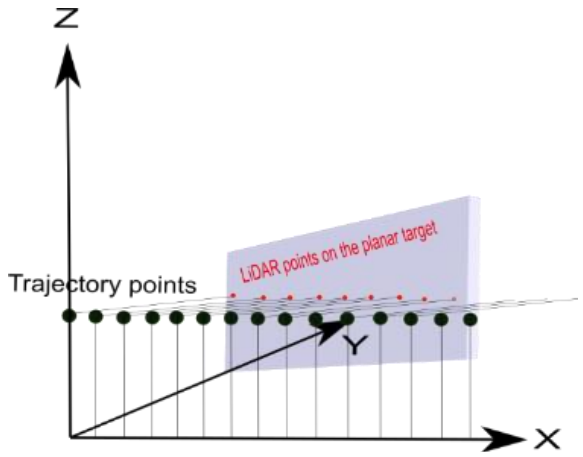

Figure 3.2 -Trajectory points (large black points) and LiDAR points (small red points)

For trajectory lines parallel to the planar target and the X-Z plane, the values of ‘y’ are zero, the values of ‘z’ are constant, and the values of ‘x’ gradually increase, as illustrated in Figure 3.2.

3.4.1.2 *Attitude Angles Transformation Matrix*

The R_{POS}^{LGF} transformation matrix consists of three attitude angles: roll (r), pitch (p), and heading (h) between LGF and POS frames. These angles define the orientation of the platform. For example, for having round-trip parallel trajectories, we consider that in the first passage, the heading angle is 0°, and in the second passage, the heading angle is 180°. In our simulation, we can change the heading angle to produce other passages, for example, 45°, 225°, 315°, and 135° headings. Figure 3.3 illustrates the simulated trajectory of the six passages with respect to the planar target.

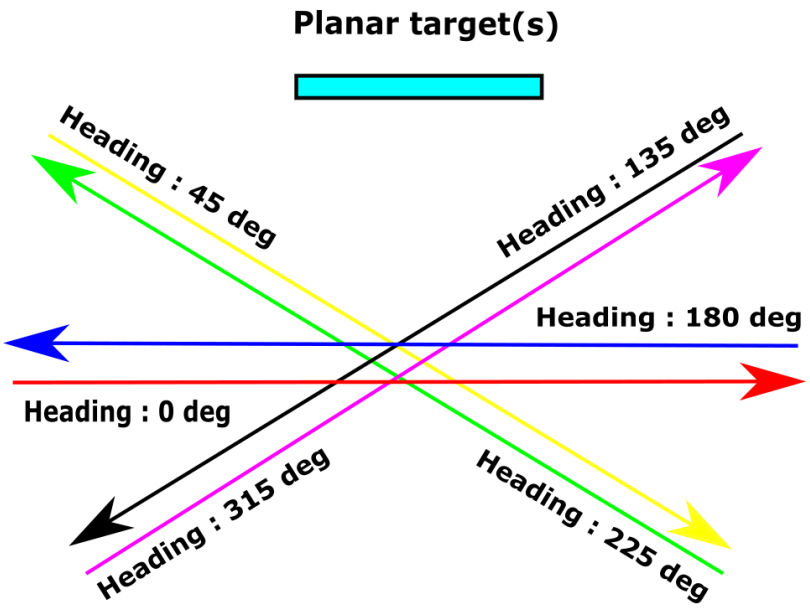

Figure 3.3 – Simulated trajectory of the six passages with respect to the planar target

This paper considers only these trajectories to simplify the analysis of systematic errors. Our objective is to consider a simple platform (vehicle) motion scenario and analyze the effect of systematic errors on the planar targets based on the proposed configurations.

3.4.1.3 *Target Point Position Vector*

The vector r_{LiDAR} describes the position of the target point w.r.t the optical center of the LiDAR scanner. This vector consists of two parameters, the $\boldsymbol{\rho}$ (range) distance from the optical center of the LiDAR scanner to the target point and $\boldsymbol{\alpha_{LiDAR}}$ (scan angle), which can be between 0° and 360°. The direct georeferencing mathematical model uses the polar coordinates representation for the r_{LiDAR} vector. In the proposed simulation design, inside the range estimation function, we directly insert systematic errors such as the boresight angle errors, lever arm errors, range offset, and scan angle offset. Section 3.4.2 will describe the systematic error insertion procedure using the range estimation function. Figure 3.4 illustrates a schematic LiDAR scanner with its corresponding spherical representation in the simulation design.

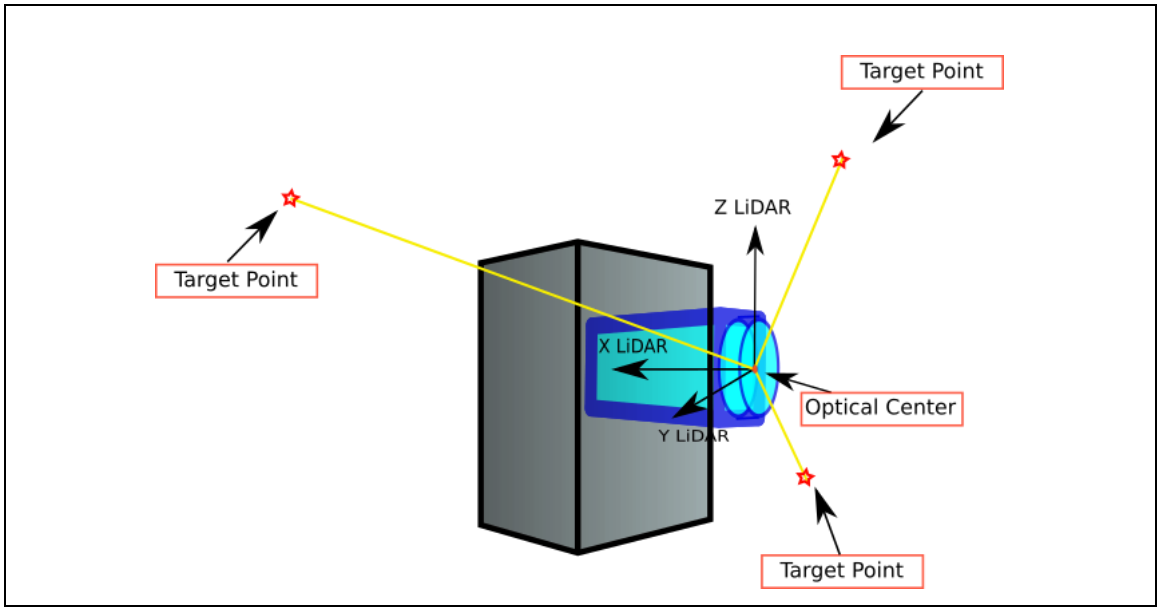

(a)

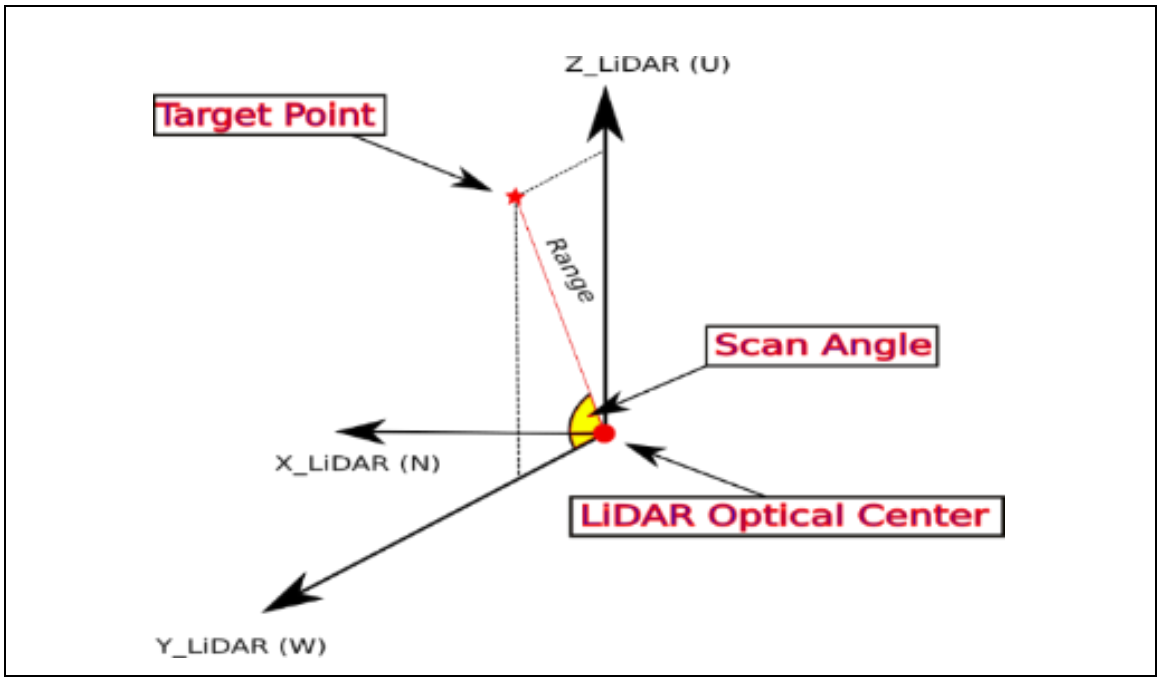

(b)

Figure 3.4 – (a) Schematic LiDAR scanner with optical center (b) Local LiDAR frame with spherical parameters representation

3.4.1.4 *POS-LiDAR Lever arm Vector*

In the proposed simulator, to simplify the design, we consider the POS-LiDAR lever arm vector, $(a_x \quad a_y \quad a_z)'_{LGF}$, as a translation vector between the LiDAR frame and

the POS frame, to be zero, which means that the POS and LiDAR are superposed in the same location. Thus, we only consider the lever arm components to have errors in the X, Y, and Z directions.

3.4.1.5 *Boresight Angles Transformation Matrix*

The R_{LiDAR}^{POS} transformation matrix consists of three boresight angles (α, β, γ) between the LiDAR frame and POS frame. This imposed boresight error affects the calculated range of the LiDAR scanner w.r.t a specific target. Because of these parameters on the range of georeferenced data, we expect that generated point clouds with imposed POS-LiDAR boresight angles will be placed at the wrong location or may even be placed outside the hypothetical planar surface.

3.4.2 LiDAR Range Estimation Function

Among the presented direct georeferencing parameters of Equation (3.1), as described in Section 3.4.1, the range ($\boldsymbol{\rho}$), which is one of the parameters of r_{LiDAR} vector has a significant role in modeling the POS-LiDAR systematic errors of an MLS. By considering the misaligned MLS due to systematic errors such as boresight and lever arm errors, we calculate the range of the LiDAR point (Morin and El-Sheimy 2002). To generate a simulated point cloud with imposed systematic errors to the system, we must be able to implicitly introduce systematic errors such as POS-LiDAR boresight angles, POS-LiDAR lever arms, LiDAR range offset, and LiDAR scan angle offset to the simulator algorithm. Ultimately, the simulator produces data affected by these misalignments created by the MLS systematic errors. In the first step, as shown in Equation (3.2), we calculate the georeferenced point without considering any systematic errors,

$$\begin{bmatrix} X \\ Y \\ Z \end{bmatrix}_{LGF} = \begin{bmatrix} P_x \\ P_y \\ P_z \end{bmatrix}_{LGF} + R_{POS}^{LGF}(r, p, h) \underbrace{\left(\boldsymbol{\rho} \begin{bmatrix} 0 \\ \cos(\alpha_{LiDAR}) \\ \sin(\alpha_{LiDAR}) \end{bmatrix} \right)}_{r_{LiDAR}} \tag{3.2}$$

In the second step, we introduce a function that explicitly calculates the range ($\boldsymbol{\rho}$) of the emitted point from an MLS with imposed systematic errors. The concept of the MLS systematic errors is exactly like in a real-world situation where we do not have any a priori knowledge about these systematic errors. Hence, we can generate misaligned points by adding systematic errors to boresight angles, lever arm vectors, range, and scan angle errors. After georeferencing the point cloud, we can observe a data misalignment coming from these POS-LiDAR systematic errors. Figure 3.5 illustrates calculating the LiDAR range in the simulation model.

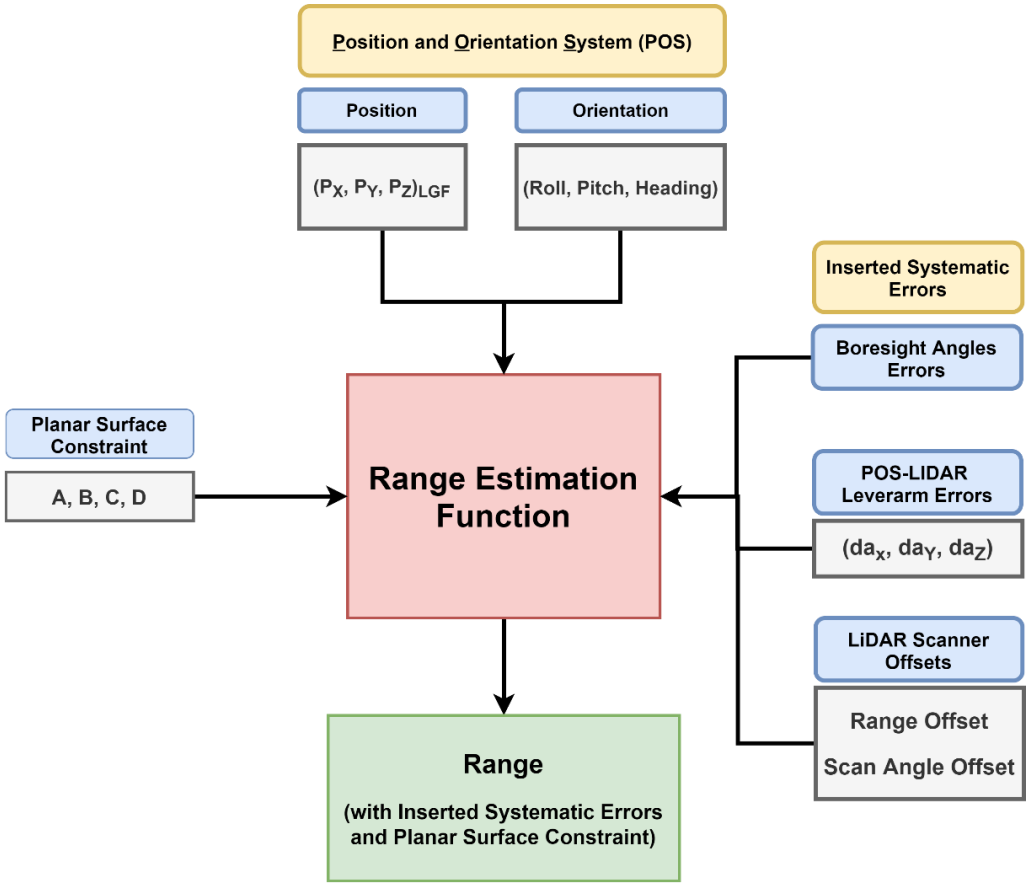

Figure 3.5 – Flowchart of the range estimation function

As mentioned before, the geometric feature used in our analysis is a planar target. Thus, we study how systematic errors of an MLS impact points constrained to lie

over a planar target. Equation (3.3) represents the mathematical model for the planar target.

$$AX_{LGF} + BY_{LGF} + CZ_{LGF} + D = 0 \quad (3.3)$$

In Equation (3.3), the $(X_{LGF}, Y_{LGF}, Z_{LGF})$ are the coordinates of the georeferenced point obtained with Equation (3.1). The plane parameters (A, B, C, D) define the hypothetical planar target where parameters A, B, and C are the normalized (unit length) normal vector of the planar target and the parameter D is the negative orthogonal distance of the planar target w.r.t the origin of the LGF coordinate system (Skaloud and Lichti 2006).

Thus, each georeferenced point generated by the simulator is constrained to lie on the hypothetical planar target. Based on this assumption, we calculate the range of each point, defined as the distance between the mobile LiDAR system and the planar target. This range variable is part of the r_{LiDAR} vector of the direct georeferencing model in Equation (3.1).

We use symbolic language to define the explicit function for range based on the georeferencing mathematical model. In this paper, we have used the MATLAB symbolic toolbox to generate the explicit function of the range. Thus, the explicit range function will be a function of all input parameters described in Figure 3.5 (blue cases), as follows:

- Position and Orientation System (POS) parameters
- Inserted systematic errors: POS-LiDAR boresight angles error, lever arm error, range offset, and scan angle offset
- Planar target constraint

3.4.3 Point to Plane Belonging Function

One of the crucial parts of the simulator design is to verify if a georeferenced point belongs to a planar surface or not. Using a mathematical model that defines an

infinite plane, we first define four corner points of our planar target with respect to the system frame. If a point is in a rectangle, the area summation of the four triangles must be equal to the area of the triangle, as illustrated in Figure 3.6. These four triangles are made by connecting the point to the four vertices of the rectangle.

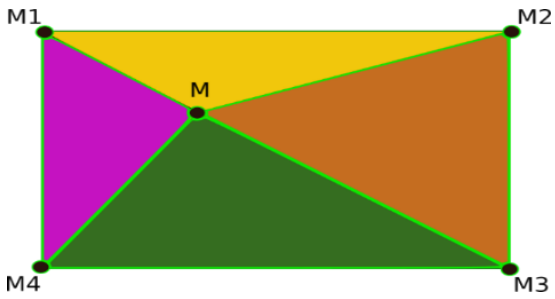

Figure 3.6 – Point M inside the rectangle M1-M2-M3-M4

The point “M” belongs to rectangle “$M1\ M2\ M3\ M4$" because the summation of the areas of the following four triangles: $\Delta M1\ M\ M2$, $\Delta M2\ M\ M3$, $\Delta M3\ M\ M4$ and $\Delta M4\ M\ M1$ is equal to the area of the rectangle "$M1\ M2\ M3\ M4$". If the point is outside the rectangle, the above summation will produce a greater value than the area of the rectangle, and therefore, the algorithm will reject it.

3.4.4 Systematic-Error Visibility Criteria Function

Until now, we explained how to generate a point cloud, which lies on a planar target using an MLS with inserted systematic errors. With this capability, we can produce various simulated point clouds with specific configurations. We define the term “Configuration” as the setup that leads to the final point cloud, which is as follows,

(1) The inclination of the planar target
(2) The passage of the MLS
(3) The dimension of the planar target
(4) The height difference between MLS and planar target

In this research, we consider parameters (1) and (2) of the configuration as variables and parameters (3) and (4) as constants.

We will have simulated point clouds on the planar target based on various configurations. To quantify the impact of systematic errors on the plane's point cloud, we introduce two types of "systematic-error visibility criteria." ***Type I,*** which makes a raw selection from the configurations, is a quantitative value based on two parameters: planarity and centroidal distance, and ***Type II,*** which makes a fine selection from the retained configurations, consists of two parameters: angular deviation and signed orthogonal distance.

Figure 3.7 details the algorithm of calculation of the centroid, eigenvalues, and the normal of the plane.

ALGORITHM 1: ALGORITHM TO CALCULATE CENTROID AND NORMAL OF A PLANE

Input: *3D coordinates of the plane*
Output: *centroid and normal of the plane*
number-of-Points ← *count the total number of points in the dataset*
Initialization of variables*: assign zero to the variable* $\boldsymbol{i, X, Y, Z, C, \lambda_1, \lambda_2, \lambda_3}$
for $(\boldsymbol{i} < \boldsymbol{number\text{-}of\text{-}Points})$ *// read all the points and accumulate their values into one variable*
    $\boldsymbol{X}$ ← *read the x coordinate of each point and add to the variable*
    $\boldsymbol{Y}$ ← *read the y coordinate of each point and add to the variable*
    $\boldsymbol{Z}$ ← *read the z coordinate of each point and add to the variable*
end
$\boldsymbol{x_c} \leftarrow \boldsymbol{X / number\text{-}of\text{-}Points}$
$\boldsymbol{y_c} \leftarrow \boldsymbol{Y / number\text{-}of\text{-}Points}$
$\boldsymbol{z_c} \leftarrow \boldsymbol{Z / number\text{-}of\text{-}Points}$
$\boldsymbol{C}$ ← *covariance matrix with 3D coordinates* ***[X, Y, Z]*** *of the plane*
$\boldsymbol{\lambda_1, \lambda_2, \lambda_3}$ ← *eigenvalues calculated based on* $\boldsymbol{C}$ *in descending mode* $\boldsymbol{\lambda_1 \geq \lambda_2 \geq \lambda_3 \geq 0}$
$\boldsymbol{n}$ ← *normal of the plane* (n_x, n_y, n_z)
$\boldsymbol{d} \leftarrow -(x_c n_x + y_c n_y + z_c n_z)$ *// perpendicular distance of the plane from the origin*

Figure 3.7 – Algorithm to calculate centroid, eigenvalues, and normal of a plane

3.4.4.1 *Type I – Planarity and centroidal distance*

As mentioned, the ***Type I*** systematic-error visibility criterion consists of two parameters, planarity, and centroidal distance, which make an initial selection from all the available configurations.

We consider the eigenvalues of the simulated point cloud covariance matrix to calculate the planarity parameter (West et al. 2004; Pauly, Keiser, and Gross 2003;

Blomley, Jutzi, and Weinmann 2016; Gross, Jutzi, and Thoennessen 2007). On the other hand, the centroidal distance calculates the distance between the hypothetical planar target's centroid and the simulated planar target and is considered a dispersion indicator. If the "*CentroidalDistance*" is considered as x_i, its normalized value between [0, 1] z_i is calculated based on Equation (3.4).

$$z_i = \frac{x_i - \min(x)}{\max(x) - \min(x)} \tag{3.4}$$

The algorithm to calculate ***Type I*** systematic-error visibility criteria is demonstrated in Figure 3.8.

ALGORITHM 2: ALGORITHM TO CALCULATE VISIBILITY CRITERIA TYPE I

Input: *3D coordinates of the simulated plane,* $\boldsymbol{C_{ref}}$ *and* $\boldsymbol{n_{ref}}$ // $\boldsymbol{n_{ref}}$ *reference plane's* // $\boldsymbol{C_{ref}}$ *reference plane's centroid*

Output: *Type I visibility criteria*

1 ***Initialization of variables****: assign zero to variable* ***Type I***

2 ***centroid*** ← *calculate the centroid of the simulated plane from algorithm 1*

3 $\boldsymbol{n}$ ← *calculate the normal of the simulated plane from algorithm 1*

4 $\boldsymbol{\lambda_1}, \boldsymbol{\lambda_2}, \boldsymbol{\lambda_3}$ ← *calculate the descendent eigenvalues of the simulated plane from algorithm 1*

5 ***planarity*** ← $(\boldsymbol{\lambda_2} - \boldsymbol{\lambda_3})/\boldsymbol{\lambda_1}$

6 ***CentroidalDistance*** ← *Euclidean distance between centroid and* $\boldsymbol{C_{ref}}$

7 ***Type I*** ← ***planarity (1- CentroidalDistance)***

Figure 3.8 – Algorithm to calculate ***Type I*** visibility criteria

The more the ***Type I*** is near a plane shape (planarity) and at the same time it is near the reference plane (CentroidalDistance near zero), the more the value of ***Type I*** criteria will be near 1. The considerable centroidal distance typically occurs when the simulated plane inclination is parallel to the direction of the LiDAR scanner beam, which decreases the accuracy of the generated point cloud (Cassol 2018).

As a result, the ***Type I*** visibility criteria applies for an initial analysis of all the possible configurations. In Figure 3.9, two samples are introduced, one for a strong (near 1) and one for a weak (near 0) Type I systematic-error visibility criteria. As we can see schematically in Figure 3.9 (a), the ***Type I*** systematic-error visibility criterion is strong because the different instances of the planar target are sufficiently close to the hypothetical plane. In Figure 3.9 (b), the ***Type I*** systematic-error visibility criterion is

weak because the different instances of the planar target are too far from the hypothetical plan. Therefore, we eliminate the latter configuration for further analysis.

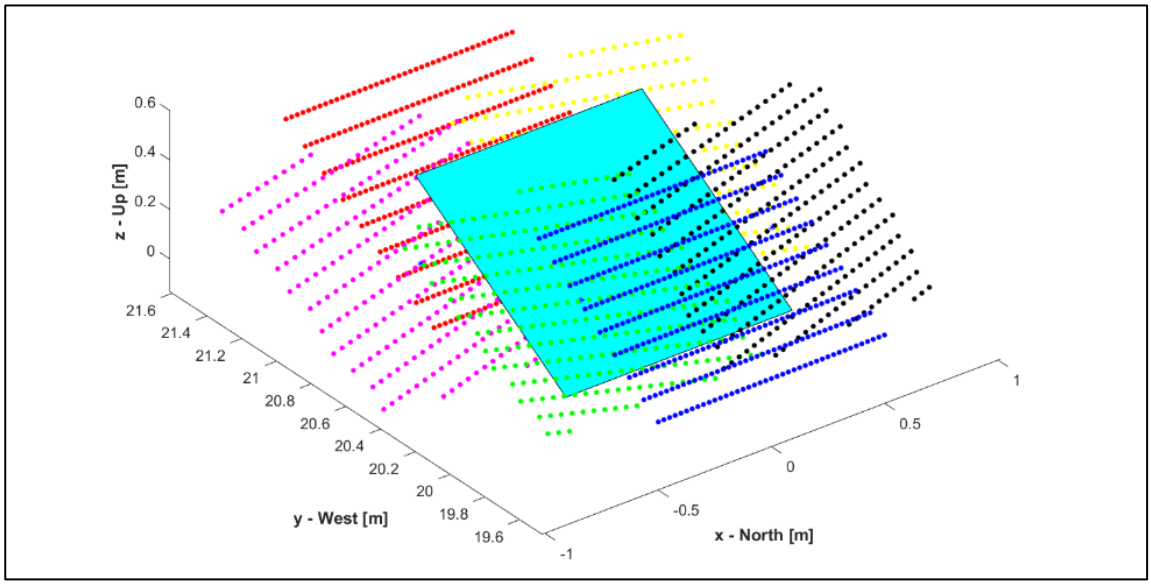

(a)

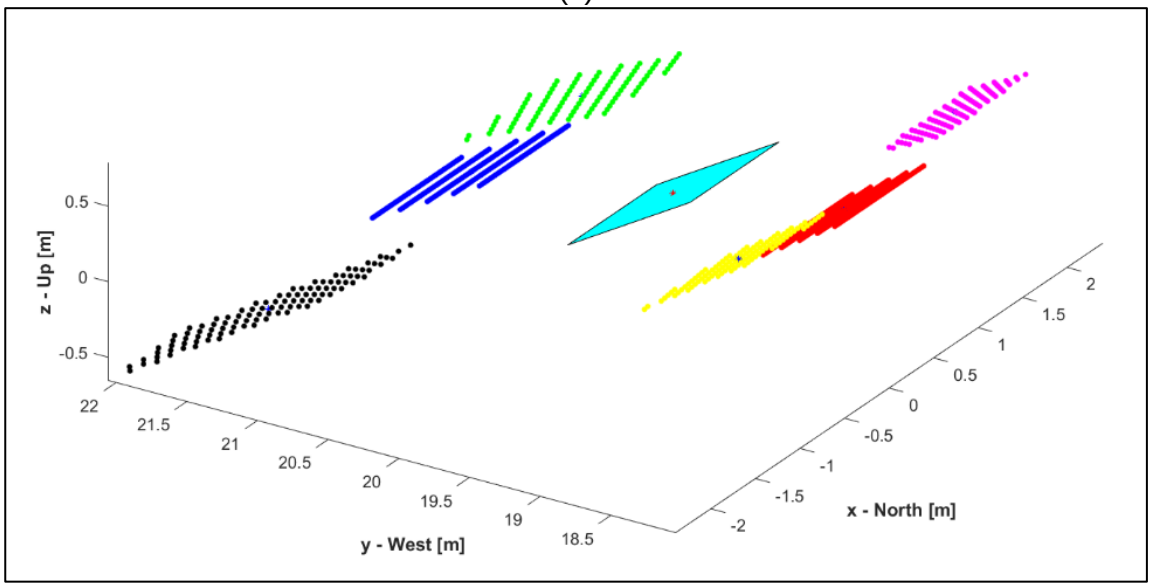

(b)

Passage	0°	180°	45°	225°	315°	135°
Color						

Figure 3.9 – (a) Strong configuration ***Type I*** systematic-error visibility criterion (-60 deg) (b) Weak configuration ***Type I*** systematic-error visibility criterion (60 deg)

3.4.4.2 *Type II – Angular Deviation and Signed Orthogonal Distance*

This section considers ***Type II*** systematic error visibility criteria, which make a more delicate selection from the retained configurations. The normal vector between the planar surfaces is a solid and simple indicator that shows the angular deviation between the hypothetical plane and the plane generated by the simulator. The signed orthogonal distance also shows the shortest distance between the centroid of the simulated planar surface point cloud and the hypothetical planar target. The algorithm to calculate both parameters of the ***Type II*** visibility criteria is demonstrated in Figure 3.10.

ALGORITHM 3: ALGORITHM TO CALCULATE VISIBILITY CRITERIA TYPE II

Input: *3D coordinates of a simulated plane* $\boldsymbol{n_{ref}}$ // $\boldsymbol{n_{ref}}$ *reference plane's normal*
Output: *Type II visibility criteria*
1 ***Initialization of variables****: assign zero to the variable* ***centroid***, ***n***, ***Type I***
2 ***centroid*** ← *calculate the centroid of the simulated plane from algorithm 1*
3 ***n*** ← *calculate the normal of the simulated plane from algorithm 1*
4 ***AngularDeviation*** ← $\boldsymbol{tan^{-1}}(\|\boldsymbol{n} \times \boldsymbol{n_{ref}}\|/(\boldsymbol{n} \,.\, \boldsymbol{n_{ref}}))$ *// this variable is always in [0°, 90°]*
5 ***OrthogonalDistance*** ← $(\boldsymbol{n_{ref}}$ ***. centroid)*** / $\|\boldsymbol{n}\|$ *// distance btw ref and simulated planes*

Figure 3.10 – Algorithm to calculate ***Type II*** visibility criteria

As shown in Figure 3.11, a systematic error of the roll boresight angle in parallel round-trip passages w.r.t the planar target impacts the generated point clouds compared to the hypothetical planar surface (a) angular deviation and (b) orthogonal distance drift. For ***Type II*** criteria, we must compare various passages and then choose the configuration with a more significant angular deviation difference and higher orthogonal distance.

Thus, ***Type I*** and ***Type II*** systematic-error visibility criteria make a raw and fine selection from configurations that ultimately generate the simulated point clouds. Configurations at their ***Type I*** and ***Type II*** criteria value attain the expected threshold and will be considered an ideal input for detecting systematic errors and will consequently be chosen for calibration of an MLS.

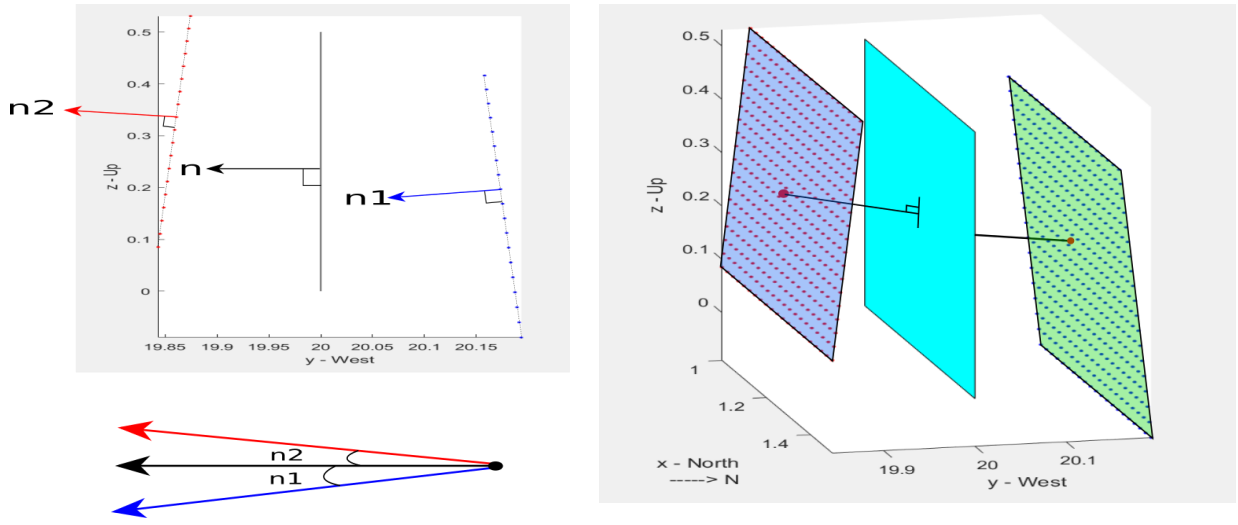

(a) (b)

Figure 3.11 – ***Type II*** systematic-error visibility criteria for roll systematic error analysis (a) angular deviation (b) signed orthogonal distance

In the next section, these two types of systematic-error visibility criteria will be used as an indicator to select the best planar target configurations.

3.5 Results and Discussions

In the analysis of systematic errors of an MLS, the objective is to find out the best configuration (which in this paper is considered the combination of Plane inclination and MLS passage) to obtain ***Type I*** and ***Type II*** systematic-error visibility criteria for each of the eight MLS systematic errors in the expected threshold. In the terrestrial MLS simulator, we consider that the system's height is fixed and is ‘h = 2.5 m’ from the ground, and the planar target is on the ground at a lower height (less than h). We consider 19 inclinations of the planar target with respect to the terrestrial MLS simulator, which varies between -90° and 90° with 10° intervals, as illustrated in Figure 3.12.

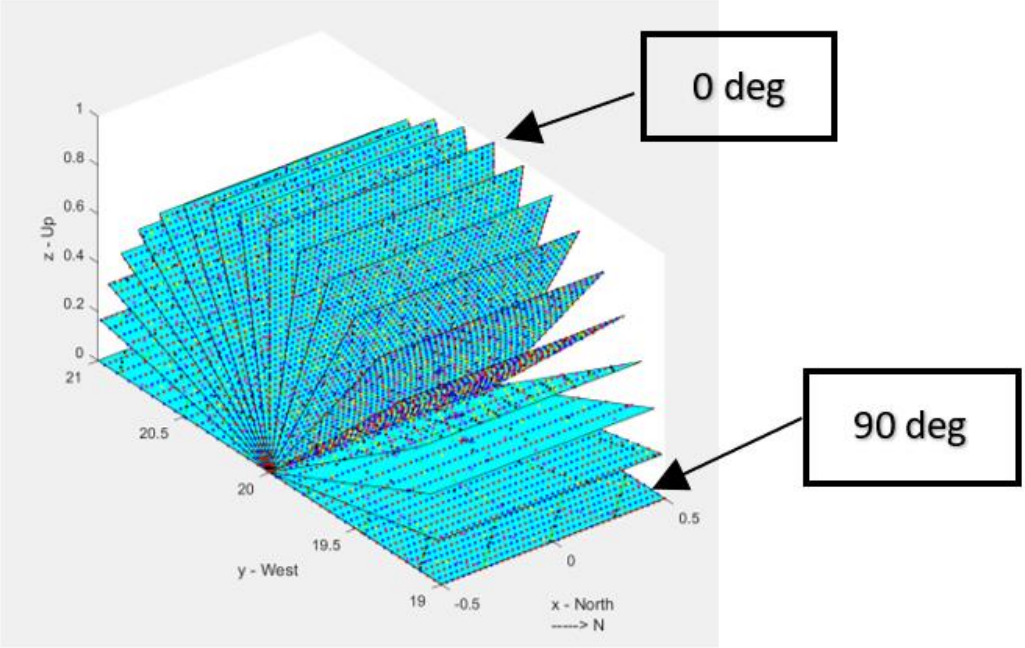

Figure 3.12 – All the 19 planar target inclinations versus a terrestrial MLS

3.5.1 Line Pattern

As previously shown in Figure 3.3, the line pattern consists of six passages with 0°, 180°, 45°, 225°, 315°, and 135° heading directions.

3.5.2 Systematic-Error Visibility Criteria Analysis

In this section, we analyze each of the eight systematic errors. Based on the ***Type I*** criteria, the configurations that produce point clouds with acceptable planar shape will have a value near 1 for the ***Type I*** criteria and proximity to the hypothetical plane (the centroidal distance around 0). Thus, we keep only the configurations that result in a ***Type I*** value around 1. Once we have selected the configurations with the ***Type I*** criteria, we then use the ***Type II*** criteria, which will make a more delicate selection and result in a single plane's inclination. The result of ***Type II*** criteria of each terrestrial MLS systematic error represents the best possible configuration to generate a point cloud with the best visibility for that specific error. A complete analysis of the pitch systematic error is performed in the following. Based on the

same procedure, we analyze the other seven MLS systematic errors and summarize the best configurations for each of them.

To demonstrate the procedure, we consider the impact of the pitch boresight angle of 2° inserted into the MLS on the hypothetical planar target. Figure 3.13 presents the values of the ***Type I*** criteria, and Figure 3.14 represents the ***Type II*** criteria for all the six MLS passages and the 19 plane inclinations. The blue box in these two figures is considered the plane's inclination that the ***Type I*** and ***Type II*** criteria are within the expected threshold.

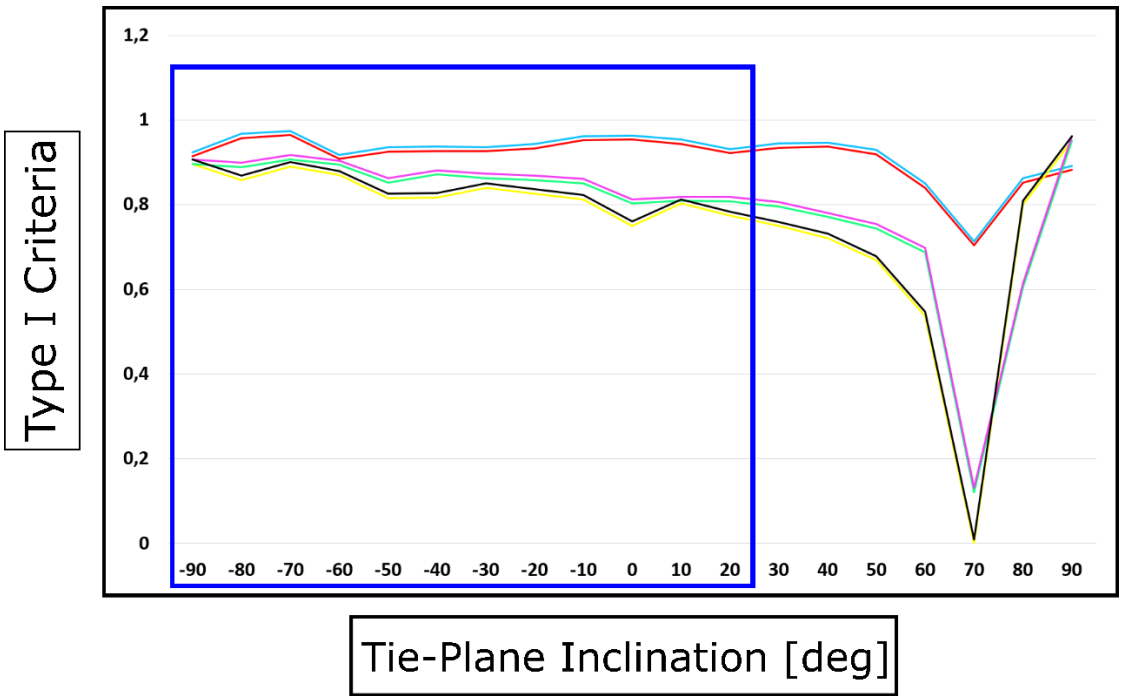

Passage	0°	180°	45°	225°	315°	135°
Color						

Figure 3.13 – Pitch boresight angle ***Type (I)*** systematic-error visibility criterion of all the possible inclinations (horizontal axis in degree)

Based on the ***Type I*** criteria, Table 3.1 represents all the possible configurations that result in the expected visibility of the pitch boresight angle systematic error.

Table 3.1 – Possible configurations for pitch boresight angle systematic error

MLS Passage Possibilities	(0°, 45°, 225°)	(0°, 135°, 225°)
	(0°, 45°, 315°)	(0°, 135°, 315°)
	(180°, 45°, 225°)	(180°, 135°, 225°)
	(180°, 45°, 315°)	(180°, 135°, 315°)
	From	To
Possible Plane Inclinations	-90°	20°

Based on the possible configurations in Table 3.1, we perform the fine selection with the ***Type II*** criteria. As shown in Figure 3.14, the best visibility configuration for the pitch boresight angle systematic error is one of the eight passage possibilities introduced in Table 3.2 – Best configurations for all systematic errors, like (180° - blue color, 135° - black color, 315° - pink color) passages and 0° inclination (vertical plane). This configuration produces the maximum value of both the signed orthogonal distance and the angular deviation when using a vertical plane (0° inclination), while we have inserted pitch boresight angle systematic error in our system. Table 3.2 summarizes the best configurations for all eight systematic errors.

Table 3.2 – Best configurations for all systematic errors based on simulated data

Systematic Error	Value	Best Configuration	
		MLS Passages	Plane Inclination
Roll boresight error	2°	(0°, 180°, 45°, 225°)	-40°
Pitch boresight error	2°	(0°, 45°, 225°)	0°
Yaw boresight error	2°	(0°, 45°, 315°)	0°
X lever arm error	10 cm	(0°, 45°, 225°)	0°
Y lever arm error	10 cm	(0°, 180°, 45°, 225°)	0°
Z lever arm error	10 cm	Nan	Nan
Range offset	10 cm	(180°, 225°)	-60°
Scan angle offset	2°	(0°, 180°, 45°, 225°)	-50°

While analyzing all MLS systematic errors, we recognized a correlation between the scan angle offset and the roll boresight angle systematic error due to the same rotational effect of two systematic errors on the planar target.

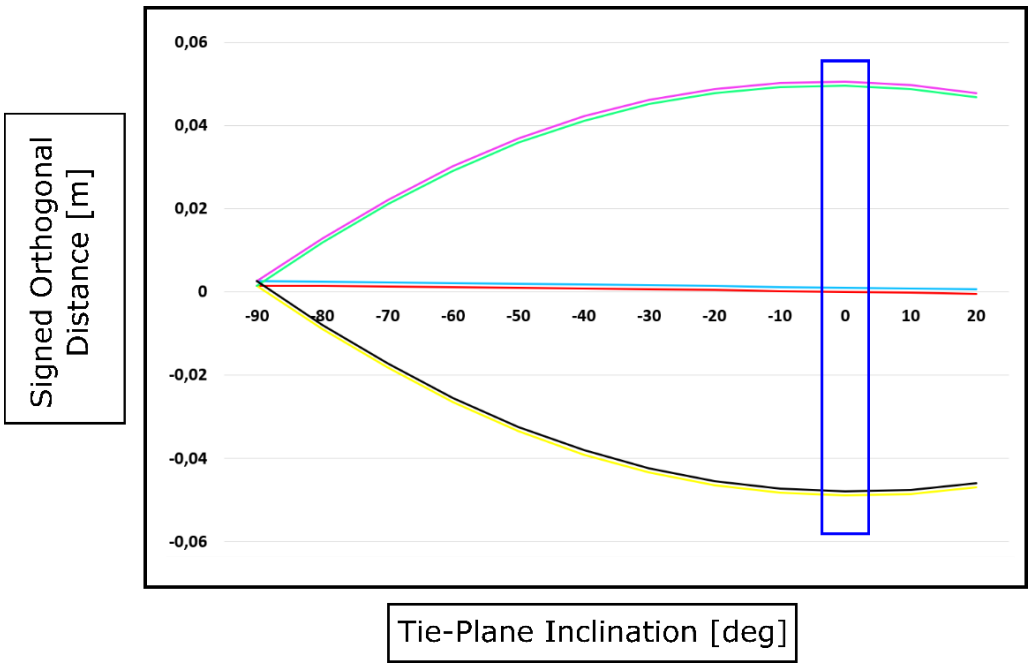

(a)

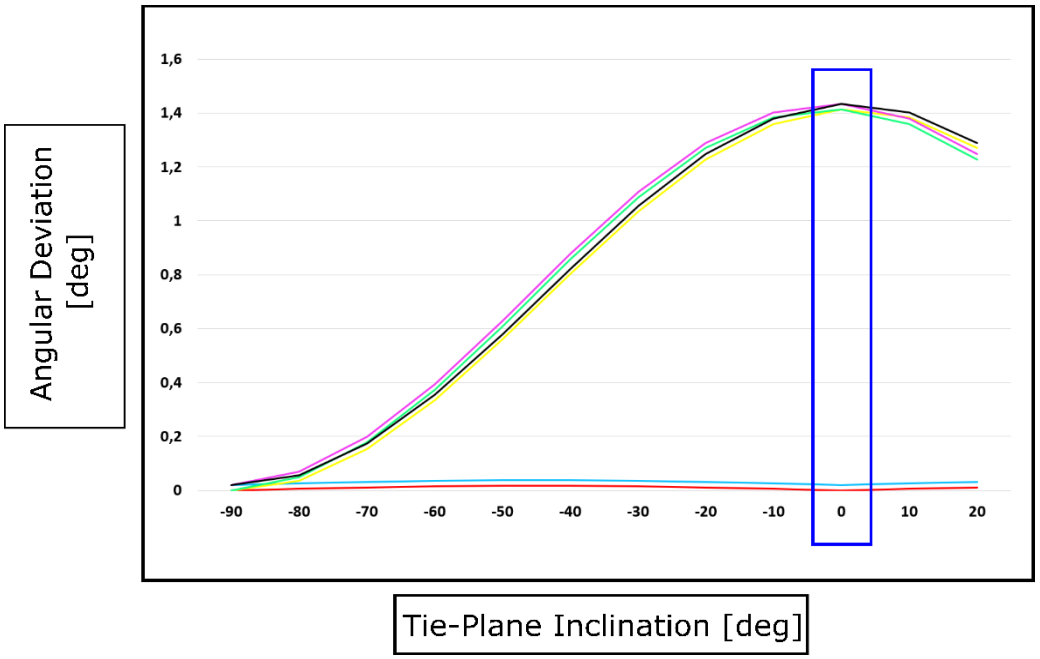

(b)

Passage	0°	180°	45°	225°	315°	135°
Color						

Figure 3.14 – Pitch boresight angle systematic error ***Type (II)*** criteria (a) Signed orthogonal distance (vertical axis in meter) and (b) Angular deviation (vertical axis in degree) of possible inclinations (horizontal axis in degree)

Also, we did not suggest any possible configuration for the Z lever arm systematic error due to the nature of the Z lever arm error, which is a translation and shift in the Z direction in a similar fashion for all the points of all passages. Thus, it is impossible to observe the Z lever arm error with our actual planar target configurations (Leslar, Hu, and Wang 2014; Skaloud and Lichti 2006). Therefore, measuring the Z lever arm with a precise and accurate surveying technique, like the total station method, is suggested. Then, this value can be entered as a constant in the georeferencing model to generate the point cloud (Leslar, Hu, and Wang 2014; Skaloud and Lichti 2006).

Based on our analysis results, most systematic errors can be assessed with a planar target of 0° inclination, represented by a vertical plane, and the remaining systematic errors with an inclined planar target between -60° and -40°. We must choose the combination of necessary passages for the line pattern passages that cover all the systematic errors. Table 3.3 suggests the best configuration (combining plane inclinations and MLS passages) to obtain expected visibility for all the terrestrial MLS systematic errors.

Table 3.3 – Suggested combination of MLS passages and planar targets with different inclinations for estimation of systematic errors of a terrestrial MLS.

Best Configurations (passages + plane inclinations)		
MLS Passage Possibilities	(1)	(0°, 180°, 45°, 225°, 135°)
	(2)	(0°, 180°, 45°, 225°, 315°)
	(3)	(0°, 180°, 315°, 135°, 45°)
	(4)	(0°, 180°, 315°, 135°, 225°)
Possible Plane Inclinations	One inclined plane (between -40° and -60°) and one vertical plane (0°)	

3.6 Experiments and Validation

To validate the proposed methodology, we implemented a real-world test with a mobile LiDAR system composed of a LiDAR scanner (Z+F 9012 profiler), an IMU (iXBlue ATLANS-C), and GNSS antenna (Septentrio), and a structure made of three planar targets as seen in Figure 3.15.

(a) (b)

Figure 3.15 – (a) Terrestrial MLS for validation test (b) Location of the validation test on OpenStreetMap with the line pattern and the location of the three planar targets

The validation test was carried out on a parking lot where we installed the three planar (horizontal, vertical, and inclined) target assembly and collected data by following our proposed six-line pattern. The dimension of each planar target is 1 m x 1 m for simplicity and applicability. To be able to compare the results of this real-data validation test with those of the simulated data from Section 3.5, we consider that the vertical planar target inclines [-10°, 10°], the inclined planar target inclines [-60°, -40°], and inclination between [70°, 90°] is considered a horizontal target. Also, we tried to follow the same line pattern presented in Figure 3.3 for the simulation. Based on the ***Type I*** analysis, five out of six passages were around 1, which is the value that defines the planarity and proximity to the centroid. Only passage P4, one of the side-looking passages whose ***Type I*** value was far below the value one, was eliminated. On the other hand, as the horizontal plane does not satisfy the ***Type I*** criterion for most of the passages, it was not used. Thus, our experiment considers only the vertical and inclined planar targets and the five passages (P1, P2, P3, P5, and P6).

We analyze the ***Type II*** criteria based on these selected configurations in the next step. For the orthogonal distance criteria with the vertical plane, the difference between the maximum value obtained in passage P6 and the minimum value obtained in passage P3 is 9.4 mm. With the inclined plane, the difference between the maximum value obtained in passage P3 and the minimum value obtained in passage P2 is 49.6 mm. Thus, the inclined plane generates point clouds with the highest orthogonal distances, demonstrating strong visibility for some of the systematic errors of the selected MLS. Based on the angular distance criteria, for the vertical plane, the difference between the maximum (P3) and minimum (P2) is 1.0892°, and for the inclined plane, the difference between the maximum (P5) and the minimum (P3) is 0.3863°. Thus, the vertical plane generates point clouds with the highest angular deviations, demonstrating strong visibility for some of the systematic errors of the selected MLS. We conclude that both planar targets (vertical and inclined) are essential to satisfy the ***Type II*** criteria and, as a result, to obtain strong visibility of all systematic errors of a terrestrial MLS.

Even though we tried as much as possible to reproduce in the real-data validation test the same configurations recommended in the simulation analysis, there are still significant differences between the real and simulation configurations, leading to different values for ***Type II*** criteria, especially for the orthogonal distance. However, these configurations produce point cloud data with the necessary deviation and drift to generate strong visibility of all systematic errors of a mobile LiDAR system.

3.7 Conclusions and Future Works

This paper analyzes eight systematic errors of an MLS with a simulation approach. We introduced the concept, design, and methodology of the MLS simulator. The advantage of adopting this simulation approach is to study each systematic error independent of other errors (e.g., trajectory-based errors and sensor noises). On the other hand, the simulator can generate point clouds on hypothetical planar targets with various configurations without any limitations. The term configuration in this paper mainly refers to the inclination of the planar target and the set of passages, known as a line pattern, followed by an MLS. To detect the best configuration of the

systematic errors of an MLS, we introduced two types of systematic-error visibility criteria, which implement a raw and a fine selection of the existing configurations. The results show that a configuration of two planar targets of 1 m x 1 m size with vertical and inclined inclination, combined with a five passages line pattern, will lead to strong visibility of the systematic errors of an MLS. This result was confirmed with a real data acquisition test. The proposed configuration in this research will lead to relevant information for the calibration of an MLS mounted on a terrestrial platform. Furthermore, the approach adopted in this paper shows that we can study the behavior (here, systematic errors) of a mobile LiDAR system (here, a terrestrial MLS), merely with a conceptual mathematical model, without the need to invest in expensive and time-consuming field tests.

In future works, we will consider more variables for the configuration parameters, like the dimension and inclination of tie-planes. Consequently, we will generate many more possible configurations that will not be easy to analyze using the proposed approach. Thus, we will adopt other techniques to optimize the selection of the best configuration with strong visibility of the systematic errors of a mobile LiDAR system.

Acknowledgments

This study was financed by PSR-SIIRI-953 and MITACS Acceleration in a research program focusing on “Automatic calibration and performance analysis of a mobile LiDAR system” through a partnership between Université Laval and CIDCO (Centre Interdisciplinaire de Développement en Cartographie des Océans), an NPO company.

3.8 References

Ackermann, F. 1999. “Airborne Laser Scanning - Present Status and Future Expectations.” *ISPRS Journal of Photogrammetry and Remote Sensing* 54 (2–3): 64–67. doi:10.1016/S0924-2716(99)00009-X.

Blomley, R., B. Jutzi, and M. Weinmann. 2016. “Classification of Airborne Laser Scanning Data Using Geometric Multi-Scale Features and Different Neighbourhood Types.” *ISPRS Annals of Photogrammetry, Remote Sensing and Spatial Information Sciences* III–3 (June): 169–176. doi:10.5194/isprsannals-iii-3-169-2016.

Brown, Scott D., Daniel D. Blevins, and John R. Schott. 2005. “Time-Gated Topographic LIDAR Scene Simulation.” *Laser Radar Technology and Applications X* 5791: 342. doi:10.1117/12.604326.

Cassol, Willian Ney. 2018. “Définition d’un Modèle d’incertitude-Type Composée Pour Les Systèmes LiDAR Mobiles.” Master Thesis, Laval University.
Cifuentes, Renato, Dimitry Van der Zande, Christian Salas-Eljatib, Jamshid Farifteh, and Pol Coppin. 2018. “A Simulation Study Using Terrestrial LiDAR Point Cloud Data to Quantify Spectral Variability of a Broad-Leaved Forest Canopy.” *Sensors (Switzerland)*. doi:10.3390/s18103357.
Filin, Sagi. 2003. “Recovery of Systematic Biases in Laser Altimetry Data Using Natural Surfaces.” *Photogrammetric Engineering and Remote Sensing* 69 (11): 1235–1242. doi:10.14358/PERS.69.11.1235.
Friess, Peter. 2006. “Toward a Rigorous Methodology for Airborne Laser Mapping.” *Proceedings EuroCOW*, 25–27.
Glennie, Craig, A. Kusari, and A. Facchin. 2016. “Calibration and Stability Analysis of the VLP-16 Laser Scanner.” *International Archives of the Photogrammetry, Remote Sensing and Spatial Information Sciences - ISPRS Archives* 40 (3W4): 55–60. doi:10.5194/isprsarchives-XL-3-W4-55-2016.
Gross, H., B. Jutzi, and U. Thoennessen. 2007. “Segmentation of Tree Regions Using Data of a Full-Waveform Laser.” *PIA 2007 - Photogrammetric Image Analysis, Proceedings*, no. March: 57–62.
Heinz, Erik, Christian Eling, Markus Wieland, Lasse Klingbeil, and Heiner Kuhlmann. 2015. “Development, Calibration and Evaluation of a Portable and Direct Georeferenced Laser Scanning System for Kinematic 3D Mapping.” *Journal of Applied Geodesy* 9 (4): 227–243. doi:10.1515/jag-2015-0011.
Heinz, Erik, Christoph Holst, Heiner Kuhlmann, and Lasse Klingbeil. 2020. “Design and Evaluation of a Permanently Installed Plane-Based Calibration Field for Mobile Laser Scanning Systems.” *Remote Sensing* 12 (3). doi:10.3390/rs12030555.
Kim, Seongjoon, Seonghong Min, Geunhan Kim, Impyeong Lee, and Chulmin Jun. 2009. “Data Simulation of an Airborne Lidar System.” *Laser Radar Technology and Applications XIV* 7323 (May 2009): 73230C. doi:10.1117/12.818545.
Kukko, Antero, Juha Hyyppä, Commission Vi, and W G Vi. 2007. “Laser Scanner Simulator for System Analysis and Algorithm Development : A Case With Forest Measurements.” *ISPRS Workshop on Laser Scanning 2007 and SilviLaser 2007*, no. May: 234–240. http://www.isprs.org/proceedings/XXXVI/3-W52/final_papers/Kukko_2007a.pdf.
Leslar, Michael, Baoxin Hu, and Jianguo Wang. 2014. “Error Analysis of a Mobile Terrestrial LiDAR System.” *GEOMATICA* 68 (September): 183–194. doi:10.5623/cig2014-303.
Lohani, Bharat, Parameshwar Reddy, and Rakesh Kumar Mishra. 2006. “Airborne Altimetric Lidar Simulator: An Education Tool.” *International Archives of the Photogrammetry, Remote Sensing and Spatial Information Science* XXXVI: 179–183.
Morin, Kris, and N El-Sheimy. 2002. “Post-Mission Adjustment Methods of Airborne Laser Scanning Data.” *FIG XXII International Congress, Washington, DC USA*, 1–12.
Pauly, Mark, Richard Keiser, and Markus Gross. 2003. “Multi-scale Feature Extraction on Point-Sampled Surfaces.” *Computer Graphics Forum* 22 (September): 281–289. doi:10.1111/1467-8659.00675.
Ravi, Radhika, and Ayman Habib. 2020. “Fully Automated Profile-Based Calibration Strategy for Airborne and Terrestrial Mobile LiDAR Systems with Spinning Multi-Beam Laser Units.” *Remote Sensing* 12 (3). doi:10.3390/rs12030401.
Ravi, Radhika, Tamer Shamseldin, Magdy Elbahnasawy, Yun Jou Lin, and Ayman Habib. 2018. “Bias Impact Analysis and Calibration of UAV-Based Mobile LiDAR System with Spinning Multi-Beam Laser Scanner.” *Applied Sciences (Switzerland)* 8 (2). doi:10.3390/app8020297.

Schenk, Anton F. 2001. “Modeling and Analyzing Systematic Errors in Airborne Laser Scanners.” *Technical Notes in Photogrammetry* 19 (January). doi:10.13140/RG.2.2.20019.25124.
Shan, Jie, and Charles Toth. 2008. *Topographic Laser Ranging and Scanning: Principles and Processing*. *CRC Press*. Taylor & Francis Group. http://www.tandfonline.com/doi/abs/10.1080/01431160903112612.
Skaloud, Jan, and Derek Lichti. 2006. “Rigorous Approach to Bore-Sight Self-Calibration in Airborne Laser Scanning.” *ISPRS Journal of Photogrammetry and Remote Sensing* 61 (1): 47–59. doi:10.1016/j.isprsjprs.2006.07.003.
Vosselman, George, and Hans-Gerd Maas. 2011. *Airborne and Terrestrial Laser Scanning*. *Whittles Publishing*. Vol. 4. Scotland: CRC Press Taylor & Francis Group. doi:10.1080/17538947.2011.553487.
Wehr, Aloysius, and Uwe Lohr. 1999. “Airborne Laser Scanning - An Introduction and Overview.” *ISPRS Journal of Photogrammetry and Remote Sensing* 54 (2–3): 68–82. doi:10.1016/S0924-2716(99)00011-8.
West, Karen, Brian Webb, James Lersch, Steven Pothier, Joseph Triscari, and Evan Iverson. 2004. “Context-Driven Automated Target Detection in 3D Data.” *Proceedings of SPIE - The International Society for Optical Engineering* 5426 (September). doi:10.1117/12.542536.
Zeng, Yadan, Heng Yu, Houde Dai, Shuang Song, Mingqiang Lin, Bo Sun, Wei Jiang, and Max Q.H. Meng. 2018. “An Improved Calibration Method for a Rotating 2D LIDAR System.” *Sensors (Switzerland)* 18 (2): 1–12. doi:10.3390/s18020497.

3.9 Complementary for Chapter 3

In Chapter 3, we introduced the analysis of terrestrial MLS systematic errors with a simulation approach, and we covered the detailed analyses of the eight systematic errors of a terrestrial MLS in Appendix C.

However, in this thesis, we are interested in the maritime context with a marine MLS. Therefore, in this complementary section, we apply the same analysis introduced in this chapter to the marine MLS context. We first briefly introduce the environment and the possibilities for setting up the predefined planar targets, and then, we present the results for ***Type I*** and ***Type II*** criteria for the configuration selection procedure. Also, we only study the impact of the three boresight angles on the tie-planes.

Figure 3.16 illustrates a marine MLS schematically in a maritime context while we set up a planar target on the quay wall. The target is considered 1 m x 1 m with a horizontal distance from the hydrographic vessel of 15 m and a vertical distance of

5m. These parameters are chosen to approach the real-world port characteristics scanning environment.

We can establish 28 possibilities for the planar target inclination with respect to the MLS, as illustrated in Figure 3.17. Each plane has a 10° rotational offset from the plane nearby.

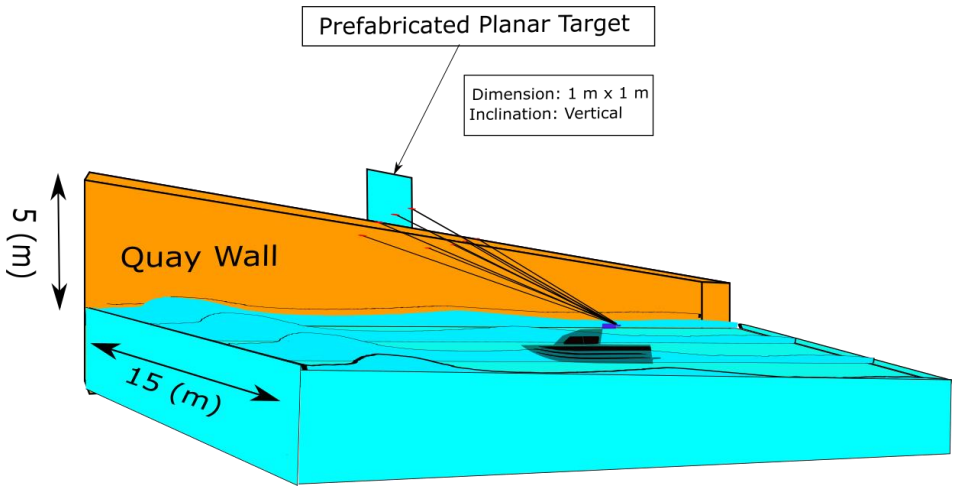

Figure 3.16 – Setup of the target and platform placement in a marine context

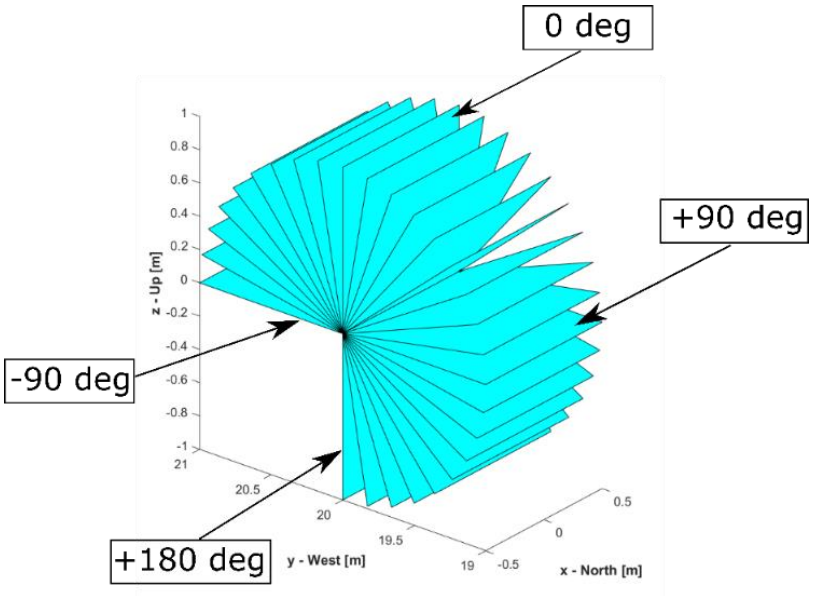

Figure 3.17 – All the possibilities in terms of inclination for a planar target in a maritime context

Based on the inclinations shown in Figure 3.17, we apply the ***Type I*** visibility criteria while inserting 2° for all three boresight angles: roll, pitch, and yaw. ***Type I***, considered raw selection criteria, eliminates the inclinations that do not satisfy the requirement of this criteria. Thus, we consider only inclinations that are between 0° (vertical plane) and 90° (horizontal plane), illustrated in Figure 3.18.

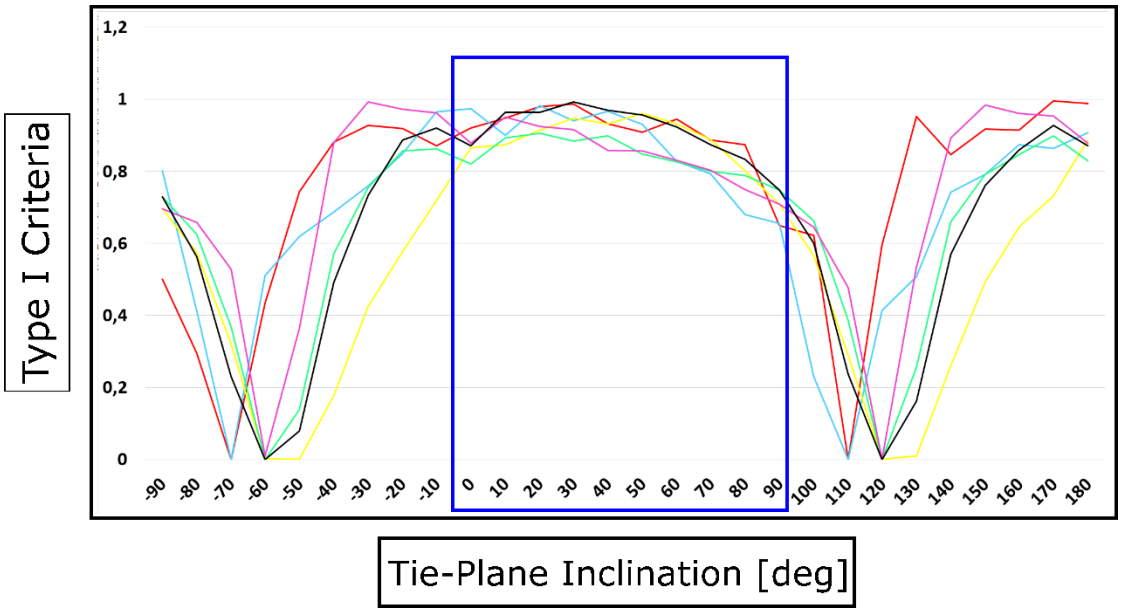

Passage	0°	180°	45°	225°	315°	135°
Color						

Figure 3.18 – Boresight angles ***Type I*** systematic-error visibility criterion (vertical axis in meter) of all the possible inclinations (horizontal axis in degree)

Along with the ***Type I*** criteria, we apply ***Type II*** for a more delicate selection of the best configuration of the planar target. This time the ***Type II*** criteria are employed on each boresight error individually. The results of these analyses are demonstrated for three boresight angles in Figure 3.19, Figure 3.20, and Figure 3.21, respectively. These three figures use the same color code as in Figure 3.18. All three boresight errors strongly impact the vertical or near-vertical plane (0°). At the same time, we must consider that these boresight angles are correlated. Thus, we may introduce other non-vertical planes that lead to a better configuration that can decorrelate these parameters. Therefore, we must

introduce other criteria for the parameters that contribute to the configuration of the planar targets, which is the topic of Section 4.2.1 of Chapter 4.

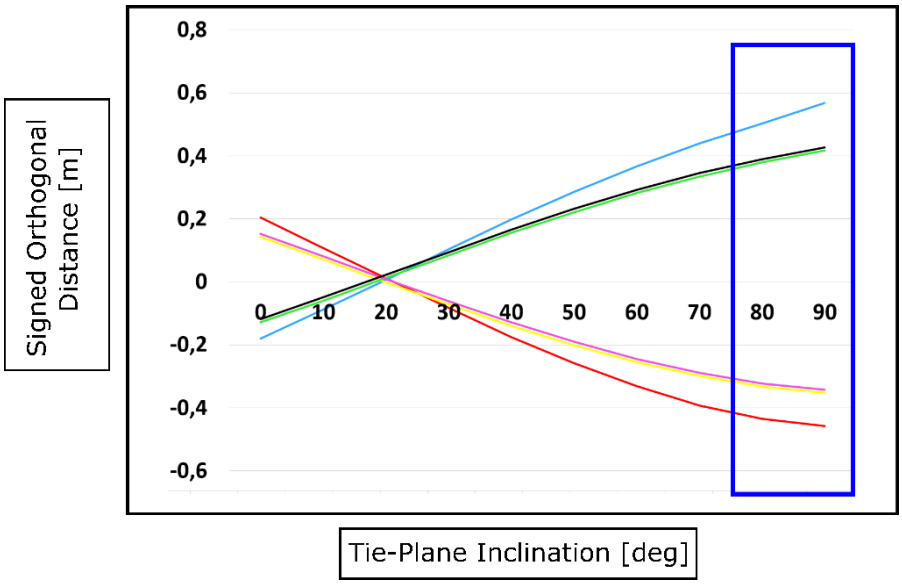

(a)

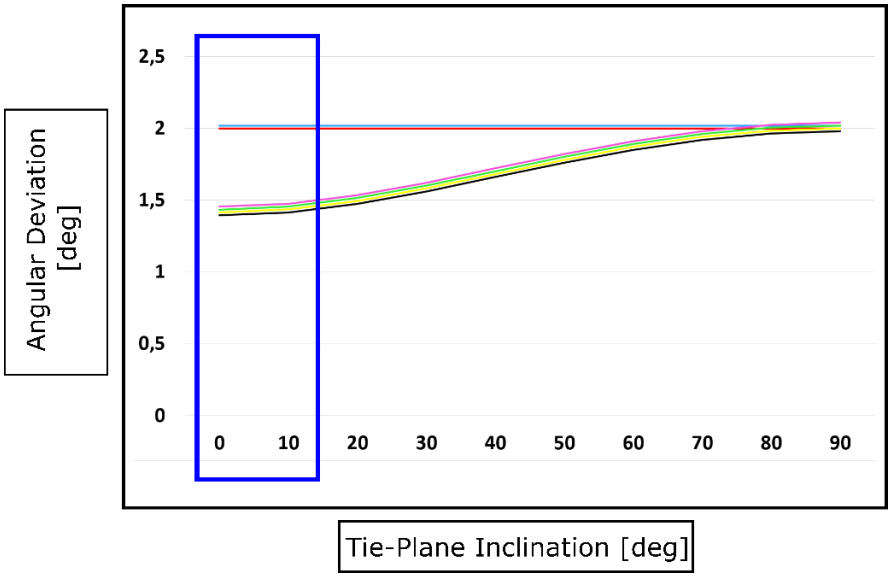

(b)

Figure 3.19 – Roll boresight angle systematic errors ***Type II*** criteria (a) Signed orthogonal distance (vertical axis in meter) (b) Angular deviation (vertical axis in degree) of possible inclinations (horizontal axis in degree)

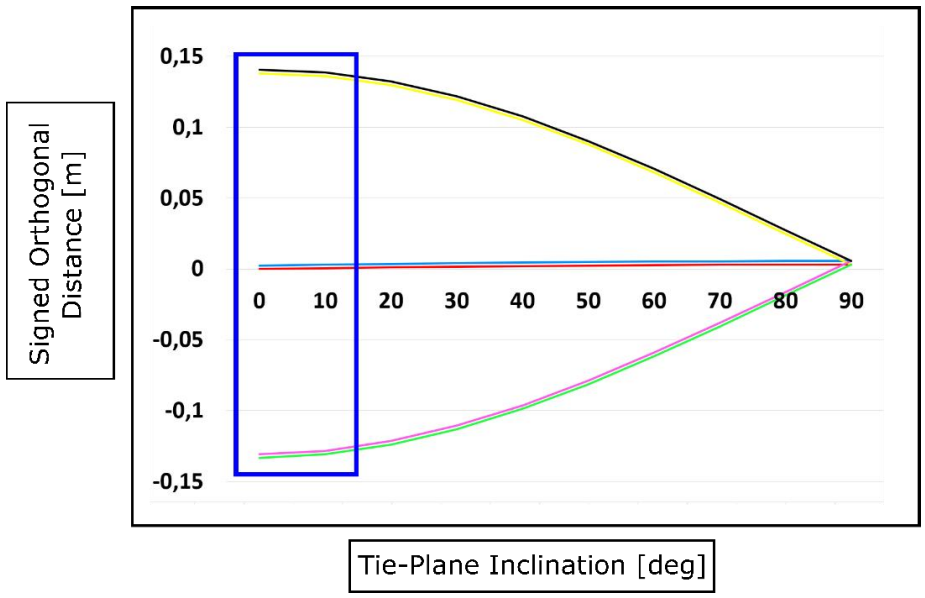

(a)

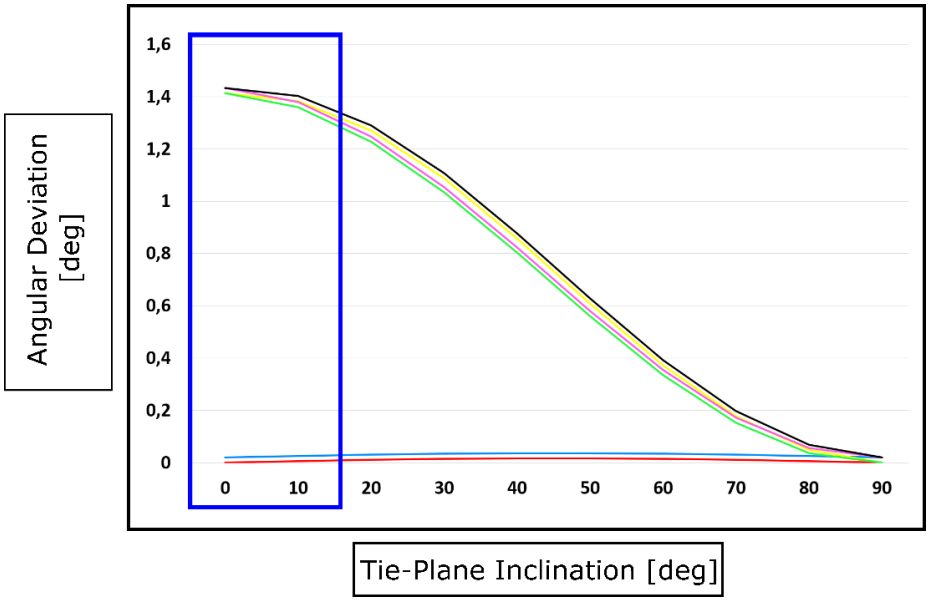

(b)

Figure 3.20 – Pitch boresight angle systematic errors ***Type II*** criteria (a) Signed orthogonal distance (vertical axis in meter) (b) Angular deviation (vertical axis in degree) of possible inclinations (horizontal axis in degree)

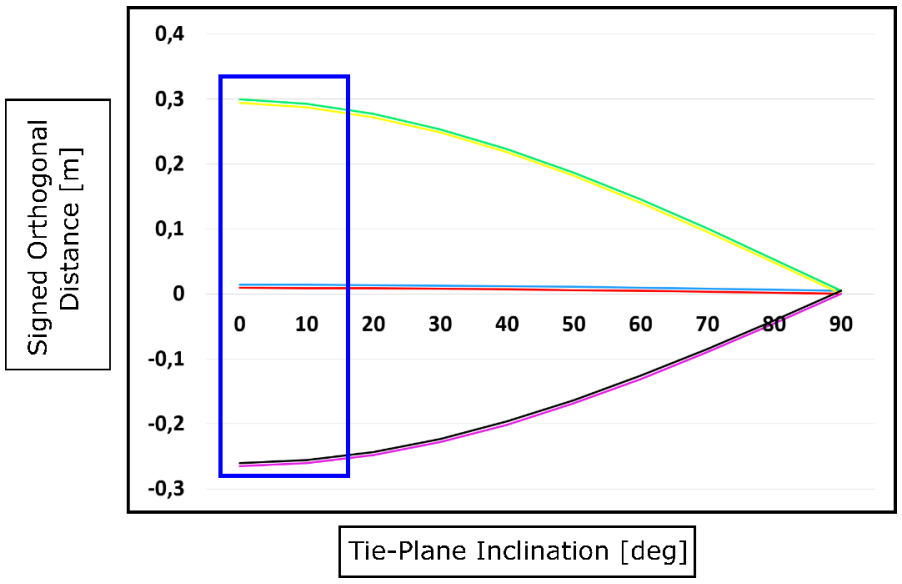

(a)

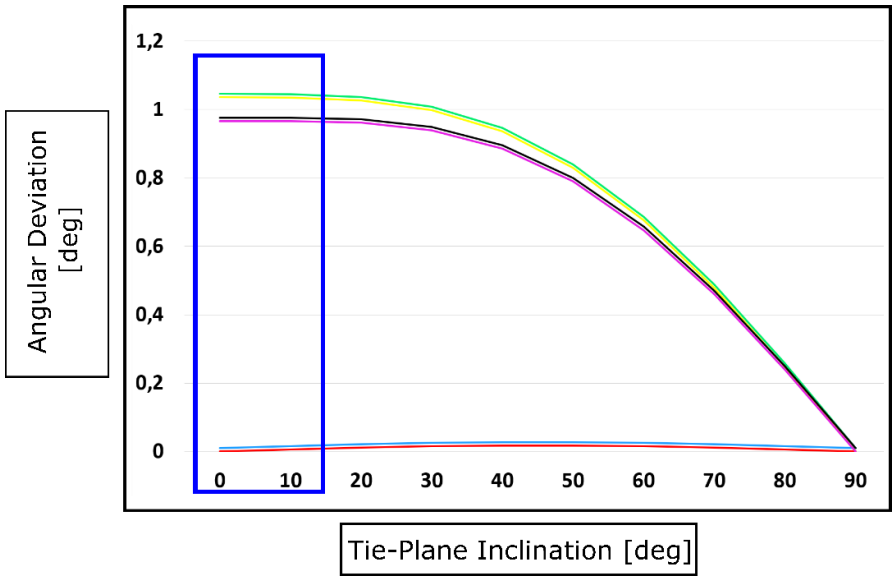

(b)

Figure 3.21 – Yaw boresight angle systematic errors ***Type II*** criteria (a) Signed orthogonal distance (vertical axis in meter) (b) Angular deviation (vertical axis in degree) of possible inclinations (horizontal axis in degree)

Chapter 4 - Case Study: Rigorous Boresight Alignment of a Marine Mobile LiDAR System Addressing the Specific Demands of Port Infrastructure Monitoring

In Chapter 3, based on an MLS systematic error analysis and a visibility analysis on simulated and real datasets, we proposed the best configuration for the tie-planes that will be input for the boresight alignment method of the MLS mounted on the hydrographic vessel.

In this chapter, while considering the recommendation of Chapter 3 that reduces the searching window considerably, we delve more into the subject by introducing other criteria to refine the selected configuration. Thus, the first part of this chapter will go further with the best configuration selection with simulated data. We then validate the best configuration with a real dataset acquired from a survey at the Port of Montreal. We describe the context of the acquisition procedure with a concise presentation of the in-house customized MLS mounted on a hydrographic vessel. The boresight alignment method based on this real-world dataset confirms the approach's accuracy, repeatability, and robustness. Comparison of planar surfaces of a tower scanned in a parallel round-trip before and after boresight alignment of the system gives a relative accuracy assessment of the proposed method. The result of the accuracy assessment is satisfactory, and as a result, the point cloud accuracy has considerably improved due to the suggested configuration of tie-planes as inputs of the boresight alignment method.

This chapter aims to respond to the third objective of the thesis, which is to evaluate the suggested configuration of the data acquisition procedure for the boresight alignment of a mobile LiDAR system in a port infrastructure monitoring context in terms of robustness, accuracy, and repeatability. Furthermore, this chapter presents

the integral of an accepted peer-reviewed journal paper submitted to the Marine Geodesy journal[4].

4.1 Résumé

La surveillance précise des infrastructures portuaires est une opération vitale menée par l'autorité portuaire. Pour opérer régulièrement dans cet environnement hautement dynamique, nous explorons le potentiel des systèmes LiDAR mobiles (SLM) marins. Pour générer un nuage de points 3D de haute qualité, le scanner LiDAR et le système de positionnement et d'orientation doivent être alignés angulairement. Dans cette recherche, nous introduisons une méthodologie d'alignement des angles de visée d'un SLM. Les résultats obtenus ont permis d'estimer avec précision les angles de roulis et de lacet avec des écarts types inférieurs à 0,002 degré et l'angle de tangage avec un écart type inférieur à 0,015 degré. Enfin, nous avons défini un site de validation contenant des surfaces planaires. La comparaison relative des nuages de points géoréférencés, avant et après l'alignement des angles de visée, démontre l'atténuation de l'impact de l'erreur systématique des angles de visée sur le nuage de points final.

4.2 Abstract

Accurate infrastructure monitoring of ports and harbors is a vital operation conducted by the port's authority. To operate regularly in this highly dynamic environment, we explore the potential of cutting-edge mobile LiDAR systems (MLS) mounted on a vessel. The LiDAR scanner and the positioning and orientation system (POS) must be angularly aligned. This procedure is also known as boresight alignment, which is necessary for generating a high-quality 3D point cloud that would satisfy the expected accuracy required in the monitoring task. This research introduces a boresight alignment methodology adapted to the port infrastructure surveillance based on prefabricated planar targets. After analyzing planar target simulated data,

[4] Shahraji, Mohsen H., and Christian Larouche. 2022. "Case Study: Rigorous Boresight Alignment of a Marine Mobile LiDAR System Addressing the Specific Demands of Port Infrastructure Monitoring." *Marine Geodesy*. Taylor & Francis, 1–33. doi:10.1080/01490419.2022.2025503.

we propose a boresight alignment site design. Then, we apply this boresight alignment site design in a real-world scenario. Obtained results estimate accurately roll and yaw angle errors with standard deviations of less than 0.002 degrees and pitch angle errors with a standard deviation of fewer than 0.015 degrees. Finally, we defined a validation site and described the procedure that uses these features to validate the quality of the estimated parameters. The relative comparison of the georeferenced point clouds before and after boresight alignment demonstrates the mitigation of the boresight systematic error impact on the final point cloud.

Keywords: port infrastructures monitoring; marine mobile LiDAR system; boresight alignment; planar targets; simulation analysis.

4.3 Introduction

Regular and accurate monitoring of port and coastal infrastructure, i.e., quay walls, concrete infrastructures, piers, wharves, jetties, and breakwaters, is a highly demanded task by port authorities that enables the rapid identification of ruined sections and consequently apply essential maintenance procedures (Alho et al. 2009; Kishi et al. 2015; Moisan et al. 2015; Rondeau and Pelletier 2013; Ruggeri, Fruzzetti, and Scarpelli 2021; Böder et al. 2011). The quay wall is the most critical structure among the port's infrastructures (De Gijt 2010). Quay wall, which is an earth-retaining structure, is used chiefly for mooring the ships, and also, it is the location where vital equipment like cranes, roads, and rails network that enables vessels' discharging and loading tasks, are installed on it (Karamperidou 2008; Böse 2011). The quay wall goes through two main loads; vertical and horizontal. The vertical load comes from trucks, cargo loads, and cranes, and the horizontal load stems from ship impacts, wind, and soil pressure (Karamperidou 2008). All these heavy loads and the high-humidity environment are the leading cause of deterioration and deformation issues of the quay walls (Firoozi et al. 2014).

In recent years, many researchers explored the potential of 3D data acquisition sensors like mobile LiDAR systems as a novel cutting-edge remote sensing approach for 3D scanning and modeling emergent objects (Thies 2011; Böder et al.

2011). At first, a static LiDAR system located on a nearby spot on the land was adopted for the 3D modeling structures like bridges and pillars (Moisan et al., 2015). Subsequently, the ability of terrestrial mobile LiDAR systems to extract dense 3D point clouds in highways and cities inspired the marine geomatics experts to integrate LiDAR with POS on the hydrographic vessel as a mobile platform to create a marine mobile LiDAR system (marine MLS). A marine MLS aims to perform a comprehensive and accurate 3D scan for surveillance and monitoring of port and coastal emergent infrastructure located above the water surface. The marine MLS has the advantage of regularly navigating through the different port sections and collecting 3D point clouds with the accuracy required for the monitoring task.

Typically, hydrographic vessels are equipped with SONAR sensors integrated with POS for bathymetric surveying. The integration of a LiDAR scanner to the SONAR and POS sensors enables the acquisition system to produce full 3D scans of the above and under the water surface infrastructures simultaneously (Dix et al. 2012; Lu et al. 2019; Shi et al. 2017; Thies 2011; Böder et al. 2011; Kishi et al. 2015).

A LiDAR scanner, while integrated into POS on a hydrographic vessel, must be aligned before fully operational and accurate. Such marine MLS has two main types of misalignment, POS-LiDAR lever arm and POS-LiDAR boresight angles. POS-LiDAR lever arm can be measured at a millimetric accuracy level by employing classical surveying instruments like a total station in laboratory-controlled conditions. The POS-LiDAR boresight angles estimation, which we will name boresight alignment, cannot be implemented in the same laboratory-controlled conditions (Thies 2011; Skaloud and Lichti 2006; Heinz et al. 2017). The boresight alignment, which is the angular alignment between two non-tangible points, the optical center of the LiDAR sensor and the gravity center of the POS, is preferable to be estimated while each of these sensors is at its highest performance. In other words, while the MLS is operational and ready to scan the environment. This constraint will prevent other sources of errors, for example, positional errors, from intervening with the boresight alignment procedure.

Since the introduction of MLS at an academic and commercial level in the last two decades, many researchers have addressed the boresight alignment problem to decrease the systematic errors of such systems and improve the quality of the final point cloud. These methods can be classified into two main categories; rigorous (system-driven) and non-rigorous (data-driven) (Kersting 2006). The data-driven approach, also known as strip adjustment, utilizes the generated point cloud to reduce the discrepancies between the points of various strips of the same scanned scene. On the other hand, the system-driven approach considers raw observations from LiDAR and POS sensors (Kersting 2006). These raw measurements are then introduced to the georeferencing mathematical model, and at the same time, they are constrained to fit on an in-situ geometric primitive like a planar target (Filin 2003; Glennie 2012; Hebel and Stilla 2012; D. Li et al. 2016; Skaloud and Lichti 2006). The major drawback of this method is its dependence on geometric surfaces, primarily available in structured environments like urban areas (Kersting 2006). Thus, in recent years, inspired by system-based boresight alignment, researchers have explored the possibility of using prefabricated planar targets (Lu et al. 2019; Heinz et al. 2017; Heinz et al. 2020; Ravi et al. 2018). Lu et al. (2019) introduced an approach to estimate the rotation and displacement systematic errors for ship-borne mobile surveying systems using planar surfaces on a calibration site.

The limitation of this approach is that it needs a specific calibration site, i.e., a calibration pool, with over ten planar in situ surfaces installed on the floor and walls, and the MLS is fixed on a crane. This setup is far less tangible than an actual scan on a surveying vessel platform (Lu et al. 2019). This systematic error estimation approach underestimates the necessity to initialize the POS sensors to achieve maximum accuracy for position and orientation observations of the marine platform. Also, there is no justification for using ten planar targets and their localization and orientation around the mobile LiDAR system. Heinz et al. (2020) introduced a comprehensive approach to designing a calibration site and evaluating the boresight calibration results. In their proposed methodology, all the planar targets must be scanned and georeferenced in advance with an accurate acquisition system such as a static scanner or a total station (Heinz et al. 2020). The method necessitates

the establishment of a well-defined and accurately measured planar-based calibration site, which is not a feasible option in a marine MLS case. Ravi et al. (2018) proposed a planar features approach based on the positional deformations of the planes. However, this approach does not justify the configurations of the planar targets and the line patterns used for the calibration procedure (Ravi et al., 2018).

Therefore, in this paper, due to the unorganized environment constraint of the port area, we address the POS-LiDAR boresight alignment issue with a system-driven approach using prefabricated planar targets. At the same time, it is necessary to define the best configuration of planar targets, i.e., the minimum number of planes, their best orientations with respect to the marine vessel platform, and the appropriate line pattern. The main contribution of this research is to present the best configuration for the boresight alignment site based on a comprehensive analysis of planar target simulated data. The detailed design procedure for this MLS planar target simulated data generator was introduced in our previous publication (Shahraji, Larouche, and Cocard 2020).

We also tested the boresight alignment site design and the proposed acquisition methodology on a real dataset at the Port of Montreal. The boresight angle uncertainties were less than 0.002º for roll and yaw angles and less than 0.015º for the pitch angle, demonstrating high accuracy. The lower accuracy for the pitch boresight error is related to the LiDAR scanner field of view, which is lateral for a marine MLS, just like a terrestrial MLS. For this lateral field of view, the pitch boresight error effect will be on the same plane as the scene of interest. Therefore, its visibility will decline, and its uncertainties will increase. In an aerial MLS where the LiDAR scanner has a nadir field of view on the scene of interest, the impact of the yaw boresight error is in the scene of interest plane, and as a result, this error is less accurate than the two other boresight errors: roll and pitch.

Furthermore, the estimation and the analysis of the correlation matrix between the boresight angles demonstrate an acceptable decorrelation between the parameters. The estimated boresight angles also were compared with the results of a LiDAR patch test (Qinsy-Validator), and the results are similar. Based on our validation

analysis of points located further away or higher up, the average error obtained with the a priori values used after the installation of the scanner has been reduced to a few cm after the boresight alignment, which is near the expected theoretical accuracy obtained from the total propagated uncertainty model of the MLS.

The rest of the paper is organized as follows; in the next section, our proposed methodology is detailed and brief results from the boresight angles simulation analysis are provided. In the following section, we present the results of real-world survey experiments at the Port of Montreal and the quality assessment of the method. Finally, in the last section, we present a discussion, our conclusions, and some other research tracks for future work.

4.4 Methodology

Figure 4.1 presents the three main phases of the methodology. First phase is the data collection carried out on the terrain and is considered the main contribution of this research. Second phase is the calibration done in a laboratory condition, which results to accurate measurement of the lever arm vector. Third phase, done in office, is the data processing for estimating the boresight error.

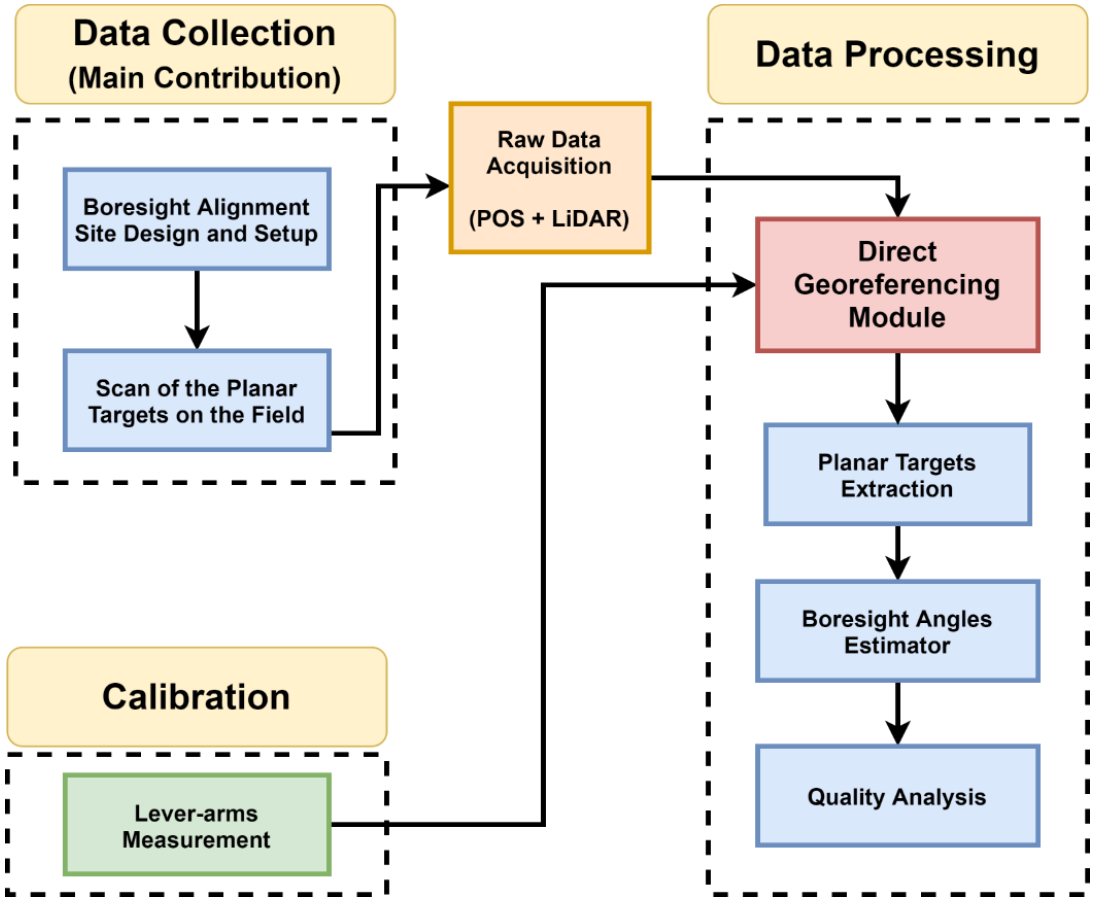

Figure 4.1– Mobile LiDAR system boresight alignment methodology

The data collection phase consists of two modules. The first module includes the boresight alignment site design and setup made of prefabricated planar targets and a pre-defined line pattern. The best inclination of planar targets and line patterns was selected based on a simulation approach (Shahraji, Larouche, and Cocard 2020). The second module consists of the scanning of planar targets in the field. The calibration phase concerns the POS-LiDAR lever arms measurement operation performed in a controlled environment like a laboratory with very accurate and conventional surveying methods. It is essential to accomplish this step before carrying out the actual boresight alignment survey. The data processing phase consists of four modules: the direct georeferencing module, the planar targets extraction and preparation module, the boresight angles estimation module, and the validation and quality analysis module. All three phases of the proposed

methodology require POS and LiDAR raw observation data. The following subsections explain each module in detail.

4.4.1 Boresight Alignment Site Design and Setup

This module, which is the main contribution of this paper, consists of the design of the boresight alignment site, installation, and acquisition of the prefabricated planar targets. To find the best configuration, we first addressed the effect of different boresight angles on simulated planar targets (Shahraji, Larouche, and Cocard 2020). With the understanding that we obtain from the behavior of boresight angles on the simulated planar target, we eventually define several configurations, then evaluate the effect of various configuration scenarios on the performance of the boresight alignment algorithm.

4.4.1.1 Boresight Angle Systematic Error Analysis

Based on the simulated planar target point cloud generator (Shahraji, Larouche, and Cocard 2020), we can better understand and analyze the effect of each boresight angle on the generated point cloud without the presence of other sources of error, i.e., blunders, sensor noises, and other random errors (Glennie 2012; Skaloud and Lichti 2006; Heinz et al. 2020).

As shown in Figure 4.2, we consider one square-shaped vertical planar target of dimensions 1m x 1m, located at 5 m height and 15 m horizontal distance of an MLS. For this analysis, we inserted a value of 2º for each simulated boresight angle. Also, we consider six passages for the scan line pattern for generating the simulated point cloud showing the target.

To study the effect of each boresight angle on the simulated vertical plane, we consider three-line patterns; round-trip parallel passages (0º-180º), round-trip side-looking passages (45º - 225º or 315º - 135º), and two-direction crossing passages (45º - 135º or 315º - 225º).

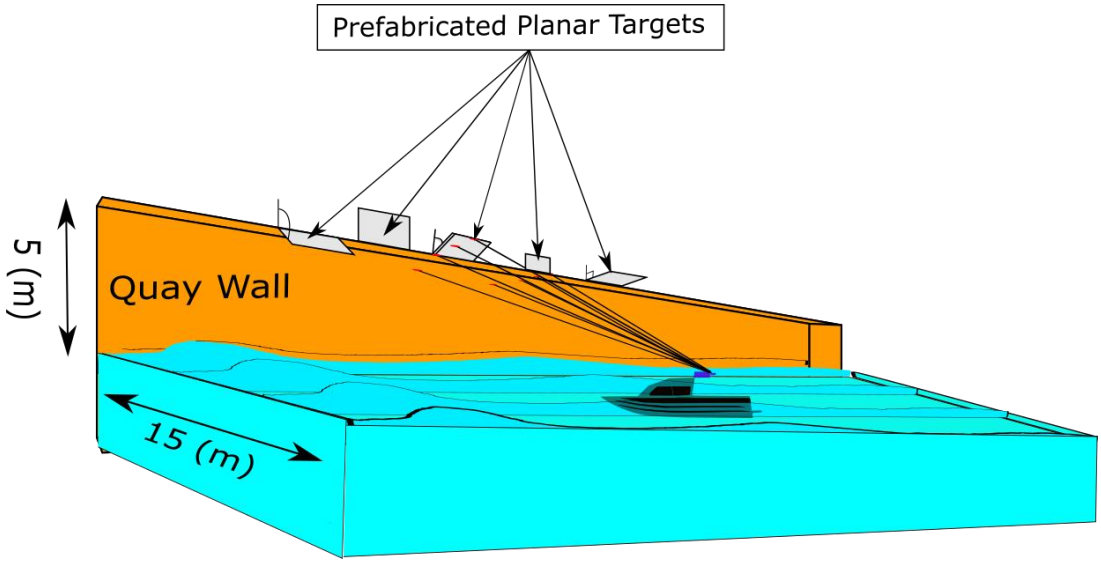

Figure 4.2– Schematic presentation of various tie-planes with different inclinations and dimensions (this figure is not to scale)

The first line pattern, i.e., round-trip parallel passage (0º - 180º), is presented in Figure 4.3.

We insert a roll boresight systematic error to analyze its impact on round-trip parallel passages. Figure 4.4 illustrates that the original vertical plane generated with a 0º roll boresight angle is represented in full cyan color and the plane generated with a 2º roll boresight angle at a 0º direction represented by the red arrow is the red dotted plane.

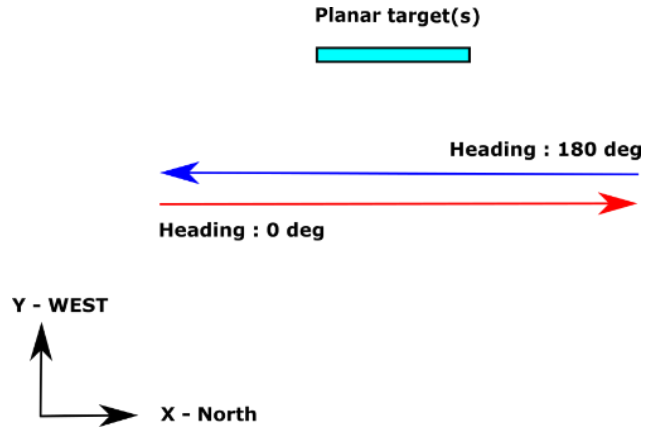

Figure 4.3 – round-trip parallel passages (0° – 180°)

The plane generated with a 2º roll boresight angle at a 180º direction, represented by the blue arrow, is the blue dotted plane. Similar symbology is used for all the other figures presented in this section. We can see a remarkable sensitivity to the roll boresight angle systematic error, as illustrated in Figure 4.4.

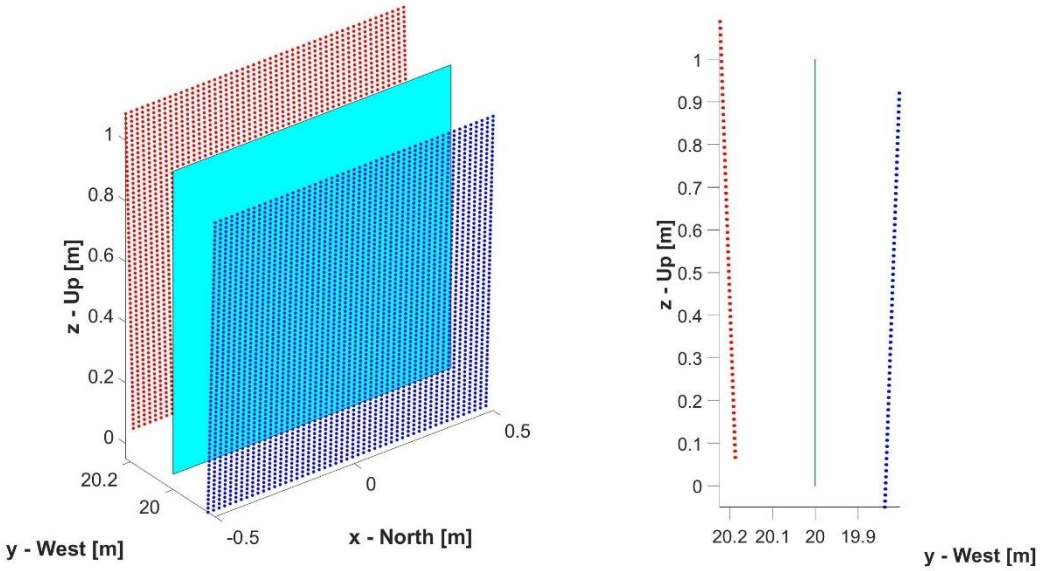

(a) (b)

Figure 4.4 – POS-LiDAR roll boresight angle systematic error (2º) effect on a vertical planar target. (a) simulated point cloud with the XYZ viewpoint. (b) simulated planar targets with YZ viewpoint. The cyan color plane is the hypothetical plane without error.

Contrary to the roll boresight angle, the other two boresight angles, pitch and yaw, have no effect on the vertical plane with a round-trip parallel pattern, presented in Figure 4.5, which means that with the insertion of a pitch or a yaw boresight angle of 2º into the simulator, all the points in the round-trip parallel passages superimpose. Thus, with round-trip parallel passages, we can decorrelate or isolate the roll boresight angle error from the other two boresight angles.

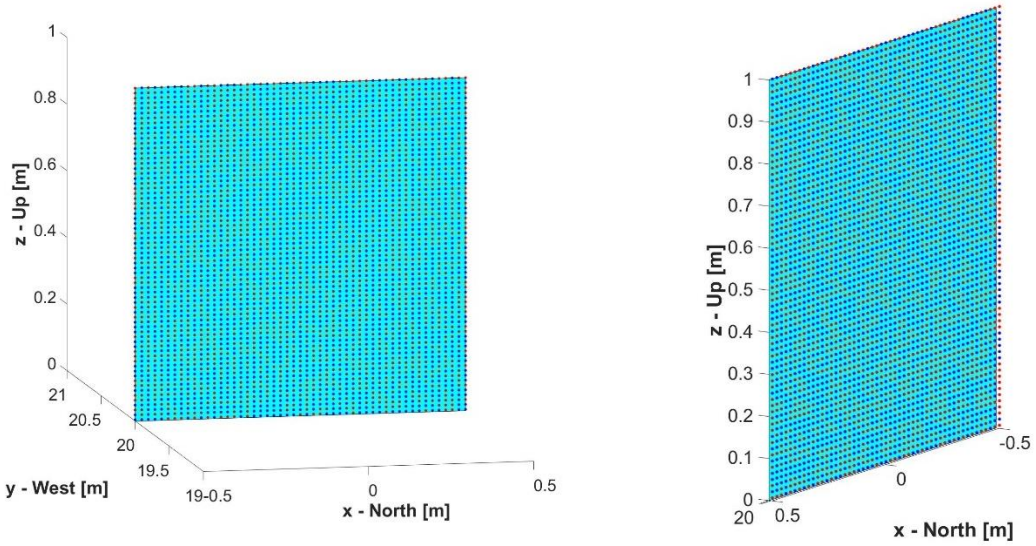

(a) (b)

Figure 4.5 – (a) POS-LiDAR pitch boresight angle systematic error (2º) effect on a vertical planar target. (b) POS-LiDAR yaw boresight angle systematic error (2º) effect on a vertical planar target.

The second line pattern, i.e., round-trip side-looking passages (45º - 225º or 315º - 135º), is presented in Figure 4.6.

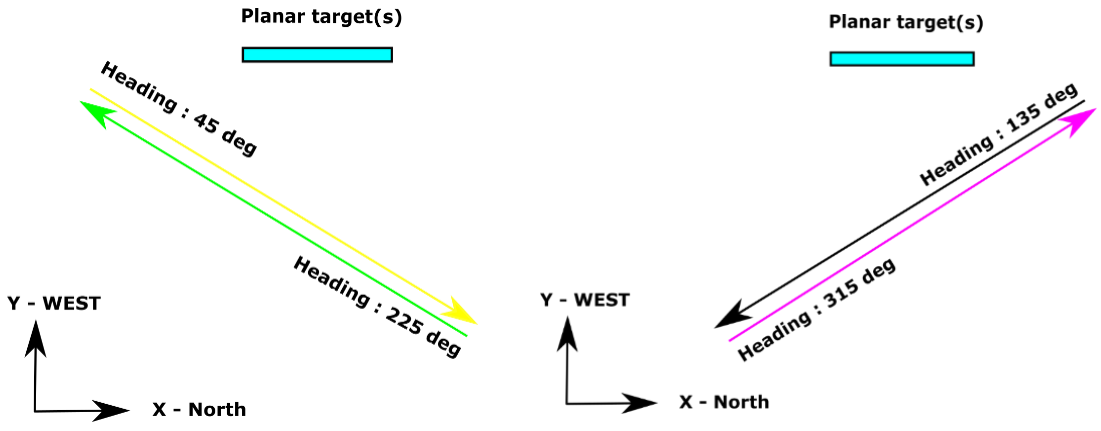

(a) (b)

Figure 4.6 – Round-trip side-looking passages. (a) 45º - 225º (b) 315º - 135º

The line pattern illustrated in Figure 4.6 is sensitive to roll and pitch boresight errors. We decorrelated the roll error with the first line pattern (0º - 180º) and considered the current passages to function as a decorrelator for the pitch error. The impact of the pitch error on a vertical planar target with the round-trip side-looking passage (45º - 225º) is illustrated in Figure 4.7. The other round-trip side-looking passage (315º - 135º) has the same effect.

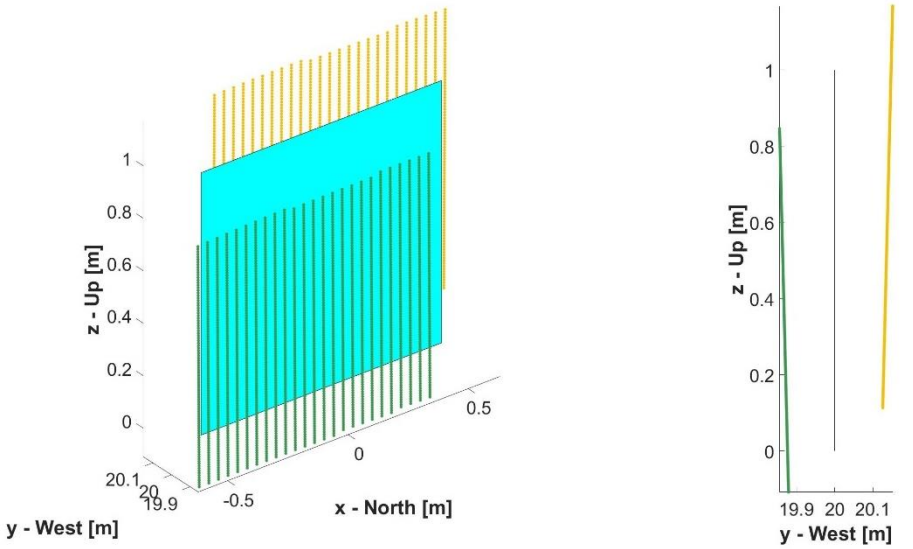

(a) (b)

Figure 4.7 – POS-LiDAR pitch boresight angle systematic error (2º) effect on a vertical planar target with round-trip side-looking passages 45º - 225º. (a) simulated point cloud with the XYZ viewpoint. (b) simulated planar targets with YZ viewpoint.

On the other hand, the yaw boresight angle systematic error does not affect the line pattern presented in Figure 4.6, which we illustrate in Figure 4.8. This result shows that the round-trip side-looking line pattern decorrelates the pitch boresight angle systematic error.

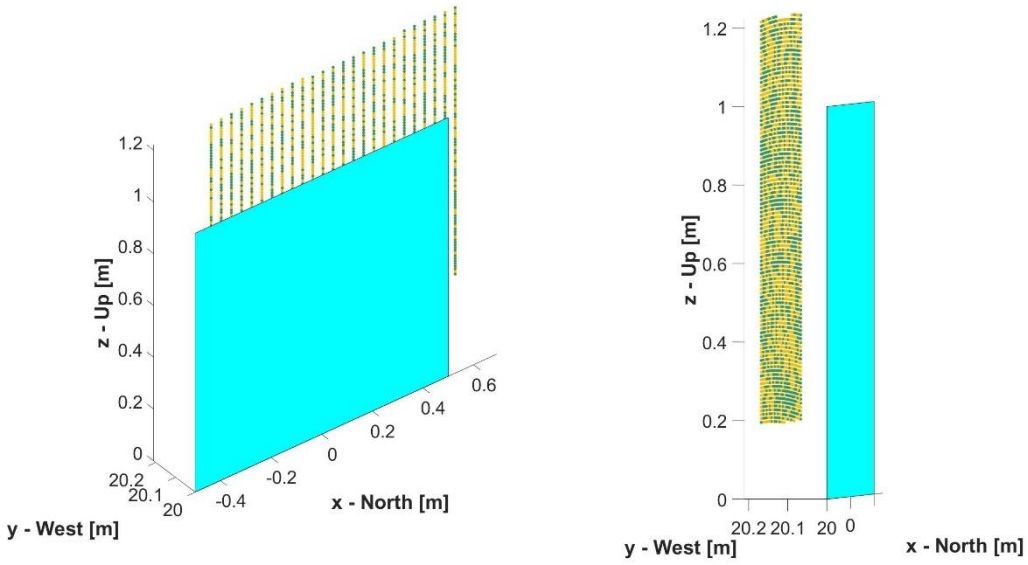

(a) (b)

Figure 4.8 – POS-LiDAR yaw boresight angle systematic error (2º) effect on a vertical planar target with round-trip side-looking passage (45º - 225º) (a) simulated point cloud with the XYZ viewpoint. (b) simulated planar targets with YZ viewpoint.

The third line pattern, i.e., the two-direction crossing passages (45º - 135º or 315º - 225º), is presented in Figure 4.9.

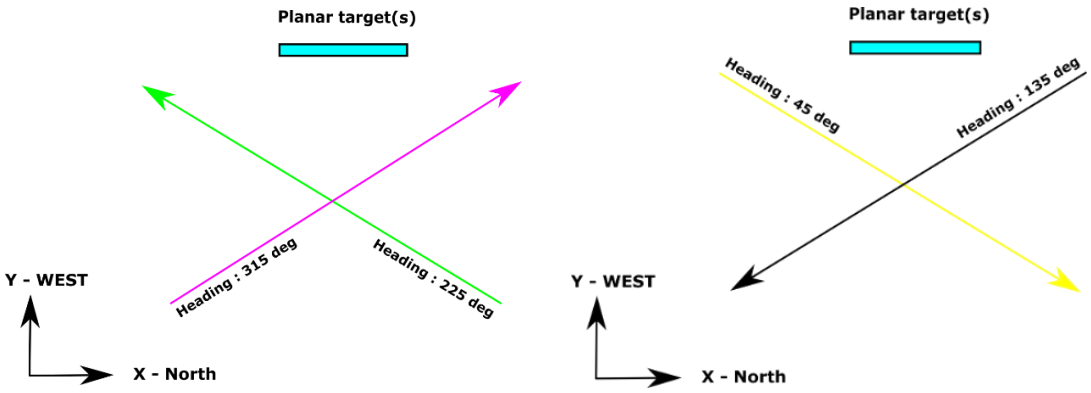

(a) (b)

Figure 4.9 – Two-direction crossing passages. (a) 315º - 225º (b) 45º - 135º

This two-direction crossing nomination is because the passages have two opposite directions. Figure 4.10 illustrates this configuration's effect on yaw boresight angle systematic error.

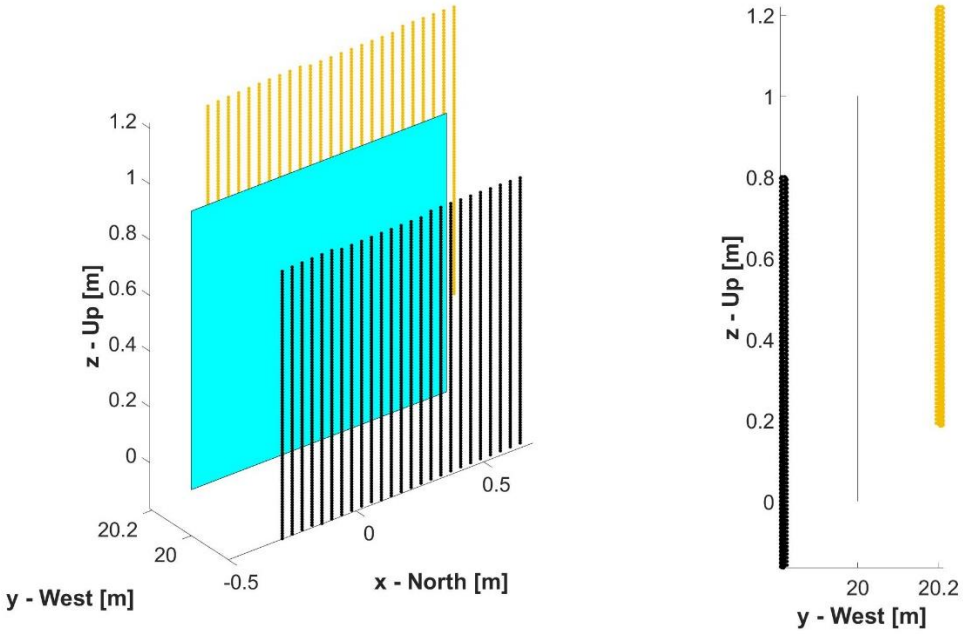

(a) (b)

Figure 4.10 – POS-LiDAR yaw boresight angle systematic error (2º) effect on a vertical planar target with round-trip two-direction crossing passage (45º - 135º). (a) simulated point cloud with the XYZ viewpoint. (b) simulated planar targets with YZ viewpoint.

Thus, the round-trip two-direction line pattern decorrelates the systematic yaw error effect. However, this line pattern does not impact the systematic pitch error based on the results presented in Figure 4.11.

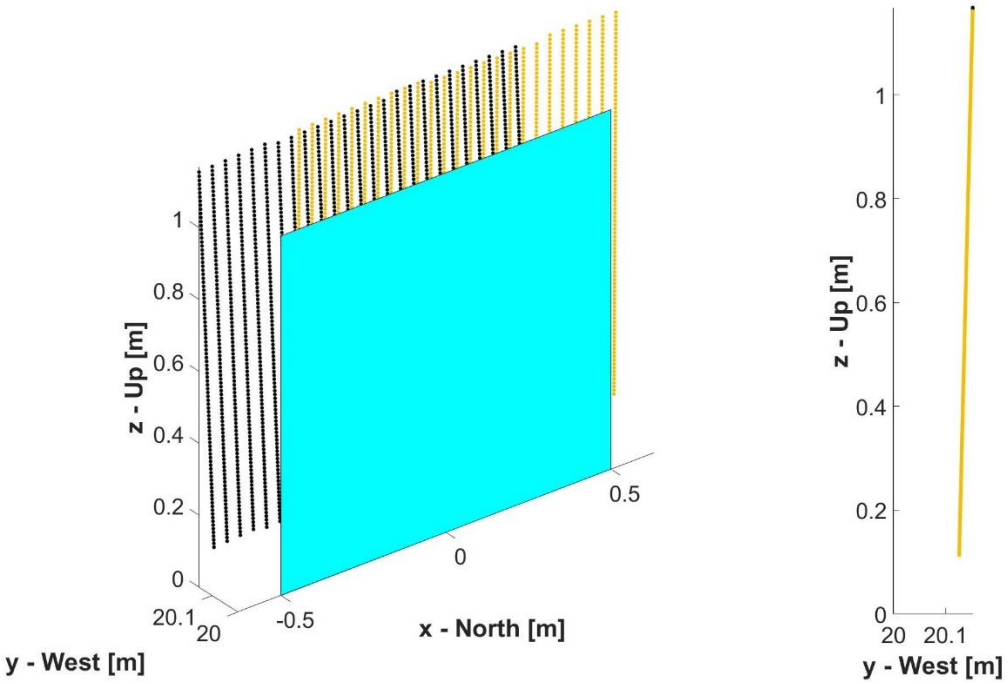

(a) (b)

Figure 4.11 – POS-LiDAR pitch boresight angle systematic error (2º) effect on a vertical planar target with round-trip two-direction crossing passage (45º - 135º) (a) simulated point cloud with the XYZ viewpoint. (b) simulated planar targets with YZ viewpoint.

Based on the preliminary analysis of the boresight systematic errors presented in this section, we can conclude that it is possible to decorrelate these three boresight angles. At least one vertical plane is needed with a combination of line pattern as follow: a parallel round-trip passage (0º - 180º) for roll boresight error, a side-looking round-trip passage (45º - 225º or 315º - 135º) for pitch boresight error, and finally, a two-directional crossing passage (45º - 135º or 315º - 225º) for yaw boresight error. At the same time, if we combine the side-looking round-trip and the two-directional crossing line pattern, the impact of the pitch and yaw on the vertical plane will intervene, and the decorrelation effect of each line pattern mitigates. Therefore, we can decorrelate the boresight angles error to some extent to the proposed line pattern. For further decorrelation of these parameters, which is essential for more accurate estimation, we explore the possibility of adding more planar targets. In the

next section, we define the best selection of planes and their characteristics for maximizing decorrelation between the three boresight angles.

4.4.1.2 Best Planar Target Configuration Selection Procedure

The configuration of a planar target is the combination of the plane specification and the line pattern that the platform follows with respect to that plane. The best configuration selection method is based on the definition of various planar targets and line patterns, followed by the generation of a simulated point cloud for each defined combination, and finally, by estimating boresight angles and their uncertainties with these simulated point clouds.

An advantage of using an iterative least-squares method to estimate the boresight angles is that it can also estimate the corresponding uncertainties (Skaloud and Lichti 2006). The boresight angles, estimated uncertainties, and the simulated point clouds generated by each configuration can then be used to create the best configuration selection index. The estimated boresight angle with the smallest uncertainty, which means the highest accuracy, is considered the best configuration.

Furthermore, we designed the simulation environment very similar to a real-world environment consisting of planar targets installed on the quay walls or the port's infrastructures higher in altitude than the platform position floating on the water surface. Thus, we assume that the horizontal distance between the platform and the planar targets is 15 m and the vertical distance is 5 m, as illustrated in Figure 4.2. We consider realistic boresight angles (dr = 2º, dp = 2º, dh = 2º) for the generation of simulated data. In our analysis, we study the following four types of scenarios:

- Scenarios based on passage direction combination of the platform with respect to planar targets
- Scenarios based on the orientation of a planar target with respect to the platform
- Scenarios based on the dimension of a planar target
- Scenarios based on the combination of planar targets (two or three planes)

Figure 4.12 illustrates the results of these different scenarios. Figure 4.12 (a) considers different combinations of passages of the six-fold line pattern on one vertical plane. As we can see, when we combine all six passages, we obtain the best results based on boresight angles standard deviations, which is the same result as the previous section analysis on each of the boresight angles individually. Thus, as we expected, a six-fold line pattern maximizes the accuracy of the estimated boresight angles. This six-fold line pattern is schematically illustrated in Figure 3.3.

The second configuration parameter is the plane's orientation with respect to the platform, as shown in Figure 4.12 (b). We consider the dimensions of the plane to be equal to 1 m x 1 m and all the six-fold line patterns in this scenario. Then, we consider seven different orientations (0º - horizontal, 15º, 30º, 45º, 60º, 75º, and 90º - vertical) of the planar target w.r.t the platform. This range of orientations is based on the boresight systematic error analysis from our previous research (Shahraji, Larouche, and Cocard 2020) that limited the orientations based on two systematic error visibility criteria; angular deviation (***Type I***) and orthogonal distance drift (***Type II***). As we can see from the results in Figure 4.12 (b), the plane orientation that provides the minimum standard deviation for the boresight angles is the vertical plane (90º).

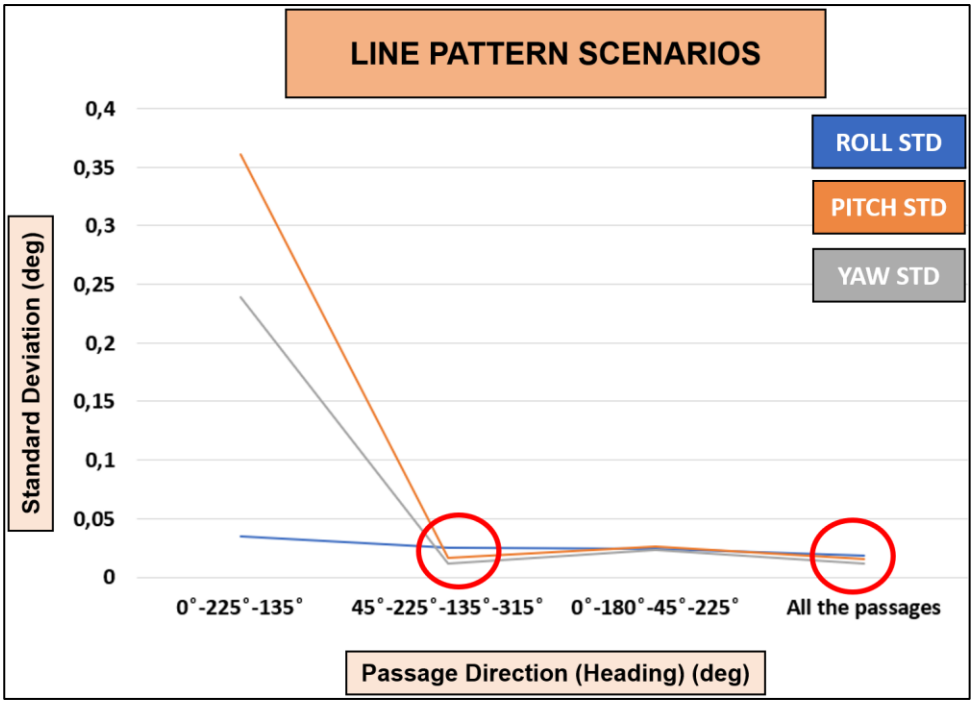
LINE PATTERN SCENARIOS
ROLL STD
PITCH STD
YAW STD
Standard Deviation (deg)
0,4
0,35
0,3
0,25
0,2
0,15
0,1
0,05
0
0°-225°-135°
45°-225°-135°-315°
0°-180°-45°-225°
All the passages
Passage Direction (Heading) (deg)

(a)

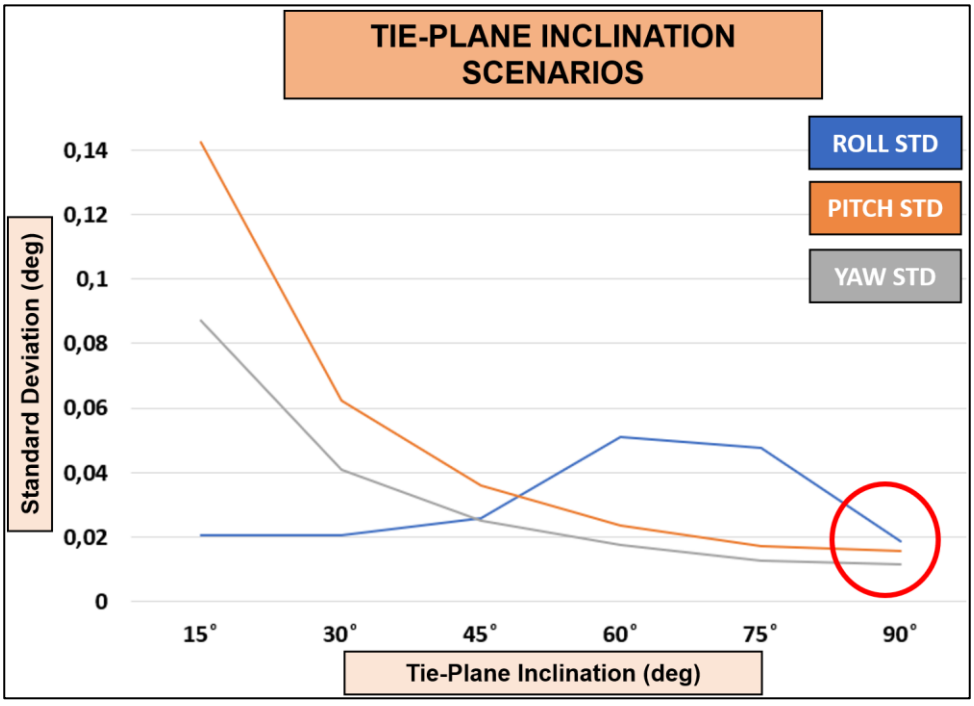
TIE-PLANE INCLINATION SCENARIOS
ROLL STD
PITCH STD
YAW STD
Standard Deviation (deg)
0,14
0,12
0,1
0,08
0,06
0,04
0,02
0
15°
30°
45°
60°
75°
90°
Tie-Plane Inclination (deg)

(b)

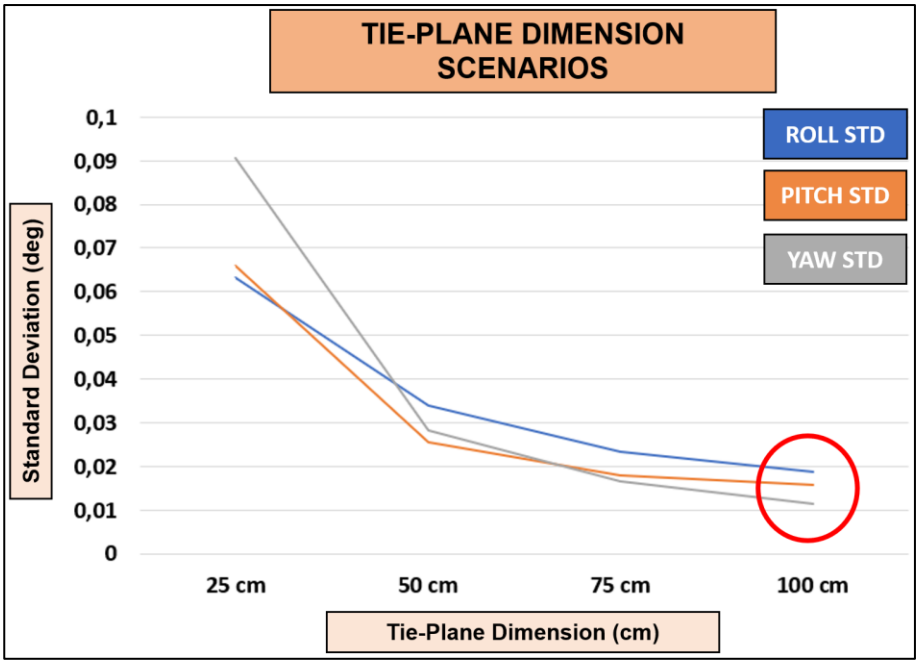

(c)

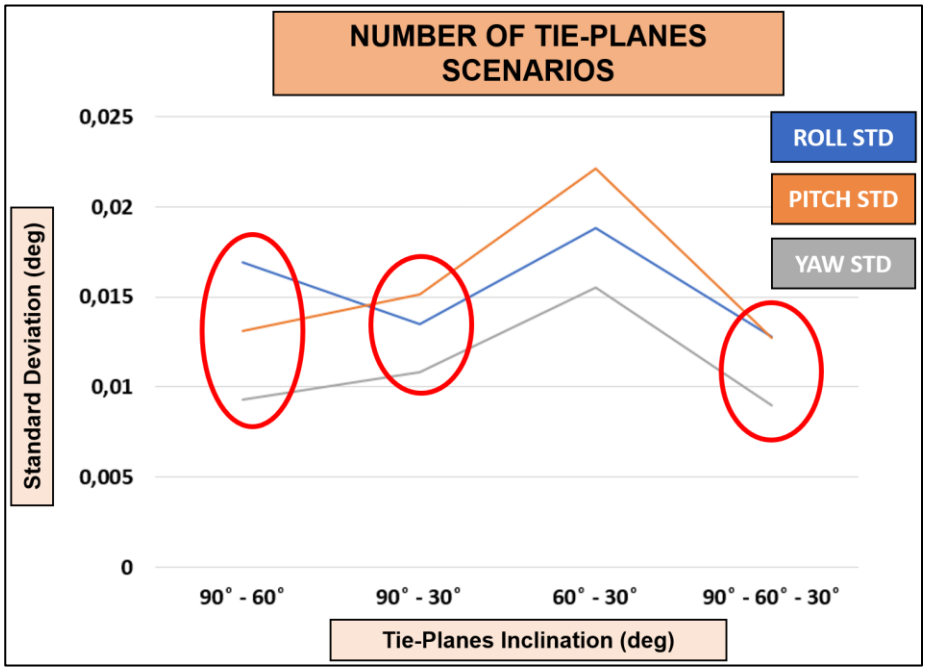

(d)

Figure 4.12 – Results of various scenarios (a) passages combination, (b) plane inclination, (c) plane dimension, (d) multiple plane combinations. The unit of the vertical axis of all four figures is the uncertainty in deg (°)

The third configuration parameter is based on the dimension of the planar target. We consider four dimensions, i. e., 25 cm, 50 cm, 75 cm, and 100 cm. As shown in Figure 4.12 (c), the planar target with vertical orientation and 100 cm dimension has the minimum standard deviation for boresight angles. The reason is that a larger target contains more points extended along the surface, which are more sensitive to the boresight angles' systematic errors. Thus, the observability of these errors augments, and as a result, the estimation of these parameters is more accurate. Figure 4.13 demonstrates the planar target's simulated data based on the three first scenarios; (a), (b), and (c).

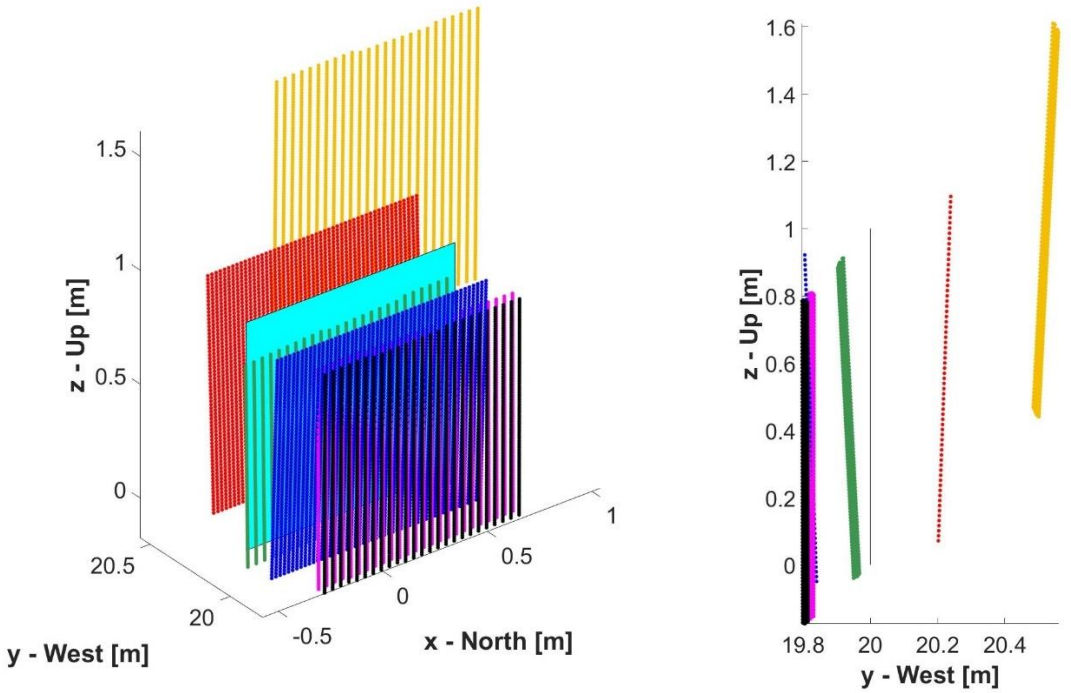

(a) (b)

Figure 4.13 – Simulated point cloud of a vertical planar target with insertion of boresight angles errors (2°) based on the results of the first three scenarios; passage combination, plane orientation, and the plane dimension analysis. (a) view XYZ. (b) view YZ.

We mentioned in the last section that boresight alignment with only one vertical planar target is not feasible in real-world situations due to other sources of errors different than boresight angles' systematic error. Thus, in the last scene of the best configuration selection analysis shown in Figure 4.12 (d), we address the effect of adding more than one planar target and study the impact of multiple planar targets

on the estimated boresight angle accuracies. Therefore, we consider the various reasonable combinations of multiple planar targets(s), two and three planes with different orientations. Our analysis results indicate that using three planes with the following three inclinations (90º, 60º, and 30º) estimates boresight angles with the minimum standard deviation. Figure 4.14 demonstrates the results of the fourth scenario with the simulated data.

Figure 4.12 (d) also shows that the result obtained with the combination of only two planes with the following two inclinations (90º and 30º) provides a very close result compared to three planes with three orientations. Therefore, combining the two planes can be considered a more feasible option for the boresight alignment estimation procedure for the marine MLS case.

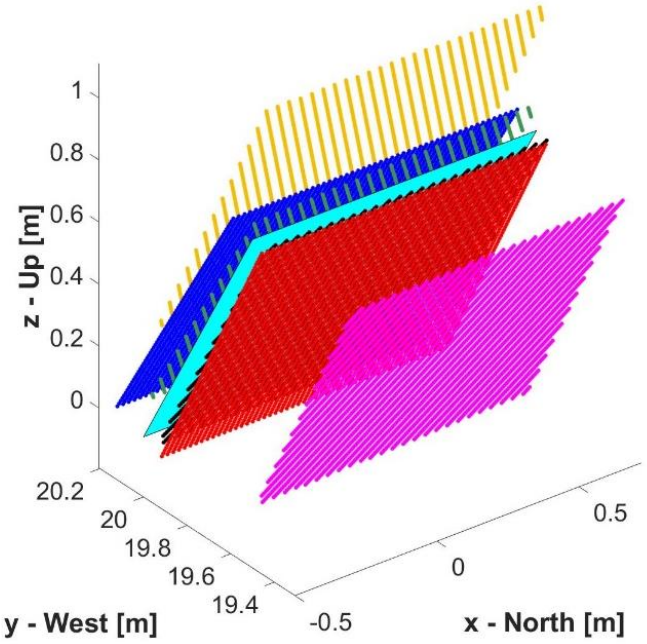

(a)

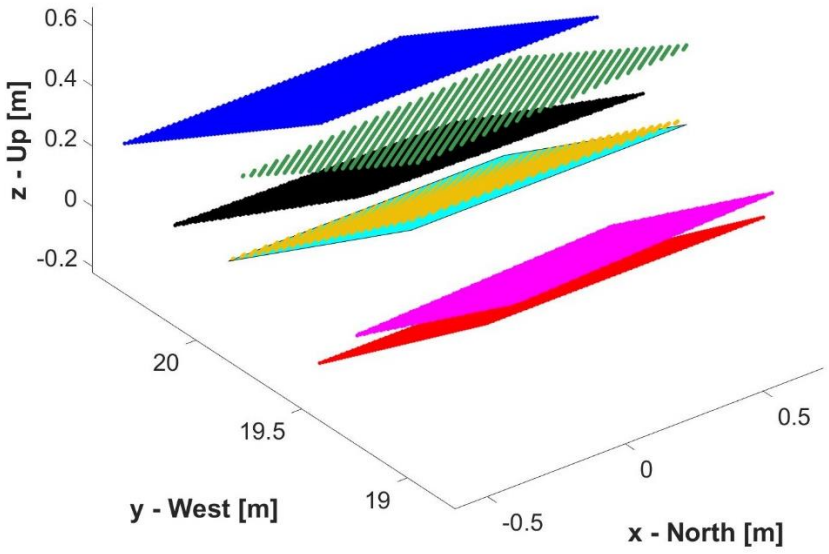

(b)

Figure 4.14 – Results of the fourth scenario, multiple plane combinations on simulated data. (a) Inclined orientation (60º) (b) Inclined orientation (30º)

4.4.2 Lever Arm Measurement

The lever arm is the vectorial translation between the POS gravity center and the LiDAR scanner optic center. Based on the analysis of these systematic errors with simulated point clouds on a planar target, we concluded that the effect of the X lever arm is parallel to the direction of the platform and that the effect of the Y lever arm is perpendicular to the direction of the platform. Regarding the Z lever arm, it is impossible, with an MLS installed on a vehicle or vessel platform, to see any effect on the planar target unless the vessel platform could scan the planes in an upside-down manner, which is not feasible in a real-world situation (Shahraji, Larouche, and Cocard 2020). The lever arm vector is correlated with boresight angle parameters. It is preferable to measure it a priori in controlled laboratory conditions with conventional surveying instruments like a total station, a static laser scanner, or a camera and close-range photogrammetry techniques (Thies 2011; Skaloud and Lichti 2006; Heinz et al. 2017).

4.4.3 Data Acquisition and Direct Georeferencing Mathematical Model

An MLS comprises two main sub-systems, the positioning and orientation system (POS) and the LiDAR scanner. The POS comprises an IMU that measures the platform's orientation and a GNSS receiver and antenna, which gives the platform's position. All these components provide the inputs for the georeferencing mathematical model of an MLS. After acquiring the raw observations from LiDAR and POS, we enter them into the direct georeferencing mathematical model.

Equation (4.1) represents the mathematical model of the direct georeferencing module of an MLS, similar to the formulation presented in different articles (Ackermann 1999; Wehr and Lohr 1999; Skaloud and Lichti 2006). The output of the Equation (4.1) model is the georeferenced point in a relative coordinate system such as a Local Geodetic Frame (LGF), which is a relative frame to the tangential plane of the area of interest on the earth.

$$\begin{bmatrix} X^{LGF} \\ Y^{LGF} \\ Z^{LGF} \end{bmatrix} = \begin{bmatrix} P_X^{LGF} \\ P_Y^{LGF} \\ P_Z^{LGF} \end{bmatrix} + R_{POS}^{LGF}(r,p,h) \left(R_{LiDAR}^{POS}(\alpha,\beta,\gamma) \begin{bmatrix} x_{LiDAR} \\ y_{LiDAR} \\ z_{LiDAR} \end{bmatrix} + \begin{bmatrix} a_X^{POS} \\ a_Y^{POS} \\ a_Z^{POS} \end{bmatrix} \right) \qquad (4.1)$$

In Equation (4.1), we recognize three frames, the *LiDAR* sensor local frame, the *POS* navigation frame, and the *mapping* frame, which we consider a Local Geodetic Frame (*LGF*). Here we describe each part of the direct georeferencing mathematical model,

- $[X^{LGF} \quad Y^{LGF} \quad Z^{LGF}]^T$ is the 3D position vector of the georeferenced point in the *LGF* frame.
- $[P_X^{LGF} \quad P_Y^{LGF} \quad P_Z^{LGF}]^T$ is the 3D position vector for each trajectory point in the *LGF* frame.
- $R_{POS}^{LGF}(r,p,h)$ is the rotation matrix made of three attitude angles: roll (r), pitch (p), and heading (h) between the gravity center in the *POS* frame and the reference point of the *LGF* frame.

- $R_{LiDAR}^{POS}(\alpha, \beta, \gamma)$ is the boresight angles rotation matrix between the *LiDAR* and POS frames. α is the roll boresight angle, β is the pitch boresight angle, and γ is the yaw boresight angle.
- $[x_{LiDAR} \quad y_{LiDAR} \quad z_{LiDAR}]^T$ is the 3D position vector of the target point with respect to the optical center of the scanner in the *LiDAR* frame.
- $[a_X^{POS} \quad b_Y^{POS} \quad a_Z^{POS}]^T$ is the 3D lever arm vector between the *LiDAR* and POS frames.

In our methodology, we use a comprehensive and explicit approach for the calculation of $R_{LiDAR}^{POS}(\alpha, \beta, \gamma)$. In the following, we present a direct mathematical formula for the rotations between the LiDAR frame and the POS frame, which is a multiplication of three rotations $R_X(\alpha)$, $R_Y(\beta)$ and $R_Z(\gamma)$, that is $R_{LiDAR}^{POS}(\alpha, \beta, \gamma) = R_Z(\gamma)R_y(\beta)\, R_x(\alpha)$ illustrated in Equation (4.2). Notice that the POS frame is in NWU (North–West–Up) convention.

$$R_{LiDAR}^{POS}(\alpha, \beta, \gamma) = \begin{pmatrix} \cos\gamma & -\sin\gamma & 0 \\ \sin\gamma & \cos\gamma & 0 \\ 0 & 0 & 1 \end{pmatrix} \begin{pmatrix} \cos\beta & 0 & \sin\beta \\ 0 & 1 & 0 \\ -\sin\beta & 0 & \cos\beta \end{pmatrix} \begin{pmatrix} 1 & 0 & 0 \\ 0 & \cos\alpha & -\sin\alpha \\ 0 & \sin\alpha & \cos\alpha \end{pmatrix} \quad (4.2)$$

After the multiplication operations, Equation (4.2) is explicitly expressed as a 3D rotation matrix given by Equation (4.3). We initialize the boresight angle parameters with approximative initial values based on an iterative least-squares adjustment procedure. Then, by considering boresight angle corrections as one part of the unknown values in the functional model, these corrections are applied to initial or corrected values of the previous iteration to refine the boresight angle parameters until convergence of the solution, which is typically reached after a few (3 or 4) iterations.

$$R_{LiDAR}^{POS}(\alpha, \beta, \gamma) = \begin{pmatrix} \cos\gamma\cos\beta & \cos\alpha\sin\gamma + \cos\gamma\sin\beta\sin\alpha & \cos\gamma\cos\alpha\sin\beta - \sin\gamma\sin\alpha \\ -\cos\beta\sin\gamma & \cos\gamma\cos\alpha - \sin\gamma\sin\beta\sin\alpha & -\cos\gamma\sin\alpha - \cos\alpha\sin\gamma\sin\beta \\ -\sin\beta & \cos\beta\sin\alpha & \cos\beta\cos\alpha \end{pmatrix} \quad (4.3)$$

4.4.4 Planar Target Extraction and Subsampling

After georeferencing all point clouds (one per scan collected on each passage), we extract the pre-defined planar targets visible on the different scans. As we expect, the point density is high, and if we use all the points on the planar targets, we will encounter intensive calculation costs during the least squares estimation process. Thus, we perform a homogeneous spatial-based subsampling method to reduce the high redundancy of the observations, which reduces the calculation cost of the method without decreasing the accuracy of the estimated parameters (Glennie 2012). We also estimate approximately the centroid and the normal of all the combined subsampled data, which will be served as a priori parameters for the boresight estimation module.

4.4.5 Boresight Angles Estimation Module

Usually, due to boresight misalignment deficiency in a mobile LiDAR system, the generated point clouds of the same planar targets acquired in multiple scans diverge and do not entirely overlap. The estimation algorithm applied here enables the estimation of the boresight angles (α, β, γ) of an MLS based on an iterative least-squares adjustment solution of a non-linear system based on direct georeferencing equations (Equation (4.1)). The method is inspired by the bundle block adjustment procedure, a proven approach used in photogrammetry (Filin 2003; Skaloud and Lichti 2006; Glennie 2012). This approach was initially adapted for boresight self-calibration of aerial mobile LiDAR systems (Skaloud and Lichti 2006). Consequently, after the boresight alignment of the MLS, a considerable improvement in the relative accuracy of the point clouds is achieved. The following paragraphs briefly present the steps for the boresight error estimation in mathematical terms.

Figure 4.15 illustrates that ***point i*** in the yellow plane (passage with 45º of heading) deviated from the original ***plane j*** (cyan color) due to boresight angle offsets between the LiDAR scanner and the POS sensor. Equation (4.4), the observation equation of the least-square adjustment process, represents the connection between ***point i*** and

plane j, which conditions a georeferenced point $(X_i^{LGF}, Y_i^{LGF}, Z_i^{LGF})$ to lie on the plane j with (a_j, b_j, c_j, d_j) parameters.

$$F(\vec{L}_i, \vec{X}_b, \vec{X}_j) = a_j X_i^{LGF} + b_j Y_i^{LGF} + c_j Z_i^{LGF} + d_j = 0 \quad (4.4)$$

The observation equation, F, is a function of the POS observations, GNSS and INS, and the LiDAR scanner local coordinates for each ***point i***, $\vec{L}_i = [P_X^{LGF}, P_X^{LGF}, P_X^{LGF}, r, p, h, x_{LiDAR}, y_{LiDAR}, z_{LiDAR}]^T$, the boresight angles parameters, $\vec{X}_b = [\alpha, \beta, \gamma]$ and finally, the ***plane j*** parameters, $\vec{X}_j = [a_j, b_j, c_j, d_j]$.

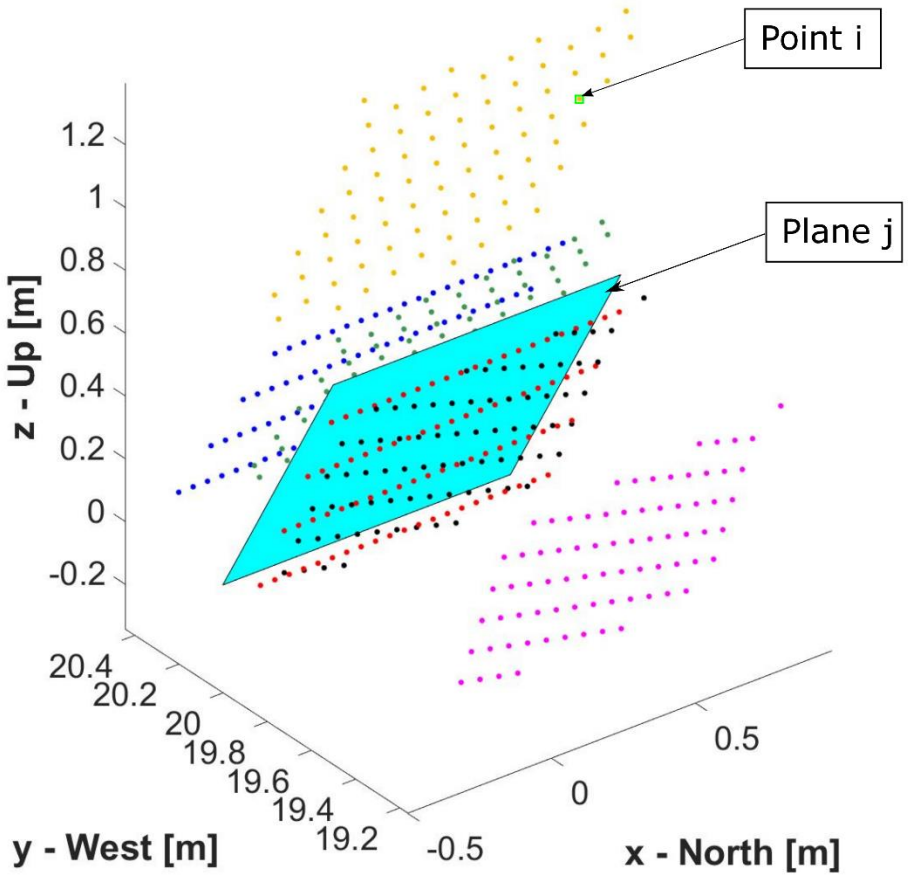

Figure 4.15 – Simulated planar target (in cyan) with different scanned instances obtained after subsampling due to boresight angle offsets.

Equation (4.5) demonstrates the constraint equation of the functional model, which consists of direction cosines of ***plane j,*** which must form a unit vector.

$$\mathrm{G}\left(\vec{X}_j\right) = a_j^2 + b_j^2 + c_j^2 - 1 = 0 \qquad (4.5)$$

The iterative least-squares adjustment procedure, which forces the ***point i*** to lie onto the original ***plane j*** and simultaneously estimates $\vec{X}_b$, $\vec{X}_j$, and their uncertainties are presented in detail in the literature (Skaloud and Lichti 2006).

4.4.6 Plane-Based Relative Accuracy Assessment

We proposed a plane-based relative accuracy assessment method for validation and quality assessment. This relative accuracy analysis and validation approach compare the same planar patches on round-trip passages before and after boresight alignment. To this end, we utilized the cloud-to-cloud comparison method available in *CloudCompare* software (Ahmad Fuad et al. 2018; Girardeau-Montaut 2021), a handy tool for point cloud analysis. Comparative results obtained with this tool are presented in the following section.

4.5 Field Experiments and Results

This section applies the proposed methodology in a real-world scenario. The main difference between a simulated and a real-world scenario is the presence of other sources of errors, like sensor noises and blunders caused by GNSS signal blockage, which can dramatically influence the quality of the MLS point cloud accuracy. To address these issues, based on the results from the previous analysis, we suggest adding more planes of different inclinations to ensure a good accuracy of the estimated boresight errors. Based on a simulated data scenario, using three tie-planes with (90º, 60º, and 30º) inclinations results in highly accurate boresight error. At the same time, utilization of two tie-planes with (90º and 30º) inclinations can also result in similar accuracy. In the real-world scenario, the two tie-planes option is considered to address the feasibility and simplicity criteria of the method. This configuration is also practical in a marine MLS boresight alignment case, which

imposes some limitations on the installation of planar targets on the quay wall and port structures.

4.5.1 Boresight Alignment Site Description

The experimental site of our proposed methodology is located at the Port of Montreal, on the St. Lawrence River in the province of Quebec, Canada. This survey was done on July 9, 2019. It is an international container port that welcomes cruise ships and considerably impacts the region's economy. The main infrastructures of this port consist of four terminals, a 25 km waterfront, 470 wharf boxes, 1161 bollards, 100 km of railroad, 14 embarkment areas, and 14 km of quay wall. Thus, routine maintenance and renovation of the port’s infrastructure and facilities is an essential task of the port’s authorities.

To prioritize the maintenance task, the port’s officials need an as-built 3D model of the port’s infrastructures in their current condition (Kalyan et al. 2016). These models give a near-to-reality perspective of the structures and facilitate analyzing the state of the port’s infrastructures and taking the necessary action to repair them. As mentioned earlier, the state-of-the-art technology for 3D data acquisition in the context of the port’s emergent infrastructure is the mobile LiDAR system installed on a vessel. To access high-quality data from the mobile LiDAR system, we must ensure that the LiDAR sensor is fully aligned with the POS.

Figure 4.16 illustrates three prominent locations; the boresight alignment site, the validation site, and the GNSS base station. The dimension of the boresight alignment site is around 250 m by 250 m (including the line pattern). The boresight alignment site is located on Quai Alexandra where there are no tall buildings or other infrastructure to cause multipath or signal occlusions for the GNSS data. On the other hand, we installed a GNSS base station within a 500 m distance from the boresight alignment site. The correction for the position was received from this base, and a more accurate POS solution was obtained after the post-processing procedure.

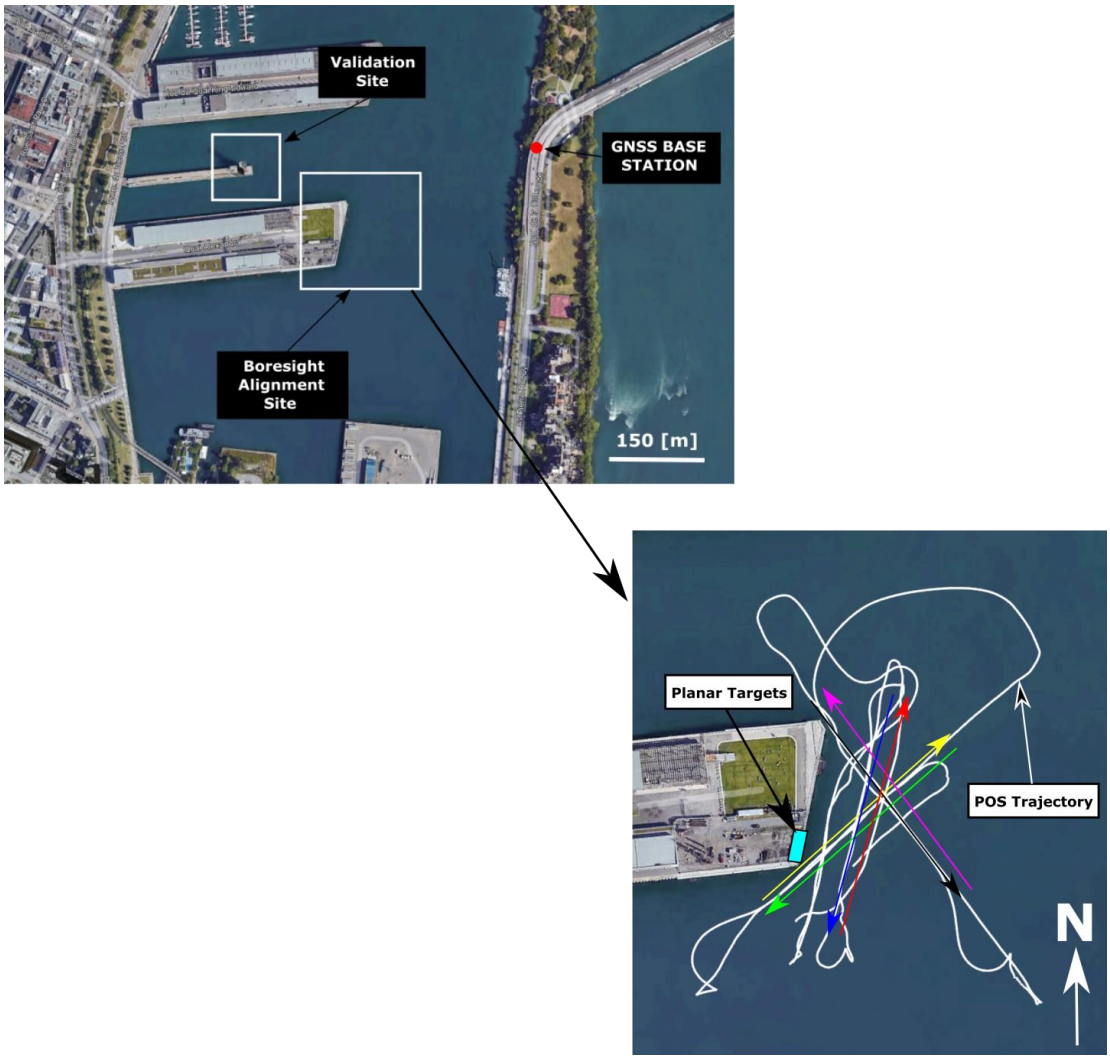

Figure 4.16 – Boresight alignment site, validation site, and GNSS base station

Based on the results of the post-processed trajectory with the APPS software (IXblue Software Manual 2017), the uncertainties of each of the six POS parameters; three positional parameters (northing, easting, and height) and three orientation parameters (heading, roll, and pitch) are calculated and presented in Figure 4.17 and Figure 4.18.

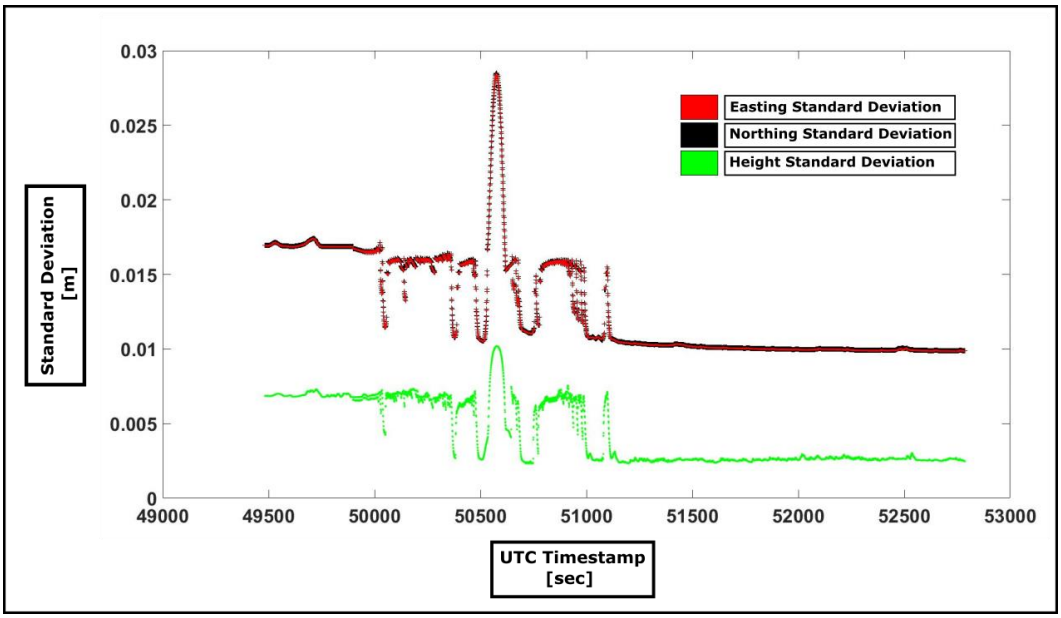

Figure 4.17 – Standard deviation of northing, easting, and height in meters of the post-processed trajectory (reported by the APPS software)

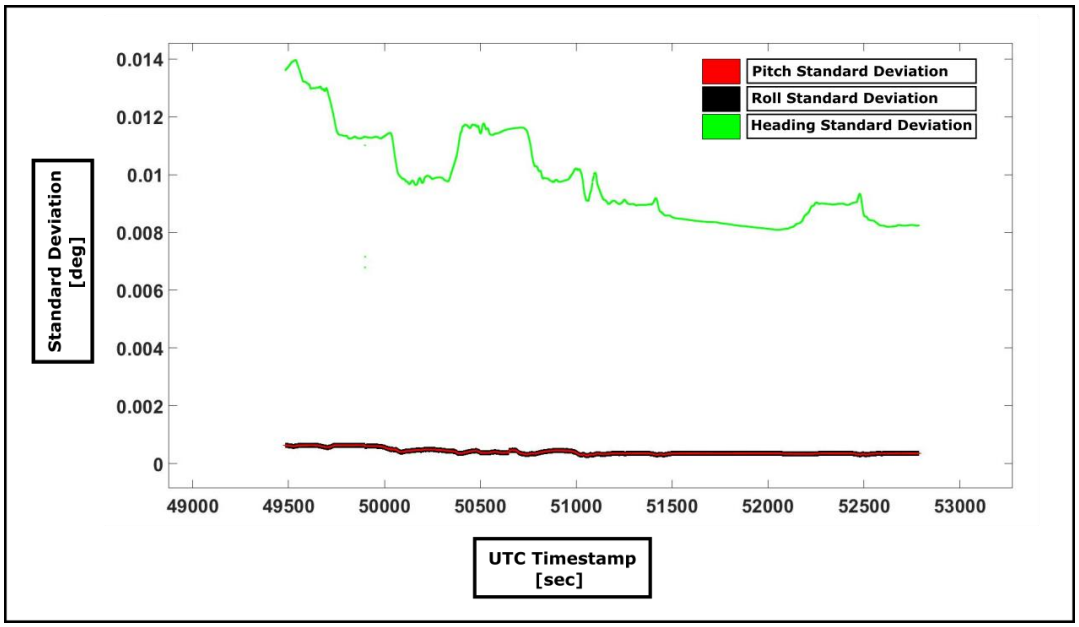

Figure 4.18 – Standard deviation of heading, roll, and pitch in degrees of the post-processed trajectory (reported by the APPS software)

As illustrated in Figure 4.17 and Figure 4.18, the accuracy of the POS parameters is within the expected threshold. The location (easting, northing, and height) standard deviation is mostly less than 2 cm, and the orientation (heading, roll, and pitch) standard deviation is around 0.012 deg.

As shown in Figure 4.19, the boresight alignment site consists of two planar targets installed on the quay walls with the following characteristics. The square-shaped vertical planar target dimensions are 123 cm x 122 cm x 1 cm, and its orientation is 90°. The rectangle-shaped inclined planar target dimensions are 123 cm x 76 cm x 1 cm, and its orientation is 45°. The material used for each plane is white melamine paper-faced chipboard MDF (medium-density fiberboard) that can easily be found in hardware stores. These two planar targets are scanned following a six-fold survey line pattern similar to the one in Figure 3.3.

Based on the alignment approach introduced in the methodology section, 3 or 4 iterations are sufficient to estimate the boresight angle parameters with these two planar targets. The point clouds of each six-fold line pattern were entered as input in the boresight alignment module.

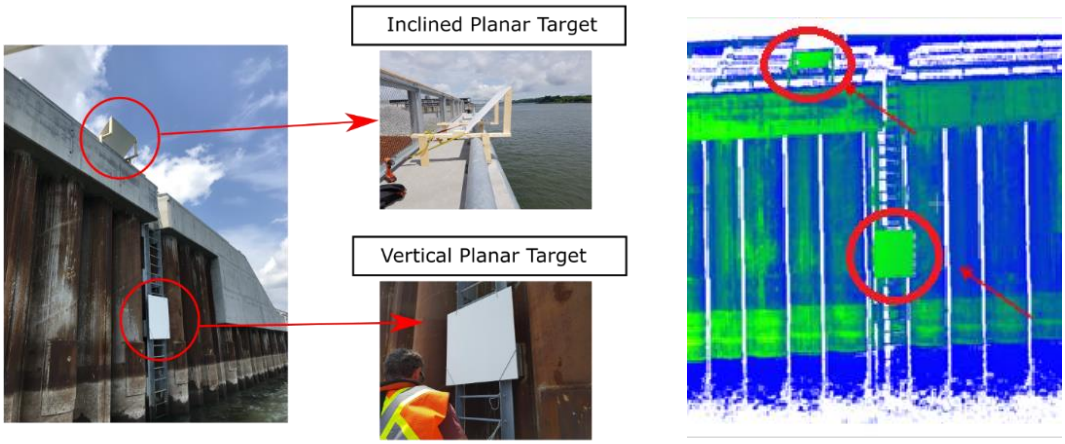

Figure 4.19 – Prefabricated planar targets installed on the quay wall for the marine MLS boresight angles estimation

4.5.2 In-house Marine MLS

This research studies the boresight alignment of an in-house customized marine MLS, as illustrated in Figure 4.20. This marine MLS comprises a Z&F 9012 2D profiler as the LiDAR scanner and a Hydrins iXBlue/Septentrio as the POS sensor. The range resolution of the 2D Laser scanner is 0.1 mm, and its beam divergence is less than 0.5 mrad, which is more accurate than the INS positioning and orientation uncertainty, bringing up to 2 to 3 cm expected total uncertainty for the final georeferenced point.

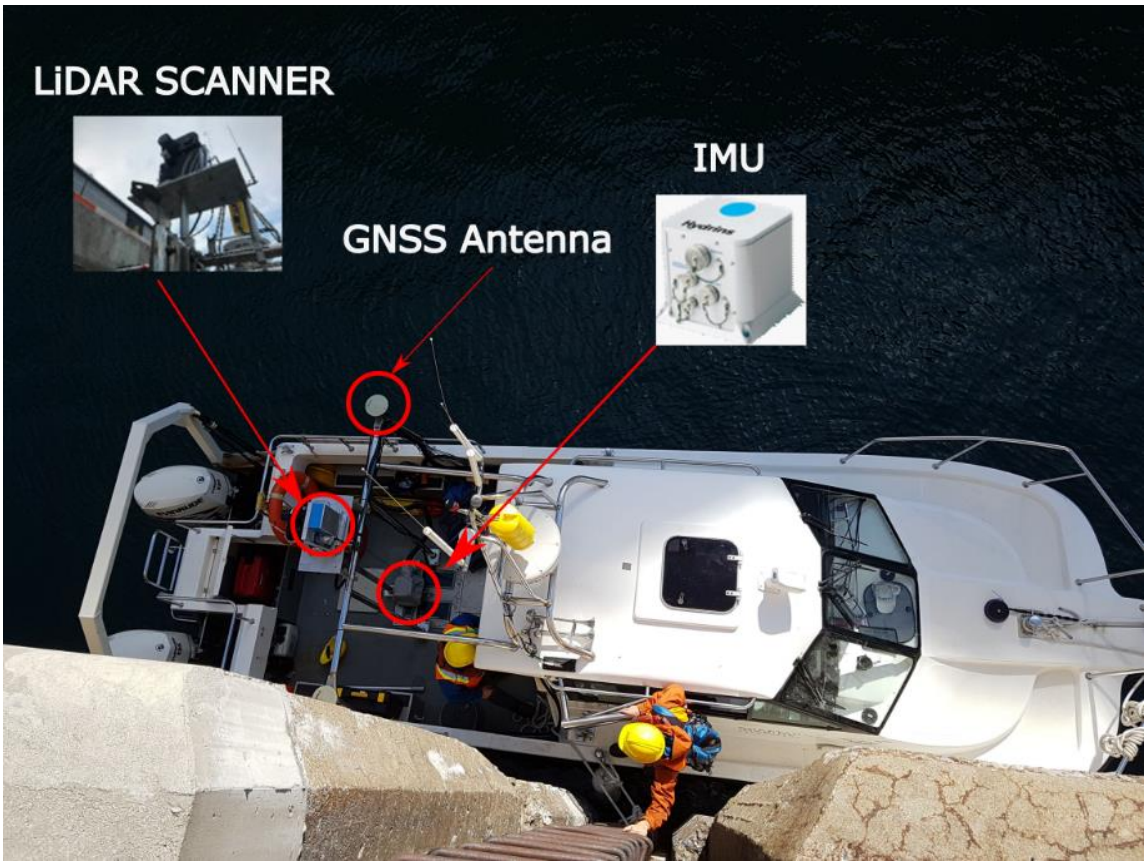

Figure 4.20 –Marine MLS for the inspection of quay walls, composed of a Hydrins iXblue INS and a Z&F 9012 2D profiler (Courtesy of CIDCO)

4.5.3 Results and Discussions

Table 4.1 shows the estimated boresight angles of the marine MLS using the approach described in this paper and applied to the Port of Montreal infrastructure.

Table 4.1 – Boresight angles with their uncertainties

Roll ± σ_{Roll}	Pitch ± σ_{Pitch}	Yaw ± σ_{Yaw}
0.208 ° ± 0.0010 °	-1.245 ° ± 0.0118 °	0.149 ° ± 0.0008 °

Table 4.2 presents the correlation matrix between the three boresight angles based on the variance-covariance matrix calculated in the least-squares solution. Based on the correlation values between the three boresight errors, which are near zero, these parameters are decorrelated with the proposed configuration for the calibration site.

Table 4.2 – Correlation matrix between the boresight angles

	Roll	Pitch	Yaw
Roll	1	-0.0034	0.0000
Pitch	-0.0034	1	0.0030
Yaw	0.0000	0.0030	1

The proposed method allows a non-expert user to efficiently implement the boresight alignment workflow in a short period before starting the actual scanning project. After installing the planar targets on the quay wall, it takes about 30 minutes to scan the two planes with the marine MLS by following the six-fold line pattern survey and another 30 minutes to estimate the boresight angles of the marine MLS by processing the calibration dataset at the office. This boresight alignment step guarantees the quality of point clouds generated by the marine MLS to a few centimeters, as we expect from this system.

The plane extraction procedure, considered semi-automatic, is presented in Figure 4.21. The non-expert operator must only select approximatively the plane in the overall georeferenced point cloud. The plane extraction module, which has two main parameters; stop criterion, i.e., a fraction of total points in planes with the default value of 0.98 and the distance threshold with the default value of 0.01 m, extract in a semi-automatic mode, the necessary planar targets. The plane extraction module

utilizes the RANSAC module in the PCL library (Fischler and Bolles 1981; Rusu, Cousins, and Garage 2011).

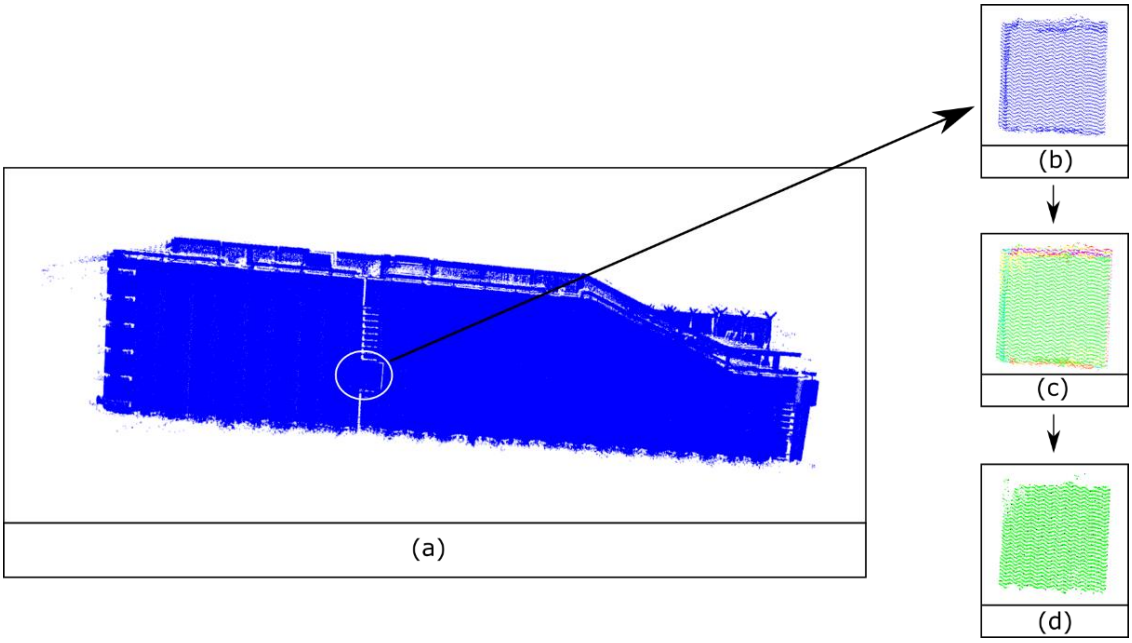

Figure 4.21 – Plane extraction procedure from overall point cloud to the final subsampled dataset. (a) overall point cloud with high-density representation. (b) approximative location of the vertical plane by a manual procedure. (c) plane extracted automatically based on the RANSAC approach. (d) subsampled dataset.

To analyze the impact of reducing the point density (subsampling) on the accuracy of the boresight angles estimation, we used data from the Port of Montreal planar targets and subsampled them at 5 cm, 10 cm, and 20 cm point density. Afterward, we take each subsampled planar target and estimate the boresight angles. Table 4.3 represents the estimated boresight angles for each of the subsampling categories.

Table 4.3 – Point density (subsampling) analysis results with processing time

Subsampling Distance (cm)	File Size (KB)	Average Point Number	Roll ± σ_{Roll}	Pitch ± σ_{Pitch}	Yaw ± σ_{Yaw}	Time (Second)
10	374	1297	0.208 ° ± 0.0010 °	-1.245 ° ± 0.0118 °	0.149 ° ± 0.0008 °	532
15	185	635	0.205 ° ± 0.0011 °	-1.242 ° ± 0.0160 °	0.148 ° ± 0.0010 °	145
20	115	396	0.209 ° ± 0.0016 °	-1.242 ° ± 0.0210 °	0.148 ° ± 0.0010 °	18

Comparing the results of the 10 cm, 15 cm, and 20 cm subsampled datasets, we observe very close boresight angles and respective uncertainty values. On the other hand, the speed of the calculations from the 20 cm subsampled dataset is much faster than the ones computed for the 10 cm and 15 cm. Based on the results of this analysis and considering a trade-off between boresight angles accuracies and the calculation cost, we suggest the adoption of a 15 cm subsampling that adequately covers the planar surface and calculates the solution in an adequate amount of time. The calculation was done with an ordinary personal computer with the following characteristics, Intel Core i7-3770 CPU @ 3.40GHz, 3401 MHz, 4 cores, 8 processors, and 4 GB RAM. The programming language used is C++, and the PCL library has been utilized to extract planar targets.

We have also compared our approach with commercial software (Qinsy Validator) that can also estimate the values of the boresight angles of our POS/LiDAR system. It first registers deviated point clouds acquired on bridges and overhead structures visible from various passages. Afterward, by applying a minimization procedure, boresight angles are estimated individually while the discrepant point clouds are fitted together. This approach is categorized in the data-driven boresight alignment method, also known as the strip adjustment technique (Kager 2004; Maas 2002; Filin and Vosselman 2004; M. J. . Crombaghs, Brugelmann, and Min 2000). The results

estimated with the LiDAR patch test method of the Qinsy Validator software on the same dataset of the Port of Montreal are presented in Table 4.4.

Table 4.4 – Estimated boresight angles with Qinsy Validator

Method Name	Roll (º)	Pitch (º)	Heading (º)
Planar Targets	0.208 ° ± 0.0010 °	-1.245 ° ± 0.0118 °	0.149 ° ± 0.0008 °
LiDAR Patch Test	0.25	-1.20	0.20

However, we observe the following limitations with the Qinsy Validator. This approach needs to have a point cloud around a pole or pillar near the scan location, which may not be accessible all the time. Also, underneath poles or bridges, there is a risk of losing GPS signals or meeting GNSS multipath effects, which can affect the data accuracy. On the other hand, the boresight alignment method described in this paper considers that the boresight angles have a natural correlation and must be estimated simultaneously. The method applied in this paper is considered a sensor-driven robust technique, which uses prefabricated planar targets without the need for specific in-situ primitives.

4.5.4 Relative Accuracy Assessment Analysis

In this section, we assess the relative accuracy of the point cloud generated by the estimated boresight error before and after boresight alignment. Therefore, we perform a relative accuracy assessment by comparing the displacement of point clouds acquired from various round-trip passages around a tower at the Port of Montreal, which is considered our validation site (Brunner 2007). To quantify our relative accuracy assessment, we use the cloud-to-cloud distance module in the *CloudCompare* open-source software (Heinz et al. 2017; Ahmad Fuad et al. 2018; Girardeau-Montaut 2021) to compare two sets of point clouds before and after the boresight alignment. Figure 4.22 presents five planar patches on the validation site we use for the relative accuracy assessment.

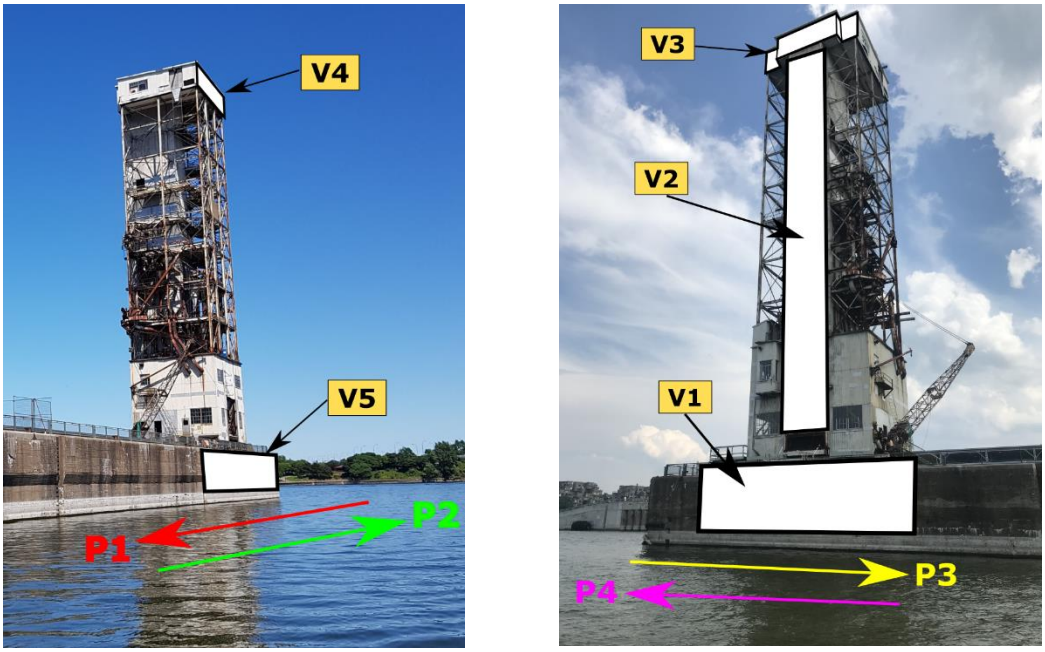

Figure 4.22 – The location of the five planar surfaces (V1 to V5) on the validation site

Figure 4.23 shows a top view of the tower showing the difference between the point clouds before and after applying the boresight alignment. We can visually recognize the enhancement of the point cloud geometric quality around the crane feature before and after the boresight alignment in Figure 4.23.

Although we witness a significant improvement in the geometric quality of the point cloud after our boresight alignment, we can go a step further and use a *cloud-to-cloud distance* measurement tool of the *CloudCompare* software. This tool performs a least-square plane model to accurately estimate the quantitative difference between point cloud data before and after boresight alignment (Ahmad Fuad et al. 2018).

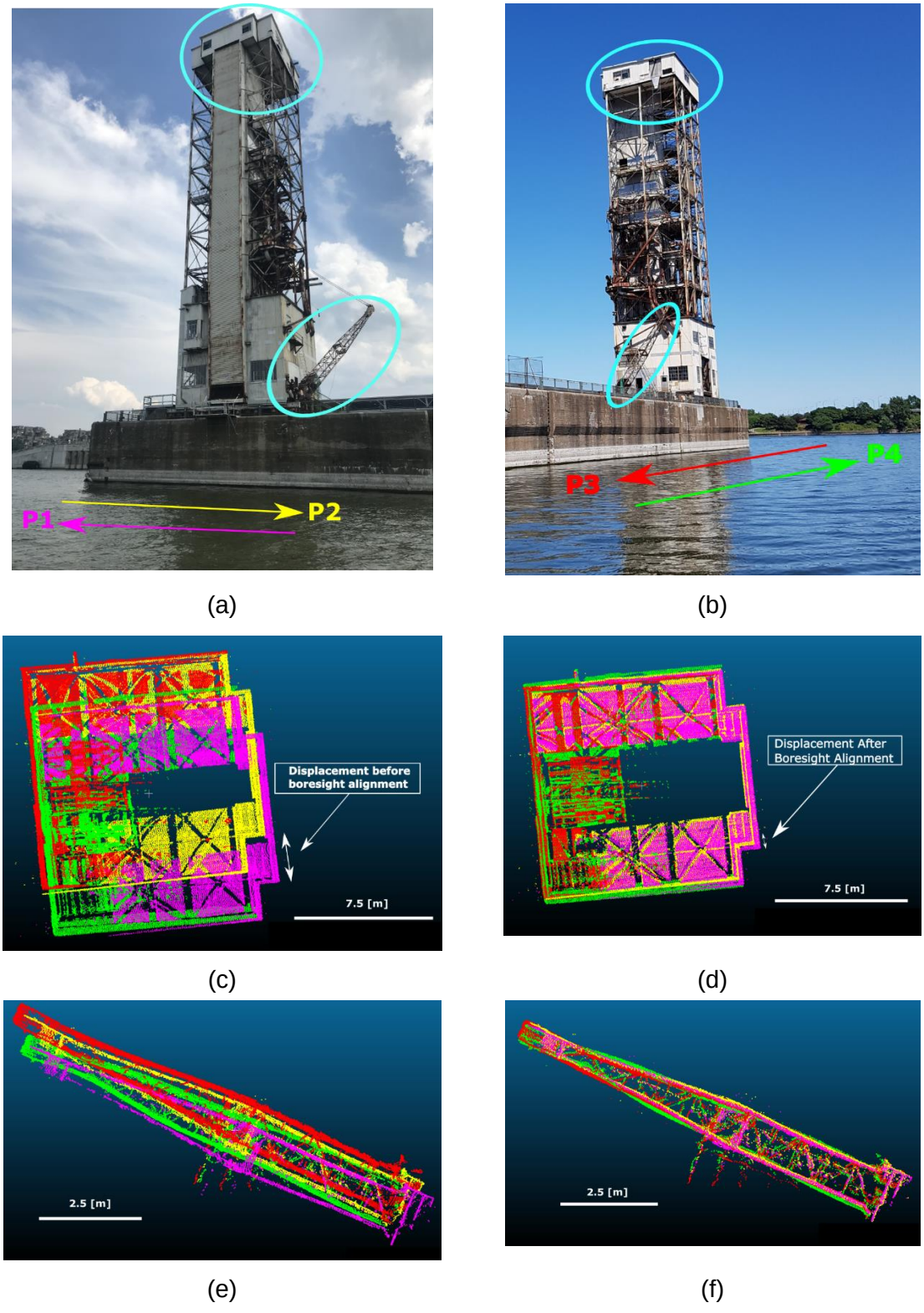

(a) (b)

(c) (d)

(e) (f)

Figure 4.23 – Schematic comparison of the validation element. (a-b) line pattern. (c-e) Tower and the Crane before boresight alignment. (d-f) after the boresight alignment

To demonstrate the results of this comparison, we present them in the form of histograms of the *cloud-to-cloud distance* module before and after boresight alignment. In Figure 4.24, we can see those histograms of validation planes V3 and V4, before and after boresight alignment, pursuing the same pattern. The blue histogram, which shows the distance between point clouds before boresight alignment, is always wider than the brown histogram, which shows a narrower distance between point clouds after the boresight alignment and has a more gaussian shape. Therefore, the boresight alignment has decreased the distance between the point clouds of corresponding validation planes visible from round-trip passages.

We can notice in Figure 4.24 a significant enhancement of the point cloud quality of validation planes V3 and V4. The longer distances between the marine MLS platform and these two validation planes, which are in the highest part of the validation site (around 40 m height), clearly show the impact of a boresight misalignment, which is more pronounced in this area than in an area located at the same height of the marine MLS platform.

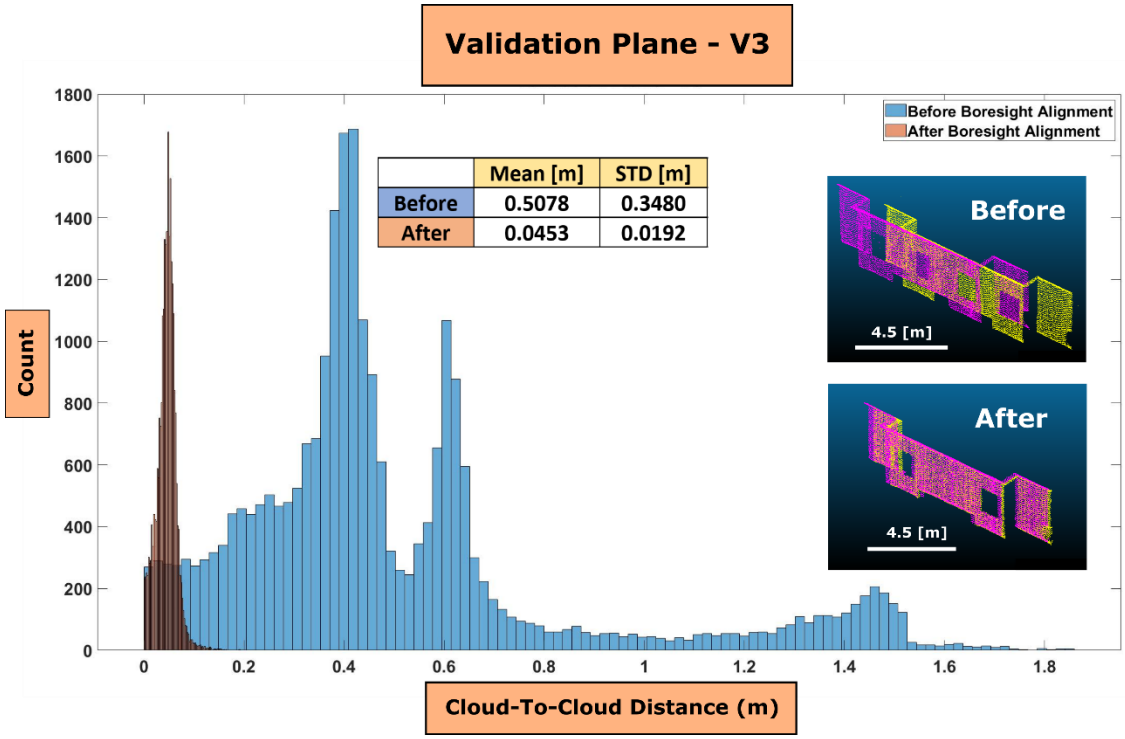

(a)

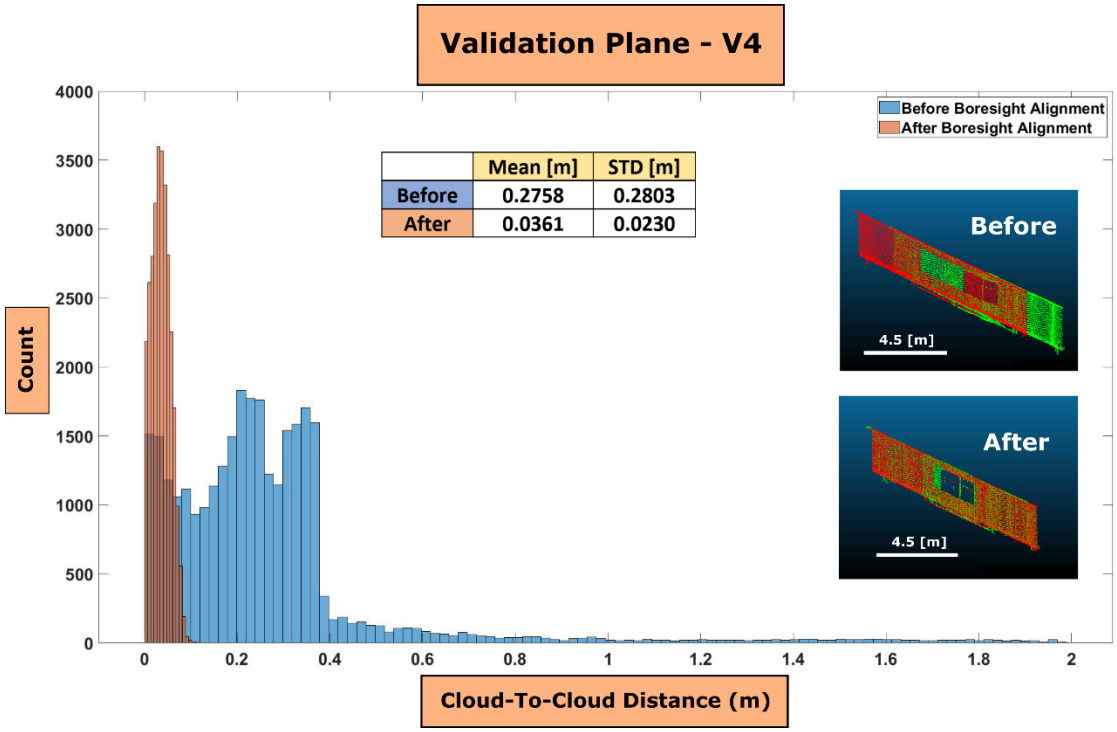

(b)

Figure 4.24 - Histograms of two validation planes (a) V3 and (b) V4 located at 40 m height w.r.t the survey platform

The results presented in Figure 4.25 also show a difference between the point cloud quality before and after the boresight alignment for planes V1 and V5, located at about the same height as the survey platform where the impact of boresight misalignment on these two validation planes is less apparent than for the two higher planes V3 and V4. This more negligible difference was expected with MLS data because of the impact of the systematic errors, as boresight angles are more noticeable in the presence of significant range distances between the platform and the targets.

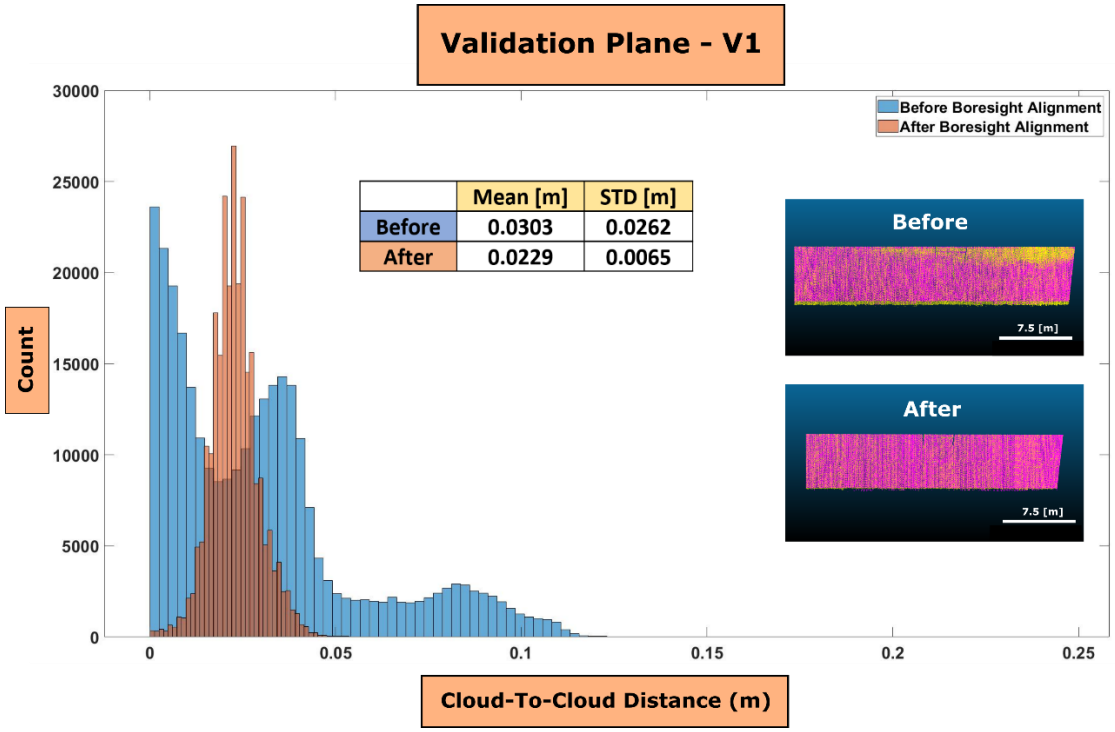

(a)

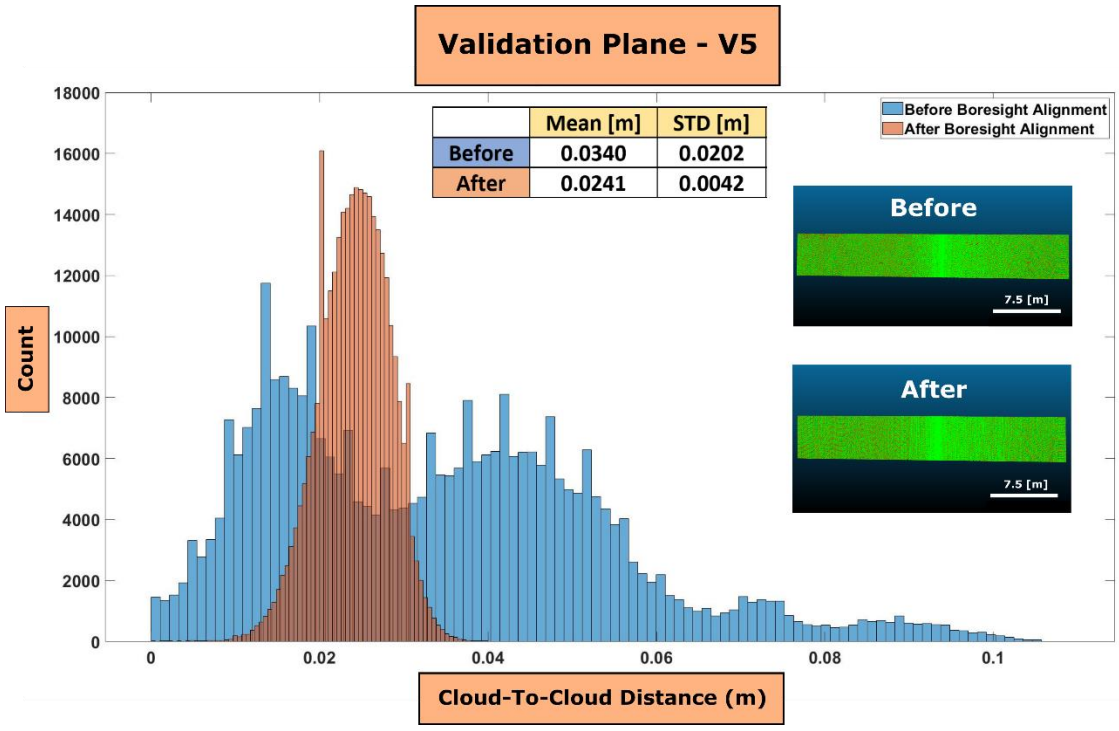

(b)

Figure 4.25 – Histogram of two validation planes, (a) V1 and (b) V5, located at the same height as the platform

Figure 4.26 illustrates the most extended validation plane (V2) that starts at the same height as the survey platform (water level) and goes up to the highest point of the validation site, about 40 m in height. We can easily see the impact of the boresight misalignment on this validation plane, which is minimal on lower points and more significant on higher points. Therefore, choosing a validation site with a significant height difference (in our case, the tower) is highly recommended to comprehensively analyze the boresight alignment method and, consequently, validate the results.

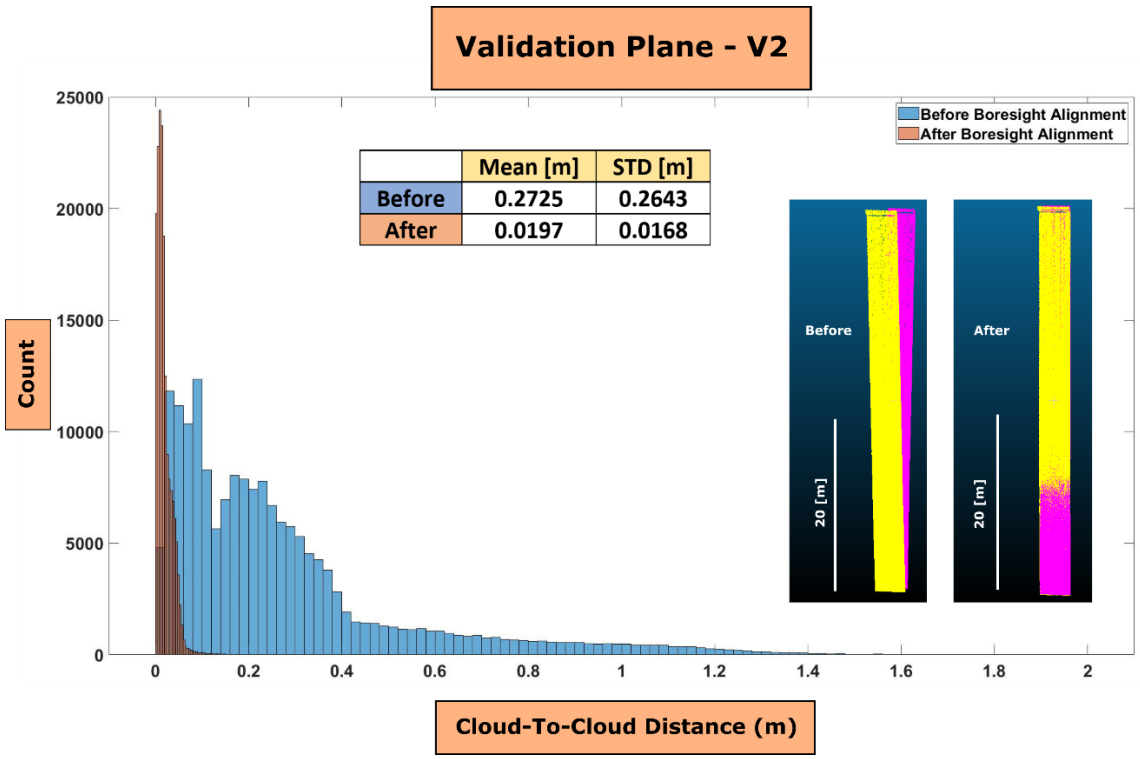

Figure 4.26 – Histogram of validation plane (V2)

4.5.5 Repeatability Analysis

We repeated the exact boresight alignment of the same marine MLS in the same area, Port of Montreal, on October 2, 2019, to analyze the proposed method's repeatability. Table 4.5 presents the result of the first and second tests of the boresight error of the marine MLS estimated with a similar procedure.

Table 4.5 – Boresight angles with their uncertainties

	Date	Roll ± σ_{Roll}	Pitch ± σ_{Pitch}	Yaw ± σ_{Yaw}
First Test	July 9, 2019	0.208 ° ± 0.0010 °	-1.245 ° ± 0.0118 °	0.149 ° ± 0.0008 °
Second Test	October 2, 2019	0.341 ° ± 0.0014 °	-0.805 ° ± 0.0110 °	0.032 ° ± 0.0006 °

We can conclude that the method is repeatable based on the results from these two tests. Therefore, as we can see, the second test on October 2, 2019, estimated boresight errors with slightly different values. The RMSE of the difference between the two boresight errors is approximately 0.47 deg, which can cause around 41 cm positioning error in 50 m.

This difference might be caused by the in-house customized MLS used in this research. This system must be mounted on the marine platform to carry out the scanning survey and dismounted when the survey is finished. These operations can displace the LiDAR scanner installation holes and deform the sensor platform in a permanent way (Hebel and Stilla 2012), which can impact the stability of the installation setup and can eventually affect the boresight angle estimation. Therefore, this research suggests repeating the procedure each time we assemble the system, especially when we have a considerable time difference between the surveys.

4.6 Conclusions

Routine monitoring of port and coastal infrastructure is vital for port authorities. This article explores the potential of a mobile LiDAR system (MLS) mounted on a vessel as a state-of-the-art 3D data acquisition technology for a high-accuracy port infrastructure monitoring application. To produce high-accuracy data, we must ensure that the MLS's two main parts, the LiDAR scanner and position and orientation system (POS), are perfectly aligned. The MLS alignment consists of two primary operations, POS-LiDAR lever arms alignment and POS-LiDAR boresight alignment. This research concentrates on the second type in the context of port environment.

Many approaches exist in the literature on the boresight alignment of mobile LiDAR systems, mainly aerial and terrestrial ones. They are divided into two main categories: system-driven and data-driven. In this paper, we adopted a system-driven robust procedure for the boresight alignment methodology due to the accessibility of the sensor's raw measurements. The inputs in this method are often primitive surfaces, primarily available as in-situ geometric objects in structured environments like urban areas. The main objective of this paper is to perform the boresight alignment of a marine MLS before acquiring accurate LiDAR point cloud data in the port environment where it is not obvious to find a variety of in-situ geometric primitives. To overcome this difficulty, we propose a novel site design for boresight alignment in the context of the maritime environment that uses prefabricated planar targets to properly align the LiDAR scanner with respect to the POS sensor. The main contribution of this research was first to explore a variety of possible configurations of prefabricated planar targets based on a simulation approach and then, based on this analysis, introduce the optimal boresight alignment site. Afterward, a real-world case successfully tested the suggested boresight alignment site. The analysis of the results illustrates that the boresight angles are estimated at very low uncertainties, i.e., less than 0.02º for the pitch and less than 0.002º for roll and yaw angles. Also, the correlation matrix demonstrates an acceptable decorrelation between the three boresight angles. Moreover, based on validation analysis, the point cloud discrepancy index (mismatch between two scans of the same object on round-trip passages) has improved considerably after enforcing the estimated boresight angles. Based on these analyses, we can conclude that with only two prefabricated planar targets, we could estimate the boresight angles of a marine MLS with high accuracy.

In the future, we would also consider the impact of POS errors on the data with a simulation approach. In the basic version of the simulator, we only addressed the boresight angles systematic errors, and we considered that the point cloud is free from POS-related errors. However, in the real-world case, due to GNSS signal loss and multipath issues, the quality of the platform's position decreases, affecting the quality of the final point cloud. We can model the effect of this error on simulated

primitives like planar surfaces and explore approaches that mitigate the trajectory-prone errors on the MLS point cloud. We would also explore the possibility of using other primitives like spheres for the boresight alignment of an MLS. We can pursue the same approach of simulating the points on spheres and trying to estimate the boresight angles by fitting all the deviated point clouds from various passages. We will also replace the planar target extraction from semi-automatic to fully automatic, leading to automatic plane-based accuracy assessment. Moreover, with the simulator design, we can optimize the configuration of the planar targets and the line pattern with more intelligent optimization methods like genetic algorithms and recursive feature elimination methods (Hartmann et al. 2019). Furthermore, we aim to scan the validation site (e.g., the tower) with a static LiDAR scanner and compare the point cloud generated after the boresight alignment of the MLS with this accurate reference point cloud for an absolute accuracy assessment.

Disclosure statement

The authors have no potential competing financial or non-financial interests in the work presented.

Funding

This study was financed by an international research project of Ministère de l'Économie et de l'Innovation (MEI) du Québec (PSR-SIIRI-953) and MITACS Acceleration research fund (IT08173) that focuses on "Automatic calibration and performance analysis of a mobile LiDAR system" through a partnership between Université Laval and CIDCO.

Data availability statement

The data supporting this study's findings are available from CIDCO (Centre Interdisciplinaire de Développement en Cartographie des Océans). Restrictions apply to the availability of these data, which were used under a research agreement for this study. Access to the marine mobile LiDAR system data (LiDAR and the SBET files) of the Port of Montreal survey will be considered upon reasonable request by the authors with the permission of CIDCO.

4.7 References

Ackermann, F. 1999. “Airborne Laser Scanning - Present Status and Future Expectations.” *ISPRS Journal of Photogrammetry and Remote Sensing* 54 (2–3): 64–67. doi:10.1016/S0924-2716(99)00009-X.

Ahmad Fuad, N., A. R. Yusoff, Z. Ismail, and Z. Majid. 2018. “Comparing the Performance of Point Cloud Registration Methods for Landslide Monitoring Using Mobile Laser Scanning Data.” *International Archives of the Photogrammetry, Remote Sensing and Spatial Information Sciences - ISPRS Archives* 42 (4/W9): 11–21. doi:10.5194/isprs-archives-XLII-4-W9-11-2018.

Alho, Petteri, A. Kukko, H. Hyyppä, H. Kaartinen, J. Hyyppä, and A. Jaakkola. 2009. “Application of Boat-Based Laser Scanning for River Survey.” *Earth Surface Processes and Landforms* 34 (March): 613–628. doi:10.1002/esp.

Böder, Volker, Thomas P. Kerstenl, Thomas Thies, and Arne Sauer. 2011. “Mobile Laser Scanning on Board Hydrographic Survey Vessels - Applications and Accuracy Investigations -.” *Hydrography in Practice, 4927*, no. May 2011: 18–22. http://www.fig.net/pub/fig2011/papers/ts05j/ts05j_boeder_kersten_et_al_4927.pdf.

Böse, Jürgen W. 2011. *Handbook of Terminal Planning*. *Operations Research/ Computer Science Interfaces Series*. Vol. 49. doi:10.1007/978-1-4419-8408-1.

Brunner, Fritz K. 2007. “On the Methodology of Engineering Geodesy.” *Journal of Applied Geodesy* 1 (2). doi:10.1515/jag.2007.008.

Crombaghs, M.J.E, R. Brugelmann, and E.J. de Min. 2000. “On the Adjustment of Overlapping Strips of Laser Altimeter Height Data.” *International Archives of Photogrammetry and Remote Sensing* 1 (17 2): 230–237.

De Gijt, J.G. 2010. “A History of Quay Walls Techniques, Types, Costs and Future.” Netherlands: TUDelft. https://repository.tudelft.nl/islandora/object/uuid:d62bbff8-e805-434a-893e-08940d58ae8c?collection=research.

Dix, Michael, Amr Abd-Elrahman, Bon Dewitt, and Lou Nash. 2012. “Accuracy Evaluation of Terrestrial LIDAR and Multibeam Sonar Systems Mounted on a Survey Vessel.” *Journal of Surveying Engineering* 138 (4): 203–213. doi:10.1061/(asce)su.1943-5428.0000075.

Filin, Sagi. 2003. “Recovery of Systematic Biases in Laser Altimetry Data Using Natural Surfaces.” *Photogrammetric Engineering and Remote Sensing* 69 (11): 1235–1242. doi:10.14358/PERS.69.11.1235.

Filin, Sagi, and George Vosselman. 2004. “Adjustment of Airborne Laser Altimetry Strips.” In *International Archives of Photogrammetry, Remote Sensing and Spatial Information Sciences 34 (Part B3)*, 285–289.

Firoozi, Ali Akbar, Mohd Raihan Taha, S. M. Mir Moammad Hosseini, and Ali Asghar Firoozi. 2014. “Examination of the Behavior of Gravity Quay Wall against Liquefaction under the Effect of Wall Width and Soil Improvement.” *Scientific World Journal* 2014 (July). Hindawi Publishing Corporation. doi:10.1155/2014/325759.

Fischler, Martin A., and Robert C. Bolles. 1981. “Random Sample Consensus: A Paradigm for Model Fitting with Applications to Image Analysis and Automated Cartography.” *Communications of the ACM* 24 (6): 381–395. doi:10.1145/358669.358692.

Girardeau-Montaut, Daniel. 2021. *Cloud Compare. 3D Point Cloud and Mesh Processing Software-Open Source Project*. http://www.cloudcompare.org/.

Glennie, Craig. 2012. “Calibration and Kinematic Analysis of the Velodyne HDL-64E S2 Lidar Sensor.” *Photogrammetric Engineering and Remote Sensing* 78 (4): 339–347. doi:10.14358/PERS.78.4.339.

Hartmann, J., I. Von Gösseln, N. Schild, A. Dorndorf, J. A. Paffenholz, and I. Neumann.

2019. “Optimisation of the Calibration Process of a K-Tls Based Multi-Sensor-System by Genetic Algorithms.” *International Archives of the Photogrammetry, Remote Sensing and Spatial Information Sciences - ISPRS Archives* 42 (2/W13): 1655–1662. doi:10.5194/isprs-archives-XLII-2-W13-1655-2019.

Hebel, Marcus, and Uwe Stilla. 2012. “Simultaneous Calibration of ALS Systems and Alignment of Multiview LiDAR Scans of Urban Areas.” *IEEE Transactions on Geoscience and Remote Sensing* 50 (6): 2364–2379. doi:10.1109/TGRS.2011.2171974.

Heinz, Erik, Christian Eling, Markus Wieland, Lasse Klingbeil, and Heiner Kuhlmann. 2017. “Analysis of Different Reference Plane Setups for the Calibration of a Mobile Laser Scanning System.” *Ingenieurvermessung*, no. July: 131–146.

Heinz, Erik, Christoph Holst, Heiner Kuhlmann, and Lasse Klingbeil. 2020. “Design and Evaluation of a Permanently Installed Plane-Based Calibration Field for Mobile Laser Scanning Systems.” *Remote Sensing* 12 (3). doi:10.3390/rs12030555.

IXblue Software Manual. 2017. *Advanced Post-Processing Software*. www.ixblue.com.

Kager, H. 2004. “Discrepancies between Overlapping Laser Scanner Strips--Simultaneous Fitting of Aerial Laser Scanner Strips.” *International Archives of Photogrammetry, Remote Sensing and Spatial Information Sciences* 35 (B1): 555–560.

Kalyan, T. Sri, Puyan A. Zadeh, Sheryl Staub-French, and Thomas M. Froese. 2016. “Construction Quality Assessment Using 3D As-Built Models Generated with Project Tango.” *Procedia Engineering* 145. Elsevier B.V.: 1416–1423. doi:10.1016/j.proeng.2016.04.178.

Karamperidou, Anastasia. 2008. “Parametric Analysis of Quay Walls with Relieving Platform, by Means of Elastic Supported Beam and Finite Element Method,” 220.

Kersting, Ana Paula Baungarten. 2006. “Quality Assurance of Multi-Sensor Systems.” *University of Calgary*. PhD Thesis, UNIVERISTY OF CALGARY.

Kishi, N., A. Asada, K. Abukawa, and K. Fujisawa. 2015. “Inspection Methods for Underwater Structures of Ports and Harbors.” *2015 IEEE Underwater Technology, UT 2015*. IEEE. doi:10.1109/UT.2015.7108265.

Li, Dong, Huadong Guo, Cheng Wang, Pinliang Dong, and Zhengli Zuo. 2016. “Improved Bore-Sight Calibration for Airborne Light Detection and Ranging Using Planar Patches.” *Journal of Applied Remote Sensing* 10 (2): 024001. doi:10.1117/1.jrs.10.024001.

Lu, Xiushan, Chengkai Feng, Yue Ma, Fanlin Yang, Bo Shi, and Dianpeng Su. 2019. “Calibration Method of Rotation and Displacement Systematic Errors for Ship-Borne Mobile Surveying Systems.” *Survey Review* 51 (364). Taylor & Francis: 78–86. doi:10.1080/00396265.2017.1362731.

Maas, Hans Gerd. 2002. “Methods for Measuring Height and Planimetry Discrepancies in Airborne Laserscanner Data.” *Photogrammetric Engineering and Remote Sensing* 68 (9): 933–940.

Moisan, Emmanuel, Pierre Charbonnier, Philippe Foucher, Pierre Grussenmeyer, Samuel Guillemin, and Mathieu Koehl. 2015. “Adjustment of Sonar and Laser Acquisition Data for Building the 3D Reference Model of a Canal Tunnel.” *Sensors (Switzerland)* 15 (12): 31180–31204. doi:10.3390/s151229855.

Ravi, Radhika, Tamer Shamseldin, Magdy Elbahnasawy, Yun Jou Lin, and Ayman Habib. 2018. “Bias Impact Analysis and Calibration of UAV-Based Mobile LiDAR System with Spinning Multi-Beam Laser Scanner.” *Applied Sciences (Switzerland)* 8 (2). doi:10.3390/app8020297.

Rondeau, Mathieu, and Frédéric Pelletier. 2013. “Using Integrated Technology to Inspect Quay Walls.” In *Port Technology International*, 1–2.

Ruggeri, Paolo, Viviene Marianne Esther Fruzzetti, and Giuseppe Scarpelli. 2021.

"Upgrading of Quay Walls at the Ravenna Port, Italy: Evaluation of the Steel Piles Degradation after a Long Working Life." *Structure and Infrastructure Engineering* 17 (2). Taylor & Francis: 249–259. doi:10.1080/15732479.2020.1736101.

Rusu, Radu Bogdan, Steve Cousins, and Willow Garage. 2011. "3D Is Here: Point Cloud Library (PCL)." *IEEE International Conference on Robotics and Automation (ICRA)*.

Shahraji, Mohsen H., Christian Larouche, and Marc Cocard. 2020. "ANALYSIS OF SYSTEMATIC ERRORS OF MOBILE LiDAR SYSTEMS: A SIMULATION APPROACH." *ISPRS Annals of Photogrammetry, Remote Sensing and Spatial Information Sciences* V-1–2020 (August): 253–260. doi:10.5194/isprs-annals-V-1-2020-253-2020.

Shi, Bo, Xiushan Lu, Fanlin Yang, Chuanyin Zhang, Yanquan Lv, and Min Cheng. 2017. "Shipborne Over- and Under-Water Integrated Mobile Mapping System and Its Seamless Integration of Point Clouds." *Marine Geodesy* 40 (2–3). Taylor & Francis: 104–122. doi:10.1080/01490419.2016.1272510.

Skaloud, Jan, and Derek Lichti. 2006. "Rigorous Approach to Bore-Sight Self-Calibration in Airborne Laser Scanning." *ISPRS Journal of Photogrammetry and Remote Sensing* 61 (1): 47–59. doi:10.1016/j.isprsjprs.2006.07.003.

Thies, Thomas. 2011. "A Vessel-Based Mobile Mapping System – From Sensor Integration to Multipurpose Products." HafenCity University Hamburg. http://www.riegl.com/uploads/tx_pxpriegldownloads/Thies_Thomas__2011_-_A_Vessel-Based_Mobile_Mapping_System__Master_Thesis__HafenCity_University_Hamburg__Germany_part1.pdf.

Wehr, Aloysius, and Uwe Lohr. 1999. "Airborne Laser Scanning - An Introduction and Overview." *ISPRS Journal of Photogrammetry and Remote Sensing* 54 (2–3): 68–82. doi:10.1016/S0924-2716(99)00011-8.

Conclusion

This chapter concludes the study carried out throughout this Ph.D. research by presenting a summary of the methodology and the essential contributions. It will also discuss the study's limitations and suggest recommendations for future works.

As mentioned earlier, a mobile LiDAR system (MLS) is a state-of-the-art 3D geospatial data acquisition system that has the potential to generate a very dense and accurate 3D point cloud of real-world scenes. MLS mainly comprises a LiDAR scanner and a positioning and orientation system (POS). To achieve an accurate point cloud, we must appropriately address all the MLS sources of error. One of the main MLS errors is a systematic error due to the rotational misalignment between the POS device and the LiDAR scanner, also known as boresight error, which can cause significant geometrical uncertainties on the final point cloud. Therefore, this is the focus of this thesis. The existing methods usually utilize the input of suitable in-situ tie-features, such as tie-point, tie-line, and tie-plane. The problem occurs in low-feature environments like rural areas, forests, ports, and harbors, where the accessibility of adequate *in-situ* features is limited. Therefore, this study aimed to develop a novel data acquisition and processing methodology to serve as input for the boresight alignment of an MLS in low-feature environments. Ultimately, this input will resolve the boresight misalignment and prepare the point cloud for high-accuracy survey-grade infrastructure inspection applications in port and harbors environments. This research suggests the following procedure to achieve this objective.

First, a comprehensive study of the existing methods that address mainly the reduction of MLS error is done. This comprehensive literature review proposes a specific categorization for the MLS systematic error reduction methods. For the selection of the MLS systematic error reduction method, a specific condition of the context of this research must be considered, which is the maritime environment. The in-situ infrastructure of a maritime environment is exposed to extreme conditions, such as humidity and salty waters, that can damage them drastically. This

phenomenon complicates the accessibility to suitable in-situ tie-features in ports and harbors. Therefore, for selecting the MLS error reduction method and the suitable tie-feature, the special condition of a low-feature maritime environment must be considered. Based on the literature review, a rigorous method using tie-planes is suggested for the boresight alignment of the marine MLS. Due to the difficulty of finding suitable in-situ tie-planes in a maritime environment, this thesis suggests the insertion of prefabricated tie-planes in the maritime environment that would eventually be used as input for the boresight alignment of the marine MLS.

Meanwhile, the utilization of prefabricated tie-planes has limitations. For example, these tie-planes could not be used in any number and dimensions. Therefore, a simulation environment is designed, and different tie-plane configurations are tested to ultimately arrive at the best result with a proper setup. A configuration of tie-planes is a combination of their numbers, their inclinations to the MLS platform, their dimensions, and the orientation of the MLS passages with respect to these tie-planes. For the analysis of different configurations, two types of criteria, ***Type I*** (planarity, linearity, and centroidal distance) and ***Type II*** (angular deviation and signed orthogonal distance), based on geometric characteristics of the point clouds, were introduced to identify the visibility of each error. Based on these analyses, the best configuration, which consists of a minimum of two prefabricated planar targets (one vertical and one inclined) and a six-fold line pattern passage, is suggested to augment the visibility of the boresight errors. The design of the simulation and the analysis performed on the simulated data were the subject of a peer-reviewed paper published in the ISPRS Annals of the Photogrammetry, Remote Sensing and Spatial Information Sciences, Volume V-1-2020, 2020 XXIV ISPRS Congress (2020 edition), named, "**Analysis of Systematic Errors of Mobile LiDAR Systems: A Simulation Approach**."

The proposed design was implemented in a real-world environment to evaluate the above configuration for the calibration site. The results demonstrated the robustness, accuracy, and repeatability of the proposed site configuration for acquiring data necessary for the boresight alignment estimation of a marine MLS in

port and harbor environments. This work was published as a peer-reviewed paper in the Marine Geodesy journal (the online publication date is January 11th, 2022). The paper's title is "**Case Study: Rigorous Boresight Alignment of a Marine Mobile LiDAR System Addressing the Specific Demands of Port Infrastructure Monitoring**."

Moreover, based on the proposed site configuration method, the installation of the targets and the scans take less than one hour to complete, and the overall time for post-processing and boresight angle estimation is between one to two hours. Although the proposed data acquisition and processing procedure are designed for tie-planes, they are adaptable to other tie-features such as spheres. Also, this method can be used in other low-feature and challenging environments like forests and rural areas.

With the help of the software development team of the project partner, CIDCO, we developed a boresight alignment software that covers all workflow steps, from acquiring calibration data to extracting prefabricated planar targets and, finally, the estimation of boresight alignment parameters. Portions of the developed software, with Matlab® source codes excerpt, are presented in Appendix B. Today, this workflow is part of the standard procedure of CIDCO for estimating the boresight angles of its marine MLS.

In summary, the contributions of this thesis are as follows,

Contribution #1: Selection of the suitable tie-feature is the context of this research's low-feature maritime environment, based on a comprehensive review of the existing MLS systematic errors reduction method.

Contribution #2: Conceptualization and design of a point cloud generator (simulator), along with two types, ***Type I*** and ***Type II,*** of MLS systematic errors visibility criteria. The simulated data is utilized to investigate different configurations of the suitable tie-feature and introduce the configuration which generates the higher visibility of the systematic errors.

Contribution #3: The development of a complete workflow for the boresight error estimation that extracts suitable tie-features as input, estimates the boresight angles of the MLS, and eventually validates the quality of the resulting point clouds. The development of this workflow is primordial for evaluating the simulated and real datasets.

In this research, we also encountered some limitations,

- First, we primarily focused on the boresight alignment issue of an MLS to improve the accuracy of the final 3D point cloud. Although the boresight angle uncertainties play an essential role in the MLS data quality, other systematic errors, random errors (i.e., sensor noises), and blunders also affect the data quality. Therefore, it is essential to consider them in the data accuracy improvement procedure.

- Second, we designed and developed a point cloud generator, also known as a simulator, based on the direct georeferencing model of the MLS. We have made some assumptions to simplify the environment that might not correspond to the real-life criteria. For example, the POS's roll and pitch attitude angles were considered zero or we assumed that the positional data is errorless, which is not the case in real-world scenarios. It is preferable not to consider these assumptions to generate simulated data reflecting real-world scenarios.

- Third, this thesis's accuracy assessment and evaluation procedures are based on a relative comparison of 3D point cloud datasets before and after boresight alignment. It is preferable to implement an absolute accuracy assessment that compares the generated 3D point cloud datasets with exterior reference data to give a more comprehensive assessment of the generated 3D point cloud with the marine MLS.

- Fourth, this thesis's proposed boresight alignment methodology is designed for a maritime context of port infrastructure inspection. We cannot necessarily

generalize the same configurations and methodology to other environments like terrestrial or aerial contexts. For that, a case study based on the specific conditions of each environment would be adequate.

In the following, we will address some suggestions for future works. In this research, we tackled the boresight alignment issue in a marine MLS, a necessary step that improves the accuracy of the generated 3D point cloud. Although the proposed boresight alignment method significantly mitigates the effect of the systematic boresight errors and enhances the accuracy of the data, we witness that the quality of the 3D point cloud in some areas and some situations vary and do not entirely satisfy the expectations. This issue is mainly due to problems related to the loss of GNSS signals that impact the accuracy of the positioning data and, as a result, the accuracy of the final point cloud. The positioning issues can happen near big boats, quay walls, or under bridges. Therefore, one of the recommendations for future works is to address the issue in the GNSS-denied environment with particular attention to port and harbor areas to improve the POS trajectory data and eventually augment the 3D point cloud accuracy.

Furthermore, the 3D geospatial acquisition system comprises a LiDAR scanner and a SONAR sensor in the port infrastructure monitoring application. It is crucial to properly align data acquired from over the water surface with the LiDAR and data acquired from under the water surface with the SONAR. Thus, registering LiDAR and SONAR data is an important issue to address.

In summary, this study broadened the utility of a marine MLS for challenging and low-feature environments that lack a variety of suitable tie-features. These tie-features are used to mitigate the system's error and augment the accuracy of the generated point cloud, which is required for applications that demand the production of high-accuracy 3D point clouds, such as infrastructure monitoring. In this thesis, we developed a novel data acquisition and processing methodology serving as the relevant input data for an accurate boresight alignment procedure that ultimately leads to a high-accuracy point cloud.

Bibliography

Ackermann, F. 1999. “Airborne Laser Scanning - Present Status and Future Expectations.” *ISPRS Journal of Photogrammetry and Remote Sensing* 54 (2–3): 64–67. doi:10.1016/S0924-2716(99)00009-X.

Ahmad Fuad, N., A. R. Yusoff, Z. Ismail, and Z. Majid. 2018. “Comparing the Performance of Point Cloud Registration Methods for Landslide Monitoring Using Mobile Laser Scanning Data.” *International Archives of the Photogrammetry, Remote Sensing and Spatial Information Sciences - ISPRS Archives* 42 (4/W9): 11–21. doi:10.5194/isprs-archives-XLII-4-W9-11-2018.

Alho, Petteri, A. Kukko, H. Hyyppä, H. Kaartinen, J. Hyyppä, and A. Jaakkola. 2009. “Application of Boat-Based Laser Scanning for River Survey.” *Earth Surface Processes and Landforms* 34 (March): 613–628. doi:10.1002/esp.

Alho, Petteri, Matti Vaaja, Antero Kukko, Elina Kasvi, Matti Kurkela, Juha Hyyppä, Hannu Hyyppä, and Harri Kaartinen. 2011. “Mobile Laser Scanning in Fluvial Geomorphology: Mapping and Change Detection of Point Bars.” *Zeitschrift Fur Geomorphologie* 55 (September 2014): 31–50. doi:10.1127/0372-8854/2011/0055S2-0044.

Allianz Global Corporate & Specialty. 2016. “ARC Marine – Marine Port Structure Guidance,” no. January 2016: 12. http://www.agcs.allianz.com/assets/PDFs/ARC/Risk Bulletins/Marine Port Structure Guidance.pdf.

Angrisano, Antonio. 2010. “GNSS/INS Integration Methods.” *Dottorato Di Ricerca (PhD) in Scienze Geodetiche e Topografiche Thesis*. Universita’degli Studi di Napoli PARTHENOPE, Naple, Italy.

Applanix. 2021. “Fugro Pelagose.” https://www.applanix.com/news/posmv-hydrographic-survey-fugro/.

Bang, Ki In, Ana Paula Kersting, Ayman Habib, and Dong Cheon Lee. 2009. “LiDAR System Calibration Using Point Cloud Coordinates in Overlapping Strips.” *American Society for Photogrammetry and Remote Sensing Annual Conference 2009, ASPRS 2009* 1: 79–90.

Bauwens, Sébastien, Harm Bartholomeus, Kim Calders, and Philippe Lejeune. 2016. “Forest Inventory with Terrestrial LiDAR: A Comparison of Static and Hand-Held Mobile Laser Scanning.” *Forests* 7 (6). doi:10.3390/f7060127.

Blomley, R., B. Jutzi, and M. Weinmann. 2016. “Classification of Airborne Laser Scanning Data Using Geometric Multi-Scale Features and Different Neighbourhood Types.” *ISPRS Annals of Photogrammetry, Remote Sensing and Spatial Information Sciences* III–3 (June): 169–176. doi:10.5194/isprsannals-iii-3-169-2016.

Böder, Volker, Thomas P. Kerstenl, Thomas Thies, and Arne Sauer. 2011. “Mobile Laser Scanning on Board Hydrographic Survey Vessels - Applications and Accuracy Investigations -.” *Hydrography in Practice, 4927*, no. May 2011: 18–22. http://www.fig.net/pub/fig2011/papers/ts05j/ts05j_boeder_kersten_et_al_4927.pdf.

Böse, Jürgen W. 2011. *Handbook of Terminal Planning*. *Operations Research/ Computer Science Interfaces Series*. Vol. 49. doi:10.1007/978-1-4419-8408-1.

Brahim, N., S. Daniel, and D. Guériot. 2008. “Potential of Underwater Sonar Systems for Port Infrastructure Inspection.” *Oceans 2008*. doi:10.1109/OCEANS.2008.5151866.

Brown, Scott D., Daniel D. Blevins, and John R. Schott. 2005. “Time-Gated Topographic LIDAR Scene Simulation.” *Laser Radar Technology and Applications X* 5791: 342. doi:10.1117/12.604326.

Brunner, Fritz K. 2007. “On the Methodology of Engineering Geodesy.” *Journal of Applied*

Geodesy 1 (2). doi:10.1515/jag.2007.008.
Burman, Helén. 2000. “Adjustment of Laserscanner Data for Correction of Orientation Errors.” *International Archives of Photogrammetry and Remote Sensing* XXXIII (17 2): 125–132.
Cai, Guowei, Ben Chen, and Tong Lee. 2011. *Unmanned Rotorcraft Systems*. doi:10.1007/978-0-85729-635-1.
Cassol, Willian Ney. 2018. “Définition d’un Modèle d’incertitude-Type Composée Pour Les Systèmes LiDAR Mobiles.” Master Thesis, Laval University.
Chan, Ting On, Derek Lichti, and Craig Glennie. 2013. “Multi-Feature Based Boresight Self-Calibration of a Terrestrial Mobile Mapping System.” *ISPRS Journal of Photogrammetry and Remote Sensing* 82. International Society for Photogrammetry and Remote Sensing, Inc. (ISPRS): 112–124. doi:10.1016/j.isprsjprs.2013.04.005.
Chen, Zequan, Jianping Li, and Bisheng Yang. 2021. “A Strip Adjustment Method of Uav-Borne Lidar Point Cloud Based on Dem Features for Mountainous Area.” *Sensors* 21 (8): 1–20. doi:10.3390/s21082782.
Chen, Ziyue, Bingbo Gao, and Bernard Devereux. 2017. “State-of-the-Art: DTM Generation Using Airborne LIDAR Data.” *Sensors (Switzerland)* 17 (1). doi:10.3390/s17010150.
Cifuentes, Renato, Dimitry Van der Zande, Christian Salas-Eljatib, Jamshid Farifteh, and Pol Coppin. 2018. “A Simulation Study Using Terrestrial LiDAR Point Cloud Data to Quantify Spectral Variability of a Broad-Leaved Forest Canopy.” *Sensors (Switzerland)*. doi:10.3390/s18103357.
Cocard, Marc. 2017. *Compensation (Notes de Cours GMT2001)*.
Costantino, Domenica, and Maria Giuseppa Angelini. 2013. “Production of DTM Quality by TLS Data.” *European Journal of Remote Sensing* 46 (1): 80–103. doi:10.5721/EuJRS20134606.
Crombaghs, M.J.E, R. Brugelmann, and E.J. de Min. 2000. “On the Adjustment of Overlapping Strips of Laser Altimeter Height Data.” *International Archives of Photogrammetry and Remote Sensing* 1 (17 2): 230–237.
Crombaghs, Marc, Sander Oude Elberink, R Brugelmann, and Erik De Min. 2002. “Assessing Height Precision of Laser Altimetry DEMs.” *INTERNATIONAL ARCHIVES OF PHOTOGRAMMETRY REMOTE SENSING AND SPATIAL INFORMATION SCIENCES* 34 (3/A). NATURAL RESOURCES CANADA: 85–90.
Csanyi, Nora, Charles Toth, Dorota Grejner-Brzezinska, and John Ray. 2005. “Improvement of LiDAR Data Accuracy Using LiDAR Specific Ground Targets.” *American Society for Photogrammetry and Remote Sensing - Annual Conference 2005 - Geospatial Goes Global: From Your Neighborhood to the Whole Planet* 1 (4): 152–162.
De Blasiis, Maria Rosaria, Alessandro Di Benedetto, and Margherita Fiani. 2020. “Mobile Laser Scanning Data for the Evaluation of Pavement Surface Distress.” *Remote Sensing* 12 (6). doi:10.3390/rs12060942.
De Gijt, J.G. 2010. “A History of Quay Walls Techniques, Types, Costs and Future.” Netherlands: TUDelft. https://repository.tudelft.nl/islandora/object/uuid:d62bbff8-e805-434a-893e-08940d58ae8c?collection=research.
Dix, Michael, Amr Abd-Elrahman, Bon Dewitt, and Lou Nash. 2012. “Accuracy Evaluation of Terrestrial LIDAR and Multibeam Sonar Systems Mounted on a Survey Vessel.” *Journal of Surveying Engineering* 138 (4): 203–213. doi:10.1061/(asce)su.1943-5428.0000075.
Farrell, Jay. 2008. *Aided Navigation: GPS with High Rate Sensors*. 1st ed. USA: McGraw-Hill, Inc.
Fekry, Reda, Wei Yao, Lin Cao, and Xin Shen. 2021. “Marker-Less UAV-LiDAR Strip

Alignment in Plantation Forests Based on Topological Persistence Analysis of Clustered Canopy Cover." *ISPRS International Journal of Geo-Information* 10 (5). doi:10.3390/ijgi10050284.
Filin, Sagi. 2003. "Recovery of Systematic Biases in Laser Altimetry Data Using Natural Surfaces." *Photogrammetric Engineering and Remote Sensing* 69 (11): 1235–1242. doi:10.14358/PERS.69.11.1235.
Filin, Sagi, and George Vosselman. 2004. "Adjustment of Airborne Laser Altimetry Strips." In *International Archives of Photogrammetry, Remote Sensing and Spatial Information Sciences 34 (Part B3)*, 285–289.
Firoozi, Ali Akbar, Mohd Raihan Taha, S. M. Mir Moammad Hosseini, and Ali Asghar Firoozi. 2014. "Examination of the Behavior of Gravity Quay Wall against Liquefaction under the Effect of Wall Width and Soil Improvement." *Scientific World Journal* 2014 (July). Hindawi Publishing Corporation. doi:10.1155/2014/325759.
Fischler, Martin A., and Robert C. Bolles. 1981. "Random Sample Consensus: A Paradigm for Model Fitting with Applications to Image Analysis and Automated Cartography." *Communications of the ACM* 24 (6): 381–395. doi:10.1145/358669.358692.
Friess, Peter. 2006. "Toward a Rigorous Methodology for Airborne Laser Mapping." *Proceedings EuroCOW*, 25–27.
Gao, Yunlong, Xianfeng Huang, Fan Zhang, Zhengwen Fu, and Chong Yang. 2015. "Automatic Geo-Referencing Mobile Laser Scanning Data to UAV Images." *International Archives of the Photogrammetry, Remote Sensing and Spatial Information Sciences - ISPRS Archives* 40 (1W4): 41–46. doi:10.5194/isprsarchives-XL-1-W4-41-2015.
Ghilani, Charles D. 2010. *Adjustment Computations Spatial Data Analysis*. Fifth. Wiley.
Girardeau-Montaut, Daniel. 2021. *Cloud Compare. 3D Point Cloud and Mesh Processing Software-Open Source Project*. http://www.cloudcompare.org/.
Glennie, Craig. 2008. "Rigorous 3D Error Analysis of Kinematic Scanning LIDAR Systems." *Journal of Applied Geodesy* 1 (3): 147–157. doi:10.1515/jag.2007.017.
Glennie, Craig. 2012. "Calibration and Kinematic Analysis of the Velodyne HDL-64E S2 Lidar Sensor." *Photogrammetric Engineering and Remote Sensing* 78 (4): 339–347. doi:10.14358/PERS.78.4.339.
Glennie, Craig, A. Kusari, and A. Facchin. 2016. "Calibration and Stability Analysis of the VLP-16 Laser Scanner." *International Archives of the Photogrammetry, Remote Sensing and Spatial Information Sciences - ISPRS Archives* 40 (3W4): 55–60. doi:10.5194/isprsarchives-XL-3-W4-55-2016.
Glennie, Craig, and Derek Lichti. 2010. "Static Calibration and Analysis of the Velodyne HDL-64E S2 for High Accuracy Mobile Scanning." *Remote Sensing* 2 (6): 1610–1624. doi:10.3390/rs2061610.
Glira, P., N. Pfeifer, C. Briese, and C. Ressl. 2015. "Rigorous Strip Adjustment of Airborne Laserscanning Data Based on the Icp Algorithm." *ISPRS Annals of the Photogrammetry, Remote Sensing and Spatial Information Sciences* 2 (3W5): 73–80. doi:10.5194/isprsannals-II-3-W5-73-2015.
Gonsalves, Michael Oliver. 2010. "A Comprehensive Uncertainty Analysis and Method of Geometric Calibration for a Circular Scanning Airborne Lidar." *ProQuest Dissertations and Theses*. The University of Southern Mississippi. http://search.proquest.com/docview/835075165/fulltextPDF/BB0E363A81F246C3PQ/1?accountid=10267.
Gross, H., B. Jutzi, and U. Thoennessen. 2007. "Segmentation of Tree Regions Using Data of a Full-Waveform Laser." *PIA 2007 - Photogrammetric Image Analysis, Proceedings*, no. March: 57–62.
Groves, Paul. 2013. *Principles of GNSS, Inertial, and Multisensor Integrated Navigation*

Systems. *GNSS Technology and Application Series*. 2nd editio. Boston ; SE - 1 vol. (xix-776 p.) : ill. ; 26 cm + 1 DVD-ROM.: Artech House. https://ieeexplore.ieee.org/document/9101092.

Guan, Haiyan, Jonathan Li, Shuang Cao, and Yongtao Yu. 2016. "Use of Mobile LiDAR in Road Information Inventory: A Review." *International Journal of Image and Data Fusion* 7 (3): 219–242. doi:10.1080/19479832.2016.1188860.

Guo, Ming, Bingnan Yan, Tengfei Zhou, Deng Pan, and Guoli Wang. 2021. "Accurate Calibration of a Self-Developed Vehicle-Borne LiDAR Scanning System." *Journal of Sensors* 2021. doi:10.1155/2021/8816063.

Hartmann, J., I. Von Gösseln, N. Schild, A. Dorndorf, J. A. Paffenholz, and I. Neumann. 2019. "Optimisation of the Calibration Process of a K-Tls Based Multi-Sensor-System by Genetic Algorithms." *International Archives of the Photogrammetry, Remote Sensing and Spatial Information Sciences - ISPRS Archives* 42 (2/W13): 1655–1662. doi:10.5194/isprs-archives-XLII-2-W13-1655-2019.

Hebel, Marcus, and Uwe Stilla. 2012. "Simultaneous Calibration of ALS Systems and Alignment of Multiview LiDAR Scans of Urban Areas." *IEEE Transactions on Geoscience and Remote Sensing* 50 (6): 2364–2379. doi:10.1109/TGRS.2011.2171974.

Heinz, Erik, Christian Eling, Lasse Klingbeil, and Heiner Kuhlmann. 2019. "Monitoring the Planarity and Subsidence of a Motorway Using Kinematic Laser Scanning." *Proceedings of the 4th Joint International Symposium on Deformation Monitoring (JISDM), Athhens, Greece*, no. May: 8.

Heinz, Erik, Christian Eling, Markus Wieland, Lasse Klingbeil, and Heiner Kuhlmann. 2015. "Development, Calibration and Evaluation of a Portable and Direct Georeferenced Laser Scanning System for Kinematic 3D Mapping." *Journal of Applied Geodesy* 9 (4): 227–243. doi:10.1515/jag-2015-0011.

Heinz, Erik, Christian Eling, Markus Wieland, Lasse Klingbeil, and Heiner Kuhlmann. 2017. "Analysis of Different Reference Plane Setups for the Calibration of a Mobile Laser Scanning System." *Ingenieurvermessung*, no. July: 131–146.

Heinz, Erik, Christoph Holst, Heiner Kuhlmann, and Lasse Klingbeil. 2020. "Design and Evaluation of a Permanently Installed Plane-Based Calibration Field for Mobile Laser Scanning Systems." *Remote Sensing* 12 (3). doi:10.3390/rs12030555.

Heinz, Erik, Markus Mettenleiter, Heiner Kuhlmann, and Christoph Holst. 2018. "Strategy for Determining the Stochastic Distance Characteristics of the 2d Laser Scanner z + f Profiler 9012a with Special Focus on the Close Range." *Sensors (Switzerland)* 18 (7). doi:10.3390/s18072253.

Hong, Seunghwan, Ilsuk Park, Jisang Lee, Kwangyong Lim, Yoonjo Choi, and Hong Gyoo Sohn. 2017. "Utilization of a Terrestrial Laser Scanner for the Calibration of Mobile Mapping Systems." *Sensors (Switzerland)* 17 (3). doi:10.3390/s17030474.

Huang, Xianfeng, Armin Gruen, Rongjun Qin, Tangwu Du, and Wei Fang. 2013. "Integration of Mobile Laser Scanning Data with UAV Imagery for Very High Resolution 3D City Modeling." *The International Symposium on Mobile Mapping Technology 2013*, no. May.

Hussnain, Zille, Sander Oude Elberink, and George Vosselman. 2018. "An Automatic Procedure for Mobile Laser Scanning Platform 6Dof Trajectory Adjustment." *International Archives of the Photogrammetry, Remote Sensing and Spatial Information Sciences - ISPRS Archives* 42 (1): 203–209. doi:10.5194/isprs-archives-XLII-1-203-2018.

Hussnain, Zille, Sander Oude Elberink, and George Vosselman. 2019. "Automatic Extraction of Accurate 3D Tie Points for Trajectory Adjustment of Mobile Laser Scanners Using Aerial Imagery." *ISPRS Journal of Photogrammetry and Remote*

Sensing 154 (May). Elsevier: 41–58. doi:10.1016/j.isprsjprs.2019.05.010.
Hussnain, Zille, Sander Oude Elberink, and George Vosselman. 2021. “Enhanced Trajectory Estimation of Mobile Laser Scanners Using Aerial Images.” *ISPRS Journal of Photogrammetry and Remote Sensing* 173 (January). Elsevier B.V.: 66–78. doi:10.1016/j.isprsjprs.2021.01.005.
Hyyppä, Eric, Xiaowei Yu, Harri Kaartinen, Teemu Hakala, Antero Kukko, Mikko Vastaranta, and Juha Hyyppä. 2020. “Comparison of Backpack, Handheld, under-Canopy UAV, and above-Canopy UAV Laser Scanning for Field Reference Data Collection in Boreal Forests.” *Remote Sensing* 12 (20): 1–31. doi:10.3390/rs12203327.
IXblue. 2019. *Hydrins INS Specifications*. www.ixblue.com.
IXblue Software Manual. 2017. *Advanced Post-Processing Software*. www.ixblue.com.
Jekeli, Christopher. 2012. *Inertial Navigation Systems with Geodetic Applications:* . De Gruyter. doi:doi:10.1515/9783110800234.
Kager, H. 2004. “Discrepancies between Overlapping Laser Scanner Strips--Simultaneous Fitting of Aerial Laser Scanner Strips.” *International Archives of Photogrammetry, Remote Sensing and Spatial Information Sciences* 35 (B1): 555–560.
Kalenjuk, Slaven, and Werner Lienhart. 2022. “A Method for Efficient Quality Control and Enhancement of Mobile Laser Scanning Data.” *Remote Sensing* 14 (4): 857. doi:https://doi.org/10.3390/ rs14040857.
Kalman, Rudolph Emil. 1960. “A New Approach to Linear Filtering and Prediction Problems.” *Transaction of the ASME-Journal of Basic Engineering* 82 (Series D): 35–45.
Kalyan, T. Sri, Puyan A. Zadeh, Sheryl Staub-French, and Thomas M. Froese. 2016. “Construction Quality Assessment Using 3D As-Built Models Generated with Project Tango.” *Procedia Engineering* 145. Elsevier B.V.: 1416–1423. doi:10.1016/j.proeng.2016.04.178.
Karamperidou, Anastasia. 2008. “Parametric Analysis of Quay Walls with Relieving Platform, by Means of Elastic Supported Beam and Finite Element Method,” 220.
Kersting, Ana Paula Baungarten. 2006. “Quality Assurance of Multi-Sensor Systems.” *University of Calgary*. PhD Thesis, UNIVERISTY OF CALGARY.
Keyetieu, Rabine, and Nicolas Seube. 2019. “Automatic Data Selection and Boresight Adjustment of LiDAR Systems.” *Remote Sensing* 11 (9): 1–18. doi:10.3390/rs11091087.
Keyetieu, Rabine, Nicolas Seube, Vignyl Djine, Gael Roue, Benoit Clement, and Pierre Bosser. 2018. “Multi-Beam Echo Sounders–INS Automatic Latency Calibration.” *Marine Geodesy* 41 (5). Taylor & Francis: 477–493. doi:10.1080/01490419.2018.1478349.
Kim, Seongjoon, Seonghong Min, Geunhan Kim, Impyeong Lee, and Chulmin Jun. 2009. “Data Simulation of an Airborne Lidar System.” *Laser Radar Technology and Applications XIV* 7323 (May 2009): 73230C. doi:10.1117/12.818545.
Kishi, N., A. Asada, K. Abukawa, and K. Fujisawa. 2015. “Inspection Methods for Underwater Structures of Ports and Harbors.” *2015 IEEE Underwater Technology, UT 2015*. IEEE. doi:10.1109/UT.2015.7108265.
Kraus, K., and N. Pfeifer. 2001. “Advanced Dtm Generation From Lidar Data.” *International Archives of Photogrammetry and Remote Sensing* XXXIV: 22–24.
Kukko, Antero, Juha Hyyppä, Commission Vi, and W G Vi. 2007. “Laser Scanner Simulator for System Analysis and Algorithm Development : A Case With Forest Measurements.” *ISPRS Workshop on Laser Scanning 2007 and SilviLaser 2007*, no. May: 234–240. http://www.isprs.org/proceedings/XXXVI/3-W52/final_papers/Kukko_2007a.pdf.

Kukko, Antero, Harri Kaartinen, Juha Hyyppä, and Yuwei Chen. 2012. “Multiplatform Mobile Laser Scanning: Usability and Performance.” *Sensors (Switzerland)* 12 (9): 11712–11733. doi:10.3390/s120911712.

Landry, Michaël. 2017. “Développement d’une Nouvelle Méthode de Calibrage Des Systèmes LiDAR Mobiles (SLM) En Laboratoire.” Master Thesis, Laval University.

Le Scouarnec, R., T. Touzé, J. B. Lacambre, and N. Seube. 2014. “A New Reliable Boresight Calibration Method for Mobile Laser Scanning Applications.” *International Archives of the Photogrammetry, Remote Sensing and Spatial Information Sciences - ISPRS Archives* 40 (3W1): 67–72. doi:10.5194/isprsarchives-XL-3-W1-67-2014.

Lee, Jaebin, Kiyun Yu, Yongil Kim, and Ayman F. Habib. 2007. “Adjustment of Discrepancies between LIDAR Data Strips Using Linear Features.” *IEEE Geoscience and Remote Sensing Letters* 4 (3): 475–479. doi:10.1109/LGRS.2007.898079.

Lefevre, Herve, Adrien Steib, Alain Claire, Alex Sekeriyan, André Couderette, Anne-Laure Pointel, Annie Viltard, et al. 2020. “The Fiber Optic Gyro ‘adventure’ at Photonetics, IXsea and Now IXblue.” *Proc. SPIE 11405, Optical Waveguide and Laser Sensors* 1140505 (May 2020): 5. doi:10.1117/12.2560791.

Leslar, Michael, Baoxin Hu, and Jianguo Wang. 2014. “Error Analysis of a Mobile Terrestrial LiDAR System.” *GEOMATICA* 68 (September): 183–194. doi:10.5623/cig2014-303.

Leslar, Michael, Jianguo Wang, and Baoxin Hu. 2016. “Boresight and Lever Arm Calibration of a Mobile Terrestrial LiDAR System.” *Geomatica* 70 (2): 97–112. doi:10.5623/cig2016-202.

Li, Dong, Huadong Guo, Cheng Wang, Pinliang Dong, and Zhengli Zuo. 2016. “Improved Bore-Sight Calibration for Airborne Light Detection and Ranging Using Planar Patches.” *Journal of Applied Remote Sensing* 10 (2): 024001. doi:10.1117/1.jrs.10.024001.

Li, Zhen, Junxiang Tan, and Hua Liu. 2019. “Rigorous Boresight Self-Calibration of Mobile and UAV LiDAR Scanning Systems by Strip Adjustment.” *Remote Sensing* 11 (4): 1–16. doi:10.3390/rs11040442.

Lindenthal, S M, V R Ussyshkin, J G Wang, and M Pokorny. 2011. “Airborne LIDAR: A Fully-Automated Self-Calibration Procedure.” *International Archives of the Photogrammetry, Remote Sensing and Spatial Information Sciences* 38. Citeseer: 5.

Liu, Ke, Hongchao Ma, Liang Zhang, Zhan Cai, and Haichi Ma. 2019. “Strip Adjustment of Airborne LiDAR Data in Urban Scenes Using Planar Features by the Minimum Hausdorff Distance.” *Sensors (Switzerland)* 19 (23). doi:10.3390/s19235131.

Liu, Wanli. 2017. “Lidar-Imu Time Delay Calibration Based on Iterative Closest Point and Iterated Sigma Point Kalman Filter.” *Sensors (Switzerland)* 17 (3): 1–19. doi:10.3390/s17030539.

Lohani, Bharat, Parameshwar Reddy, and Rakesh Kumar Mishra. 2006. “Airborne Altimetric Lidar Simulator: An Education Tool.” *International Archives of the Photogrammetry, Remote Sensing and Spatial Information Science* XXXVI: 179–183.

Lu, Xiushan, Chengkai Feng, Yue Ma, Fanlin Yang, Bo Shi, and Dianpeng Su. 2019. “Calibration Method of Rotation and Displacement Systematic Errors for Ship-Borne Mobile Surveying Systems.” *Survey Review* 51 (364). Taylor & Francis: 78–86. doi:10.1080/00396265.2017.1362731.

Maas, Hans Gerd. 2002. “Methods for Measuring Height and Planimetry Discrepancies in Airborne Laserscanner Data.” *Photogrammetric Engineering and Remote Sensing* 68 (9): 933–940.

Moisan, Emmanuel, Pierre Charbonnier, Philippe Foucher, Pierre Grussenmeyer, Samuel Guillemin, and Mathieu Koehl. 2015. “Adjustment of Sonar and Laser Acquisition Data for Building the 3D Reference Model of a Canal Tunnel.” *Sensors (Switzerland)*

15 (12): 31180–31204. doi:10.3390/s151229855.
Mokroš, Martin, Tomáš Mikita, Arunima Singh, Julián Tomaštík, Juliána Chudá, Piotr Wężyk, Karel Kuželka, et al. 2021. “Novel Low-Cost Mobile Mapping Systems for Forest Inventories as Terrestrial Laser Scanning Alternatives.” *International Journal of Applied Earth Observation and Geoinformation* 104. doi:10.1016/j.jag.2021.102512.
Morin, Kris, and N El-Sheimy. 2002. “Post-Mission Adjustment Methods of Airborne Laser Scanning Data.” *FIG XXII International Congress, Washington, DC USA*, 1–12.
Munim, Ziaul Haque, and Hans-Joachim Schramm. 2018. “The Impacts of Port Infrastructure and Logistics Performance on Economic Growth: The Mediating Role of Seaborne Trade.” *Journal of Shipping and Trade* 3 (1). Journal of Shipping and Trade: 1–19. doi:10.1186/s41072-018-0027-0.
Munjy, Riadh. 2015. “Simultaneous Adjustment of LIDAR Strips.” *Journal of Surveying Engineering* 141 (1): 04014012. doi:10.1061/(asce)su.1943-5428.0000139.
Nagarajan, Sudhagar, and Shahram Moafipoor. 2018. “Boresight Calibration of Low Point Density Lidar Sensors.” *Photogrammetric Engineering and Remote Sensing* 84 (10): 619–627. doi:10.14358/PERS.84.10.619.
Ndir, Papa Médoune. 2019. “Implantation et Évaluation de La Performance d’une Méthode d’ajustage En Mode Statique Des Systèmes Lidar Mobiles Terrestres.” Master Thesis, Laval Univeristy.
Novatel. 2021. “Heave.” https://novatel.com/products/firmware-options-pc-software/gnss-receiver-firmware-options/heave.
Olsen, Michael J., Gene V. Roe, Craig Glennie, Fred Persi, Persi Consulting, Marcus Reedy, David Evans, et al. 2013. “Guidelines for the Use of Mobile Lidar in Transportation Applications Final Guidelines.” *Transportation Research*, no. February 2013: 208.
Pauly, Mark, Richard Keiser, and Markus Gross. 2003. “Multi-scale Feature Extraction on Point-Sampled Surfaces.” *Computer Graphics Forum* 22 (September): 281–289. doi:10.1111/1467-8659.00675.
Petovello, Mark G. 2003. “Real-Time Integration of a Tactical-Grade IMU and GPS for High-Accuracy Positioning and Navigation.” University of Calgary.
Pothou, A., Charles Toth, S. Karamitsos, and A. Georgopoulos. 2008. “An Approach to Optimize Reference Ground Control Requirements for Estimating LIDAR/IMU Boresight Misalignment.” *International Archives of the Photogrammetry, Remote Sensing and Spatial Information Sciences - ISPRS Archives* 37.
Puente, Iván, Mercedes Solla, Higinio González-Jorge, and Pedro Arias. 2013. “Validation of Mobile LiDAR Surveying for Measuring Pavement Layer Thicknesses and Volumes.” *NDT and E International* 60. Elsevier: 70–76. doi:10.1016/j.ndteint.2013.07.008.
Ravi, Radhika, and Ayman Habib. 2020. “Fully Automated Profile-Based Calibration Strategy for Airborne and Terrestrial Mobile LiDAR Systems with Spinning Multi-Beam Laser Units.” *Remote Sensing* 12 (3). doi:10.3390/rs12030401.
Ravi, Radhika, Tamer Shamseldin, Magdy Elbahnasawy, Yun Jou Lin, and Ayman Habib. 2018. “Bias Impact Analysis and Calibration of UAV-Based Mobile LiDAR System with Spinning Multi-Beam Laser Scanner.” *Applied Sciences (Switzerland)* 8 (2). doi:10.3390/app8020297.
Rentsch, Matthias, and Peter Krzystek. 2012. “Lidar Strip Adjustment with Automatically Reconstructed Roof Shapes.” *Photogrammetric Record* 27 (139): 272–292. doi:10.1111/j.1477-9730.2012.00690.x.
Ressl, Camillo, Gottfried Mandlburger, and Norbert Pfeifer. 2009. “Investigating Adjustment of Airborne Laser Scanning Strips Without Usage of Gnss/Imu Trajectory Data.” *Laser Scanning 2009, IAPRS* XXXVIII (1): 195–200.

Ressl, Camillo, Norbert Pfeifer, and Gottfried Mandlburger. 2012. “Applying 3D Affine Transformation and Least Squares Matching for Airborne Laser Scanning Strips Adjustment Without Gnss/Imu Trajectory Data.” *The International Archives of the Photogrammetry, Remote Sensing and Spatial Information Sciences* XXXVIII-5/ (May): 67–72. doi:10.5194/isprsarchives-xxxviii-5-w12-67-2011.

Riegl. 2022. “Riegl Laser Measurement Systems.” http://www.riegl.com/fileadmin/gallery/mobil/mls_vmx-250_scanningsystem_korea.JPG.

Rondeau, Mathieu, and Frédéric Pelletier. 2013. “Using Integrated Technology to Inspect Quay Walls.” In *Port Technology International*, 1–2.

Rönnholm, P., X. Liang, A. Kukko, A. Jaakkola, and J. Hyyppä. 2016. “Quality Analysis and Correction of Mobile Backpack Laser Scanning Data.” *ISPRS Annals of Photogrammetry, Remote Sensing and Spatial Information Sciences* III–1 (June): 41–47. doi:10.5194/isprsannals-iii-1-41-2016.

Ruggeri, Paolo, Viviene Marianne Esther Fruzzetti, and Giuseppe Scarpelli. 2021. “Upgrading of Quay Walls at the Ravenna Port, Italy: Evaluation of the Steel Piles Degradation after a Long Working Life.” *Structure and Infrastructure Engineering* 17 (2). Taylor & Francis: 249–259. doi:10.1080/15732479.2020.1736101.

Rusu, Radu Bogdan, Steve Cousins, and Willow Garage. 2011. “3D Is Here: Point Cloud Library (PCL).” *IEEE International Conference on Robotics and Automation (ICRA)*.

Ryding, Joseph, Emily Williams, Martin J. Smith, and Markus P. Eichhorn. 2015. “Assessing Handheld Mobile Laser Scanners for Forest Surveys.” *Remote Sensing* 7 (1): 1095–1111. doi:10.3390/rs70101095.

Schaer, Philipp. 2010. *In-Flight Quality Assessment and Data Processing for Airborne Laser Scanning*. Institut für Geodäsie und Photogrammetrie.

Schenk, Anton F. 2001. “Modeling and Analyzing Systematic Errors in Airborne Laser Scanners.” *Technical Notes in Photogrammetry* 19 (January). doi:10.13140/RG.2.2.20019.25124.

Sentry, Matthew, Abdelmalek Bouazza, Riadh Al-Mahaidi, Darren Loidl, Chris Bluff, and Len Carrigan. 2007. “Advancements in Ground Anchors: Carbon Fibre Reinforced Polymer (CFRP) Strands.” In *Ground Anchorages and Anchored Structures in Service 2007: Proceedings of the Two Day International Conference Organised by the Institution of Civil Engineers and Held in London on 26 and 27 November 2007*, 321–330.

Seube, Nicolas, Alan Picard, and Mathieu Rondeau. 2012. “A Simple Method to Recover the Latency Time of Tactical Grade IMU Systems.” *ISPRS Journal of Photogrammetry and Remote Sensing* 74. International Society for Photogrammetry and Remote Sensing, Inc. (ISPRS): 85–89. doi:10.1016/j.isprsjprs.2012.09.001.

Shahraji, Mohsen H., and Christian Larouche. 2022. “Case Study: Rigorous Boresight Alignment of a Marine Mobile LiDAR System Addressing the Specific Demands of Port Infrastructure Monitoring.” *Marine Geodesy* 45 (3). Taylor & Francis: 295–327. doi:10.1080/01490419.2022.2025503.

Shahraji, Mohsen H., Christian Larouche, and Marc Cocard. 2020. “ANALYSIS OF SYSTEMATIC ERRORS OF MOBILE LiDAR SYSTEMS: A SIMULATION APPROACH.” *ISPRS Annals of Photogrammetry, Remote Sensing and Spatial Information Sciences* V-1–2020 (August): 253–260. doi:10.5194/isprs-annals-V-1-2020-253-2020.

Shan, Jie, and Charles Toth. 2008. *Topographic Laser Ranging and Scanning: Principles and Processing*. *CRC Press*. Taylor & Francis Group. http://www.tandfonline.com/doi/abs/10.1080/01431160903112612.

Shi, Bo, Yuntian Bai, Shun Zhang, Ruofei Zhong, Fanlin Yang, Shizhu Song, and Guoyu

Li. 2021. “Reference-Plane-Based Approach for Accuracy Assessment of Mobile Mapping Point Clouds.” *Measurement: Journal of the International Measurement Confederation* 171. Elsevier Ltd: 108759. doi:10.1016/j.measurement.2020.108759.
Shi, Bo, Xiushan Lu, Fanlin Yang, Chuanyin Zhang, Yanquan Lv, and Min Cheng. 2017. “Shipborne Over- and Under-Water Integrated Mobile Mapping System and Its Seamless Integration of Point Clouds.” *Marine Geodesy* 40 (2–3). Taylor & Francis: 104–122. doi:10.1080/01490419.2016.1272510.
Skaloud, Jan, and Derek Lichti. 2006. “Rigorous Approach to Bore-Sight Self-Calibration in Airborne Laser Scanning.” *ISPRS Journal of Photogrammetry and Remote Sensing* 61 (1): 47–59. doi:10.1016/j.isprsjprs.2006.07.003.
Skaloud, Jan, and Philipp Schaer. 2003. “Towards A More Rigorous Boresight Calibration.” In *ISPRS International Workshop on Theory, Technology and Realities of Inertial / GPS Sensor Orientation, Commission 1, WG I/5*. Castelldefels, Spain.
Skaloud, Jan, and Philipp Schaer. 2007. “Towards Automated LiDAR Boresight Self-Calibration.” *International Archives of the Photogrammetry, Remote Sensing and Spatial Information Sciences - ISPRS Archives* 36 (5C55).
Skog, Isaac. 2007. “GNSS-Aided INS for Land Vehicle Positioning and Navigation.” KTH Royal Institute of Technology.
Soilán, Mario, Ana Sánchez-Rodríguez, Pablo Del Río-Barral, Carlos Perez-Collazo, Pedro Arias, and Belén Riveiro. 2019. “Review of Laser Scanning Technologies and Their Applications for Road and Railway Infrastructure Monitoring.” *Infrastructures* 4 (4). doi:10.3390/infrastructures4040058.
Song, Bo, Zhou Guoqing, and Feng Wang. 2021. “Multi-Feature Airborne Lidar Strip Adjustment Method Combined with Tensor Voting Algorithm.” In *2021 IEEE International Geoscience and Remote Sensing Symposium IGARSS*, 8049–8052.
Soudarissanane, Sylvie, Roderik Lindenbergh, Massimo Menenti, and P J G Teunissen. 2009. “Incidence Angle Influence on the Quality of Terrestrial Laser Scanning Points.” In *Proceedings ISPRS Workshop Laserscanning 2009, 1-2 Sept 2009, Paris, France*.
Stewart, Mark G., and Emilio Bastidas-Arteaga. 2019. *Corrosion of Concrete and Steel Structures in a Changing Climate*. *Climate Adaptation Engineering: Risks and Economics for Infrastructure Decision-Making*. Elsevier Inc. doi:10.1016/B978-0-12-816782-3.00004-8.
Stockwell, Walter. 2003. *Angle Random Walk*. *Crossbow Technology, Inc.* http://www.xbow.com/.
Talaya, J, R Alamus, E Bosch, A Serra, W Kornus, and A Baron. 2004. “Integration of a Terrestrial Laser Scanner with GPS/IMU Orientation Sensors.” In *Proceedings of the XXth ISPRS Congress*, 35:1049–1055.
Thies, Thomas. 2011. “A Vessel-Based Mobile Mapping System – From Sensor Integration to Multipurpose Products.” HafenCity University Hamburg. http://www.riegl.com/uploads/tx_pxpriegldownloads/Thies_Thomas__2011_-_A_Vessel-Based_Mobile_Mapping_System__Master_Thesis__HafenCity_University_Hamburg__Germany_part1.pdf.
Toth, Charles K., N Csanyi, and D A Grejner-Brzezinska. 2002. “Automating the Calibration of Airborne Multisensor Imaging Systems.” *FIG XXII International Congress*, 1–14.
TrimbleGeospatial. 2022. “Trimble MX50.” https://geospatial.trimble.com/products-and-solutions/trimble-mx50.
United Nations Publications. 2020. “Review of Maritime Transport.” In *United Nations Conference on Trade and Development*. Geneva: United Nations Publications. doi:10.18356/edeca49a-en.

Valdez, Benjamín, Jorge Ramirez, Amir Eliezer, Michael Schorr, Rogelio Ramos, and Ricardo Salinas. 2016. “Corrosion Assessment of Infrastructure Assets in Coastal Seas.” *Journal of Marine Engineering and Technology* 15 (3): 124–134. doi:10.1080/20464177.2016.1247635.

van der Sande, Corné, Sylvie Soudarissanane, and Kourosh Khoshelham. 2010. “Assessment of Relative Accuracy of AHN-2 Laser Scanning Data Using Planar Features.” *Sensors* 10 (9): 8198–8214. doi:10.3390/s100908198.

Vosselman, George. 2002. “Strip Offset Estimation Using Linear Features.” In *3rd International Workshop on Mapping Geo-Surfical Processes Using Laser Altimetry*, 9.

Vosselman, George, and Hans-Gerd Maas. 2011. *Airborne and Terrestrial Laser Scanning*. *Whittles Publishing*. Vol. 4. Scotland: CRC Press Taylor & Francis Group. doi:10.1080/17538947.2011.553487.

Wang, Yanjun, Qi Chen, Qing Zhu, Lin Liu, Chaokui Li, and Dunyong Zheng. 2019. “A Survey of Mobile Laser Scanning Applications and Key Techniques over Urban Areas.” *Remote Sensing* 11 (13): 1–20. doi:10.3390/rs11131540.

Wehr, Aloysius, and Uwe Lohr. 1999. “Airborne Laser Scanning - An Introduction and Overview.” *ISPRS Journal of Photogrammetry and Remote Sensing* 54 (2–3): 68–82. doi:10.1016/S0924-2716(99)00011-8.

West, Karen, Brian Webb, James Lersch, Steven Pothier, Joseph Triscari, and Evan Iverson. 2004. “Context-Driven Automated Target Detection in 3D Data.” *Proceedings of SPIE - The International Society for Optical Engineering* 5426 (September). doi:10.1117/12.542536.

Wilkinson, Benjamin, H. Andrew Lassiter, Amr Abd-Elrahman, Raymond R. Carthy, Peter Ifju, Eben Broadbent, and Nathan Grimes. 2019. “Geometric Targets for UAS Lidar.” *Remote Sensing* 11 (24). doi:10.3390/rs11243019.

Williams, Keith, Michael J. Olsen, Gene V. Roe, and Craig Glennie. 2013. *Synthesis of Transportation Applications of Mobile LIDAR*. *Remote Sensing*. Vol. 5. doi:10.3390/rs5094652.

Wyllie, Katrina, Grant Froelich, Karen Cove, and Karen Hart. 2012. “Process for Capturing Real World Features from 3D Laser Scanned Point Clouds,” no. May 2012: 1–14.

Yan, Zhaojin, Rufei Liu, Liang Cheng, Xiao Zhou, Xiaoguang Ruan, and Yijia Xiao. 2019. “A Concave Hull Methodology for Calculating the Crown Volume of Individual Trees Based on Vehicle-Borne LiDAR Data.” *Remote Sensing* 11 (6): 623. doi:10.3390/rs11060623.

You, Rey Jer, and Chao Liang Lee. 2020. “Accuracy Improvement of Airborne Lidar Strip Adjustment by Using Height Data and Surface Feature Strength Information Derived from the Tensor Voting Algorithm.” *ISPRS International Journal of Geo-Information* 9 (1). doi:10.3390/ijgi9010050.

Zeng, Yadan, Heng Yu, Houde Dai, Shuang Song, Mingqiang Lin, Bo Sun, Wei Jiang, and Max Q.H. Meng. 2018. “An Improved Calibration Method for a Rotating 2D LIDAR System.” *Sensors (Switzerland)* 18 (2): 1–12. doi:10.3390/s18020497.

Zhang, J., W. Jiang, and S. Jiang. 2012. “AUTOMATED MOUNTING BIAS CALIBRATION for AIRBORNE LIDAR SYSTEM.” *ISPRS Annals of the Photogrammetry, Remote Sensing and Spatial Information Sciences* 1 (September): 263–268. doi:10.5194/isprsannals-I-4-263-2012.

Zhang, Yongjun, Xiaodong Xiong, Maoteng Zheng, and Xu Huang. 2015. “LiDAR Strip Adjustment Using Multifeatures Matched with Aerial Images.” *IEEE Transactions on Geoscience and Remote Sensing* 53 (2). IEEE: 976–987. doi:10.1109/TGRS.2014.2331234.

Zoller & Frohlich GmbH. 2012. *Z+F PROFILER 9012 Manual - Advanced Users*. Germany: Zoller + Frohlich GmbH.

Zoller & Frohlich GmbH. 2022. “Z&F Profiler 9012.” https://www.zofre.de/en/laser-scanners/2d-laser-scanner/z-f-profilerr-9012.

Appendix A – In-house Mobile LiDAR System Integration

This appendix introduces the work behind integrating the different components selected for the setup of the customized in-house terrestrial mobile LiDAR system. For this, specialists of Jakarto Cartographie 3d inc., a project partner, contributed to the design and integration of the system and the fabrication of the PPS cables that linked the POS device to the LiDAR scanner and synchronized the GNSS time to the scanner time. Figure A.1 shows some components and accessories used to connect and synchronize the primary sensors of our customized in-house MLS.

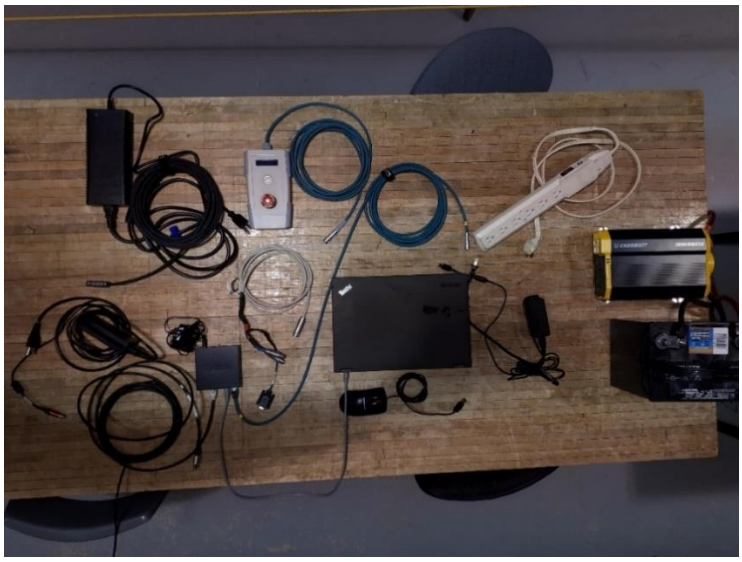

Figure A.1 – Main components and accessories of our customized in-house MLS

After integrating all main components (the LiDAR scanner and the POS device) and accessories, we installed and tested them on a trolley to ensure the system could adequately collect the data. Second, we installed and operated the system on a road vehicle and collected datasets on a long road corridor, as seen in Figure A.2.

(a)

(b)

(c)

Figure A.2 – Test of the customized MLS on the various platforms; trolley (a) and road vehicle (b and c)

Figure A.3 illustrates the surveyed corridor on the campus of Laval University with this assembled MLS and a small portion of the collected point cloud.

(a)

(b)

Figure A.3 – (a) Trajectory of the acquisition test on the campus of Laval University. (b) A portion of the georeferenced point cloud around the Pavillon Casault of Laval University.

By analyzing the data collected on this field test, we can observe a vital boresight alignment issue in the georeferenced point cloud, as presented in Figure A.4. Thus, for the next test, we concentrated our efforts on the estimation of the boresight angles of the POS-LiDAR components.

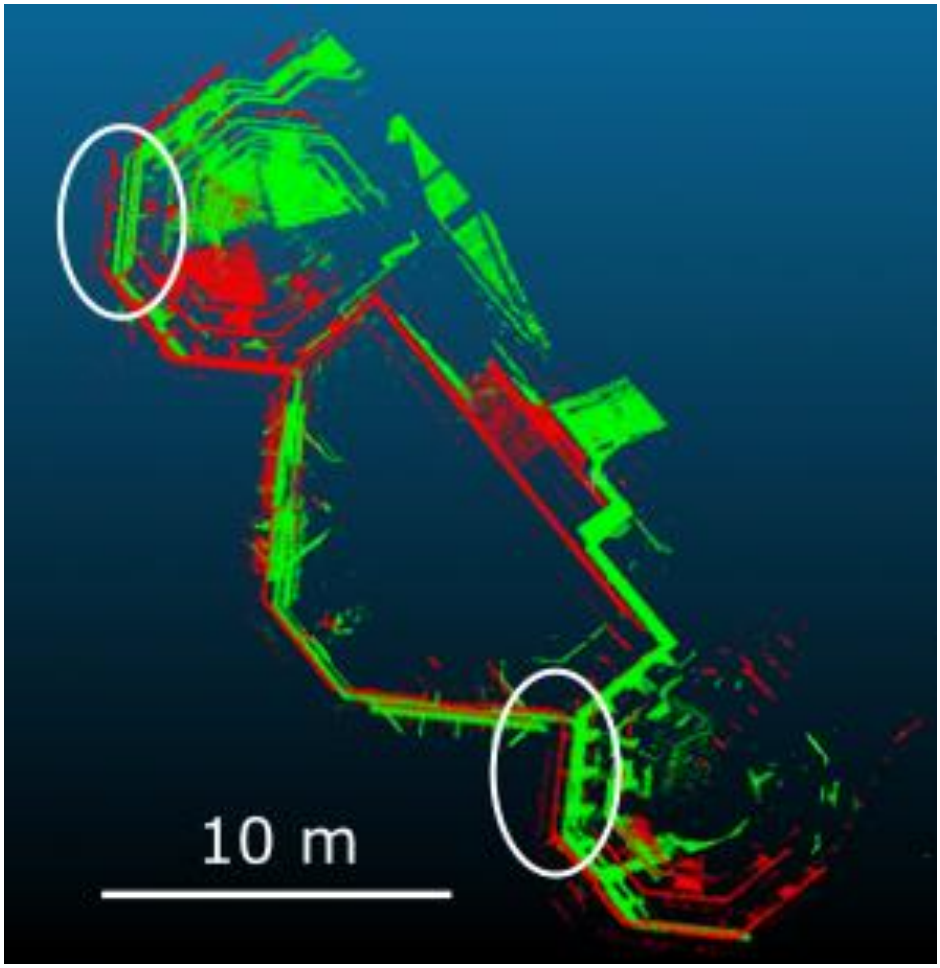

Figure A.4 – Boresight misalignment effect (white circles) of point clouds collected on a building facade in round-trip passages presented in two colors (green and red).

Based on the initial scanning results of a scene from various passages, we can see that the point clouds do not match, and we know that this deviation is caused by the boresight misalignment of the POS-LiDAR systems. Thus, to improve the quality of the final point clouds, we must estimate the POS-LiDAR boresight angles. Therefore, we suggested a boresight alignment method using a prefabricated planar target that we scanned with a specific line pattern, as illustrated in Figure A.5. This test was performed on November 7th, 2018, at the Laval University campus.

(a)

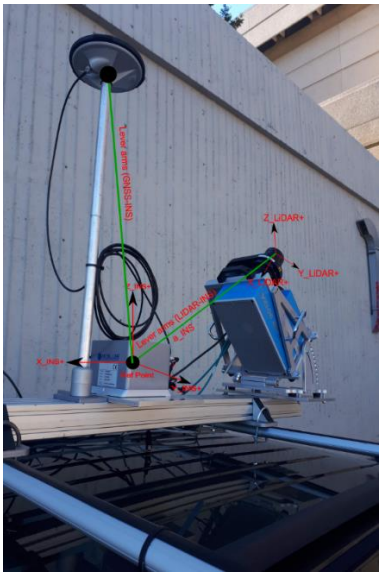

(b)

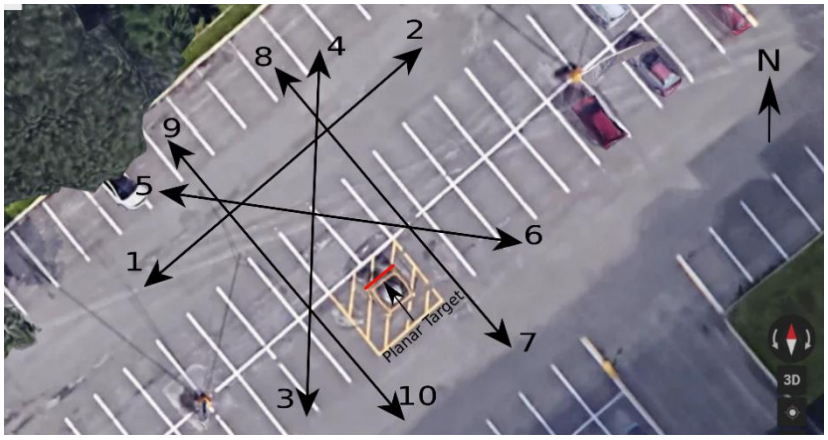

(c)

Figure A.5 – Boresight alignment procedure with one vertical planar target. (a) Planar target in vertical orientation w.r.t the terrestrial MLS. (b) The terrestrial MLS is installed on a road vehicle platform. (c) the line pattern followed by the terrestrial MLS.

The idea behind the suggested method is to facilitate the boresight alignment task and make it easier for a non-expert operator to estimate the boresight angles at any place and any time with a robust and reliable approach. As illustrated in Figure A.6, the obtained result of the planar target demonstrates a deviation between the scanned point clouds of the plane, primarily due to systematic errors, especially the boresight misalignment issue.

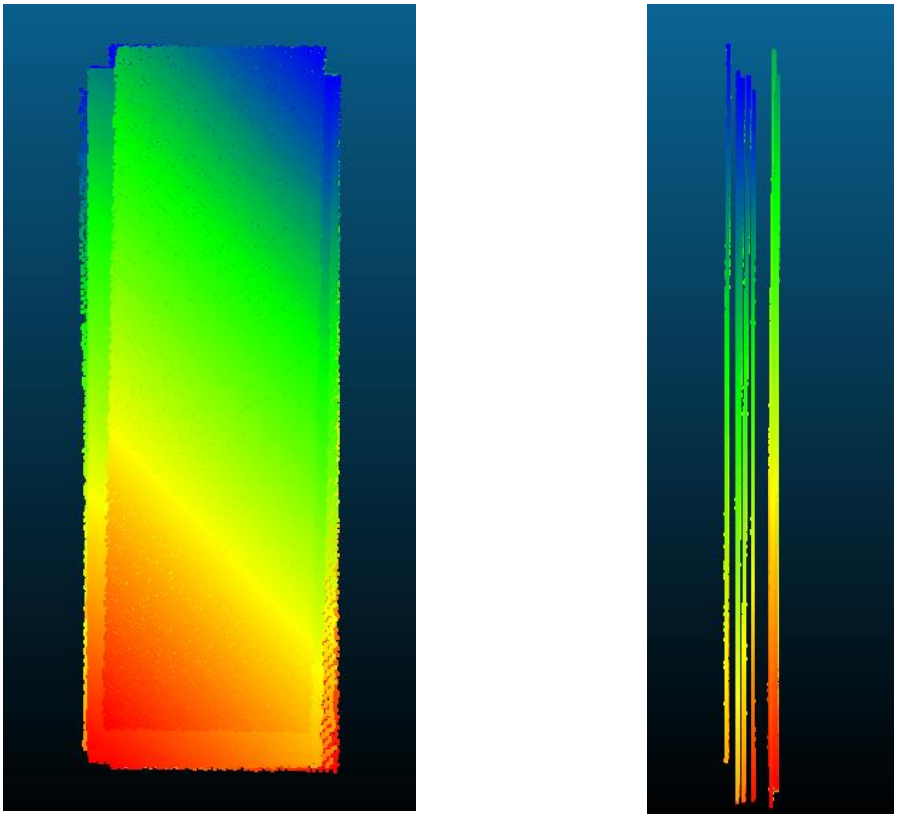

(a) (b)

Figure A.6 – Deviation between various scans of the vertical planar target caused by MLS errors (a) Front view (b) Side view. The colour on the points is with respect to the timestamp of scans, blue signifies the lower time, and red signifies the higher time.

Based on our initial analysis of the results, we concluded that with one vertical planar target, the boresight alignment algorithm does not converge to a solution. Therefore, only one vertical plane located at a lower altitude than the scanner is insufficient to estimate the boresight angles of a terrestrial MLS. Thus, we need more planar targets with various configurations to be able to estimate the systematic errors of an MLS. To study different planar configurations and line patterns, we designed an MLS simulator, presented in detail in Chapter 3. This simulation-based approach helped us to study the effects of each systematic error of an MLS without the interference of other systematic errors or system noises.

Appendix B – Software Development

In this research, due to the customized nature of the in-house marine mobile LiDAR system, we developed a workflow for processing the raw data received from the POS and the LiDAR scanner and producing georeferenced 3D point clouds. The workflow is divided into two main parts: the “Input Data Preparation” and the “LISPAC Software Package” processing. Figure B.1 represents the first part of the overall workflow.

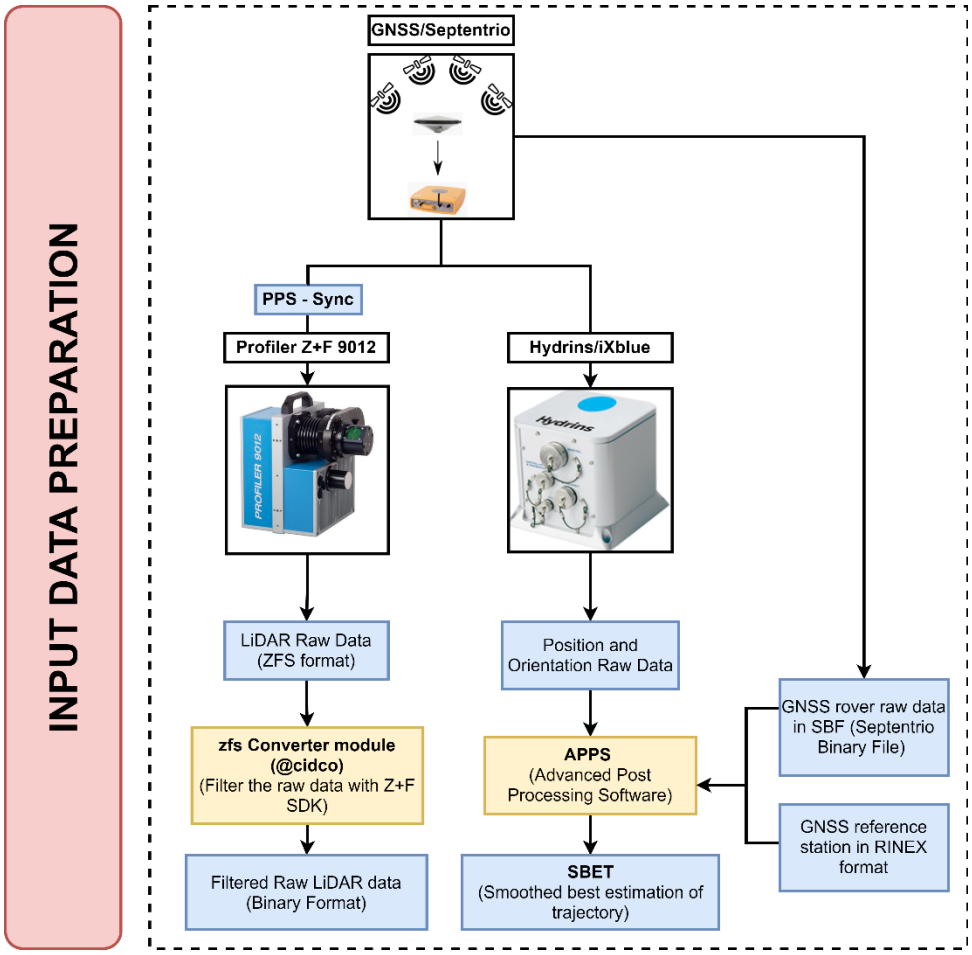

Figure B.1 – Input data preparation part of the overall workflow

In the input data preparation part, we gather raw data from the LiDAR scanner and the INS, process them, and export them for the LISPAC software package, as illustrated in Figure B.2.

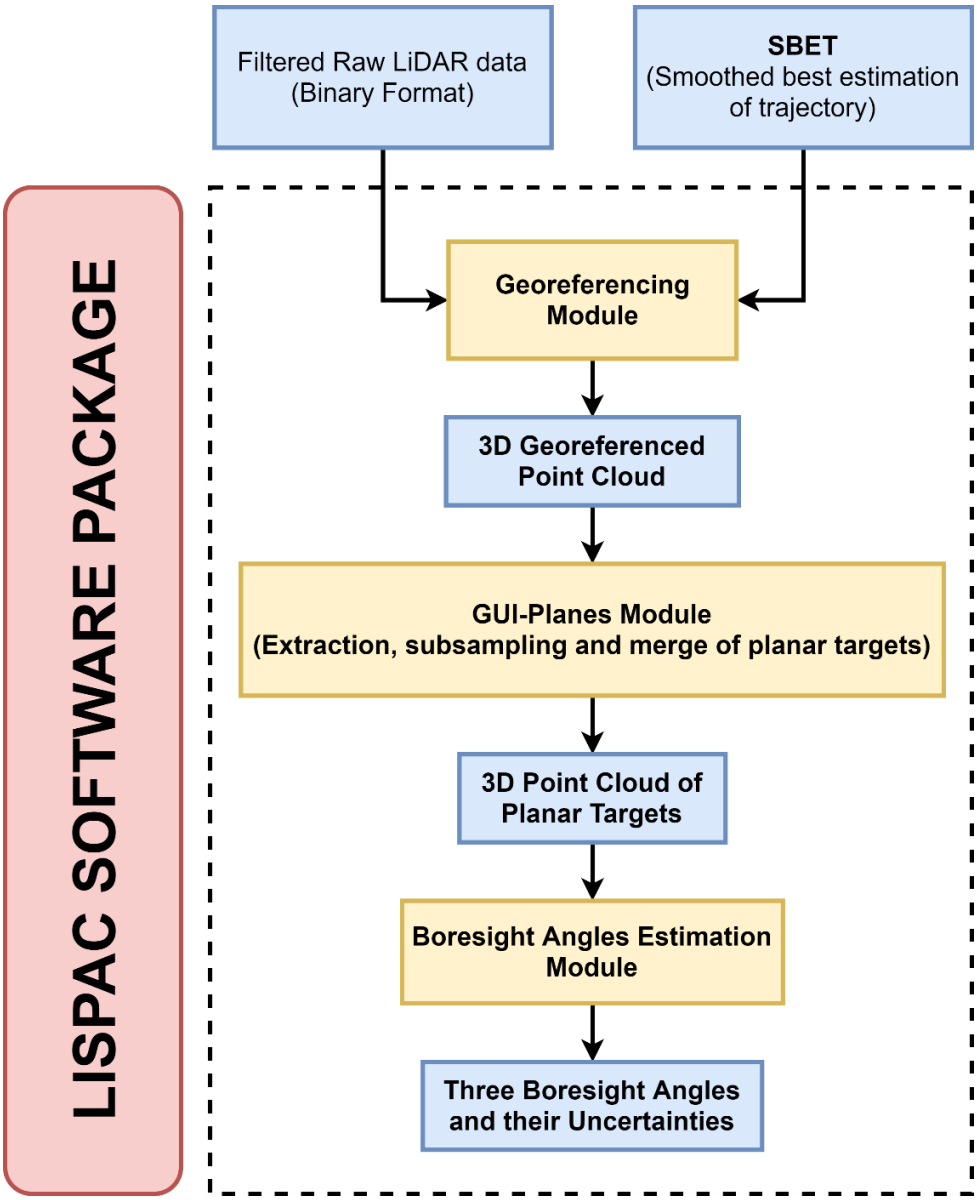

Figure B.2 – LISPAC Software Package developed in a collaboration between Laval University and CIDCO

The LISPAC software package takes the input data prepared in the last part of the workflow, and it generates a 3D georeferenced point cloud of the scanned scene with the planar targets located in them with its "*Georeferencing*" module. Then, with the "*GUI-Planes*" module, the planar targets are extracted in a semi-automatic mode. The software operator localizes a point in the middle of the planar target, and after that, the plane detection algorithm defines the whole plane's point cloud. In the next

step, the software operator fixes a subsampling rate, and finally, the essential points of each scanned planar target with the specific line pattern are merged into an individual file. The next step is to use the point cloud that contains the various scans of the planar targets in an iterative adjustment procedure, which produces the best possible fit of the planar targets and simultaneously estimates the boresight angles.

The first prototype of the suggested method in this research has been implemented in MATLAB®, which the source code can be found in the following link https://github.com/MHS1985/phd_thesis.

This section is divided into three sub-sections: Georeferencing module, *PlanePreparation* module, and *BoresightEstimation* module.

B.1 Georeferencing Module

The inputs for this module are the raw Z+F® LiDAR data and the corresponding interpolated POS data. The POS data come in SBET format and contain positioning data (*Northing, Easting, and Ellipsoid Height*) and attitude data (*Roll, Pitch, and Heading*). Due to the higher acquisition frequency of LiDAR data (1 MHz) with respect to POS data (200 Hz), we applied linear interpolation to assign position and orientation data to each ZF LiDAR point.

First, we calculate the coordinate of the points in the LGF coordinate system based on Figure B.3. For “Linear Interpolation,” we use the *interp1* function in MATLAB®.

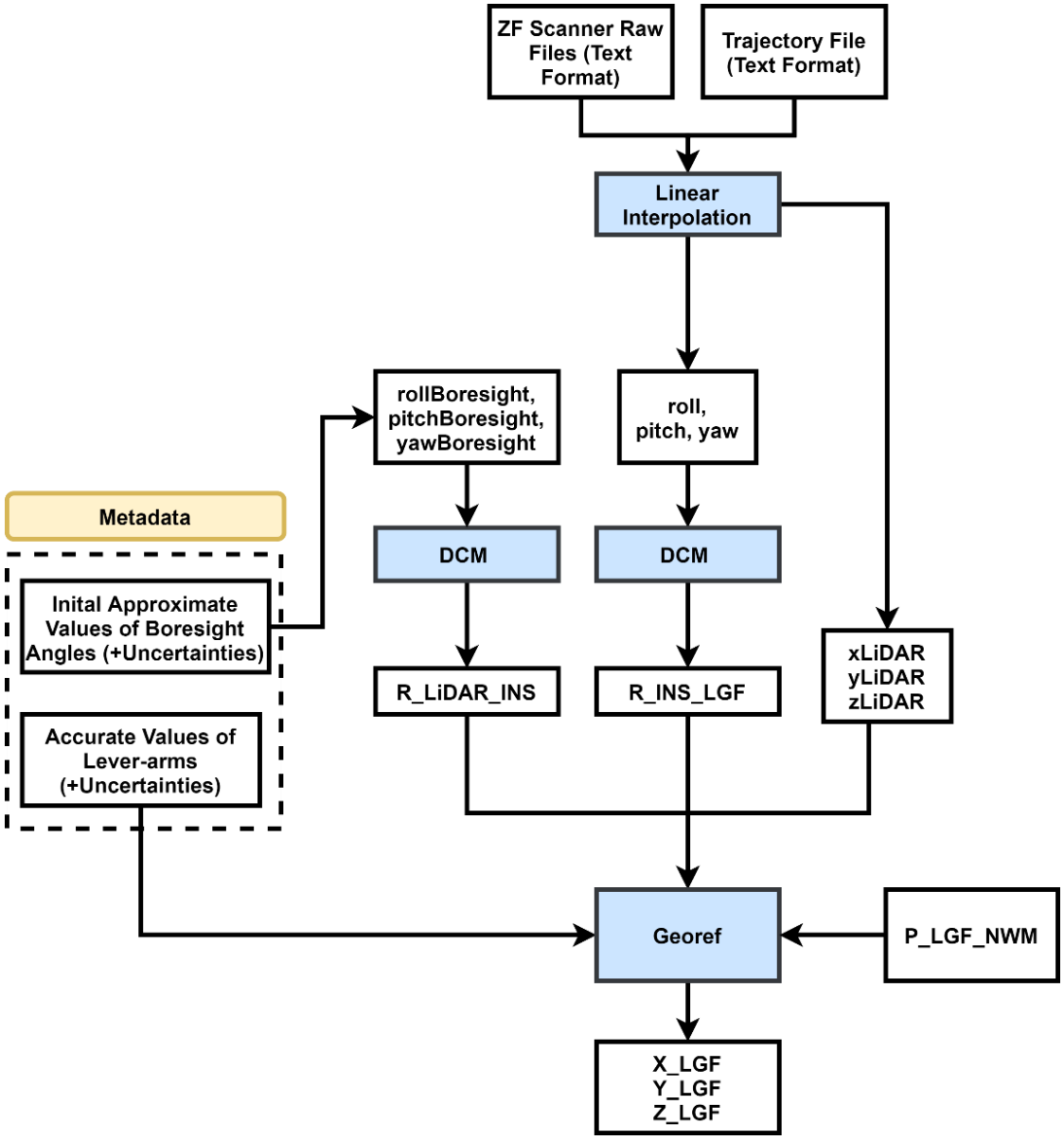

Figure B.3 – Algorithm that produces the georeferenced coordinates of the LiDAR points. The blue boxes represent the functions that we use in the georeferencing module.

In Figure B.4, the P_LGF_NWU is calculated based on the algorithm demonstrated in Figure B.3.

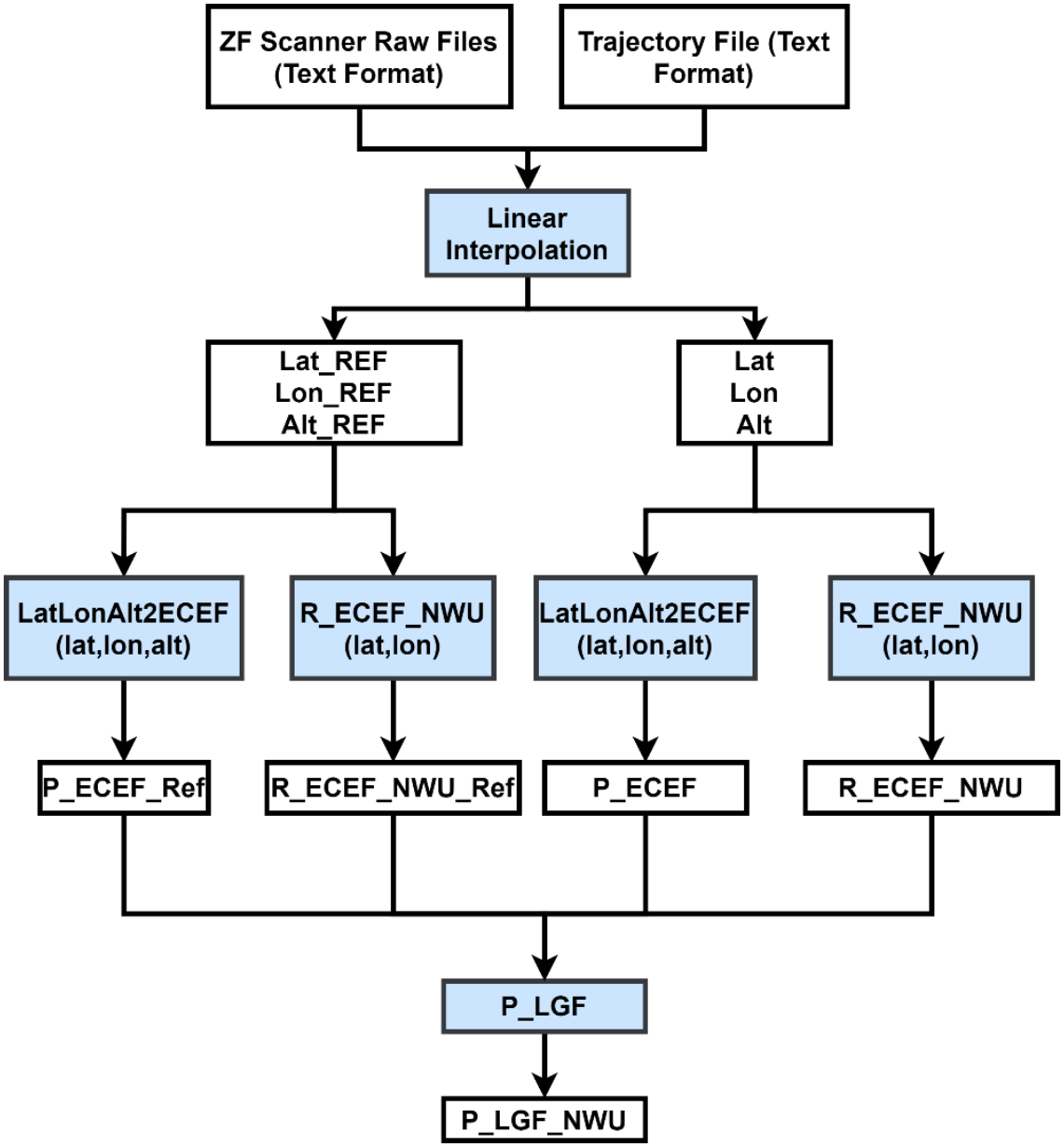

Figure B.4 – The algorithm calculates the points' coordinates in the LGF coordinate system. The blue boxes are the functions that we use in the georeferencing module.

Algorithms for calculating different parts of the direct georeferencing model (Equation (3.1)) are presented in Figure B.5 and Figure B.6.

$$\begin{bmatrix} X^{LGF} \\ Y^{LGF} \\ Z^{LGF} \end{bmatrix} = \underbrace{\begin{bmatrix} P_X^{LGF} \\ P_Y^{LGF} \\ P_Z^{LGF} \end{bmatrix}}_{\text{ALGORITHM 1}} + \underbrace{R_{POS}^{LGF}(r,p,h)}_{\text{ALGORITHM 2}} \left(\underbrace{R_{LiDAR}^{POS}(\alpha,\beta,\gamma)}_{\text{ALGORITHM 2}} \begin{bmatrix} x_{LiDAR} \\ y_{LiDAR} \\ z_{LiDAR} \end{bmatrix} + \begin{bmatrix} a_X^{POS} \\ a_Y^{POS} \\ a_Z^{POS} \end{bmatrix} \right)$$

ALGORITHM 1: ALGORITHM TO CALCULATE PLGF

Input: *Position of the trajectory in the Geographic Coordinate System (Latitude and Longitude)*
Output: *Position of the trajectory in the Local Geodetic Frame (LGF)*
number-of-Points ← *count the total number of points in the trajectory*
Initialization of variables*: assign zero to the variable* $\boldsymbol{i, \lambda, \varphi, \lambda_{Ref}, \varphi_{Ref}}$
for (i $<$ ***number-of-Points)*** *// read all the points and accumulate their values into one variable*
    $\boldsymbol{\lambda}$ ← *read the λ coordinate of each point and add to the variable*
    $\boldsymbol{\varphi}$ ← *read the φ coordinate of each point and add to the variable*
end
$\boldsymbol{\lambda_{Ref}}$ ← ***λ / number-of-Points***
$\boldsymbol{\varphi_{Ref}}$ ← ***φ / number-of-Points***
R_{ECEF}^{LGF} ← $\boldsymbol{\lambda_{Ref}, \varphi_{Ref}}$ *// Rotation matrix (Equation (B.1)) between ECEF frame and LGF*
$P_{ECEF}(\lambda_{Ref}, \varphi_{Ref})$ ← $\boldsymbol{\lambda_{Ref}, \varphi_{Ref}}$ *// Translation vector (Equation (B.2)) between ECEF*
for (i $<$ ***number-of-Points)*** *// read all the points and calculate the* P_{ECEF} *for each position*
    P_{ECEF} ← *calculate the* P_{ECEF} *for each position*
    P_{LGF} ← *calculate the* P_{LGF} *for each position with Equation (B.3)*
end

Figure B.5 – Algorithm 1 to calculate PLGF

Equation (B.1) calculates the rotation matrix between the Earth Centric Earth Fixed (ECEF) frame and the LGF, with the latitude and longitude entries coming from the GNSS sensor. Equation (B.2) calculates the 3D coordinates of a point in the ECEF frame. The output of the two Equations (B.1) and (B.2) is used as input in Equation (B.3). To calculate the 3D coordinates of the point in the LGF, we use Equation (B.3). The detail of this equations is discussed in inertial navigation systems references (Groves 2013; Jekeli 2012).

$$R_{ECEF}^{LGF}(\lambda_{Ref}, \varphi_{Ref}) = \begin{bmatrix} -\cos(\lambda_{Ref})\sin(\varphi_{Ref}) & -\sin(\lambda_{Ref})\sin(\varphi_{Ref}) & \cos(\varphi_{Ref}) \\ \sin(\lambda_{Ref}) & -\cos(\lambda_{Ref}) & 0 \\ \cos(\lambda_{Ref})\cos(\varphi_{Ref}) & \sin(\lambda_{Ref})\cos(\varphi_{Ref}) & \sin(\varphi_{Ref}) \end{bmatrix} \quad \text{(B.1)}$$

$$P_{ECEF} = \begin{pmatrix} x \\ y \\ z \end{pmatrix}_{ECEF} = \begin{bmatrix} (N_E + h)cos\varphi cos\lambda \\ (N_E + h)cos\varphi sin\lambda \\ (N_E(1 - e^2) + h)sin\varphi \end{bmatrix} \quad \text{(B.2)}$$

$$P_{LGF} = R_{ECEF}^{LGF}(\lambda_{Ref}, \varphi_{Ref})\left[P_{ECEF}(\lambda, \varphi) - P_{ECEF}(\lambda_{Ref}, \varphi_{Ref})\right] \quad \text{(B.3)}$$

ALGORITHM 2: ALGORITHM TO CALCULATE R_{POS}^{LGF} AND R_{LiDAR}^{POS}

Input: *Attitude observations of the POS (r, p, h) and initial boresight angles (α, β, γ)*
Output1: *Rotation Matrix between POS frame and LGF frame*
Output2: *Rotation Matrix between LiDAR frame and POS frame*
number-of-Points ← *count the total number of points in the trajectory*
Initialization of variables*: assign zero to the variable* ***i***
for (i < ***number-of-Points)*** *// read all the points and calculate the rotation matrix*
    $M_X(r)$ ← *read the roll attitude angle*
    $M_Y(p)$ ← *read the pitch attitude angle*
    $M_Z(h)$ ← *read the heading attitude angle*
    // Calculate the rotation matrix for each trajectory point
    $R_{INS}^{LGF}(r, p, h) \leftarrow M_Z(h)M_Y(p)M_X(r)$
end
// Calculate the rotation matrix between LiDAR frame and POS frame
$M_Z(\gamma)$ ← *read the γ roll boresight angle*
$M_Y(\beta)$ ← *read the β pitch boresight angle*
$M_X(\alpha)$ ← *read the α yaw boresight angle*
$R_{LiDAR}^{INS} \leftarrow M_Z(\gamma)M_Y(\beta)M_X(\alpha)$

Figure B.6 – Algorithm 2 to calculate R_{POS}^{LGF} and R_{LiDAR}^{POS}

B.2 Plane Preparation Module

In this section, we present in detail the theory and the model that enable us to extract the necessary information from each planar target and produce the input data for the boresight angles estimation module illustrated in Figure B.7. Firstly, we visualize the georeferenced point cloud from each passage. This data contains all the scanned instances of the planar targets. Secondly, we manually select a point on the plane, and thirdly, with the available RANSAC tool in the Point Cloud Library package (Rusu, Cousins, and Garage 2011), which is a robust plane extraction algorithm, we extract all the points on the planar targets while removing the outliers effectively. The extracted planar target points without outliers will augment the performance of the method, which depends in a significant part on the extracted planes' reliability (van der Sande, Soudarissanane, and Khoshelham 2010).

Fourthly, we perform a spatial subsampling to reduce the volume of the points on each plane. Fifthly, we fit a plane to the point cloud of each plane and define the initial and approximative normal vector for each point. The approximative normal

value is essential for the boresight angles estimation algorithm. The last step of data preparation for the boresight angles estimation algorithm is to merge all the selected points from all the passages for each planar target and create a single file for each plane. Thus, if we have two planar targets, we will have two final input files that will be introduced to the boresight angles estimation algorithm.

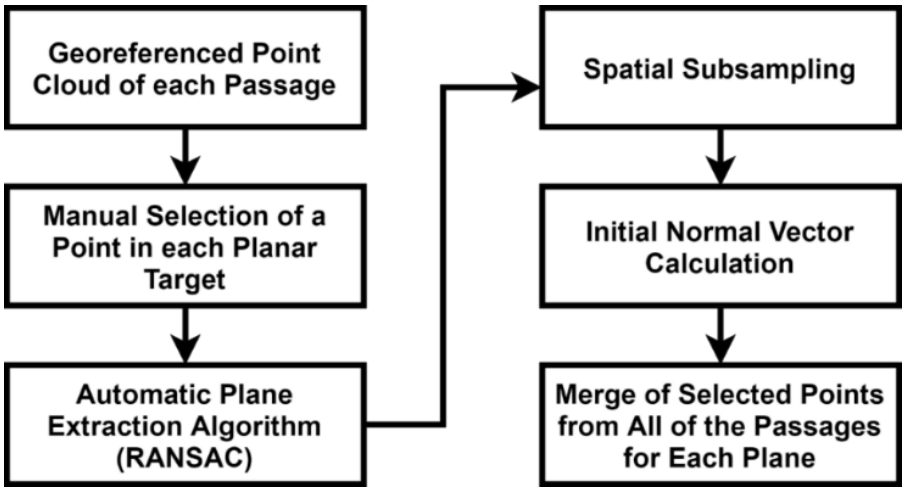

Figure B.7 – Input data preparation procedure for the boresight error estimation module

This procedure is done for each planar target, and at the end, we will have a file for each plane. Most of the plane extraction in the MATLAB prototype is manual, and here we present the function that estimates the initial normal vector for each plane that will serve as input parameters for the boresight angles estimation module, presented in Appendix A.3.

This procedure has been automated in the LISPAC software package, which is designed based on the proposed prototype developed in this thesis. For each planar target, we merge all the point clouds of all the passages and add the initial normal vector to the raw LiDAR and POS data. Figure B.8 illustrates the LISPAC interface from the visualization of the georeferenced point cloud to the extraction of each planar target.

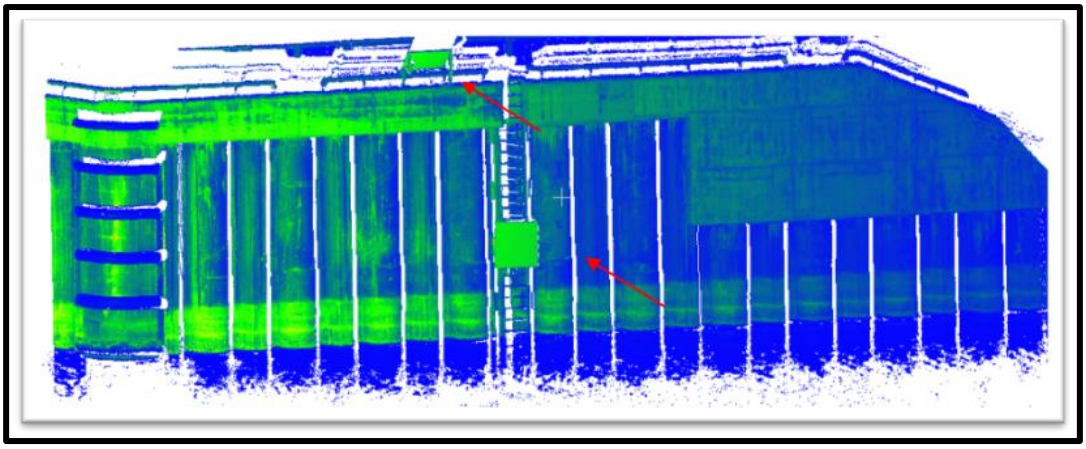

(a)

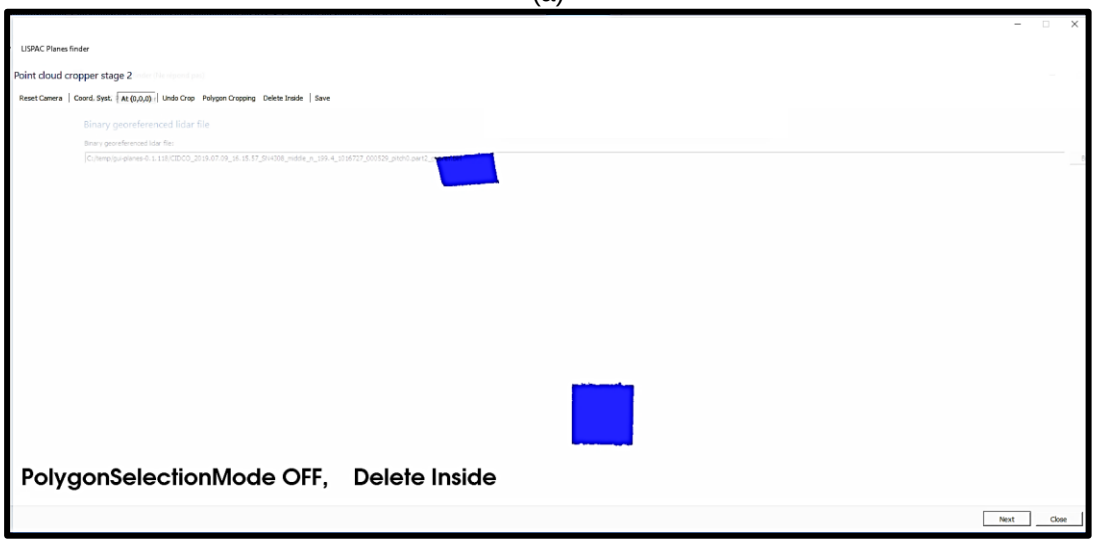

(b)

Figure B.8 – LISPAC Plane Finder Module. (a) we define a point in the point cloud. (b) the module automatically extracts the planar targets.

B.3 Boresight Estimation Module

In this section, we present the theory and the mathematical model that enable us to estimate the boresight angles and their uncertainties. Figure B.9 illustrates the details of the boresight angles estimation module.

We can enter the least-squares iterative procedure with the input prepared in the previous section. The algorithm estimates the boresight angle values and their respective uncertainties in the first iteration. The iterations continue until the

statistical tests are satisfied. In a typical case, it takes 3 to 4 iterations to converge to a solution.

In Figure B.9, we introduce more details of the iterative least-squares procedure.

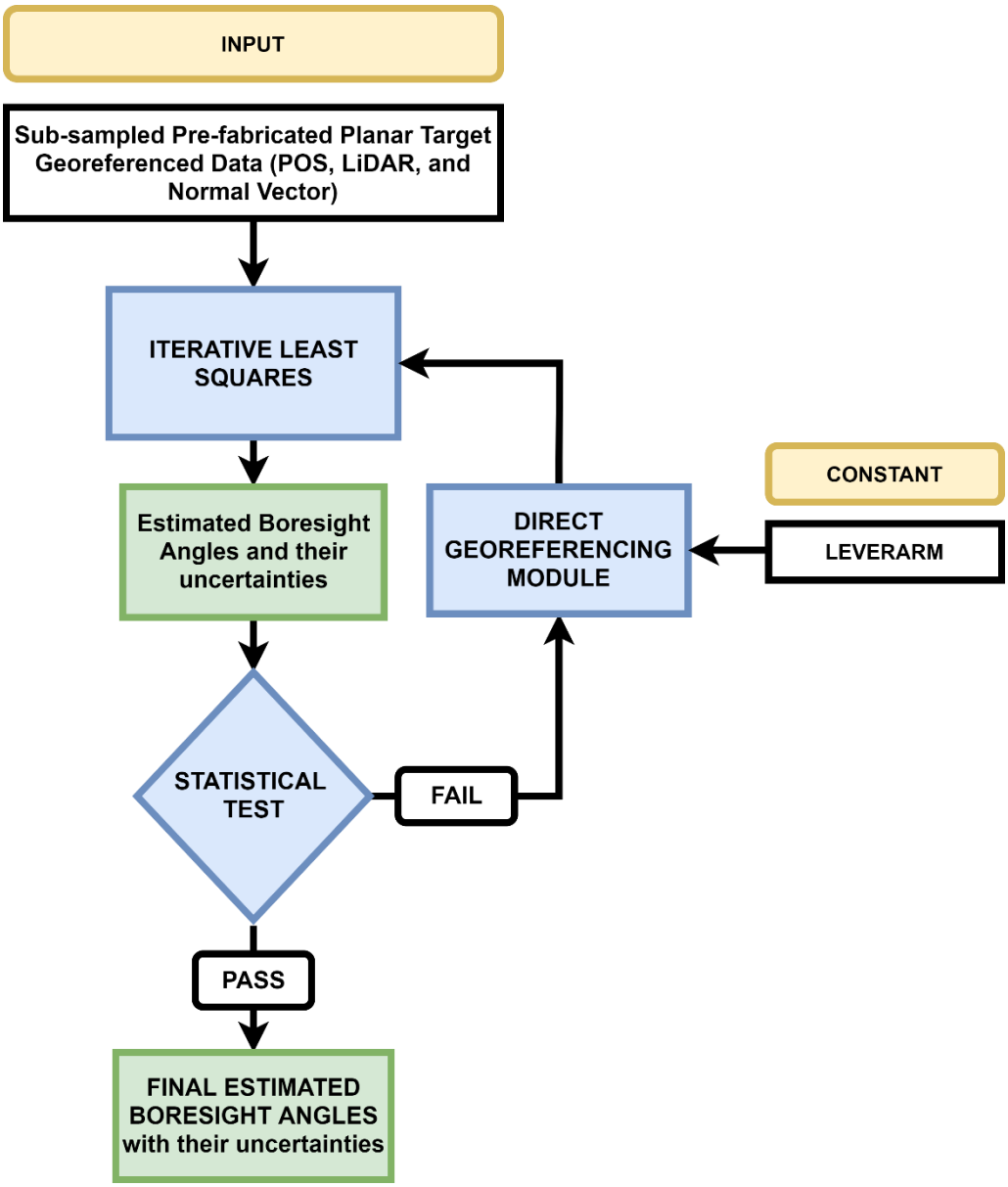

Figure B.9 – Boresight angles estimation module. Blue boxes are the functions that we utilize in the boresight estimation module. The white boxes are the input parameters from the sensors and the planar extraction module. The green boxes are the output for each step.

Table B.1 represents the indices of the matrices (defining their size) used in the least-squares technique and enables us to understand the equations easily and to be able to implement them in our software in a simple manner.

Table B.1 – Definition of the indices used in the matrices of the least-squares technique

# $points/Conditions$	pts
# $planar\ target$/Constraints	$c\ = pls$
#.$observations$	$n = 9\ \times pts$
# $unknowns$	$u_0 = \ 3 + 4\ \times pls$
# $equations$	$n_0 = r + \ u_0 + c$

Firstly, in Equation (B.4), we define the matrix A, which is the partial derivatives of Equation (4.4) w.r.t the unknowns vector $x_{[u_0 \times 1]} = \ (\alpha, \beta, \gamma, a_i, b_i, c_i, d_i)$.

$$A_{[n_0 \times u_0]} = \left[\frac{\partial F}{\partial \alpha}\ \frac{\partial F}{\partial \beta}\ \frac{\partial F}{\partial \gamma}\ \frac{\partial F}{\partial a_i}\ \frac{\partial F}{\partial b_i}\ \frac{\partial F}{\partial c_i}\ \frac{\partial F}{\partial d_i}\right] \tag{B.4}$$

Secondly, in Equation (B.5), we define the matrix B, which is the partial derivative of Equation (4.4) with respect to observations vector $(P_X^{LGF}, P_X^{LGF}, P_X^{LGF}, r, p, h, x_{LiDAR}, y_{LiDAR}, z_{LiDAR})$.

$$B_{[n_0 \times n]} = \begin{bmatrix} [B_{1\times 9}] & \emptyset & \emptyset & \cdots \\ \emptyset & [B_{2\times 9}] & \emptyset & \cdots \\ \vdots & \emptyset & \ddots & \vdots \end{bmatrix} \tag{B.5}$$

$$With\ \ B_{[i\times 9]} = \left[\frac{\partial F}{\partial P_{x^{LGF}}}\ \frac{\partial F}{\partial P_{y^{LGF}}}\ \frac{\partial F}{\partial P_{z^{LGF}}}\ \frac{\partial F}{\partial r}\ \frac{\partial F}{\partial p}\ \frac{\partial F}{\partial h}\ \frac{\partial F}{\partial x_{LiDAR}}\ \frac{\partial F}{\partial y_{LiDAR}}\ \frac{\partial F}{\partial z_{LiDAR}}\right]$$

Thirdly, to define Q_{ll}, we consider the uncertainties related to each observation parameter, presented in Equation (B.6).

$$Q_{ll} = \begin{bmatrix} [Q_{ll_1}]_{9\times 9} & \emptyset & \emptyset & \ldots \\ \emptyset & [Q_{ll_1}]_{9\times 9} & \emptyset & \cdots \\ \vdots & \emptyset & \ddots & \vdots \end{bmatrix} \tag{B.6}$$

$$With \quad Q_{ll_i} = diagMatrix \left[\sigma^2_{P_{x^{LGF}}} \ \sigma^2_{P_{y^{LGF}}} \ \sigma^2_{P_{z^{LGF}}} \ \sigma^2_r \ \sigma^2_p \ \sigma^2_h \ \sigma^2_{x_{LiDAR}} \ \sigma^2_{y_{LiDAR}} \ \sigma^2_{z_{LiDAR}}\right]$$

Fourthly, in Equation (B.7), we define the disclosure matrix,

$$w_{[n_0 \times 1]} = a_i X_{LGF} + b_i Y_{LGF} + c_i Z_{LGF} + d_i \tag{B.7}$$

Equations (B.4), (B.5), (B.6), and (B.7) lead to Equation (B.8), which calculates the unknown parameters.

$$(A^T (B Q_{ll} B^T)^{-1} A) x_{[u_0 \times 1]} = -A^T (B Q_{ll} B^T)^{-1} w \tag{B.8}$$

The constraints are defined by Equation (4.5) which is first linearized based on Equation (B.9),

$$A_{c_{[n_c \times u_0]}} x_{[u_0 \times 1]} = w_{c_{[n_c \times 1]}} \tag{B.9}$$

$$with \ A_{c_{[n_c \times u_0]}} = \left[\frac{\partial G}{\partial dr} \ \frac{\partial G}{\partial dp} \ \frac{\partial G}{\partial dh} \ \frac{\partial G}{\partial a_i} \ \frac{\partial G}{\partial b_i} \ \frac{\partial G}{\partial c_i} \ \frac{\partial G}{\partial d_i}\right]$$

$$\text{and } w_{c_{[n_c \times 1]}} = a_i^2 + b_i^2 + c_i^2 - 1$$

To consider the constraints in the overall least-squares procedure, we arrive at Equation (B.10),

$$x_{[u_0 \times 1]} = (A^T (B Q_{ll} B^T)^{-1} A + A_c^T P_c A_c)^{-1} (-A^T (B Q_{ll} B^T)^{-1} - A_c^T P_c w_c) \tag{B.10}$$

$$P_{c_{[n_c \times n_c]}} = \begin{bmatrix} \frac{1}{\sigma_c^2} & 0 & \dots \\ 0 & \frac{1}{\sigma_c^2} & 0 \\ \vdots & 0 & \ddots \end{bmatrix} \qquad \sigma_c^2 \ \rightarrow very \ small \ value \ like \ 10^{-6}$$

A posterior variance factor which is considered one of the iteration loop parameters in presented in Equation (B.11),

$$v = Q_{ll}B^T M^{-1}(AN^{-1}A^T M^{-1} - I)w$$
$$S_0^2 = \frac{v^T P v}{df} \tag{B.11}$$

Finally, we consider Equation (B.12) to estimate the boresight angles' standard deviations.

$$Q_{xx} = (A^T(BQ_{ll}B^T)^{-1}A)^{-1} \tag{B.12}$$

$$\sigma_{dr} = \sqrt[2]{Q_{xx}(1,1)} \qquad \sigma_{dp} = \sqrt[2]{Q_{xx}(2,2)} \qquad \sigma_{dy} = \sqrt[2]{Q_{xx}(3,3)}$$

The above procedures are from various well-established literature in least-squares adjustments in surveying and geodesy (Ghilani 2010; Cocard 2017; Skaloud and Lichti 2006). The algorithm of boresight estimation is presented in Figure B.10.

ALGORITHM 3: ALGORITHM TO ESTIMATE BORESIGHT ANGLES (α, β, γ)

Input1: n_x, n_y, n_z, d *// Normal of the plane targets*
Input2: $x_{LiDAR}, y_{LiDAR}, z_{LiDAR}$ *// Plane points coordinates in LiDAR frame*
Input3: $\boldsymbol{\sigma}_{x_{LiDAR}}, \boldsymbol{\sigma}_{y_{LiDAR}}, \boldsymbol{\sigma}_{z_{LiDAR}}$ *// Uncertainties of plane points in LiDAR frame*
Input4: $r, p, h, \boldsymbol{\sigma}_r, \boldsymbol{\sigma}_p, \boldsymbol{\sigma}_h$ *// POS attitudes of plane points & their uncertainties*
Input5: $\boldsymbol{P}_{LGF}, \boldsymbol{\sigma}_{\boldsymbol{P}_{LGF}}$ *// POS positions in LGF of plane points & their uncertainties*
Output: *Boresight Angles* (α, β, γ) *and their Uncertainties*

Initialization of variables: *assign 1 to the variable* $\Delta\boldsymbol{x}$ *// Correction differences*
Initialization of variables: *assign 0 to the variables* $\alpha, \beta, \gamma, \boldsymbol{\sigma}_\alpha, \boldsymbol{\sigma}_\beta, \boldsymbol{\sigma}_\gamma$
number-of-Points ← *count the total number of points on the planes*
while ($\Delta\boldsymbol{x}$ > ***eps)***
    Initialization of variables*: assign zero to the variable* ***i***
    for (***i*** < ***number-of-Points***) *// read all the points and calculate the rotation matrix*
        $(X^{LGF}, Y^{LGF}, Z^{LGF})$ ← Re-georeferencing the points
        A ← *Design Matrix*
        B ← *Observation Matrix*
        Q_{ll} ← *Weight Matrix*
        W ← *Closure Vector*
        Ac ← *Constraint Design Matrix*
        Pc ← *Constraint Weight Matrix*
        Wc ← *Constraint Closure Vector*
    end
    $M \leftarrow BQ_{ll}B^T$
    $N \leftarrow A^TM^{-1}A + A_c^TP_cA_c$
    $n \leftarrow -A^TM^{-1}W - A_c^TP_cW_c$
    $\Delta\boldsymbol{x} \leftarrow norm(N^{-1}n)$
    $\Delta\alpha, \Delta\beta, \Delta\gamma \leftarrow \Delta\boldsymbol{x}$ *// the three first elements of the correction vector*
    $\alpha \leftarrow \alpha + \Delta\alpha$
    $\beta \leftarrow \beta + \Delta\beta$
    $\gamma \leftarrow \gamma + \Delta\gamma$
end
$Q_{xx} \leftarrow N^{-1}$
$\boldsymbol{\sigma}_\alpha, \boldsymbol{\sigma}_\beta, \boldsymbol{\sigma}_\gamma \leftarrow Q_{xx}$ *// the sqrt of the three first elements on the diagonal of the matrix*
disp $(\alpha, \beta, \gamma, \boldsymbol{\sigma}_\alpha, \boldsymbol{\sigma}_\beta, \boldsymbol{\sigma}_\gamma)$

Figure B.10 - Algorithm 3 for the estimation of boresight angles and their uncertainties

Appendix C – Further Analysis of Systematic Errors of Mobile LiDAR Systems

C.1 Introduction

Chapter 3 has discussed the systematic errors of a terrestrial MLS with simulated point clouds, and Section 3.5.2 presents the detailed results and analysis of the pitch boresight angle. This chapter presents the results of the other seven systematic errors in detail. These seven remaining systematic errors are as follows: roll boresight error, yaw boresight error, X lever arm error, Y lever arm error, Z lever arm error, range offset error, and scan angle offset error. For each of these systematic errors, we visually introduce their ***Type I*** and ***Type II*** visibility criteria and a brief discussion on the effect of each systematic error on the planar targets' simulated point clouds.

C.2 Simulation-Based Systematic Errors Analysis

This section discusses in detail the behavior of systematic errors of a terrestrial MLS. Based on the theoretical and conceptual aspects developed in Chapter 3, we generate a simulated point cloud based on various scenarios.

C.2.1 Roll Boresight Error

In this section, to study the impact of the roll boresight angle, we inserted 2˚ roll boresight error into the MLS simulator and analyzed the impact on the hypothetical planar target. The inclination of the plane varies between -60° and 30°. Figure C.1 presents the values for the ***Type I*** criterion for all the six MLS passages and the 19 plane inclinations. The blue box in Figure C.1 is considered the plane's inclination, and the ***Type I*** criterion is within the expected threshold.

Figure C.2 illustrates the values for the ***Type II*** criteria. The blue box in Figure C.2 is considered the plane's orientation that the ***Type II*** criteria are within the expected threshold.

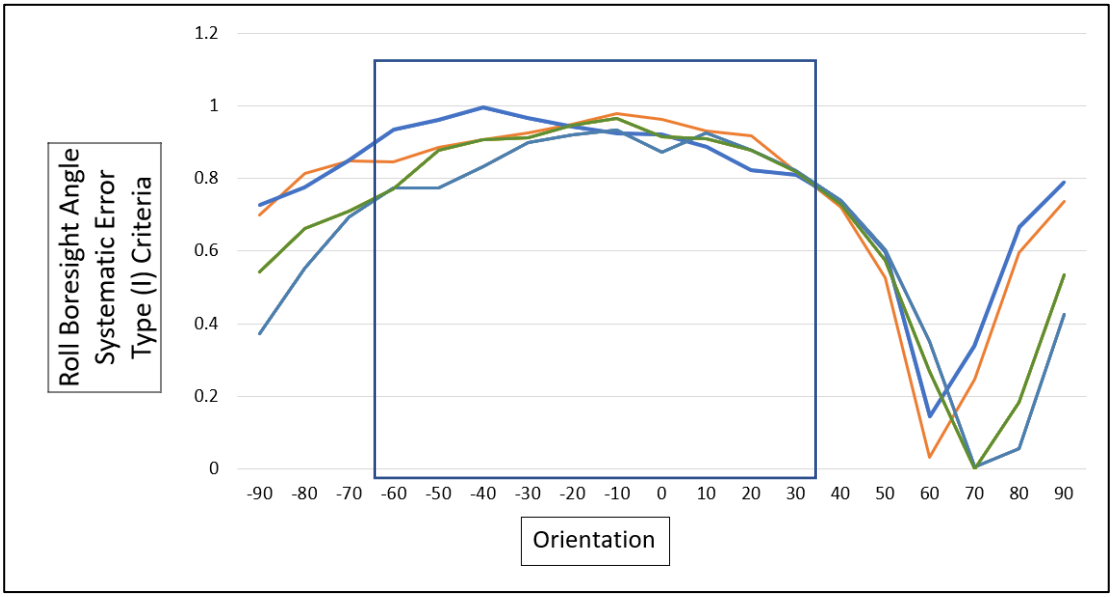

Figure C.1– Roll boresight angle ***Type I*** systematic-error visibility criterion (vertical axis in meter) of all the possible orientations or inclinations (horizontal axis in degree)

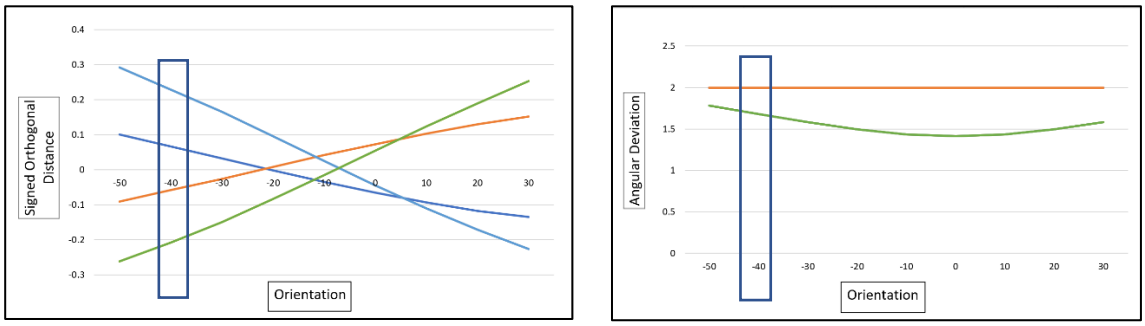

(a) (b)

Passage	0°	180°	45°	225°	315°	135°
Color						

Figure C.2 – Roll boresight angle systematic error ***Type II*** criteria (a) Signed orthogonal distance (vertical axis in meter) and (b) Angular deviation (vertical axis in degree) of possible orientations or inclinations (horizontal axis in degree)

Based on the results of the ***Type II*** visibility criteria, illustrated in Figure C.2, for inserting the roll boresight angle on an MLS, a planar target with an orientation of -40° with respect to terrestrial MLS is considered as the optimum value.

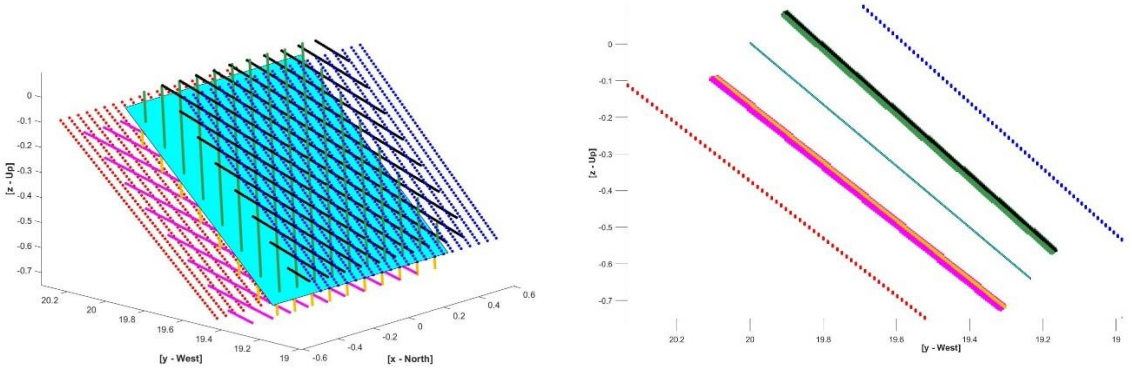

(a) (b)

Figure C.3 – Schematic presentation of a simulated point cloud of a terrestrial MLS simulator with inserted roll boresight angle. (a) side-looking view. (b) Y-Z view.

To go further in our analysis, we use the schematic results of the selected orientation (30°) as illustrated in Figure C.3.

Thus, based on our analysis, we suggest a planar target of 1m x 1m with a 30° orientation and a round-trip parallel and one side round-trip (45°-225° or 315°-135°) in any of the two sides of the planar target, to achieve the optimum configuration for the roll boresight angle.

C.2.2 Yaw Boresight Error

In this section, to study the impact of the yaw boresight angle, we inserted 2° yaw boresight error into the MLS simulator and analyzed the impact on the hypothetical planar target. The orientation of the plane varies between -60° and 30°. Figure C.4 presents the values for the ***Type I*** criterion for all the six MLS passages and the 19 plane inclinations. The blue box in Figure C.4 is considered the plane's inclination, and the ***Type I*** criterion is within the expected threshold. Figure C.5 illustrates the values for the ***Type II*** criterion. The blue box in Figure C.5 is considered the plane's orientation that the ***Type II*** criterion is within the expected threshold.

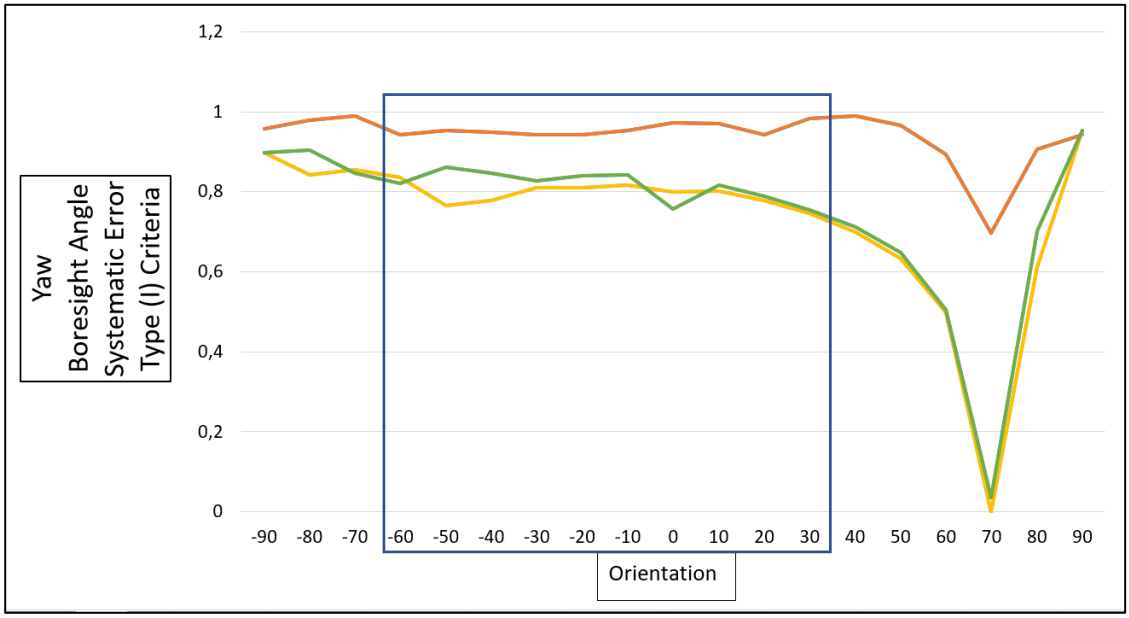

Figure C.4– Yaw boresight angle ***Type I*** systematic-error visibility criterion (vertical axis in meter) of all the possible orientations or inclinations (horizontal axis in degree)

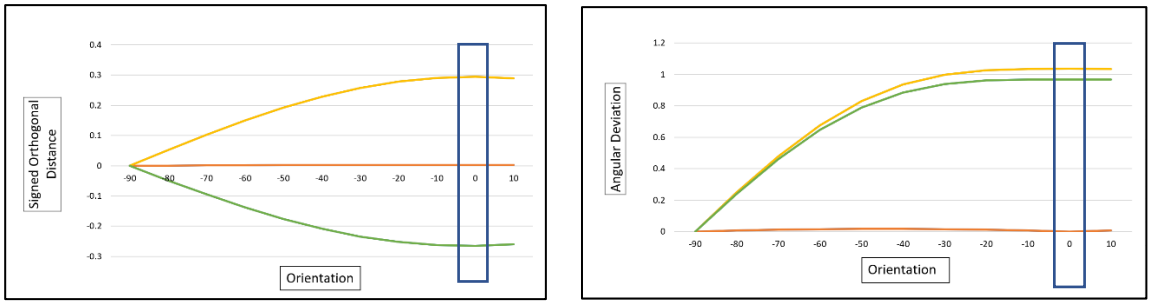

(a) (b)

Passage	0°	180°	45°	225°	315°	135°
Color						

Figure C.5 – Yaw boresight angle systematic error ***Type II*** criterion (a) Signed orthogonal distance (vertical axis in meter) and (b) Angular deviation (vertical axis in degree) of possible orientations or inclinations (horizontal axis in degree)

For the yaw boresight angle, the inclination of 0° (vertical plane) is the optimum value, as shown in Figure C.6.

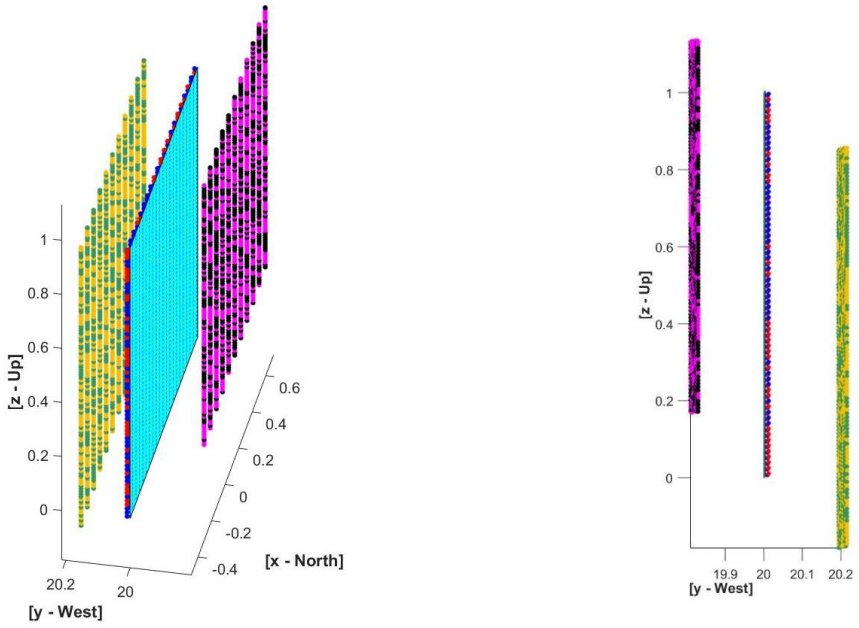

(a) (b)

Figure C.6 – Schematic presentation of a simulated point cloud of a terrestrial MLS simulator with inserted heading boresight angle. (a) side-looking view. (b) Y-Z view.

Thus, we suggest a vertical planar target of 1m x 1m with 0° inclinations and one of the round-trips parallel to the planar target (0° or 180°) and a round-trip on each of the two sides of the planar target (45°-315° or 45°-135° or 225°-315° or 225°-315°), to achieve the optimum configuration for the yaw boresight angle.

C.2.3 X Lever arm Error

In this section, to study the impact of the X lever arm systematic error, we inserted an error of 10 cm into the MLS simulator and analyzed the impact on the hypothetical planar target. The inclination of the plane varies between -90° and 30°. Figure C.7 presents the values for the ***Type I*** criterion for all the six MLS passages and the 19 plane inclinations. The blue box in Figure C.7 is considered the plane's inclination, and the ***Type I*** criterion is within the expected threshold.

Figure C.8 illustrates the values for the ***Type II*** criteria. The blue box in Figure C.8 is considered the plane's inclination, and the ***Type II*** criteria are within the expected threshold.

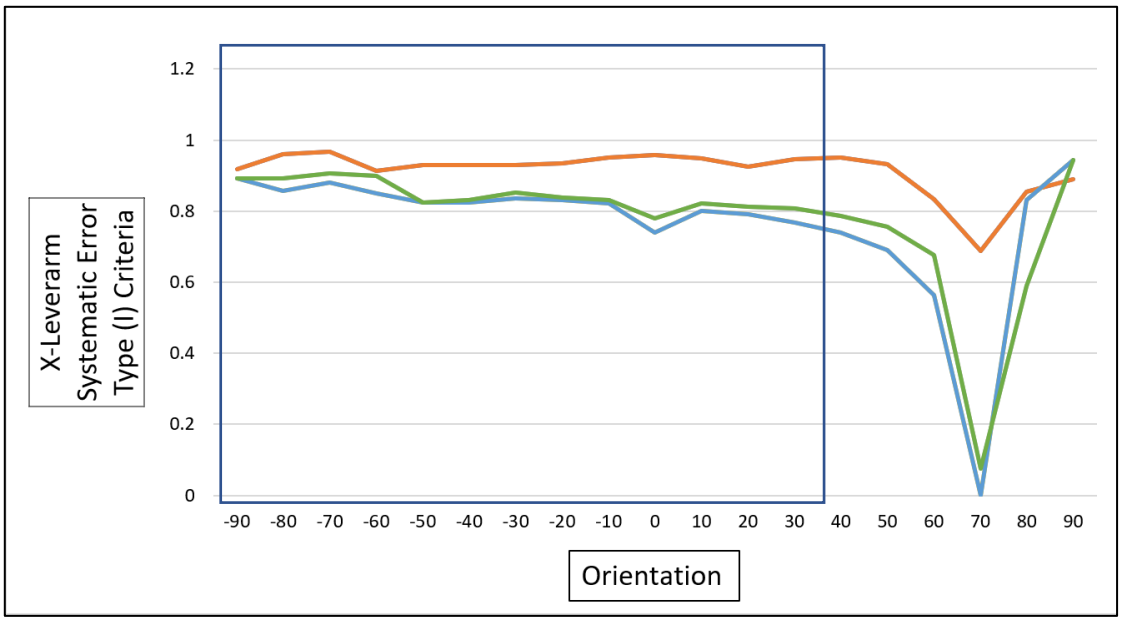

Figure C.7 – X lever arm ***Type I*** systematic-error visibility criterion (vertical axis in meter) of all the possible orientations or inclinations (horizontal axis in degree)

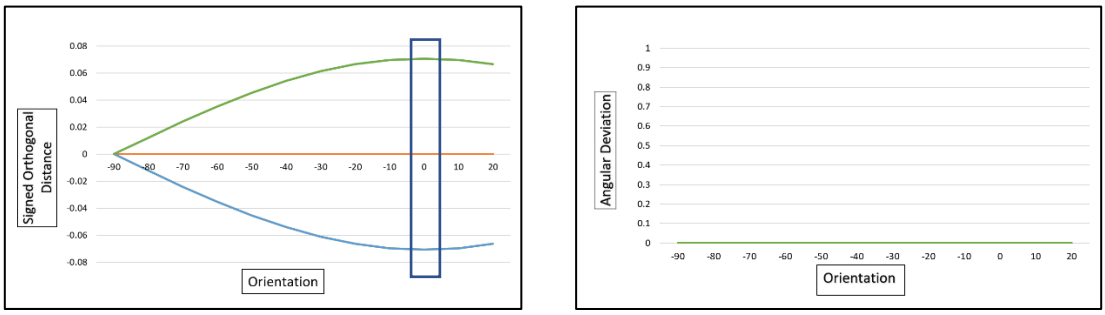

(a) (b)

Passage	0°	180°	45°	225°	315°	135°
Color						

Figure C.8 – X lever arm systematic error ***Type II*** criteria (a) Signed orthogonal distance (vertical axis in meter) and (b) Angular deviation (vertical axis in degree) of possible orientations or inclinations (horizontal axis in degree)

For the X lever arm, the inclination of 0° is the optimum value, as we can see in Figure C.8. As we expect and see in Figure C.9, lever arm systematic errors, which are translations. The generated point cloud will not have any rotations contrary to

the boresight angle systematic errors, which is valid for all the lever arms in the X, Y, and Z directions.

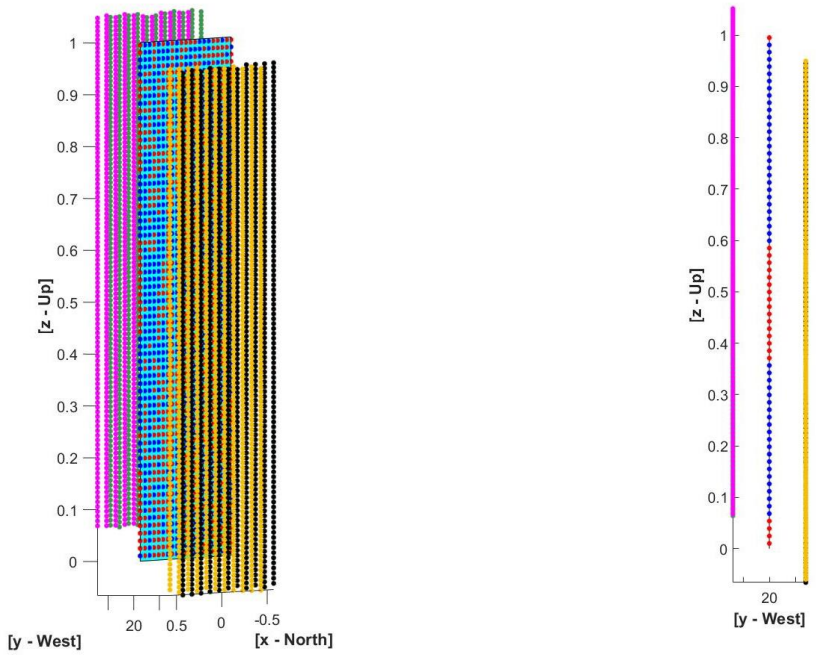

(a) (b)

Figure C.9 – Schematic presentation of a simulated point cloud of a terrestrial MLS simulator with the inserted X lever arm. (a) side-looking view. (b) Y-Z view.

Thus, based on our analysis, we suggest a planar target of 1m x 1m with 0° inclination and one of the round-trips parallel to the planar target (0° or 180°) and a side round-trip of one of the sides of the planar target (45°-225° or 315°-135°), to achieve the optimum configuration for the X lever arm.

C.2.4 Y Lever arm Error

In this section, to study the impact of the Y lever arm systematic error, we inserted an error of 10 cm into the MLS simulator and analyzed the impact on the hypothetical planar target. The inclination of the plane varies between -90° and 30°. Figure C.10 presents the values for the ***Type I*** criterion for all the six MLS passages and the 19 plane inclinations. The blue box in Figure C.10 is considered the plane's inclination, and the ***Type I*** criterion is within the expected threshold.

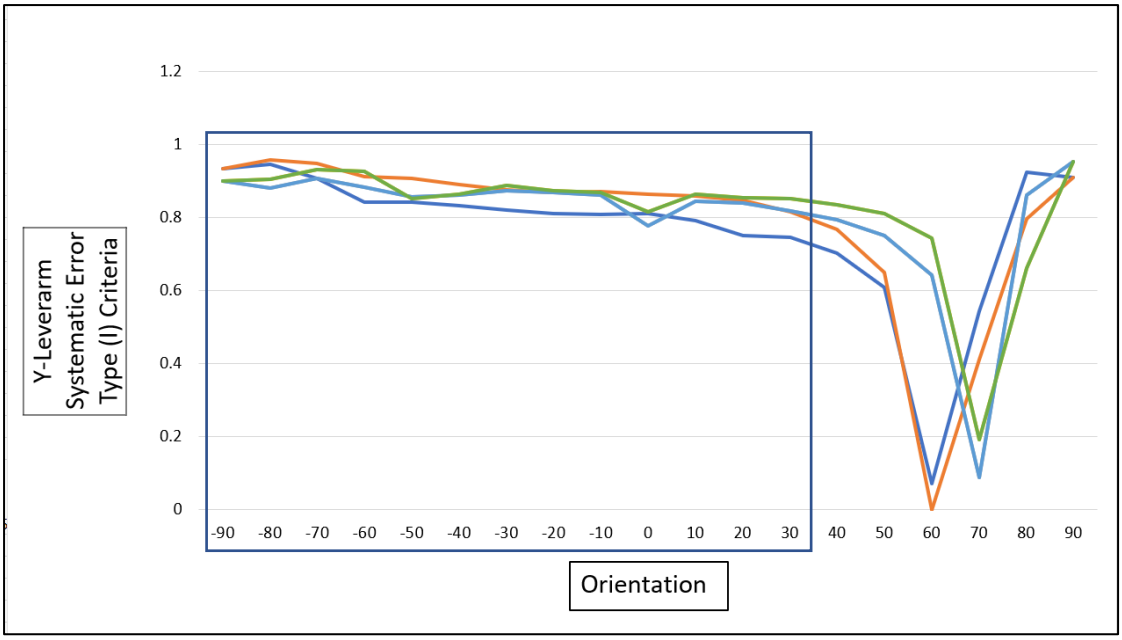

Figure C.10 – Y lever arm ***Type I*** systematic-error visibility criterion (vertical axis in meter) of all the possible orientations or inclinations (horizontal axis in degree)

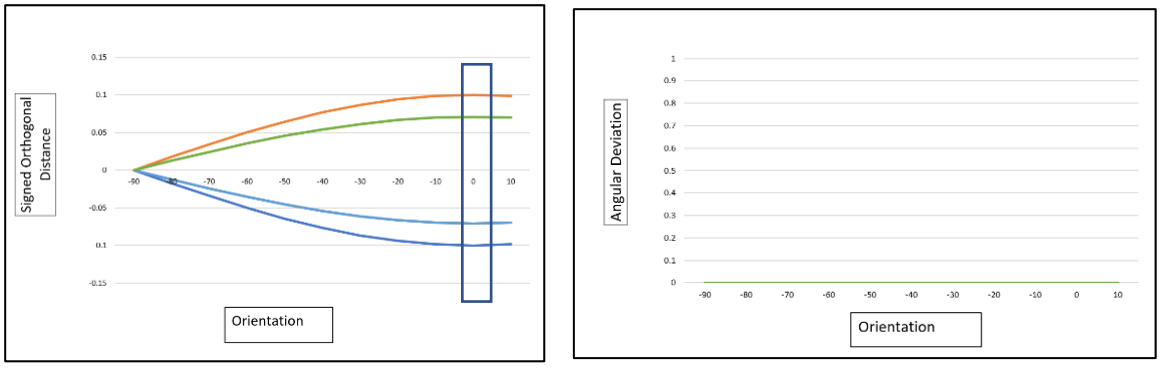

(a) (b)

Passage	0°	180°	45°	225°	315°	135°
Color						

Figure C.11 – Y lever arm systematic error ***Type II*** criteria (a) Signed orthogonal distance (vertical axis in meter) and (b) Angular deviation (vertical axis in degree) of possible inclinations (horizontal axis in degree)

Figure C.11 illustrates the values for the ***Type II*** criteria. The blue box in Figure C.11 is considered the plane's inclination, and the ***Type II*** criteria are within the expected threshold.

For the Y lever arm error, the inclination of 0° is the optimum value, as we can see in Figure C.11. As we expect, for the lever arm, systematic errors are translations. The generated point cloud will not have any rotations contrary to the boresight angle systematic errors, which is valid for all the lever arms in the X, Y, and Z directions.

Thus, based on our analysis, as we illustrate in Figure C.12, we suggest a planar target of 1m x 1m with 0° inclination and a full round-trip parallel to the planar target (0° - 180°) and a round-trip of one of the sides of the planar target (45°-225° or 315°-135°), to achieve the optimum configuration for the Y lever arm.

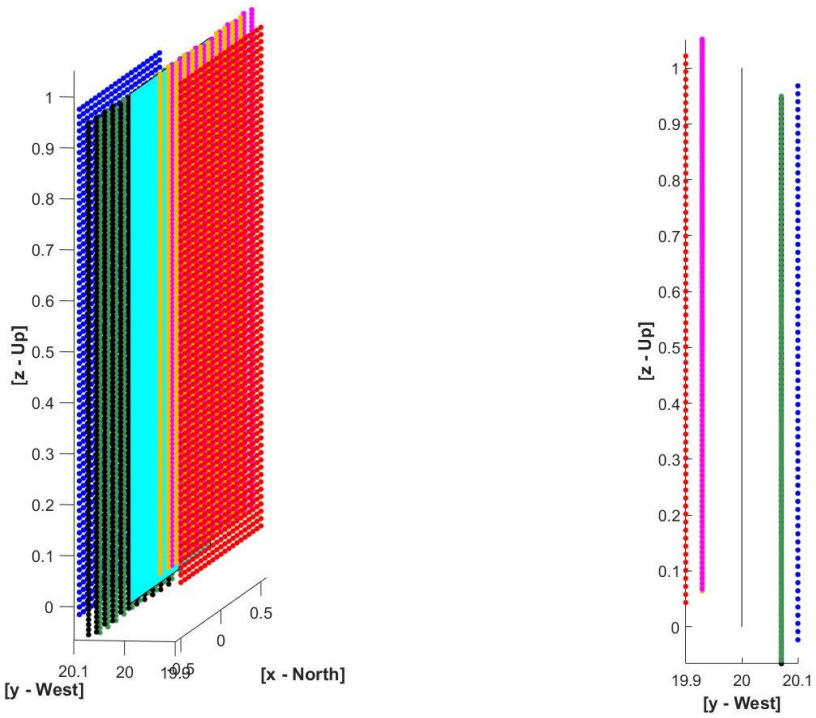

(a) (b)

Figure C.12 – Schematic presentation of a simulated point cloud of a terrestrial MLS simulator with the inserted Y lever arm. (a) side-looking view. (b) Y-Z view.

C.2.5 Z Lever arm Error

In this section, to study the impact of the Z lever arm systematic error, we inserted a Z lever arm error of 10 cm into the MLS simulator and analyzed the impact on the hypothetical planar target. The inclination of the plane varies between -90° and 30°. Figure C.13 presents the values for the ***Type I*** criterion for all the six MLS passages and the 19 plane inclinations. The blue box in Figure C.13 is considered the plane's inclination, and the ***Type I*** criteria are within the expected threshold.

Figure C.14 illustrates the values for the ***Type II*** criterion, and as we can see, all the passages superpose each other. For the Z lever arm, we do not recognize any difference between the various inclinations of the planar target. Nevertheless, as we can see in Figure C.15, we choose the orientation of -60˚.

If we insert the Z lever arm systematic error to a terrestrial MLS and we scan the hypothetical plane with a six-line pattern (0˚ - 180˚ - 45˚ - 225˚ - 315˚ - 135˚), the impact of such error on a planar target is the same and as we can see all the generated point cloud will lay on the same planar target.

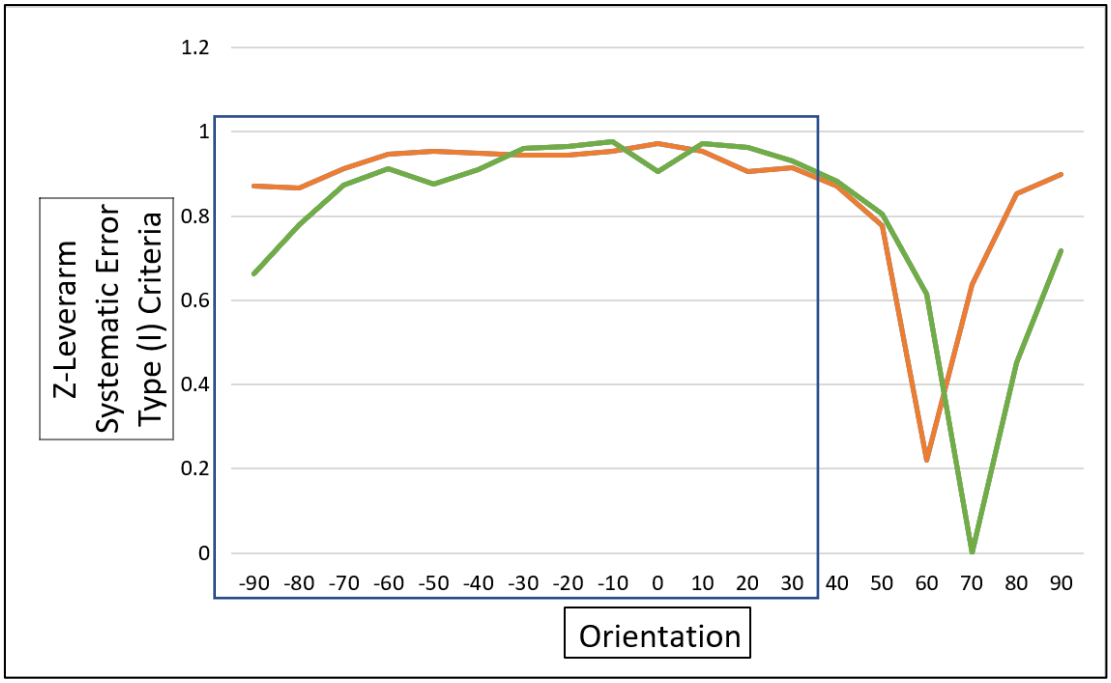

Figure C.13 – Z lever arm ***Type I*** systematic-error visibility criterion (vertical axis in meter) of all the possible orientations or inclinations (horizontal axis in degree)

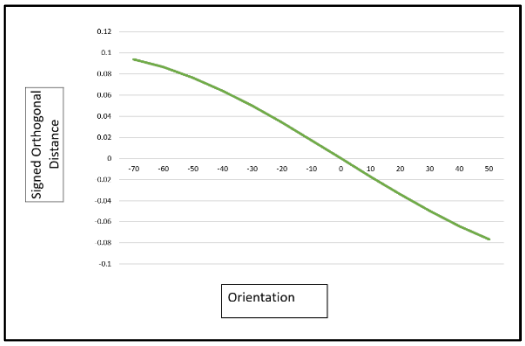

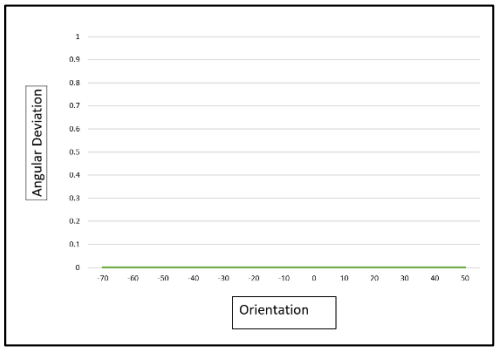

(a) (b)

Passage	0°	180°	45°	225°	315°	135°
Color						

Figure C.14 – Z lever arm systematic error ***Type II*** criterion (a) Signed orthogonal distance (vertical axis in meter) and (b) Angular deviation (vertical axis in degree) of possible orientations or inclinations (horizontal axis in degree)

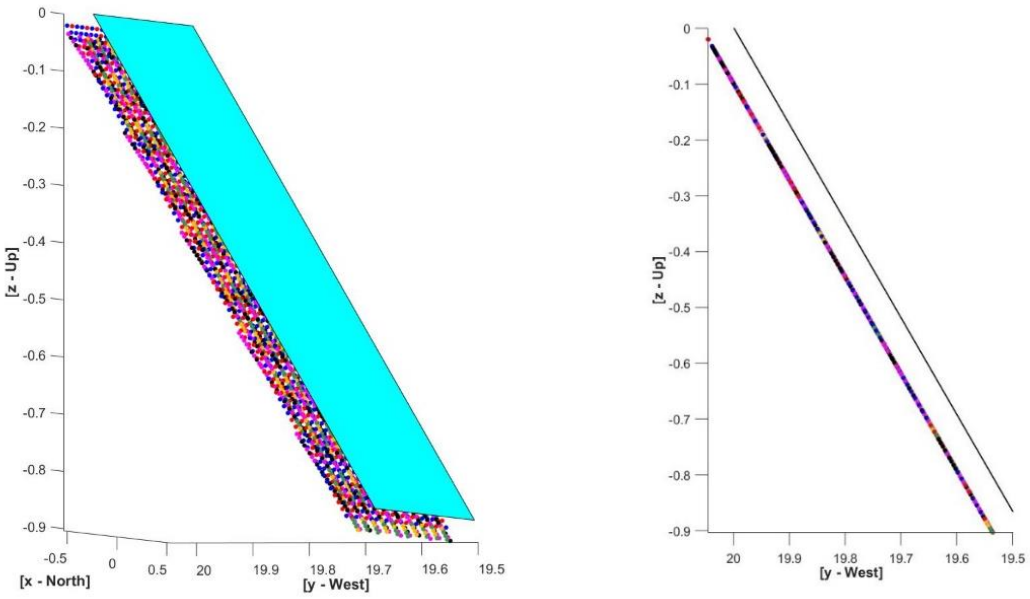

(a) (b)

Figure C.15 – Simulated point cloud of a terrestrial MLS simulator with the inserted Z lever arm. (a) side-looking view. (b) Y-Z view.

The only possibility, as illustrated in Figure C.16, for the detection of the impact of a Z lever arm systematic error on a planar target is that the platform scans the plane in a parallel passage with the constraint that in one direction, the platform must be upside down, which is impossible in a terrestrial or marine MLS.

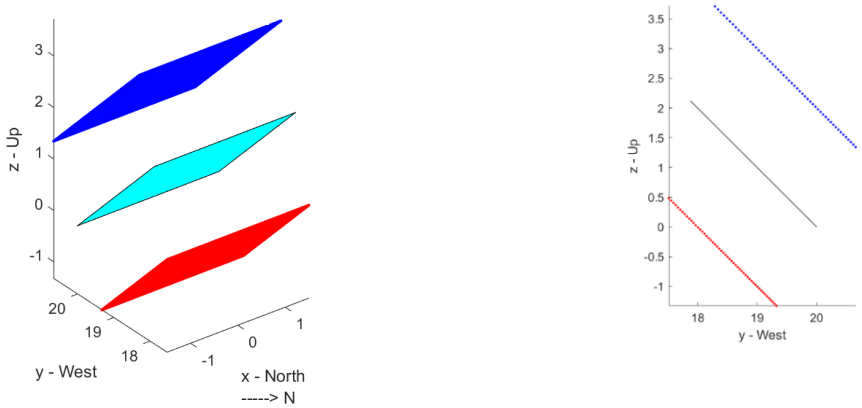

(a) (b)

Figure C.16 – Schematic presentation of a simulated point cloud of a marine MLS simulator with an inserted Z lever arm in two opposite directions. (a) side-looking view. (b) Y-Z view.

C.2.6 LiDAR Range Offset Error

In this section, to study the impact of LiDAR range offset systematic error, we inserted a range offset of 10 cm into the MLS simulator and analyzed the impact on the hypothetical planar target. The inclination of the plane varies between -40° and 10°. Figure C.17 presents the values for the ***Type I*** criterion for all the six MLS passages and the 19 plane inclinations. The blue box in Figure C.17 is considered the plane's inclination, and the ***Type I*** criterion is within the expected threshold.

Passage	0°	180°	45°	225°	315°	135°
Color						

Figure C.18 illustrates the values for the ***Type II*** criterion, and the blue box is considered the plane's inclination that the ***Type II*** criterion is within the expected threshold. For LiDAR range offset, the inclination of -60° is the optimum value, as shown in Figure C.18.

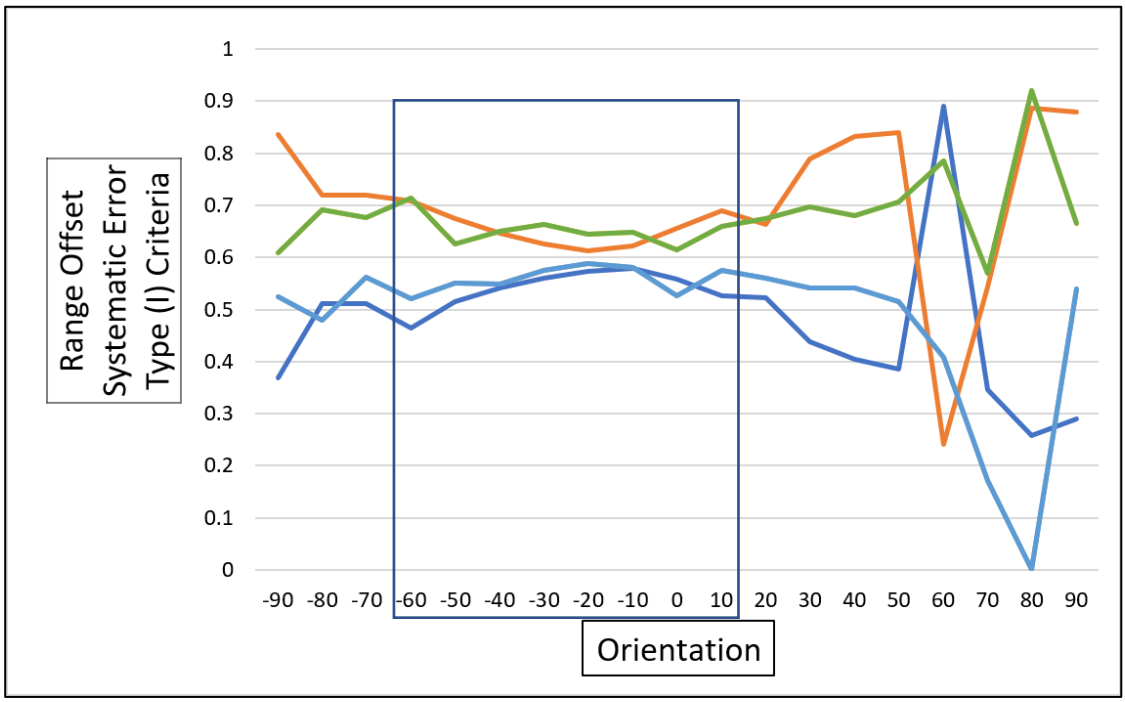

Figure C.17 – LiDAR range offset ***Type I*** systematic-error visibility criterion (vertical axis in meter) of all the possible orientations or inclinations (horizontal axis in degree)

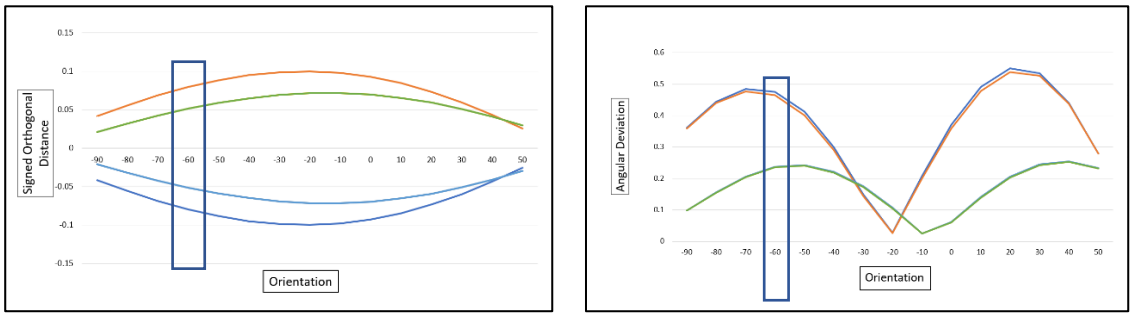

(a) (b)

Passage	0°	180°	45°	225°	315°	135°
Color						

Figure C.18 – LiDAR range offset systematic error ***Type II*** criteria (a) Signed orthogonal distance (vertical axis in meter) and (b) Angular deviation (vertical axis in degree) of possible orientations or inclinations (horizontal axis in degree)

Thus, based on our analysis and Figure C.19, we suggest a planar target of 1m x 1m with -60° inclination and a full round-trip parallel to the planar target (0° - 180°) and a side round-trip of one of the sides of the planar target (45°-225° or 315°-135°), to achieve the optimum configuration for the range offset systematic error.

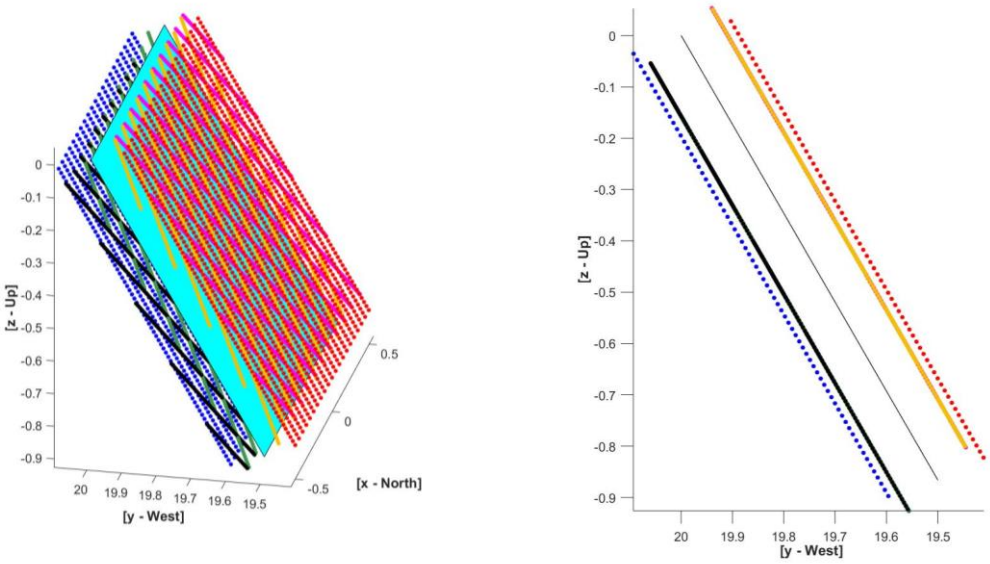

(a) (b)

Figure C.19 – Schematic presentation of a simulated point cloud of a terrestrial MLS simulator with inserted range offset. (a) side-looking view. (b) Y-Z view.

C.2.7 LiDAR Scan Angle Offset Error

In this section, to study the impact of the LiDAR scan angle offset systematic error, we inserted a scan angle offset of 1º into the MLS simulator and analyzed the impact on the hypothetical planar target. The inclination of the plane varies between -50° and 10°. Figure C.20 presents the values for the ***Type I*** criterion for all the six MLS passages and the 19 plane inclinations. The blue box in Figure C.20 is considered the plane's inclination, and the ***Type I*** criterion is within the expected threshold.

Figure C.21 illustrates the values for the ***Type II*** criterion with the blue box considering the plane's inclination that the ***Type II*** criteria are within the expected threshold. For LiDAR range offset, the inclination of 30° is the best value, as shown in Figure C.21.

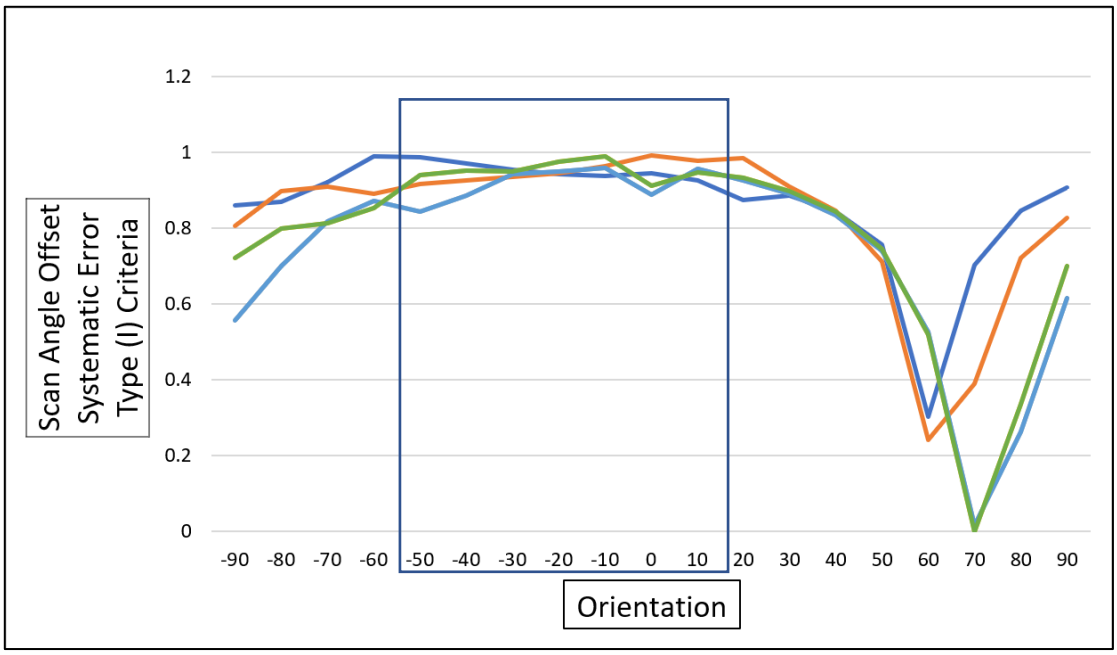

Figure C.20 – LiDAR scan angle offset ***Type I*** systematic-error visibility criterion (vertical axis in meter) of all the possible orientations (horizontal axis in degree)

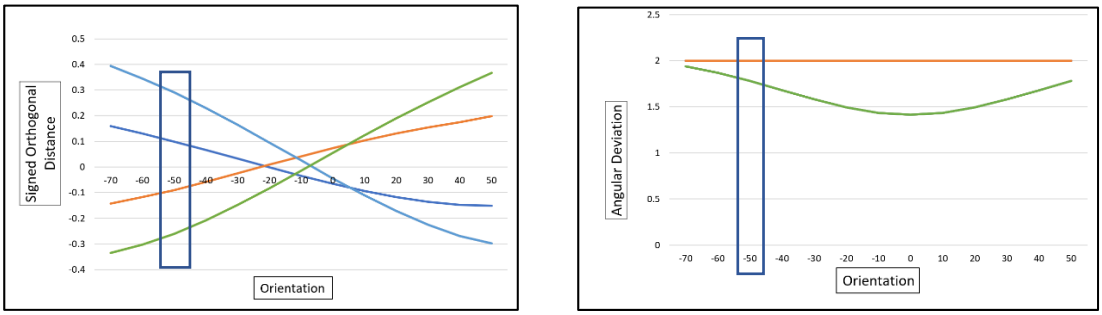

(a) (b)

Passage	0°	180°	45°	225°	315°	135°
Color						

Figure C.21 – LiDAR scan angle systematic error ***Type II*** criteria (a) Signed orthogonal distance (vertical axis in meter) and (b) Angular deviation (vertical axis in degree) of possible orientations or inclinations (horizontal axis in degree)

Thus, based on our analysis and Figure C.22, we suggest a planar target of 1m x 1m with -50° inclination and a full round-trip parallel to the planar target (0° - 180°)

and a side round-trip of one of the sides of the planar target (45°-225° or 315°-135°), to achieve the optimum configuration for the scan angle offset systematic error.

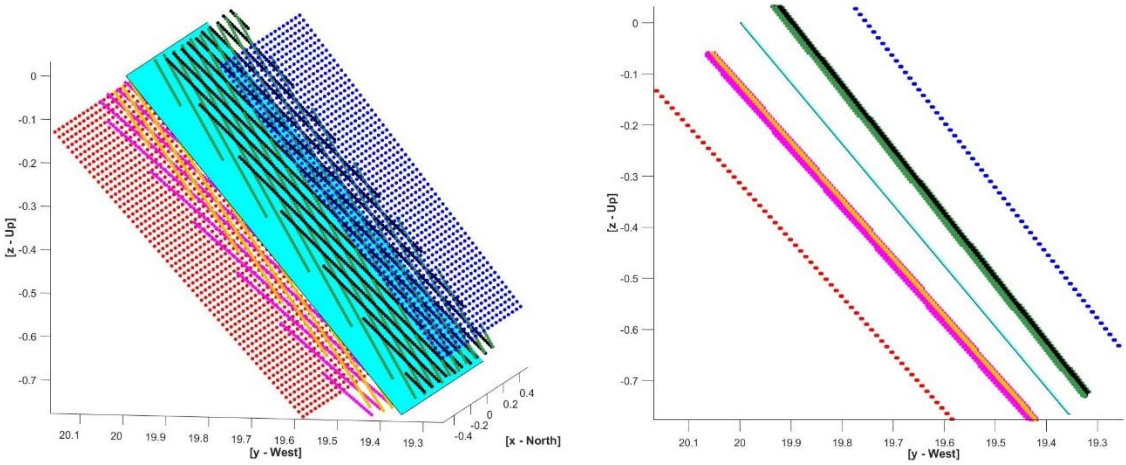

(a) (b)

Figure C.22 – Simulated point cloud of a terrestrial MLS simulator with a scan angle offset. (a) side-looking view. (b) Y-Z view.

C.3 Conclusions

In this appendix, we complemented Chapter 3 by presentation of the results and analysis of all eight systematic errors of a terrestrial MLS. The results show that to have strong visibility of the systematic errors of an MLS mounted on a terrestrial platform, the best configuration consists of two to three planar targets of 1m x 1m size with vertical, inclined, and horizontal orientations installed in a lower height than the LiDAR scanner, combined with a five passages line pattern.